



ISSN 1811-1165 (Print)  
ISSN 2413-2179 (Online)

# EURASIAN PHYSICAL TECHNICAL JOURNAL

VOLUME 19, NO. 1(39), 2022

THE REPUBLIC OF KAZAKHSTAN

[phtj.ksu.kz](http://phtj.ksu.kz)

# EURASIAN PHYSICAL TECHNICAL JOURNAL

p - ISSN 1811-1165  
e - ISSN 2413-2179

Volume 19, No. 1(39), 2022

1<sup>st</sup> issue – March, 2004

## Journal Founder:

**E.A. BUKETOV KARAGANDA  
UNIVERSITY**

**Е.А. БӨКЕТОВ АТЫНДАҒЫ  
ҚАРАҒАНДЫ УНИВЕРСИТЕТІ**

**КАРАГАНДИНСКИЙ УНИВЕРСИТЕТ  
ИМЕНИ Е.А. БУКЕТОВА**

### Contact information:

Editorial board of EAPhTJ (Build. 2, room 216)  
E.A. Buketov Karaganda University  
Universitetskaya Str., 28, Karaganda,  
Kazakhstan, 100024  
Subscription index: 75240

Tel: +7(7212) 77-04-03  
Fax: +7(7212) 77-03-84  
E-mail: ephjt@mail.ru

Signed to print on 28.03.2022  
Format 60x84 1/8. Offset paper.  
Volume 17.75 p.sh. Circulation 300 copies.  
Agreed price. Order No. 50.

Басуға 28.03.2022 ж. қол қойылды.  
Пішімі 60×84 1/8. Офсеттік қағазы.  
Көлемі 17,75 ес.-б.т. Таралымы 300 дана.  
Бағасы келісім бойынша. Тапсырыс № 50.

Подписано в печать 28.03.2022.  
Формат 60 × 84 1/8. Офсетная бумага.  
Объем 17,75 печ.л. Тираж 300 экз.  
Цена договорная. Заказ № 50.

Printed in the Publishing House  
of the Karaganda Buketov University

Е.А. Бөкетов атындағы Қарағанды  
университеті баспасының баспаханасында  
басылып шықты

Отпечатано в Издательстве  
Карагандинского университета  
им. Е.А. Букетова

## Chief EDITOR

**Sakipova S.E.**, E.A.Buketov Karaganda University, Karaganda,  
Kazakhstan

## EDITORIAL BOARD

**Aringazin A.K.**, L.N. Gumilyov Eurasian National University, Nur-  
Sultan, Kazakhstan

**Dzhumanov S.**, Institute of Nuclear Physics, Uzbekistan Academy of  
Sciences, Tashkent, Uzbekistan

**Ibrayev N.Kh.**, Institute of Molecular Nanophotonics, E.A.Buketov  
Karaganda University, Kazakhstan

**Jakovics A.**, Institute of Numerical Modelling, University of Latvia,  
Riga, Latvia

**Kadyrzhanov K.K.**, L.N. Gumilyov Eurasian National University,  
Nur-Sultan, Kazakhstan

**Kucherenko M.G.**, Director of the Laser and Information Biophysics  
Centre, Orenburg State University, Orenburg, Russia

**Kuritnyk I.P.**, Department of Electronics and Automation, High  
school in Oswiecim, Poland

**Miau J.J.**, Department of Aeronautics and Astronautics, National  
Cheng Kung University, Tainan, Taiwan

**Narimanova G.N.**, Tomsk State University of Control Systems and  
Radioelectronics, Tomsk, Russia

**Potapov A.A.**, V.A. Kotelnikov Institute of Radio Engineering and  
Electronics of RAS, Moscow, Russia

**Pribaturin N.A.**, Institute of Thermal Physics, SB RAS, Novosibirsk,  
Russia

**Saulebekov A.O.**, Kazakhstan Branch of Lomonosov Moscow State  
University, Nur-Sultan, Kazakhstan

**Senyut V.T.**, Joint Institute of Mechanical Engineering of National  
Academy of Sciences of Belarus, Minsk, Belarus

**Shrager E.R.**, National Research Tomsk State University, Tomsk,  
Russia

**Stoiev M.**, South-West University «Neofit Rilski», Blagoevgrad,  
Bulgaria

**Suprun T.**, Institute of Engineering Thermophysics of NASU, Kyiv,  
Ukraine

**Trubitsyn A.A.**, Ryazan State Radio Engineering University,  
Ryazan, Russia

**Zeinidenov A.K.**, E.A Buketov Karaganda University, Karaganda,  
Kazakhstan

**Zhanabaev Z.Zh.**, Al-Farabi Kazakh National State University,  
Almaty, Kazakhstan

## TECHNICAL EDITORS

**Kambarova Zh.T.**, **Akhmerova K.E.**, E.A. Buketov Karaganda  
University, Karaganda, Kazakhstan

© Karaganda Buketov University, 2022

© Қарағанды Бөкетов университеті, 2022

Registration Certificate No. 4382-Zh, November 7, 2003.

Re-registration Certificate No.KZ50VPY00027647, October 6, 2020 issued by Information Committee  
of the Ministry of Information and Public Development of the Republic of Kazakhstan

## CONTENTS

<b>PREFACE</b> .....	4
<b>MATERIALS SCIENCE</b>	
1. <i>Surzhikov A.P., Malyshev A.V., Lysenko E.N., Stary O.</i> TEMPERATURE DEPENDENCES OF THE INITIAL PERMEABILITY OF LITHIUM-TITANIUM FERRITES PRODUCED BY SOLID-STATE SINTERING IN THERMAL AND RADIATION-THERMAL MODES .....	5
2. <i>Kozlovskiy A.L.</i> STUDY OF THE WEAR RESISTANCE DEGRADATION KINETICS OF ALN CERAMIC UNDER HEAVY ION IRRADIATION .....	10
3. <i>Dzhumanov S., Kurbanov U.T., Khudayberdiev Z.S.</i> METAL-INSULATOR TRANSITIONS IN DOPED <i>La</i> -BASED SUPER CONDUCTORS WITH SMALL-RADIUS DOPANTS.....	15
4. <i>Rakhadilov B.K., Satbaeva Z.A., Kozhanova R.S., Kowalewski P., Bayatanova L.B., Kalitova A.A.</i> EFFECT OF THE STRUCTURE FORMED AFTER BULK AND SURFACE HARDENING ON THE HARDNESS AND WEAR RESISTANCE OF 20Cr2Ni4A STEEL .....	20
5. <i>Aimukhanov A.K., Zeinidenov A.K., Rozhkova X.S., Akhatova Zh.Zh.</i> INFLUENCE OF PHTHALOCYANINE NANOSTRUCTURES ON OPTICAL AND PHOTOVOLTAIC CHARACTERISTICS OF A POLYMER SOLAR CELL .....	26
6. <i>Zeinidenov A.K., Aimukhanov A.K., Omarbekova G.I., Ilyassov B.R.</i> IMPACT OF THE ANNEALING TEMPERATURE OF In <sub>2</sub> O <sub>3</sub> FILMS ON THE PHOTOVOLTAIC CHARACTERISTICS OF A POLYMER SOLAR CELLS .....	34
<b>ENERGY</b>	
7. <i>Kaluzhsky D.L., Mekhtiyev A.D., Neshina Y.G., Alkina A.D., Sarsikheyev Y.Z.</i> THERMAL POWER PLANT BASED ON A FREE PISTON ENGINE AND A RECIPROCATING GENERATOR .....	40
8. <i>Novoselov I.Yu., Shrager E.R., Tikhonov A.</i> SYNTHESIS OF URANIUM-THORIUM OXIDE POWDERS IN LOW-TEMPERATURE PLASMA OF HIGH FREQUENCY TORCH DISCHARGE .....	50
9. <i>Obukhov S.G., Plotnikov I.A., Klimova G.N.</i> A NEW METHOD FOR DETERMINING PARAMETERS OF PHOTOVOLTAIC MODULE BASED ON THE DATA FROM TECHNICAL SPECIFICATION .....	55
<b>ENGINEERING</b>	
10. <i>Senyut V.T.</i> RESEARCH ON THE STRUCTURE OF THE MATERIAL BASED ON NANO- AND MICRO-SIZED CUBIC BN SYNTHESIZED FROM MECHANICALLY ACTIVATED GRAPHITE-LIKE BN WITH THE ADDITION OF ALUMINUM UNDER HPHT CONDITIONS.....	65
11. <i>Volokitina I.E., Volokitin A.V., Panin E.A., Latypova M.A., Kassymov S.S.</i> MICROSTRUCTURE EVOLUTION OF STEEL-ALUMINUM WIRE DURING DEFORMATION BY "EQUAL-CHANNEL ANGULAR PRESSING-DRAWING" METHOD.....	73
12. <i>Kubich V.I., Cherneta O.G., Yurov V.M., Baltabekov A.S., Guchenko S.</i> TRIBOLOGICAL CONTACT IN MATERIALS SYSTEMS "CuCrNiZrTi - M500", "CuCrNiZrTi - 5140H", "CuCrNiZrTi - 3310H" .....	78
13. <i>Uteпов Ye.B., Tolkynbayev T.A., Aniskin A., Akhazhanov S.B., Zharassov Sh.Zh., Tulebekova A.S., Akishev M.S.</i> ASSEMBLING A MULTISENSORY DEVICE FOR MONITORING AND ASSESSING CONCRETE CURING CONDITIONS.....	90
14. <i>Nussupbekov B.R., Sakipova S.E., Edris A., Khassenov A.K., Nussupbekov U.B., Bolatbekova M.</i> ELECTROHYDRAULIC METHOD FOR PROCESSING OF THE PHOSPHORUS CONTAINING SLUDGES .....	99

---

---

**PHYSICS AND ASTRONOMY**

15. <i>Yadawa P.K., Rai S., Chaurasiya N., Prajapati A.K.</i> INVESTIGATION OF INTERMETALLIC GD/FEAL TERNARY COMPOUND BY ELASTIC, THERMOPHYSICAL AND ULTRASONIC ANALYSIS.....	105
16. <i>Hwashed Waleed S.</i> NUCLEAR STRUCTURE OF THE HEAVIEST BORON ISOTOPE .....	113
17. <i>Kassenova T.K.</i> PARAMETRIZED EIGHT-VERTEX MODEL AND KNOT INVARIANT $10_{136}$ .....	119
<b>SUMMARIES</b> .....	127
<b>INFORMATION ABOUT AUTHORS</b> .....	138
<b>GUIDELINES FOR AUTHORS</b> .....	140

**Dear authors and readers!**

**Dear Colleagues!**

It's already becoming a tradition to inform our readers with most important achievements of the "Eurasian Physical Technical Journal".

Since 2019, Eurasian phys. tech. j. has been indexed in the Scopus database and has a ranking in the SJR-platform (SCImago Journal and Country Rank). We are proud that on the SJR-platform our Journal is included in the Q3 quartile on Energy and Engineering - <http://www.scimagojr.com/journalsearch.php?q=21100920795&tip=sid&clean=0>

The Open Access "Eurasian Physical Technical Journal status provides free access to published full-text articles in PDF format, in addition to domestic databases of electronic libraries and on the EBSCO website.

We also invite you to take part in the work of the 12th International Scientific Conference "Chaos and Structures in Nonlinear Systems. Theory and Experiment", which will be held on June 17-19, 2022 on the basis of the Toraigyrov University (Pavlodar, Kazakhstan). The conference sections:

1. Dynamic chaos, self-organization in nonlinear systems, in astrophysics, in condensed environments.
2. Energy, automation and telecommunications.
3. Information technologies and methodological problems in the development of modern society and education.
4. Innovative technologies, achievements and development prospects in engineering.
5. Ecology and safety in the technosphere: contemporary problems and solutions

As part of the conference, it's planned to leave the participants to the picturesque Bayanaul, located on the shore of Lake Sabyndykol. Detailed information is available at <https://sci-conf.tou.edu.kz/index.php?lang=rus>

Publication of articles in Open Access according to the Gold Open Access model means unlimited and free access is available, it's absolutely free of charge for readers and all interested persons. To compensate for the editing, reviewing and publishing processes cost of an author's fee (Open Access Fee) is charged. Payment details are on the site.

In this issue, readers can find articles aimed at solving modern topical problems of technical physics. On behalf of the editorial board of the Eurasian Physical and Technical Journal, I express my sincere gratitude to our experts who took the time to review the articles submitted to the journal. Without their highly professional work and patience, this release would not have been possible.

We hope that the proposed scientific works will interest our readers.

I'll be glad to see you among our authors of the next issues.

Best regards,

ch. editor, prof. Saule Sakipova

March, 2022

DOI 10.31489/2022No1/5-9

UDC 538.9

## TEMPERATURE DEPENDENCES OF THE INITIAL PERMEABILITY OF LITHIUM-TITANIUM FERRITES PRODUCED BY SOLID-STATE SINTERING IN THERMAL AND RADIATION-THERMAL MODES

Surzhikov A.P.<sup>1</sup>, Malyshev A.V.<sup>1</sup>, Lysenko E.N.<sup>1</sup>, Stary O.<sup>2</sup><sup>1</sup>Tomsk Polytechnic University, Tomsk, Russia, malyshev@tpu.ru<sup>2</sup>Ceské vysokéučenitěchnické v Prague, Prague, Czech Republic

*The paper investigates the features of phase and structural transformations in lithium-titanium ferrites with regard to the time and temperature of solid-state sintering in thermal and radiation-thermal modes. These properties are studied with using the temperature dependence of the initial permeability. It is shown that electron beam exposure during solid-state sintering sharply accelerates the dissolution of impurity inclusions in ferrites. Also phase homogeneity of lithium-titanium ferrites products increase. The obtained results can be used for increasing of the phase homogeneity in ferrite production.*

**Keywords:** lithium ferrites, solid-state sintering, electron beams, high temperatures, initial permeability.

### Introduction

Electromagnetic properties are the key requirements imposed on ferrite materials during their production and operation. It is known that these properties depend on chemical composition of the mixture and the ferrite manufacturing technique. The main manufacturing operation that largely determines electromagnetic properties of the ferrite material is extremely time-consuming sintering of compacted products. Two-stage introduction of components, additional mixing of ferrite with ferrite powder of similar composition, liquid phase, forced sintering, and ultrasonic assisted sintering are the techniques used to activate sintering [1–10]. These sintering modes increase the occurrence of impurity phases, which decrease chemical and structural homogeneity of the material and deteriorate its electromagnetic properties.

In addition, the impurity phase concentration cannot always be decreased by temperature regime of sintering, especially in case of thermally unstable compounds such as lithium ferrispinels. In recent years, the effect of ionizing radiation fluxes has gained momentum in manufacturing and modification of materials. A fundamental phenomenon of a multiple increase in the speed of multicomponent powder synthesis [11–14] and sintering of compacts [15–19] induced by radiation-thermal mode was discovered. Sintering of lithium-titanium ferrites under specific conditions of a combined effect of high temperatures and intense electron fluxes is the most well studied process [20–22]. The patterns of ferrite compaction were revealed, and a multiple increase in the compaction rate of lithium-titanium ferrites under these sintering conditions was shown [23–25]. Magnetic properties of ferrimagnets are the key functional properties. It is known that any ferrite manufacturing technique is ultimately aimed at achieving the designed performance level. The root causes and features of the formation of ferrite magnetic properties are of particular interest. Therefore, data on phase transformations in ferrites during radiation-thermal (RT) sintering can be important and productive. The paper investigates the features of phase transformations of ferrite ceramics sintered in RT mode using the temperature dependence of the initial permeability. A comparative study of ferrite samples sintered in thermal (T) mode was performed to reveal the radiation effect. XRD analysis cannot be implemented for lithium ferrites due to overlapping of the main lines of the  $\text{LiFe}_5\text{O}_8$ ,  $\text{LiFeO}_2$ , and  $\text{Fe}_3\text{O}_4$  phases.

### 1. Experimental part

#### 1.1 Materials

The study investigates lithium-titanium ferrite powders synthesized from a mechanical mixture of oxides and carbonates containing 11.2 wt%  $\text{Li}_2\text{CO}_3$ , 18.65 wt%  $\text{TiO}_2$ , 7.6wt%  $\text{ZnO}$ , and 2.74 wt%  $\text{MnCO}_3$ , and the rest of the mixture is  $\text{Fe}_2\text{O}_3$ . For pressing, 10% solution of polyvinyl alcohol is added in an amount of

12 wt% of the mixture. Compacts are made in the form of annular cores 2 mm thick, with an inner and outer diameter of 18 mm and 14 mm, respectively, by single-action cold pressing using a PGr-10 press.

### 1.2 Characterization techniques

The optimal compacting pressure is chosen experimentally. It is found that the compacting pressure in the range of (110–200) MPa is optimal to provide an acceptable density of both green and sintered samples. The pressing mode employed was as follows:  $P=130$  MPa; 1 min pressing time; RT and T modes of compact sintering. In RT sintering, the compacts were exposed to a pulsed electron beam with energy of (1.5–2.0) MeV generated by the ILU-6 accelerator. The pulse beam current was (0.5–0.9) A, the irradiation pulse duration was 500  $\mu\text{s}$ , the pulse repetition rate was (5–50) Hz, and the compact heating rate was 1000 C/min. The samples were irradiated in a lightweight chamotte box with a wall bottom 15 mm thick. The exposed side of the box was covered with a radiation-transparent cover with a mass thickness of 0.1  $\text{g}\cdot\text{cm}^{-1}$ . Temperature was measured using a control sample placed in close proximity to the sintered compacts.

T sintering was performed in a preheated chamber electric furnace, which provided a heating rate comparable to radiation heating rate. The cell design and temperature control technique are similar to those used for RT sintering. Sintering in both modes was performed in air. Methods for measuring initial permeability ( $\mu_i$ ) available in literature were analyzed, and the method chosen was based on measurement of the ring core inductance in an alternating magnetic field [26].

Measurements were performed for samples sintered in different modes with a single-layer winding uniformly distributed around the core perimeter during sample cooling from the temperature point that intentionally exceeded the Curie point (about 620 K) using an E7-12 inductance meter at 1 MHz frequency. Temperature dependence of  $\mu_i$  was determined from temperature dependence of inductance by formula 1:

$$\mu_i = L/L_0, \quad (1)$$

where  $L$  and  $L_0$  are winding inductance with and without a ferrite core.

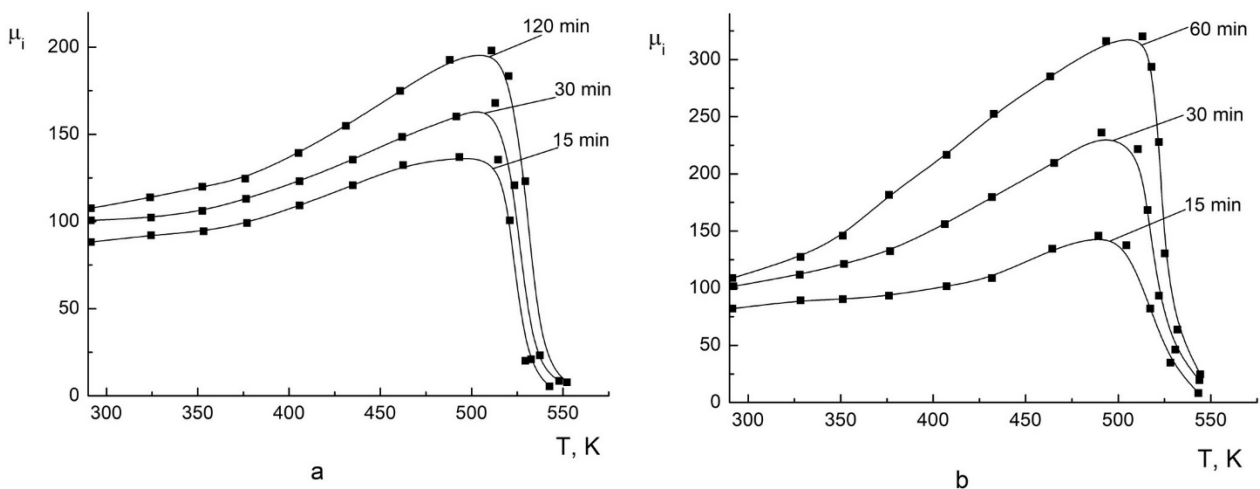
The minimum value of the inductance  $L$  at temperature above the Curie point was taken for inductance of the winding without a core  $L_0$ . The validity of using  $L_0$  as winding inductance is confirmed by direct calculation performed for toroidal rectangular cores by formula 2:

$$L_0 = 2 \cdot 10^{-3} \cdot N^2 \cdot h \cdot \ln(D_2/D_1) \quad (\mu\text{H}/\text{cm}), \quad (2)$$

where  $N$  is the number of turns;  $h$  is sample thickness;  $D_1$  and  $D_2$  are the inner and outer diameter of the core.

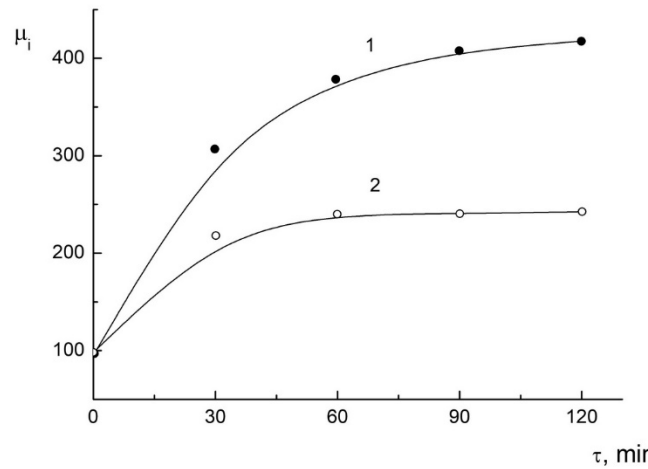
## 2. Results and discussion

Fig. 1 shows the curves of initial permeability  $\mu_i$  against temperature for ferrites sintered at 1373 K in T and RT modes. All curves in Fig. 1 demonstrate an increase in initial permeability at increased temperature with its maximum achieved near the Curie point.



**Fig.1.** Temperature dependence of  $\mu_i$  for ferrites sintered at 1373 K in T (a) and RT (b) modes for different sintering time

After the maximum, permeability steeply declines and remains stable beyond the Curie point. The  $\mu_i$  value at the temperature dependence maximum ( $\mu_{i \max}$ ) grow as sintering time increases, and the rate of its growth in RT mode significantly exceeds the growth rate of  $\mu_{i \max}$  in T mode. The kinetic dependences of initial permeability are shown in Fig. 2.



**Fig. 2.** Dependence of  $\mu_{i \max}$  on time of ferrite sintering at 1373 K in T (1) and RT (2) modes

The data in Fig. 2 show a more complete inclusion removal for RT mode. The difference in sample density (1 h sintering time) was  $\sim 5\%$ , and the difference in  $\mu_{i \max}$  was  $\sim 32\%$  in both sintering modes, therefore it can be assumed that inclusion removal is not due to porosity removal, but due to probable dissolution of impurity phases in the main product. The features of the temperature drop  $\mu_i(T)$  were analyzed based on the graphs of the rate of decrease in permeability  $d\mu_i/dT$  against temperature plotted in Fig. 3.

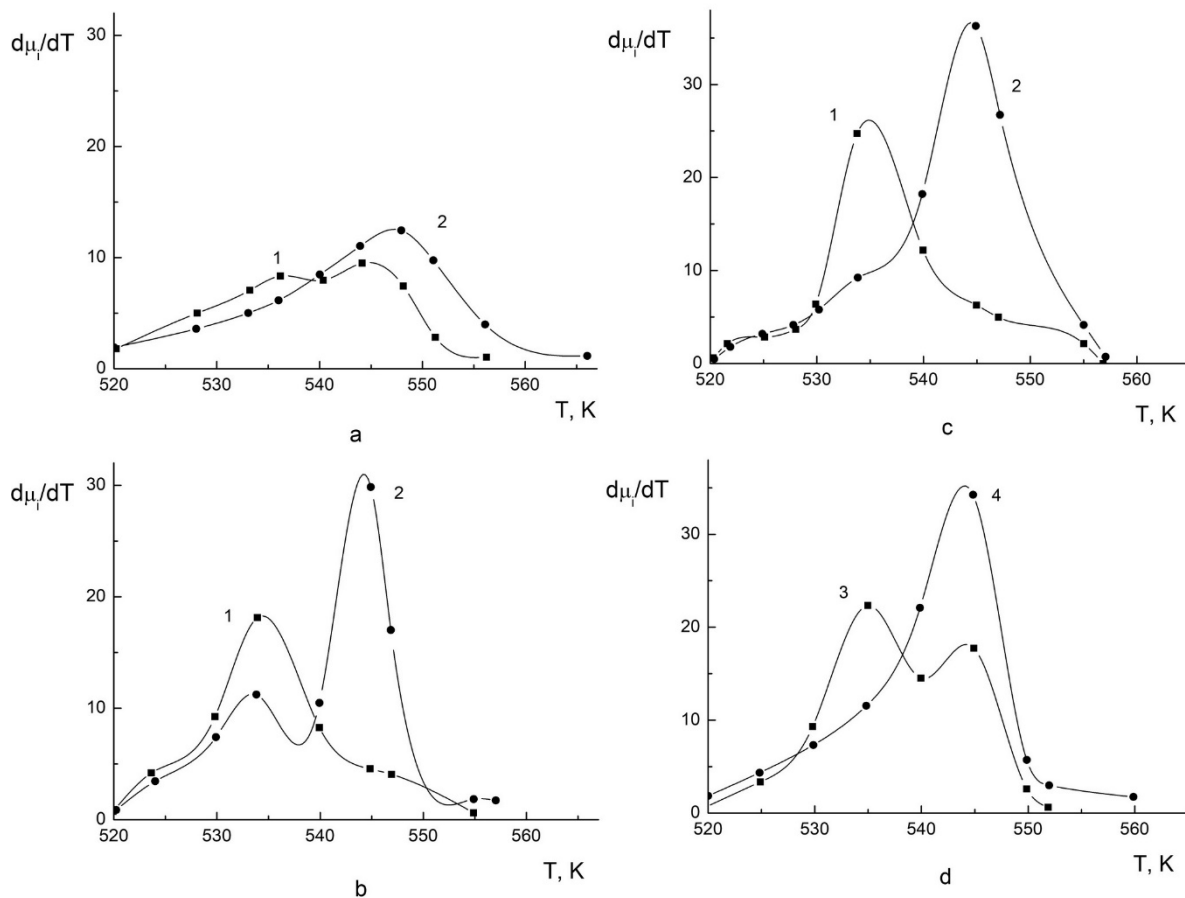


**Fig. 3.** Temperature dependences of the rate of decrease in  $\mu_i$  near the Curie point for ferrites with various sintering time: a) 15 min; b) 30 min; c) 60 min; d) 300 min (3) and 600 min (4). 1, 3, 4 – T sintering mode, 2 – RT sintering mode



As can be seen, these dependences exhibit two distinct and consistently repeated peaks at 537 and 548 K. This indicates at least two chemically similar magnetic phases in the sample. Typically, a low-temperature phase predominates at early (up to 2 h) sintering stages in T mode (Fig. 3, *a, b, c*). Sintering for 5 h equalizes the content of both phases (Fig. 3*d*, curve 3), and after 10 h sintering, a high-temperature phase dominates (Fig. 3*d*, curve 4) [27, 28].

RT sintering yields a qualitatively different result a high-temperature phase dominates at all sintering stages, although traces of the low-temperature phase were detected as well (Fig. 3, *a, b, c*). No correlation is found for the change in the content of both phases, which can imply that a high-temperature magnetic phase is formed mainly due to non-magnetic inclusions [29, 30].

## Conclusion

In this article, from a comparative study of temperature dependencies of initial permeability lithium ferrites at radiation-thermal and thermal solid-phase sintering, the share of the radiation component in the formation of electromagnetic parameters of the material is established.

The scientific significance of the results is determined by data on the temperature dependences of the initial permeability shows that electron beam exposure during sintering of lithium-titanium ferrite compacts sharply accelerates dissolution of impurity inclusions.

The possibility of using an electron beam to increase phase homogeneity of ferrite products during their manufacturing makes the study results practically relevant.

The next step is to study the same patterns in liquid-phase ferrite sintering under the same radiation-thermal and thermal conditions. In addition, the share of the radiation component in such sintering will be determined and the results of this article will be compared with subsequent studies. Also, the effects will be determined depending on the type of sintering.

## Acknowledgments

The research is funded by the Ministry of Education and Science of the Russian Federation as part of the "Science" Program (project No. FSWW-2020-0014). This research was supported by TPU development program.

## REFERENCES

- 1 Letyuk L.M., Nifontov V.A., Babich E.A., Gorelik S.S. Effect of low-melting additives on the formation of the microstructure and the properties of ferrites with a rectangular hysteresis loop. *Izv. Akad. Nauk Neorg. Mater.* 1976, Vol. 12, pp. 2023 – 2026. [in Russian]
- 2 Dmitriev M.V., Letyuk L.M., Shipko M.N. Study of oxygen diffusion in the surface layers of Mn-Zn ferrites. *Technical physics.* 1982, Vol. 27, pp. 338 – 339.
- 3 Letyuk L.M. Recrystallization of ferrites and its effect on the processes of microstructure formation in ferrosinels. *Soviet Powder Metallurgy and Metal Ceramics.* 1980, Vol. 19, No. 5, pp. 359 – 364.
- 4 Zinovik M.A., Zinovik E.V. Ferrites with rectangular and square hysteresis loops. *Powder Metallurgy and Metal Ceramics.* 2005, Vol. 44, pp. 66 – 74.
- 5 Letyuk L.M., et al. Special features of the formation of the microstructure of ferrites sintered in the presence of a liquid phase. *Izv. Vysshikh Uchebnykh Zavedenij. Chernaya Metallurgiya.* 1979, Vol. 11, pp. 124 – 127. [in Russian]
- 6 Micheli A.L. Preparation of lithium ferrites by coprecipitation. *IEEE Transactions on Magnetics.* 1970, Vol. 6, pp. 606 – 608.
- 7 Surzhikov A.P., Pritulov A.M., Lysenko E.N., et al. Calorimetric investigation of radiation-thermal synthesized lithium pentaferrite. *J. Therm. Anal. Calorim.* 2010, Vol. 101, No. 1, pp. 11 – 13.
- 8 Minin V.M. Effect of sintering conditions on the microstructure and electromagnetic properties of Li-Mg-Mn ferrite memory elements. *Soviet Powder Metallurgy and Metal Ceramics.* 1982, Vol. 21, pp. 698 – 701.
- 9 Zahir R., Chowdhury F.-U.-Z., Uddin M.M., et al. Structural, magnetic and electrical characterization of Cd substituted Mg ferrites synthesized by double sintering technique. *J. Magn. Magn. Mater.* 2016, Vol. 410, pp. 55 – 62.
- 10 Manjura Hoque S., Abdul Hakim M., Mamun Al, et al. Study of the bulk magnetic and electrical properties of MgFe<sub>2</sub>O<sub>4</sub> synthesized by chemical method. *Materials Sciences and Applications.* 2011, Vol. 2, pp. 1564 – 1569.
- 11 Surzhikov A.P., Pritulov A.M., Lysenko E.N., et al. Influence of solid-phase ferritization method on phase composition of lithium-zinc ferrites with various concentration of zinc. *Journal of Thermal Analysis and Calorimetry.* 2012, Vol. 109, No. 1, pp. 63 – 67.

- 12 Yurov V.M., Baltabekov A.S., Laurinas V.C., Guchenko S.A. Dimensional effects and surface energy of ferroelectric crystals. *Eurasian Physical Technical Journal*. 2019, Vol. 16, No. 1, pp. 18 – 23.
- 13 Lyakhov N.Z., Boldyrev V.V., Voronin A.P., Gribkov O.S., Bochkarev I.G., Rusakov S.V., Auslender V.L. Electron beam stimulated chemical reaction in solids. *J. Therm. Anal. Calorim.* 1995, Vol. 43, pp. 21 – 31.
- 14 Sharma P., Uniyal P. Investigating thermal and kinetic parameters of lithium titanate formation by solid-state method. *J. Therm. Anal. Calorim.* 2017, Vol. 128, pp. 875 – 882.
- 15 Salimov R.A., Cherepkov V.G., Golubenko J.I., et al. D.C. high power electron accelerators of ELV-series: status, development, applications. *J. Radiation Phys. Chem.* 2000, Vol. 57, pp. 661 – 665.
- 16 Cleland M.R., Parks L.A. Medium and high-energy electron beam radiation processing equipment for commercial applications. *Nucl. Instr. Meth. B.* 2003, Vol. 208, pp. 74 – 89.
- 17 Mehnert R. Review of industrial applications of electron accelerators. *Nucl. Instr. Meth. B.* 1996, Vol. 113, pp. 81 – 87.
- 18 Neronov V.A., Voronin A.P., Tatarintseva M.I., Melekhova T.E., Auslender V.L. Sintering under a high-power electron beam. *J. Less-Common Metals*. 1986, Vol. 117, pp. 391 – 394.
- 19 Ershov B.G. Radiation technologies: their possibilities, state, and prospects of application. *Herald of the Russian Academy of Sciences*. 2013, Vol. 83, No. 5, pp. 437 – 447.
- 20 Surzhikov A.P., Frangulyan T.S., Ghyngazov S.A. A thermoanalysis of phase transformations and linear shrinkage kinetics of ceramics made from ultrafine plasm-chemical  $ZrO_2(Y)-Al_2O_3$  powders. *Journal of Thermal Analysis and Calorimetry*. 2014, Vol. 115, No. 2, pp. 1439 – 1445.
- 21 Stary O., Malyshev A.V., Lysenko E.N., Petrova A. Formation of magnetic properties of ferrites during radiation-thermal sintering. *Eurasian phys. tech. j.* 2020, Vol. 17, No. 2, pp. 6 – 10.
- 22 Boldyrev V.V., Voronin A.P., Gribkov O.S., Tkachenko E.V., Karagedov G.R., Yakobson B.I., Auslender V.L. Radiation-thermal synthesis. Current achievement and outlook. *J. Solid State Ion.* 1989, Vol. 36, pp. 1 – 6.
- 23 Surzhikov A.P., Frangulyan T.S., Ghyngazov S.A., Vasil'ev I.P., Chernyavskii A.V. Sintering of zirconia ceramics by intense high-energy electron beam. *Ceramics Int.* 2016, Vol. 42, No. 12, pp. 13888 – 13892.
- 24 Nikolaev E.V., Astafyev A.L., Nikolaeva S.A., et al. Investigation of electrical properties homogeneity of Li-Ti-Zn ferrite ceramics. *Eurasian phys. tech. j.* 2020, Vol. 17, No. 1, pp. 5 – 12.
- 25 Sharipov M.Z., Hayitov D.E., Rizoqulov M.N., Islomov U.N., Raupova I.B. Domain structure and magnetic properties of terbium ferrite-garnet in the vicinity of the magnetic compensation point. *Eurasian Physical Technical Journal*. 2019, Vol. 16, No. 2(32), pp. 21 – 25.
- 26 Smith J., Wijn H.P.J. *Ferrites: Physical properties of ferromagnetic oxides in relation to their technical application*. 1959, Eindhoven, Phillips Technical Library, 233p.
- 27 Neronov V.A., Voronin A.P., Tatarintseva M.I., et al. Sintering under a high-power electron beam. *Journal of the Less Common Metals*. 1986, Vol. 117, pp. 391 – 394.
- 28 Geguzin J.E. *Physics of Sintering*. 1984, Moscow, Nauka, 360p. [in Russian]
- 29 Takane S., Umeda H., Aoki T., Murase T. Influence of  $Al_2O_3$  Addition on the temperature dependence of initial permeability of NiCuZn ferrites. *Key Eng. Mater.* 2011, Vol. 485, pp. 225 – 228.
- 30 Malyshev A.V., Petrova A.B., Surzhikov A.P., Sokolovskiy A.N. Effect of sintering regimes on the microstructure and magnetic properties of LiTiZn ferrite ceramic. *Ceramics Int.* 2019, Vol. 45, pp. 2719 – 2724.

DOI 10.31489/2022No1/10-14

UDC 538.971

## STUDY OF THE WEAR RESISTANCE DEGRADATION KINETICS OF ALN CERAMIC UNDER HEAVY ION IRRADIATION

Kozlovskiy A.L.<sup>1,2</sup>

<sup>1</sup>L.N. Gumilyov Eurasian National University, Nur-Sultan, Kazakhstan, [kozlovskiy.a@inp.kz](mailto:kozlovskiy.a@inp.kz)

<sup>2</sup>Institute of Nuclear Physics, Almaty, Kazakhstan

*This work is devoted to the study of changes in the strength properties of AlN ceramics, in particular, the dry friction coefficient and parameters of wear resistance and surface defectiveness, depending on the dose of irradiation with heavy Xe<sup>22+</sup> ions with an energy of 200 MeV. Interest in these ceramics is due to their high thermal conductivity, hardness and wear resistance, as well as excellent insulating properties, which makes them promising candidate materials in nuclear power, rocket engineering and microelectronics. At the same time, the operation of these ceramics under conditions of external influences, such as mechanical friction, pressure on the surface, as well as the effect of ionizing radiation, requires additional research and obtaining new data on the stability and retention of properties during the entire service life. During the studies carried out, it was found that at low irradiation doses of 10<sup>10</sup>-10<sup>11</sup> ions/cm<sup>2</sup>, which are characterized by the formation of single point defects and a low probability of surface degradation as a result of the initialization of gas swelling processes, the dry friction coefficient practically does not change, which indicates ceramics high mechanical friction resistance. However, an increase in the irradiation fluence up to 10<sup>12</sup> ion/cm<sup>2</sup>, which is characterized by the processes of overlapping radiation-induced damaged areas, a deterioration in the dry friction coefficient is observed after 15000 test cycles, which indicates fatigue wear of the ceramic surface and degradation as a result of external influences.*

**Keywords:** radiation defects, nitride ceramics, wear resistance, dry friction coefficient, heavy ions.

### Introduction

One of the key parameters responsible for the life of ceramic materials is the preservation of long-term resistance to external mechanical and radiation effects arising during their use [1,2]. At the same time, the rapid development of a new direction in materials science associated with the transition from steels and alloys to ceramic materials and their widespread use under conditions of increased radiation backgrounds, mechanical influences and high temperatures requires new knowledge about the mechanisms of material degradation. Interest in these ceramic materials, in particular ceramics based on aluminum or silicon nitride, is due to their excellent mechanical strength, thermal conductivity, as well as corrosion resistance and good insulating properties [3-5]. All these indicators open up broad prospects for the use of these materials as a basis for structural materials for the walls of fuel rods of high-temperature nuclear reactors or as a basis for materials of inert matrices of nuclear fuel. Moreover, in most cases, these materials are subjected to high mechanical stresses and friction during operation, which can lead to the destruction of the contacting surfaces and their deformation [6-8]. In the case when materials during operation are exposed not only to mechanical stress, but also to radiation exposure, taking into account the deformation processes caused by radiation is important, since it can have a negative effect on the mechanical and strength properties of the material surface [9,10]. As a rule, at low radiation doses, the accumulation of radiation damage is limited due to the isolation of point defects and defect regions formed during the passage of incident ions through the material. In this case, the isolation of defective areas leads to the appearance of additional microdistortions and deformations in the structure [11-13]. In the case when the defect areas overlap, the concentration of microdistortions and deformations increases, in this case their accumulation in the structure of the damaged layer can lead to the appearance of nonequilibrium states or amorphization. The accumulation of microdistortions in the structure of the near-surface layer leads to overvoltage of the structure and partial extrusion and swelling of the near-surface layer, accompanied by a sharp change in the surface relief, which can negatively affect not only the strength properties of ceramics, but also the frictional characteristics [14-

16]. In turn, the nature of the effect of surface defectiveness is a very important issue in radiation materials science and the study of the strength properties of ceramics exposed to irradiation [17,18].

The aim of this work is to study the change in the dry friction coefficient and wear resistance of ceramics exposed to irradiation with heavy  $\text{Xe}^{22+}$  ions at various radiation doses. The strength characteristics were determined at different values of the load on the swinging body in order to determine the change in the value of the dry friction coefficient and wear resistance under various external influences. The choice of the type of irradiation ions and radiation exposure doses is due to the possibility of simulation of radiation damage in the near-surface layer, which is most susceptible to external influences under mechanical stresses.

## 1. Experimental part

Ceramics based on aluminum nitride (AlN), which has high hardness and resistance to external influences, were selected as objects of research. The samples under study have a polycrystalline structure of the hexagonal type; the density of ceramics, according to the passport data, is  $3.26 \text{ g/cm}^3$ . Before irradiation, the surface of the samples was mechanically polished in order to eliminate any roughness and irregularities.

Simulation of radiation damage was carried out at the DC-60 (Nur-Sultan, Kazakhstan) heavy ion accelerator.  $\text{Xe}^{22+}$  ions with an energy of 200 MeV were chosen as the ion flux, the irradiation doses were  $10^{10}$ - $10^{12} \text{ ion/cm}^2$ . The choice of this type of ions with an energy of 200 MeV is due to the possibility of simulating radiation-induced damage in the structure of the near-surface layer with a thickness of 12-15 microns, comparable in the effect of uranium fission fragments during the uranium fission reaction in a nuclear reactor and further interaction of fission fragments with the materials of the walls of the fuel rods, so and inert nuclear fuel matrices. Irradiation doses were selected based on theoretical calculations and experimental works [18-20], according to which, in the case of irradiation with doses of  $10^{10}$ - $10^{11} \text{ ions/cm}^2$ , the main defects arising in the structure are point defects and dislocations, which are isolated from each other due to low radiation doses. The isolation of defects is due to the radii of the damaged areas, which for the selected ions with these energies are no more than 5-7 nm. For irradiation doses of  $10^{12} \text{ ions/cm}^2$ , according to theoretical calculations, the so-called effect of overlapping radiation-induced damaged areas can be observed, which leads to the accumulation of defects and dislocations in the structure of the near-surface damaged layer and the appearance of distortions and deformations in the structure.

Study of the strength properties of the ceramic surface, in particular, dry friction coefficient and wear resistance of ceramics before and after irradiation was determined using the tribological method. The number of test cycles was 20000, the load on the metal ball was from 50 to 200 N.

## 2. Results and discussion

Figure 1 shows the results of cyclic wear resistance tests at various values of the load on the swinging body in order to determine the value of the dry friction coefficient. As a reference sample, a ceramic sample in its original state, unaffected by external influences. The dry friction coefficient for the initial sample was 0.44-0.45 at a load of 50 N, while no changes in this value were observed during 20000 consecutive cyclic impacts, except within the statistical error. The absence of changes in the dry friction coefficient during long-term tests indicates a high resistance to external mechanical influences, as well as a high wear resistance of the surface of unirradiated ceramics. An increase in the load from 50 to 150 N does not lead to significant changes in the dry friction coefficient for the original sample, which in turn confirms the high wear resistance to external mechanical influences of various forces. An increase in the load to 200 N leads to an insignificant increase in the dry friction coefficient for the initial sample from 0.44-0.45 to 0.46-0.48, which indicates the appearance of a small resistance at high stresses.

For irradiated samples at doses of  $10^{10}$ - $10^{11} \text{ ion/cm}^2$ , the change in the dry friction coefficient both in the case of the initial stage of testing and during cyclic tests is practically not observed, which indicates a high resistance to external radiation effects of the near-surface layer. Small changes in the initial values of the dry friction coefficient can be caused by a slight imperfection of the surface of the samples caused by the emerging deformations of the crystal structure and a change in the surface roughness. It should be noted that, in this case, the deformations and distortions of the structure are of a local isolated nature due to the formation of isolated defect regions along the trajectory of incident heavy ions in the material [18]. In the case of dielectric ceramics irradiated with heavy ions, the main changes caused by the interaction of ions

with the target material are related to both the redistribution of the electron density and the formation of heterogeneities in its distribution.

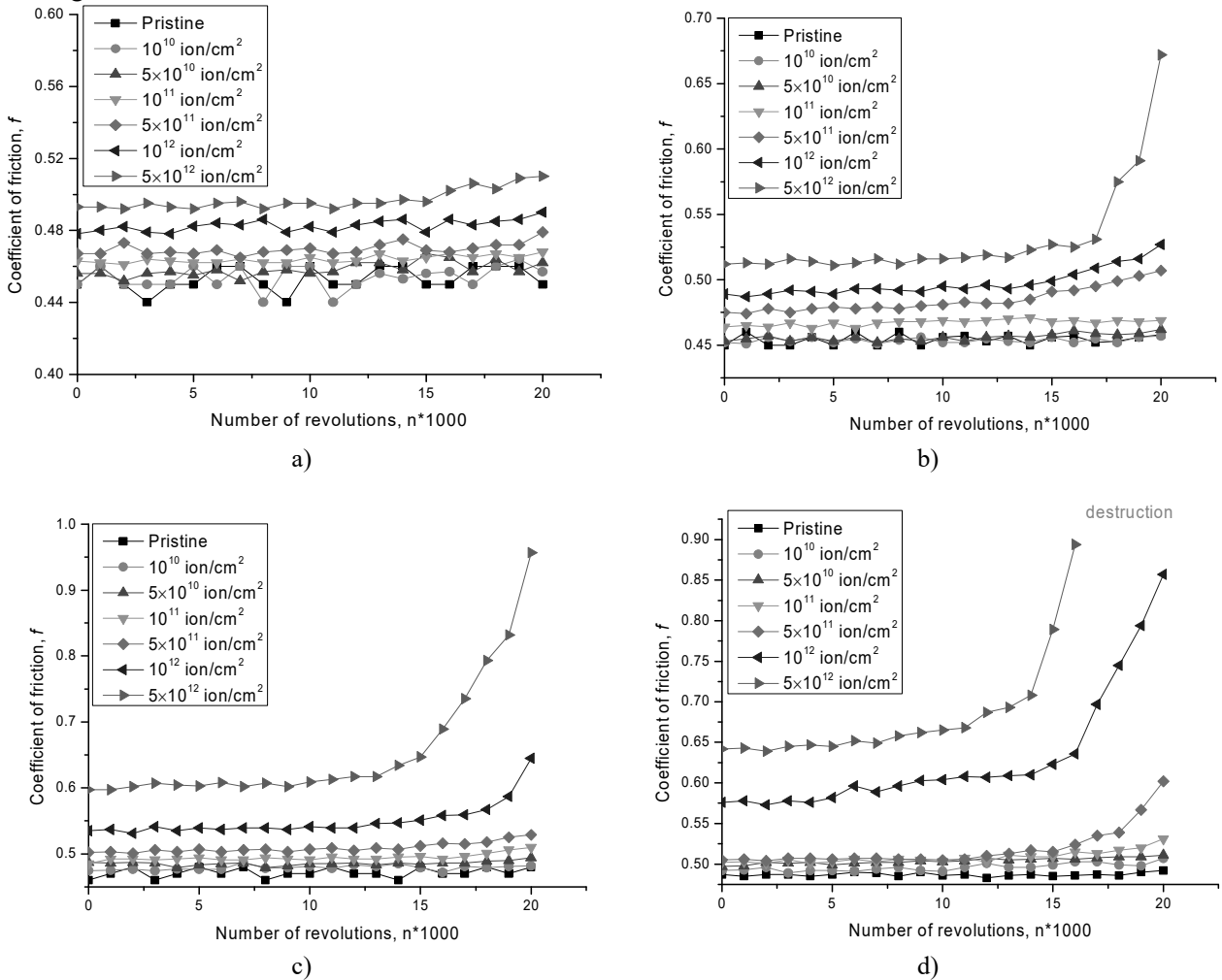


**Fig.1.** Cyclic tests for determination of dry friction coefficient at different stresses:  
a) 50 N; b) 100 N; c) 150 N; d) 200 N

Also, a small contribution is made by atomic displacements arising from inelastic collisions of ions with atoms of the crystal lattice. At the same time, due to the dielectric nature of ceramics, the change in the electron density caused by irradiation does not have the ability to recover and relax, as it happens in metals, where the electron mobility is high enough. The result of such interactions is a change in covalent bonds in the structure, as well as the formation of nonequilibrium regions with altered properties, which leads to deformation and distortion of irradiated layer. However, the nature of these changes, as well as their effect on changes in structural and strength properties, as shown earlier, has a pronounced dependence not only on the energy of incident ions, but primarily on the irradiation fluence.

Analysis of dry friction coefficient dependencies for samples irradiated with doses of  $10^{10}$ - $10^{11}$  ion/cm<sup>2</sup> showed that no significant changes in the value of the coefficient were observed, which indicates the preservation of a high degree of resistance to radiation-induced damage and their effect on the wear resistance of the surface layer. The main changes in the dry friction coefficient are observed for samples irradiated with doses of  $5 \times 10^{11}$ - $5 \times 10^{12}$  ion/cm<sup>2</sup>, for which, according to theoretical estimates, the presence of overlaps of defective areas in the structure of the near-surface layer is characteristic. In this case, changes in the dry friction coefficient occur not only at the beginning of the tests, which is associated with deformation of the surface and an increase in the friction resistance, but also a sharp increase in the dry friction coefficient after 15000-17000 test cycles. This increase is primarily associated with a sharp deterioration of the surface associated with the appearance of hillock-like inclusions, the formation of which is caused by the squeezing out of defective regions from the volume, as well as by the swelling of the irradiated layer.

The formation of hillocks or hillock-like inclusions at doses above  $10^{11}$  ion/cm<sup>2</sup>, as well as the mechanisms of their formation, were shown in [19,20], according to which deformation processes caused by irradiation lead to disordering of the structure, as well as amorphization of the structure of the damaged layer. Consequently, the resulting defects accumulate in the disorder regions, which causes the appearance of nonequilibrium highly distorted and deformed inclusions, leading to swelling of the surface near the joints and grain boundaries. At the same time, the accumulation of such inclusions leads to a sharp deterioration in the structural and heat-conducting properties, which in turn can also affect the wear resistance.

According to the data presented in Figure 1, an increase in the load at irradiation doses of  $5 \times 10^{11}$ - $5 \times 10^{12}$  ion/cm<sup>2</sup> leads to an increase in the dry friction coefficient, which indicates an increase in surface defectiveness, as well as a decrease in crack resistance and wear resistance. It should be noted that at a maximum load of 200 N, for samples irradiated with a dose of  $5 \times 10^{12}$  ion/cm<sup>2</sup>, after 15000 cycles, a sharp increase in the dry friction coefficient by 1.5-2 times was observed, which indicates the destruction of the surface and the formation of a large number of cracks. Evaluation of ceramic surface defect index depending on irradiation dose and subsequent mechanical action was carried out by comparison of dry friction coefficient indices depending on external effect type with reference sample index. The results are shown in Figure 2 as a comparative chart.

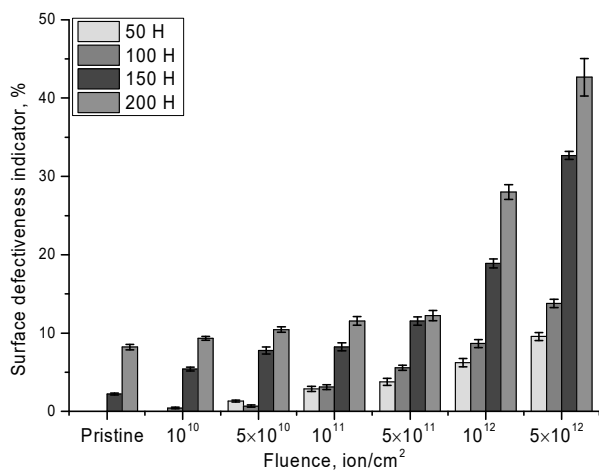


**Fig.2.** Diagram of the samples surface defectiveness index depending on sample load parameter at the beginning of test

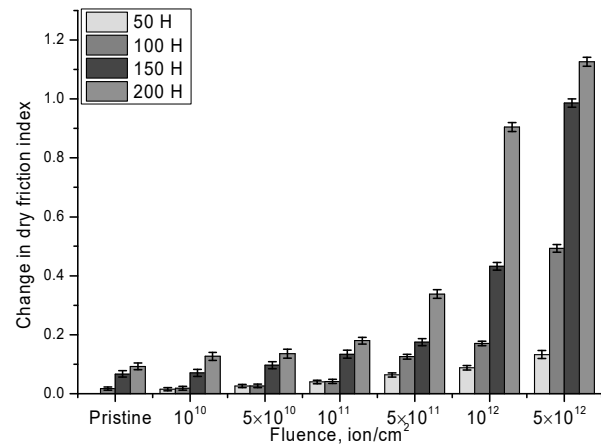


**Fig.3.** Diagram of dry friction coefficient depending on load parameter

As can be seen from the data of the comparative diagram, the greatest deterioration of surface defects is observed for  $5 \times 10^{11}$ - $5 \times 10^{12}$  ion/cm<sup>2</sup> radiation doses, while with an increase in load, the surface defects increase by 3-4 times. Such a sharp increase indicates a deterioration in wear resistance and a decrease in crack resistance of the surface of samples exposed to high-dose irradiation. The wear resistance of the ceramic surface during testing was evaluated by comparative analysis of changes in dry friction indicators after a series of cyclic tests. The results are shown in Figure 3. As can be seen from the presented data of the diagram, in the case of irradiation doses of  $10^{10}$ - $10^{11}$  ions/cm<sup>2</sup>, the change in the dry friction coefficient after 20000 tests is insignificant and does not exceed 5-7 % of the initial value, which indicates a high resistance to deformation and surface degradation as a result of mechanical tests. However, an increase in the radiation dose leads to a sharp deterioration in the dry friction coefficient, as well as its increase by a factor of 0.5-1.2, which indicates a strong surface destruction and an increase in friction resistance due to the formation of defective inclusions and a decrease in the crack resistance of the surface.

## Conclusion

In conclusion, based on the data obtained, it can be concluded that AlN ceramics have a high degree of crack resistance and wear resistance at low mechanical stresses in the irradiated state at doses of  $10^{10}$ - $5 \times 10^{12}$  ion/cm<sup>2</sup>. However, in the case of high stresses (more than 100 N), a sharp deterioration in wear resistance is observed for samples irradiated with doses above  $10^{11}$  ion/cm<sup>2</sup>, which is associated with the accumulation of

defects in the near-surface layer of ceramics and surface deformation as a result of swelling and formation of hillocks. The obtained dependencies of change in wear resistance of irradiated ceramics can be used later for development of design documentation on use of these ceramics as structural materials exposed to both radiation and mechanical stresses.

#### Funding

This research was funded by the Science Committee of the Ministry of Education and Science of the Republic of Kazakhstan (No. AP08051975).

#### REFERENCES

- 1 Grigoriev S., et al. Wire electrical discharge machining, mechanical and tribological performance of TiN reinforced multiscale SiAlON ceramic composites fabricated by spark plasma sintering. *Applied Sciences*. 2020, Vol. 11.2, pp. 657-665.
- 2 Chen Juanjuan, et al. Mechanical and tribological properties of h-BN/ZrO<sub>2</sub>/SiC solid-lubricating ceramic composites. *Tribology International*, 2021, Vol.160, pp. 107061-107080.
- 3 Li Yongxia, et al. Effect of Mo particle size on microstructure and mechanical properties of spark plasma sintered silicon nitride. *Materials Science and Engineering: A*, 2021, Vol. 814, pp. 141155.
- 4 Karipbayev, Zh, et al. Time-resolved luminescence excited with N<sub>2</sub> laser of YAG: Ce Ceramics formed by electron beam assisted synthesis. *Eurasian Physical Technical Journal*, 2021, Vol. 17.1 (33), pp. 73-76.
- 5 Tang Peng, et al. Influence of grain orientation on hardness anisotropy and dislocation behavior of AlN ceramic in nanoindentation. *Ceramics International*, 2021, Vol. 47.14, pp. 20298-20309.
- 6 Dehghani Hadi, et al. The effect of AlN-Y<sub>2</sub>O<sub>3</sub> compound on properties of pressure less sintered SiC ceramics-A review. *International Journal of Refractory Metals and Hard Materials*, 2021, Vol.95, pp. 105420.
- 7 Wei Zhilei, et al. Preparation of unidirectional porous AlN ceramics via the combination of freeze casting and combustion synthesis. *Journal of Materials Science & Technology*, 2022, Vol.100, pp. 161-168.
- 8 Kadyrzhanov, K. K., Tinishbaeva K., Uglov V.V. Investigation of the effect of exposure to heavy Xe<sup>22+</sup> ions on the mechanical properties of carbide ceramics. *Eurasian Physical Technical Journal*, 2021, Vol. 17 (33), pp. 46-53.
- 9 Eremin, E. N., Yurov V. M., Guchenko S.A. Wear resistance and tribological properties of high entropy coatings CrNiTiZrCu. *Eurasian Physical Technical Journal*, 2021, Vol. 17 (33), pp.13-18.
- 10 Zinkle S.J., Skuratov V.A., Hoelzer D.T. On the conflicting roles of ionizing radiation in ceramics. *Nuclear Instruments and Methods in Physics Research section B: Beam Interactions with Materials and Atoms*, 2002, Vol.191.1-4, pp. 758-766.
- 11 Yano T., et al. Neutron irradiation damage in aluminum oxide and nitride ceramics up to a fluence of 4.2×10<sup>26</sup>n/m<sup>2</sup>. *Journal of nuclear materials*, 2000, Vol.283, pp. 947-951.
- 12 Yano T., et al. Neutron irradiation effects on isotope tailored aluminum nitride ceramics by a fast reactor up to 2×10<sup>26</sup> n/m<sup>2</sup>. *Journal of Nuclear Materials*, 2004, Vol. 329, pp. 1471-1475.
- 13 Dukenbayev K., et al. The investigation of various type irradiation effects on aluminum nitride ceramic. *Journal of Materials Science: Materials in Electronics*, 2019, Vol. 30.9, pp. 8777-8787.
- 14 Kucheyev S.O., et al. Ion-beam-produced damage and its stability in AlN films. *Journal of applied physics*, 2002, Vol. 92.7, pp. 3554-3558.
- 15 Trinkler Laima, Baiba Berzina. Recombination luminescence in aluminum nitride ceramics. *Physica status solidi (b)*, 2014, Vol. 251.3, 542-548.
- 16 Zinkle S.J., Skuratov V.A., Hoelzer D.T. On the conflicting roles of ionizing radiation in ceramics. *Nuclear Instruments and Methods in Physics Research section B: Beam Interactions with Materials and Atoms*, 2002, Vol. 191.1-4, pp. 758-766.
- 17 Hu Quanli, et al. Study of radiation defects for AlN ceramics under O<sup>+</sup> irradiation. *Nuclear Instruments and Methods in Physics Research Section B: Beam Interactions with Materials and Atoms*, 2000, Vol. 166, pp. 70-74.
- 18 Zinkle S. J., Kinoshita C. Defect production in ceramics. *Journal of Nuclear Materials*, 1997, Vol.251, pp. 200-217.
- 19 Kozlovskiy A., et al. Dynamics of changes in structural properties of AlN ceramics after Xe<sup>+</sup> 22 ion irradiation. *Vacuum*, 2018, Vol. 155, pp. 412-422.
- 20 Kozlovskiy A. Influence of irradiation temperature on properties change of AlN ceramics. *Vacuum*, 2018, Vol. 158, pp. 93-100.

DOI 10.31489/2022No1/15-19

UDC 537.312.62; 538.945

## METAL-INSULATOR TRANSITIONS IN DOPED *La*-BASED SUPER CONDUCTORS WITH SMALL-RADIUS DOPANTS

Dzhumanov S., Kurbanov U.T., Khudayberdiev Z.S.

Institute of Nuclear Physics, Uzbekistan Academy of Sciences, Tashkent, Uzbekistan, [dzhumanov@inp.uz](mailto:dzhumanov@inp.uz)

*In this work, we study the possibility of realizing two distinct mechanisms of metal-insulator transitions in hole-doped cuprates induced by the localization of charge carriers near the small-radius impurities and in a deformable lattice (i.e. in the absence of impurities). The purpose of this research is to determine the criteria (i.e. conditions) for the existence of the localized states of hole carriers and solve the problem of metal-insulator transitions in La-based cuprates. The advantage of La-based cuprate versus other types of cuprates is that two distinct metal-insulator transitions in La-based cuprates driven by the strong carrier-impurity-phonon and carrier-phonon interactions occur simultaneously in a wider doping range from the lightly doped to heavily doped regime. We show that at very low doping, the separate levels of hole carriers localized near impurities and in a deformable lattice are formed in the charge-transfer gap of the cuprates. As the doping level increases towards underdoped region, the energy levels of such charge carriers start to form energy bands which gradually broaden with increasing doping. We propose a new two-carrier cuprate superconductor model for studying two distinct metal-insulator transitions occurring simultaneously in hole-doped La-based cuprate compounds. We demonstrate that when hole carriers reside in impurity and polaron bands, these metal-insulator transitions in La-based superconductors with small-radius dopants occur accordingly in a wide doping range and relatively lower doping levels.*

**Keywords:** Hole-doped cuprates; Carrier localization; Metal-insulator transitions.

### Introduction

The mechanisms of the localization of charge carriers and metal-insulator transitions in undoped and doped materials have been central problems of the condensed matter physics for many decades [1-10]. According to the one-electron band theory, crystalline solids are metals with a partially filled valence band or insulators with a completely filled valence band. Such a classification of solids into metals and insulators was originally proposed by Wilson [11]. According to the Wilson's band theory of non-interacting electrons, metal-insulator transitions in crystalline solids can occur when two band will overlap due to the change in volume (under pressure) or temperature of the materials. This one-electron band theory has been very successful in describing many crystalline materials. But it is turned to be inadequate for transition metal oxides with a partially filled *d*-electron band, which are insulators [6,7].

Since in conventional simplified band theory, the most important features of many-body systems, such as strong Coulomb repulsion between electrons (i.e., electron-electron correlation), disorder in atomic and electronic subsystems and electron-lattice interaction were ignored. Further, Mott [1] and Anderson [12] suggested the ideas of the localization of electrons and metal-insulator transitions due to the strong electron-electron correlation and structural disorder, respectively. These correlation- and disorder-induced metal-insulator transitions called Mott and Anderson metal-insulator transitions were discussed as the basic mechanisms of the localization of charge carriers in crystalline and non-crystalline solids [3,6,7,9]. Mott considered a half-filled *d*-electron band (with bandwidth  $W$  and on-site Coulomb repulsion  $U_d$  between electrons) or a perfect crystal lattice of one-electron hydrogen-like atoms with the lattice constant  $a$ . According to Mott, the electrons of the half-filled valence band are delocalized at small  $a$  (or large  $W$ ) satisfying the condition  $W/U_d > 1$  and characterized by metal-like conductivity. When  $a$  is increased, the band is continuously narrowed. The electrons of this narrow band are localized at their respective atoms and the crystalline material is converted into an antiferromagnetic insulator due to the splitting of the half-filled band into upper and lower Hubbard bands at  $W/U_d < 1$ . This model of a perfect crystal structure is not relevant to real crystalline solids in which there is a certain degree of disorder (e.g., vacancies, impurities, displaced atoms, and deformed chemical bonds). Therefore, Anderson considered the possibility of the localization of



non-interacting electrons due to disorder. Anderson used a crystalline array of potential wells with a random potential  $V_0$ , varying between the limits  $\pm(1/2)V_0$ .

Metal-insulator transitions in doped semiconductors and copper-oxide (cuprate) compounds have been previously studied for the case of the existence of one type of charge carriers [3,6,7,9,13]. However, in these materials, doped charge carriers can reside near dopants (impurities) as bound carriers and in defect-free regions of the crystal lattice as polaronic carriers. Therefore, such two types of charge carriers can coexist in doped semiconductors and high-temperature cuprate superconductors, and the criterion for metal-insulator transition in the case of two coexisting charge carriers will differ from the criterion for metal-insulator transition obtained in the one-carrier semiconductor or high- $T_c$  superconductor model [14]. These circumstances were not previously considered in the studying metal-insulator transitions in doped materials. In this work, we will consider the possibility of realizing two different mechanisms of metal-insulator transitions occurring simultaneously in hole-doped  $La$ -based cuprate superconductors with small radius dopants, where two types of charge carriers are residing in the impurity and polaron bands. The goal of choosing  $La$ -based cuprates for study the mechanisms of metal-insulator transitions is that these systems (as distinct from other types of cuprate compounds) allow us to study two different types of metal-insulator transitions occurring simultaneously in a wide doping range from the lightly doped to heavily doped regime and to compare the key differences between these metal-insulator transitions, which are driven by the strong carrier-impurity-phonon and carrier-phonon interactions, in hole-doped  $La$ -based cuprates.

### 1. New criteria for metal-insulator transitions in doped $La$ -based cuprates defined within two-carrier cuprate superconductor model

If the electron-phonon interactions near dopants (impurities) are weak, the simple hydrogen-like impurity centers are formed in doped cuprates [9]. Such a situation is realized in  $La_{2-x}Sr_xCuO_4$  (LSCO) and  $La_{2-x}Ba_xCuO_4$  (LBCO), in which the radius of both the  $Sr^{2+}$  and the  $Ba^{2+}$  is larger than that of  $La^{3+}$ , so that for  $Sr^{2+}$  and  $Ba^{2+}$  the sign of the deformation potential is negative [15]. It follows that the hole-lattice interactions near the large-radius dopants in LSCO and LBCO are suppressed by the repulsive impurity potential and hole carriers are localized at a distance from the dopants  $Sr^{2+}$  and  $Ba^{2+}$  and form the hydrogen-like impurity centers. In this case the Mott's metal-insulator transition in the single-carrier solid model is driven by the electron correlation in such impurity centers and can occur only very low doping levels ( $x \leq 0.02$ ) in LSCO and LBCO and the other type of metal-insulator transition in these materials driven by the strong hole-lattice interactions can take place also in the single-carrier solid model at more higher doping levels.

Another interesting question is how small-radius dopants (impurities) in doped cuprates affect the carrier localization and related metal-insulator transition. The signs of deformation potentials of holes and small-radius dopants are positive in  $La_{2-x}Ba_xM_yCuO_4$  (where  $M=Ca^{2+}$ ) and  $La_{2-x-y}Nd_ySr_xCuO_4$ , where the carrier-impurity-phonon interaction is attractive near the small-radius dopants (e.g.  $Ca^{2+}$  and  $Nd^{3+}$  ions). Therefore, the substitution of small-radius ions  $Ca^{2+}$  and  $Nd^{3+}$  for  $La^{3+}$  ions in  $La$ -based cuprates leads to the combined impurity- and phonon-assisted self-trapping of hole carriers with the formation of non-hydrogen-like localized impurity states which can form an impurity band at high doping levels. We assume that some part of hole carriers are localized near small-radius dopants and other part of hole carriers are self-trapped in a deformable lattice with the formation of large polarons. We now take into account these circumstances in the study of the metal-insulator transitions driven by the strong carrier-impurity-phonon and carrier-phonon interactions in  $La$ -based cuprates with small-radius dopants ( $Ca^{2+}$  and  $Nd^{3+}$ ). We argue that when the hole carriers are localized near impurities and in a deformable lattice with the formation of impurity centers and polarons, as observed in  $La$ -based cuprates [16], the conditions for carrier localization or criteria for metal-insulator transitions are quite different. In the following, we will determine these new criteria for metal-insulator transitions in a two-carrier cuprate superconductor model that is better applicable to doped  $La$ -based cuprates with small-radius dopants than other  $La$ -based cuprates with large-radius dopants.

It is natural to assume that the impurity centers and polarons can form superlattices and impurity and polaron bands in doped cuprates. When two coexisting types of charge carriers in doped materials are residing in the impurity and polaron bands, the Fermi energy  $\varepsilon_{FI}$  of charge carriers in the impurity band and the Fermi energy  $\varepsilon_{FP}$  in the polaron band can be defined as

$$\varepsilon_{FI} = \hbar^2(3\pi^2 f_I n)^{2/3} / 2m_I \quad (1)$$

and

$$\varepsilon_{Fp} = \hbar^2(3\pi^2(1-f_I)n)^{2/3}/2m_p \quad (2)$$

where  $f_I$  is the fraction of charge carriers residing in the impurity band,  $m_I$  is the mass of such charge carriers,  $m_p$  is the mass of large polarons,  $n$  is the concentration of doped charge carriers.

In a two-carrier cuprate superconductor model, the conditions for carrier localization or the new criteria for metal-insulator transitions will be different from the criteria for metal-insulator transitions defined in the single-carrier cuprate superconductor model [14] and can be written as

$$\frac{E_I}{\varepsilon_{FI}} = \frac{2E_I m_I}{\hbar^2(3\pi^2 f_I n)^{2/3}} \geq 0.5 \frac{a_I}{R_I}, \quad (3)$$

and

$$\frac{E_p}{\varepsilon_{Fp}} = \frac{2E_p m_p}{\hbar^2(3\pi^2(1-f_I)n)^{2/3}} \geq 0.5 \frac{a_p}{R_p}, \quad (4)$$

where  $E_I$  is the binding energy of the charge carriers which are bound to the impurity centers,  $a_I$  is the lattice parameter of the impurity superlattice,  $R_I$  is the radius of the impurity center,  $E_p$  is the polaron binding energy,  $a_p$  is the lattice parameter of the polaron superlattice,  $R_p$  is the polaron radius. Now, the criteria (3) and (4) for certain level of doping  $n=n_c$  can be written as

$$x = x_{cl} = \frac{n_c}{n_a} = \frac{1}{3\pi^2 f_I n_a} \left[ \frac{4m_I E_I R_I}{\hbar^2 a_I} \right]^{3/2} \quad (5)$$

and

$$x = x_{cp} = \frac{n_c}{n_a} = \frac{1}{3\pi^2(1-f_I)n_a} \left[ \frac{4m_p E_p R_p}{\hbar^2 a_p} \right]^{3/2} \quad (6)$$

where  $n_a = 1/V_a$  is the density of the host lattice atoms,  $V_a$  is the volume per  $CuO_2$  formula unit in the cuprates.

We assume that the impurities centers and polarons form simple cubic superlattices. For simple cubic superlattices of impurity centers and polarons, lattice parameters can be determined as  $a_I = 2R_I$  and  $a_p = 2R_p$ . Therefore, applying the criteria (5) and (6) for metal-insulator transitions to these impurity centers and polarons, we obtain the following critical doping levels corresponding to the metal-insulator transitions driven by the strong carrier-impurity-phonon and carrier-phonon interactions:

$$x_{cl} = \frac{V_a}{3\pi^2 f_I \hbar^3} [2m_I E_I]^{3/2} \quad (7)$$

and

$$x_{cp} = \frac{V_a}{3\pi^2(1-f_I)\hbar^3} [2m_p E_p]^{3/2}. \quad (8)$$

At such critical doping levels, the transitions from insulating state to metallic state or from metallic state to insulating state occur in doped cuprates. The quantity of both  $E_I$  and  $E_p$  depends on the high-frequency  $\varepsilon_\infty$  and static  $\varepsilon_0$  dielectric constants, as well as on the ratio  $\eta = \varepsilon_\infty/\varepsilon_0$ .

## 2. Results and discussion

The expressions (7) and (8) for  $x_{cl}$  and  $x_{cp}$  contain two pairs of key parameters ( $m_I$ ,  $E_I$  and  $m_p$ ,  $E_p$ ) characterizing the effective masses of charge carriers in their localized states and carrier-impurity-phonon and carrier-phonon interactions, which result in the formation of the localized impurity state and polaronic state. Using the criteria (7) and (8), one can determine the possibility of realizing different mechanisms of metal-insulator transitions in doped  $La$ -based cuprate compounds with small-radius dopants. In particular, these expressions allow us to calculate the critical doping levels  $x_{cl}$  and  $x_{cp}$ , at which the metal-insulator transitions occur in  $La_{2-x}Ba_xCa_yCuO_4$  and  $La_{2-x-y}Nd_ySr_xCuO_4$ . The volume per  $CuO_2$  formula unit  $V_a$  in  $La$ -based cuprate superconductors is equal to  $190 \text{ \AA}^3$ .

## 2.1. Metal-insulator transitions driven by the strong carrier-impurity-lattice interactions in doped cuprate superconductors $La_{2-x}Ba_xCa_yCuO_4$ and $La_{2-x-y}Nd_ySr_xCuO_4$ with small-radius dopants

Using the expression (7), we calculate the critical doping levels  $x_{cl}$ , at which the metal-insulator transitions driven by the strong carrier-impurity-lattice interactions occur in  $La_{2-x}Ba_xCa_yCuO_4$  and  $La_{2-x-y}Nd_ySr_xCuO_4$ . By taking  $m_l = 2.0m_e$ ,  $E_I = (0.0741-0.1240)$  eV (at  $\epsilon_\infty = 3.5-4.5$  and  $\eta = 0.02$ ) [17] and  $f_I = 0.5$ , we find the following critical doping levels  $x_{cl} = 0.098-0.213$  at which the metal-insulator transitions occur in  $La_{2-x}Ba_xCa_yCuO_4$  and  $La_{2-x-y}Nd_ySr_xCuO_4$  from the underdoped to heavily overdoped regime in the regions of the crystal lattice containing impurities. The calculated results for  $x_{cl}$  at  $\eta = 0.02$  and different values of  $E_I$  and  $\epsilon_\infty$  are presented in Table 1. From these results, it follows that when  $\epsilon_\infty$  decreases, the metal-insulator transitions occur at more higher doping levels.

**Table 1.** The calculated critical doping levels  $x_{cl}$  at  $\eta = 0.02$  and different values of  $E_I$  and  $\epsilon_\infty$

$E_I = 0.1240$ eV, $\epsilon_\infty = 3.5$		$E_I = 0.0943$ eV, $\epsilon_\infty = 4$		$E_I = 0.0741$ eV, $\epsilon_\infty = 4.5$	
$f_I$	$x_{cl}$	$f_I$	$x_{cl}$	$f_I$	$x_{cl}$
0.5	0.213	0.5	0.141	0.5	0.098

## 2.2. Metal-insulator transitions driven by the strong carrier-lattice interactions in the cuprate superconductors $La_{2-x}Ba_xCa_yCuO_4$ and $La_{2-x-y}Nd_ySr_xCuO_4$ with small-radius dopants

Using the expression (8), we calculate the critical doping levels  $x_{cp}$ , at which the metal-insulator transition driven by the strong carrier-lattice interactions occur in  $La_{2-x}Ba_xCa_yCuO_4$  and  $La_{2-x-y}Nd_ySr_xCuO_4$ . In our calculations, we now take  $m_p = 1.8m_e$  and use the values of  $E_p = (0.0640 - 0.1063)$  eV (at  $\epsilon_\infty = 3.5-4.5$  and  $\eta = 0.02$ ) [17]. When the fraction of charge carriers in the polaronic band is equal to  $f_p = 1 - f_I = 0.5$ , we find the following critical doping levels  $x_{cp} = 0.067-0.144$  at which the metal-insulator transitions occur in  $La_{2-x}Ba_xCa_yCuO_4$  and  $La_{2-x-y}Nd_ySr_xCuO_4$  from the underdoped to optimally doped regime in the regions of the crystal lattice without impurities. The calculated results for  $x_{cp}$  at  $\eta = 0.02$  and different values of  $E_p$  and  $\epsilon_\infty$  are presented in Table 2. As can be seen from Table 2, the metal-insulator transitions occur at more higher doping levels with decreasing  $\epsilon_\infty$  from 4.5 to 3.5.

**Table 2.** The calculated critical doping levels  $x_{cp}$  at  $\eta = 0.02$  and different values of  $E_p$  and  $\epsilon_\infty$

$E_p = 0.1063$ eV, $\epsilon_\infty = 3.5$		$E_p = 0.0811$ eV, $\epsilon_\infty = 4$		$E_p = 0.0640$ eV, $\epsilon_\infty = 4.5$	
$f_p$	$x_{cp}$	$f_p$	$x_{cp}$	$f_p$	$x_{cp}$
0.5	0.144	0.5	0.096	0.5	0.067

## Conclusion

We have studied the possibility of realizing two new and fundamentally different mechanisms of metal-insulator transitions in *La*-based cuprate compounds with small-radius dopants (impurities) in a pertinent two-carrier superconductor model. We have demonstrated that the proposed two-carrier *La*-based cuprate superconductor model is more realistic than the previously studied single-carrier model of this superconductor, which was considered by many researchers (see Refs. [3,6,9,11,12,14]). This new model predicts much more reliable results for metal-insulator transitions in doped *La*-based cuprates than other existing results predicted by the single-carrier cuprate superconductor model. We have argued that none of the previously proposed theoretical models considering only one type of localized charge carriers in doped cuprates, are capable of accounting for the full body of experimental data [6,9,18-21] and the metal-insulator transitions observed in a wide doping range from the lightly doped to heavily doped regime in a *La*-based cuprates with small-radius dopants. The scientific significance of our obtained results is that the metal-insulator transitions in *La*-based cuprate compounds occur not only in underdoped regime in accordance with experimental results [18] but also in the two distinct doping ranges, namely, from the underdoped to

optimally doped ( $0.06 \leq x \leq 0.15$ ) and from the underdoped to heavily overdoped ( $0.06 \leq x \leq 0.21$ ) regimes in full accordance with the existing experimental results [18-21]. We have shown that the metal-insulator transitions in these cuprate superconductors are induced by the localization of hole carriers near the small-radius dopants and in the regions without such impurities. We have found that the criteria for metal-insulator transitions driven by the hole-impurity-lattice and hole-lattice interactions are quite different. According to our two-carrier cuprate superconductor model, the metal-insulator transitions occur first in the regions without small-radius impurities at intermediate doping levels ( $x < 0.15$ ) and then in the regions with such impurities at more higher doping levels reaching up to  $x \geq 0.21$ . Thus, our results indicate that in *La*-based cuprate superconductors, two distinct metal-insulator transitions occur simultaneously in a wide range of doping, namely, from the lightly doped to heavily overdoped regime, as observed in various experiments [18-21]. We note that in some experiments (see Ref. [18]) the dopant concentrations in  $\text{Bi}_2\text{Sr}_{2-x}\text{La}_x\text{CuO}_{6+d}$  and  $\text{La}_{2-x}\text{Sr}_x\text{CuO}_4$  for study of metal-insulator transitions were chosen the underdoped and optimally doped regimes respectively, and in other experiments, the concentration of dopants in  $\text{La}_{2-x-y}\text{Nd}_y\text{Sr}_x\text{CuO}_4$  and  $\text{La}_{2-x}\text{Sr}_x\text{CuO}_4$  was selected from lightly doped mode ( $x=1/8$ ) to heavily doped mode ( $x > 0.2$ ) [20,21].

### Acknowledgments

This work is partially supported by the Foundation of the Fundamental Research, Grant F-FA-2021-433.

### REFERENCES

1. Mott N. F. The Basis of the Electron Theory of Metals, with Special Reference to the Transition Metals. *Proc. Phys. Soc. London*. 1949, Vol. A62, pp. 416 - 422.
2. Hubbard J. Electron correlations in narrow energy bands. II. The degenerate band case. *Proc. Roy. Soc. London*. 1964, Vol. A277, pp. 237-259; Electron correlations in narrow energy bands. III. An improved solution. *Proc. Roy. Soc. London*. 1964, Vol. A281, pp. 401-419.
3. Mott N.F. *Metal-Insulator Transitions*. Taylor and Francis, London, 1990, 286 p.
4. Lavrov A.N., Gantmakher V.F. Low-temperature resistivity of under doped cuprates. *Phys. Usp.* 1998, Vol.41, pp. 223-226.
5. Abrikosov A.A. Resonant tunneling in high- $T_c$  superconductors. *Phys.Usp.* 1998, Vol.41, pp. 605-616.
6. Imada M., Fujimory A., Tokura Y. Metal-insulator transitions. *Rev. Mod. Phys.* 1998, Vol. 70, pp. 1039-1263.
7. Walz F. The Verwey transition- a topical review. *J. Phys.: Condens. Matter*. 2002, Vol.14, pp. R285-R340.
8. Vedenev S.I. High temperature superconductors in strong and superstrong magnetic fields. *Usp. Fiz. Nauk*, 2012, Vol.182, pp.669-676.
9. Dzhumanov S. *Theory of Conventional and Unconventional Superconductivity in the High- $T_c$  Cuprates and Other Systems*. Nova Science Publishers, New York, 2013, 356 p.
10. Dzhumanov S., et al. Formation of intermediate coupling optical polarons and bipolarons. *Phys. Lett. A*. 2019, Vol. 383, pp.1330-1335.
11. Wilson A. H. The theory of Electronic Semi-Conductors. *Proc. Roy. Soc. London*. 1931, Vol. A133, pp. 458-491; The theory of electronic semi-conductors. II. *Proc. Roy. Soc. London*, 1931, Vol. A134, pp. 277-287.
12. Anderson P.W. Absence of Diffusion in Certain Random Lattices. *Phys. Rev.* 1958, Vol. 109, pp. 1492-1505.
13. Damascelli A., Hussain Z., Shen Z.X. Angle-resolved photoemission studies of the cuprate superconductors. *Rev. Mod. Phys.* 2003, Vol.75, pp.473-541.
14. Dzhumanov S., Kurbanov U.T. The new metal-insulator transitions and nanoscale phase separation in doped cuprates. *Super lattices and Microstructures*, 2015, Vol.84, pp. 66-71.
15. Toyozawa Y. Electron induced lattice relaxations and defect reactions. *Physica B*, 1983, Vol.116, pp. 7-17.
16. Kastner M.A., Birgeneau R.J., Shirane G., Endoh Y. Magnetic, transport and optical properties of monolayer copper oxides. *Rev. Mod. Phys.* 1998, Vol. 70, pp. 897-928.
17. Dzhumanov S., et al. Possible mechanisms of carrier localization, metal-insulator transitions and stripe formation in homogeneous hole-doped cuprates. *J. Phys. Chem. Solids*. 2012, Vol.73, pp. 484- 494.
18. Ono S., et al. Low-temperature normal state of  $\text{Bi}_2\text{Sr}_{2-x}\text{La}_x\text{CuO}_{6+d}$ : comparison with  $\text{La}_{2-x}\text{Sr}_x\text{CuO}_4$ . *Physica C*. 2001, Vol.357-360, pp. 138-141.
19. Anshukova N.V., et al. The effect of super structural ordering on the properties of high-temperature oxide superconductor systems. *Zh. Eksp. Teor. Fiz.* 2003, Vol. 123, pp. 1188-1199. [in Russian]
20. Sakita Sh., et al. Structural transitions and localization in  $\text{La}_{2-x-y}\text{Nd}_y\text{Sr}_x\text{CuO}_4$  with  $p$  similar to  $1/8$ . *J. Phys. Soc. Jpn.* 1999, Vol.68, pp. 2755-2761.
21. Koike Y., et al. *Cu*-site-substitution effects on the  $1/8$  anomaly in the high- $T_c$  cuprates and on the anomaly at  $x=0.21$  in  $\text{La}_{2-x}\text{Sr}_x\text{CuO}_4$ . *Physica C*. 2001, Vol. 357-360, pp. 82-88.

## EFFECT OF THE STRUCTURE FORMED AFTER BULK AND SURFACE HARDENING ON THE HARDNESS AND WEAR RESISTANCE OF 20Cr2Ni4A STEEL

Rakhadilov B.K.<sup>1</sup>, Satbaeva Z.A.<sup>1\*</sup>, Kozhanova R.S.<sup>1</sup>, Kowalewski P.<sup>2</sup>,  
Bayatanova L.B.<sup>1</sup>, Kalitova A.A.<sup>3</sup>

<sup>1</sup>"Plasma Science" LLP, Ust-Kamenogorsk, Kazakhstan, [satbaeva.z@mail.ru](mailto:satbaeva.z@mail.ru)

<sup>2</sup>Wroclaw University of Science and Technology, Wroclaw, Poland

<sup>3</sup>Institute of Composite Materials, Ust-Kamenogorsk, Kazakhstan

*The article presents the results of a comparative study of the effect of bulk and surface hardening on the structure and properties of 20Cr2Ni4A steel. Surface hardening was carried out by the electrolytic plasma method. Bulk quenching was carried out by heating to a temperature of 870 °C, followed by cooling in water and oil. The structural-phase states of 20Cr2Ni4A steel samples were studied by metallographic and X-ray structural analysis. Tribological tests of the samples were carried out according to the ball-disk scheme, and the microhardness of the samples was also determined. It has been determined that after volumetric and surface hardening, the hardness and wear resistance of 20Cr2Ni4A steel increase. In this case, the most significant change is observed in samples that have undergone electrolytic plasma hardening. It has been established that high values of hardness and wear resistance of 20Cr2Ni4A steel after electrolytic plasma hardening are associated with the formation of fine-needle martensite.*

**Keywords:** structure; phase composition; electrolytic plasma hardening; microhardness; wear resistance.

### Introduction

One of the most effective ways to improve the service characteristics of structural steels is the development of optimal heat treatment modes. This makes it possible to obtain products with certain specified characteristics that meet operational requirements, and on the other hand, to predict changes in the properties of parts and structures during manufacture and operation [1-3]. The martensitic structure, as a rule, provides structural steels with good physical and mechanical properties. To obtain a martensitic structure in steels, they are subjected to bulk or surface hardening. Case hardening is widely used to improve the durability of friction joint parts, which often experience high shock loads. Since, they must have high strength and hardness of the surface layer, combined with sufficient ductility of the core. The main difference between surface hardening and bulk thermal hardening is the short duration of the surface layer heating process and the high cooling rate due to heat dissipation into the inner layers of the metal. These factors influence greatly the structure of the hardened layer. The cooling rate manifests itself in the refinement of the structure of the surface layer. At present, high-frequency [4], gas-flame [5], plasma [6], electron-beam [7] and laser processing [8] are widely used for surface thermal hardening of steel parts in industry. Among them, plasma surface hardening has a number of advantages over the existing methods of thermal surface hardening in terms of its technical and economic indicators and the results of comparative analysis. The main advantage of plasma thermal hardening in comparison with laser hardening is the time spent on surface treatment, since the area of action of a plasma arc is larger than that of a plasma beam [6, 9].

One of the promising methods of plasma surface hardening is electrolytic plasma hardening [10-12]. During electrolytic plasma hardening, heating and cooling of the part is carried out in a water-based electrolyte. The plasma layer is formed in the gap between the liquid (electrolyte) electrode and the surface of the product when voltage is applied [12]. The result of a short stay of steel at hardening temperatures, as well as the occurrence of phase transformations in the temperature range above equilibrium, is an increase in the mechanical properties of the material in comparison with bulk hardening. In connection with the above, the goal of this research is to study the effect of bulk and surface hardening on the structure, hardness and wear resistance of 20Cr2Ni4A steel.

## Materials and methods

Structural alloyed 20Cr2Ni4A steel was used as the research object. Table 1 shows the chemical composition of the studied steel. Samples of 20Cr2Ni4A steel with dimensions of 10x10 mm were subjected to bulk and surface hardening. Bulk hardening of 20Cr2Ni4A steel samples was carried out in an evacuated quartz tube in a laboratory tubular furnace according to the following modes: quenching from a temperature of 870 °C, the holding time at a temperature of 870 °C was 0.5 h, and cooling was performed in water and oil. The first sample was cooled in water; the second sample was cooled in oil to room temperature.

**Table 1.** Chemical composition of 20Cr2Ni4A steel

Steel name	C	Si	Mn	Ni	S	P	Cr	Cu
20Cr2Ni4A	0.16-0.22	0.17-0.37	0.3-0.6	3.25-3.65	up to 0.025	up to 0.025	1.25-1.65	up to 0.3

Surface hardening of 20Cr2Ni4A steel samples was carried out by the electrolytic plasma method on an installation consisting of a 30-kW DC source, an electrolytic cell, a bath, a pump, a heat exchanger, and a stainless steel anode [12-14]. The EPH process was carried out in an electrolyte from an aqueous solution containing sodium carbonate (20%) and urea (10%) in the following mode: the applied voltage between the anode and the sample was 320 V, the current density was 25 A/cm<sup>2</sup>, and the plasma exposure time was 2 sec. In this mode, the samples were heated to ~ 850-900 °C. Cooling was carried out in a flowing electrolyte after turning the voltage off. Figure 1 shows a schematic view of the installation.

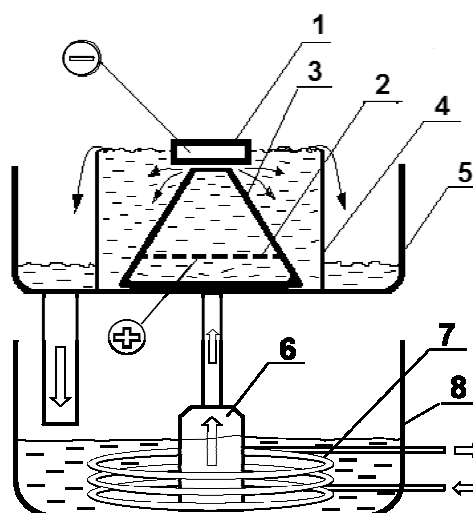
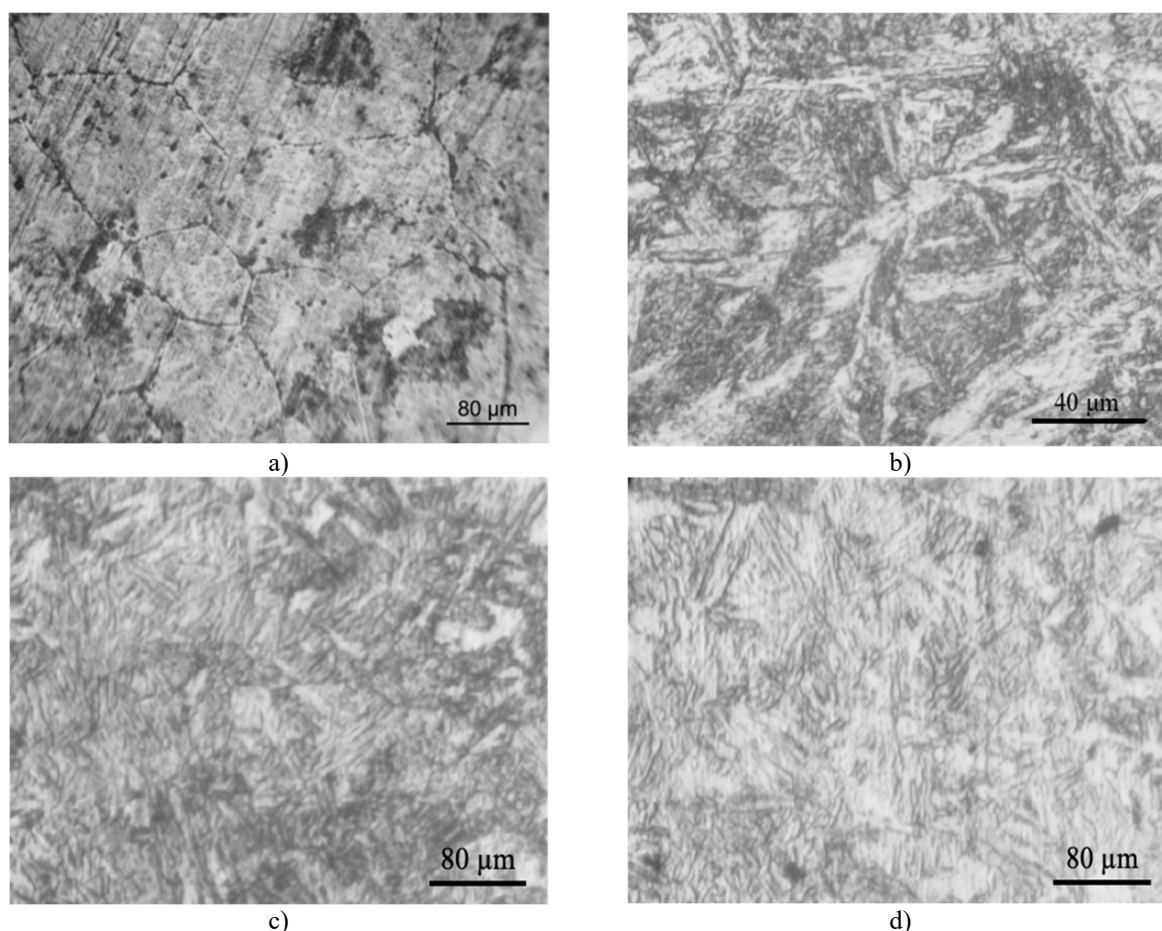


**Fig.1.** Scheme of the installation for electrolytic plasma treatment:  
 1 – processed sample (cathode), 2 – stainless steel anode, 3 – cone-shaped partition, 4 – electrolytic cell,  
 5 – pallet, 6 – pump, 7 – heat exchanger, 8 – bath with electrolyte

The study of the phase composition of 20Cr2Ni4A steel samples before and after bulk and surface hardening was carried out on X'PertPRO X-ray diffractometer in Cu K $\alpha$  radiation in a continuous recording mode in the angle range from 20 to 85 °. Metallographic analysis was performed in a bright field on Altami MET 5C microscope at various magnifications. The microhardness of the samples was measured by the method of indentation of a diamond indenter on PMT-3M device in accordance with GOST 9450-76, at a load of 100 g and holding for 10 sec. Tribological tests were carried out on TRB3 tribometer under dry friction; a chromium-plated 100Cr6 ball with a diameter of 6 mm was used as a counter body; the friction path was 50 m at a speed of 3 cm/s and a load of 5 N.

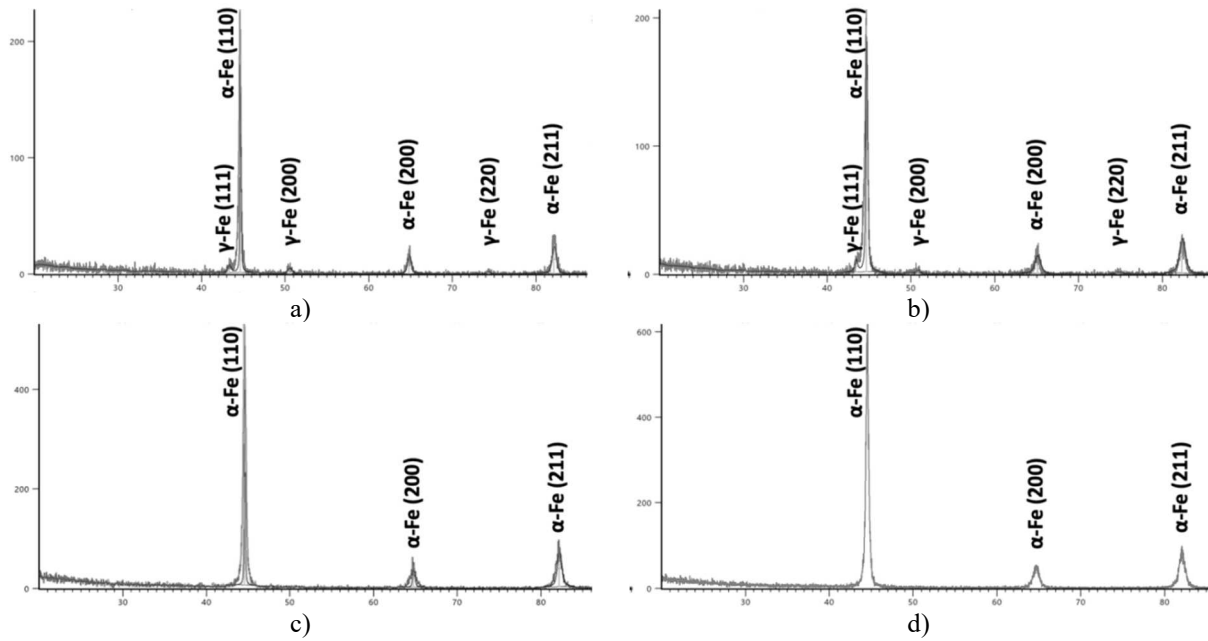
## Results and discussion

Figure 2 shows the microstructure of 20Cr2Ni4A steel before and after bulk and surface hardening. Metallographic analysis showed that 20Cr2Ni4A steel in the initial state consists of a ferrite-pearlite structure. Pearlite makes up  $\sim 10\%$  of the total volume. The average grain size of ferrite is  $\sim 97 \mu\text{m}$ . After electrolytic plasma hardening and bulk hardening, a martensitic structure is formed. At the same time, after electrolytic plasma hardening, fine-acicular martensite with retained austenite is formed, and after bulk hardening in water and oil, coarse-acicular martensite with a small content of retained austenite is formed. After electrolytic plasma hardening and bulk hardening in water, undissolved cementite is observed in the steel structure. Electrolytic plasma hardening of the surface led to the formation of a highly inhomogeneous structure in the hardened zone. Due to the incompleteness of the austenitization processes in the hardened layer, fine-acicular martensite, undissolved cementite and retained austenite were formed (Fig. 2b).



**Fig.2.** Microstructure of 20Cr2Ni4A steel before (a) and after surface (b) bulk hardening from  $T = 870 \text{ }^{\circ}\text{C}$  in water (c) and in oil (d)

The phase composition of the samples was studied before and after surface and bulk hardening. Figure 3 shows X-ray diffraction patterns of 20Cr2Ni4A steel samples. X-ray structural analysis showed that, in the initial states of 20Cr2Ni4A steel, diffractograms contain lines of the  $\alpha$ -phase and weak reflections of austenite. After electrolytic plasma hardening, lines of the  $\alpha$ -phase and weak reflections of austenite are also observed. Moreover, after bulk hardening in water and oil, only the lines of the  $\alpha$ -phase are present in the diffractogram. In this case, after surface and bulk hardening, broadening of the  $\alpha$ -phase line is observed, which indicates the formation of martensite. On the diffraction patterns of the samples after hardening, no cementite reflections were found, apparently, this is due to their low concentration, which does not allow detection by X-ray diffraction analysis.



**Fig.3.** X-ray diffraction patterns of 20Cr2Ni4A steel before (a) and after surface (b) bulk hardening from  $T = 870$  °C in water (c) and in oil (d)

Hardness is one of the most important properties of the surface layer, which strongly depends on the rate of heating and cooling during hardening. Therefore, we studied the changes in the microhardness of 20Cr2Ni4A steel depending on the type and mode of hardening. Figure 4 shows the microhardness of 20Cr2Ni4A steel before and after surface and bulk hardening. After surface and bulk hardening, the microhardness of 20Cr2Ni4A steel increases. At the same time, the maximum increase in hardness is observed in samples treated by electrolytic plasma hardening. An increase in hardness up to 2 times during electrolytic plasma hardening is associated with the formation of fine-needle martensite. We found that after electrolytic plasma hardening a small amount of residual austenite is formed. But in spite of this the hardness is significantly higher than in traditional heat treatment. This is due to the formation of a highly dispersed metastable structure with a much higher density of dislocations in the surface layer [14, 15].

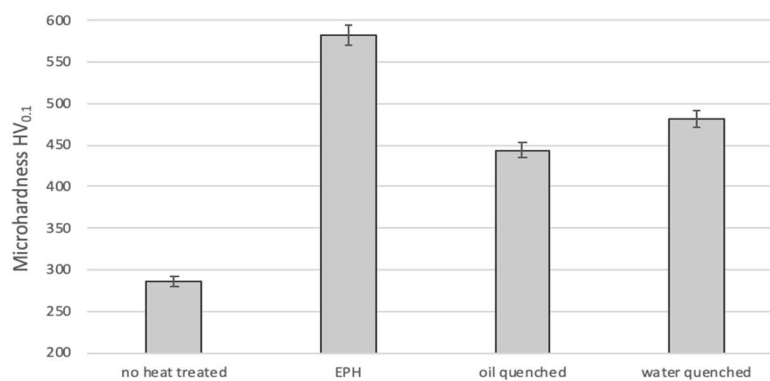


**Fig.4.** Microhardness of 20Cr2Ni4A steel before and after surface and bulk hardening

Figure 5 shows the results of tribological tests of 20Cr2Ni4A steel samples according to the ball-disk scheme. The wear resistance of the samples was characterized by the wear volume of the samples. The measurement results showed insignificant changes in the coefficient of friction (Figure 5a). Figure 5b shows that the hardened samples have a low wear rate compared to the original sample. At the same time, the highest wear resistance is shown by samples treated by electrolytic plasma hardening and bulk water hardening. The high wear resistance of these samples is due to the high hardness of the surface, as well as



high internal stresses that are formed during rapid cooling. Bulk hardening is accompanied by the formation of internal stress fields, the magnitude of which depends on the type of stress concentrator. Therefore, after bulk hardening, annealing is performed to relieve internal stress. In steels, stress concentrators are not microcracks, but the hard and brittle microstructures constituting them - carbides, or rather, local accumulations of carbides.

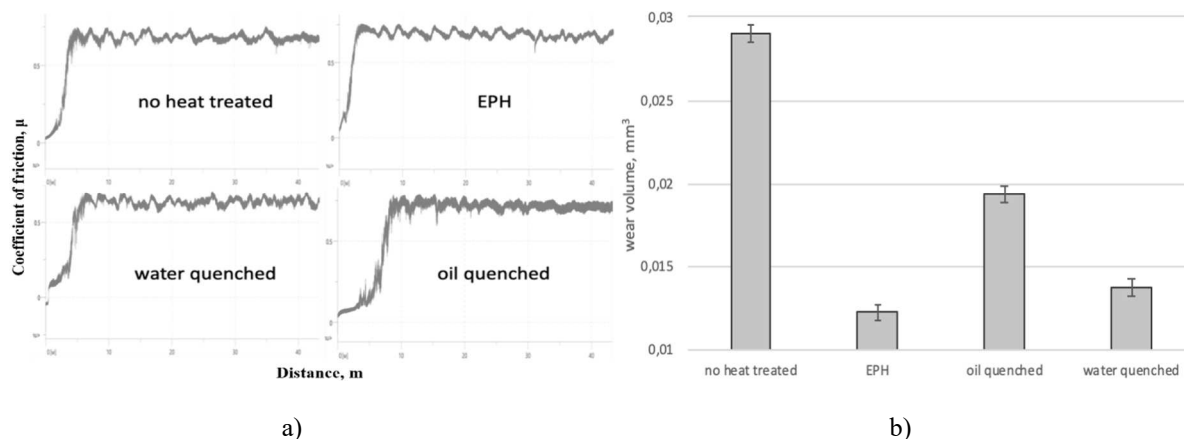


**Fig.5.** Graphs of the change in the coefficient of friction (a) and the wear volume (b) of 20Cr2Ni4A steel samples before and after surface and bulk hardening

For steels that have undergone electrolytic plasma hardening, there is no need for annealing due to the small thickness of the hardened layer. In this case, after electrolytic plasma hardening, the steel base remains viscous and the structure contains a significant amount of retained austenite, which acts as a damper during the propagation of microcracks and stresses.

Thus, plasma electrolytic hardening leads to an increase in the physical and mechanical properties of parts made of 20Cr2Ni4A steel. This is due to the fact that a structure with a high dislocation density is formed on the surface. A high degree of dissolution of the carbide phase, refinement of the grain structure, and an increase in the density of defects in the crystal structure after plasma electrolyte hardening leads to an increase in the operational properties of 20Cr2Ni4A chromium-nickel steel.

## Conclusion

1. Based on metallographic and X-ray structural analyzes, it was determined that after electrolytic plasma hardening, fine-acicular martensite with retained austenite is formed, and after bulk hardening in water and oil, coarse-acicular martensite is formed with a small content of retained austenite. At the same time, after electrolytic plasma hardening and bulk hardening in water, undissolved cementite is observed in the steel structure.

2. It was determined that after surface and bulk hardening the microhardness of 20Cr2Ni4A steel increases. At the same time, the maximum increase in hardness is observed in samples treated with electrolytic plasma hardening. It was found that an increase in hardness up to 2 times during electrolytic plasma hardening is associated with the formation of fine-acicular martensite and the formation of a highly dispersed metastable structure with a high density of dislocations in the surface layer.

3. Tribological tests have shown that the hardened samples have high wear resistance compared to the initial samples. At the same time, the highest wear resistance was shown by samples treated with electrolytic plasma hardening and bulk water hardening. The high wear resistance of these samples is due to the high hardness of the surface, as well as high internal stresses that form during rapid cooling. At the same time, after EPH, the steel base remains viscous and a significant amount of retained austenite is present in the structure, which acts as a damper during the propagation of microcracks and stresses.

## Acknowledgments

This paper was performed within the grant financing of scientific research for 2021-2023 of Committee of the Science of the Ministry of Education and Science of the Republic of Kazakhstan. Grant (AP09058547).

## REFERENCES

- 1 Kurdyumov V.G., Utevsky L.M., Entin R.I. *Transformations in iron and steel*. Moscow, 1977, 236p. [in Russian]
- 2 Schastlivtsev V.M., Mirzaev D.A., Yakovleva I.L. *The structure of thermally processed steel*. Moscow, Metallurgiya, 1994, 288 p. [in Russian]
- 3 Vassilyeva A.G. *Deformation hardening of hardened structural steels*. Moscow, Mashinostroenie, 1981, 231p. [in Russian]
- 4 Ivancivsky V., Parts K., Popov V. Depth Distribution of Temperature in Steel Parts during Surface Hardening by High Frequency Currents. *Applied Mechanics and Materials*. 2015, 788, pp. 129 – 135. <https://doi.org/10.4028/www.scientific.net/amm.788.129>
- 5 Petrov G.L., Burov N.G., Abramovich V.R. *Technology and equipment for gas-flame processing of metals*. Leningrad, Mashinostroenie, 1978, 277 p. [in Russian]
- 6 Leshchinsky L.K., Samotugin S.S., Pirch I.I., Komar V.I. *Plasma surface hardening: monograph*. Kiev, 1990, 109p. [in Russian]
- 7 Poletika I.M., Golkovsky M.G., Perovskaya M.V. Electron beam hardening of the surface layer of steel outside vacuum. *Physical Mesomechanics*. 2006, No. 9, pp. 181-184.
- 8 Smirnova N.A., Misyurov A.I. Features of structure formation during laser processing. *Engineering journal: science and innovations*, 2012, No. 6 (6), pp. 115-129. [in Russian]
- 9 Safonov E.N. *Plasma hardening of machine parts. Monograph*. Berlin, Direkt-Media, 2014, 165 p.
- 10 Belkin P.N., Kusmanov S.A. Plasma Electrolytic Hardening of Steels: Review. *Surface Engineering and Applied Electrochemistry*. 2016, Vol.52, No.6, pp. 531-546. doi:10.3103/S106837551606003X.
- 11 Rakhadilov B., Zhurerova L., Pavlov A. Method of Electrolyte-Plasma Surface Hardening of 65G and 20GL Low-Alloy Steels Samples. *IOP Conf. Series: Materials Science and Engineering*, 2016, Vol.142, pp. 1-7.
- 12 Rakhadilov B.K., Buranich V.V., Satbayeva Z.A., et al. The cathodic electrolytic plasma hardening of the 20Cr2Ni4A chromium-nickel steel. *Journal of Materials Research and Technology*, 2020, Vol.9, No. 4, pp. 6969-6976.
- 13 Zhurerova L.G., Rakhadilov B.K., Popova N.A., et al. Effect of the PEN/C surface layer modification on the microstructure, mechanical and tribological properties of the 30CrMnSiA mild-carbon steel. *Journal of Materials Research and Technology*. 2019, Vol.9, No. 1, pp.78-85.
- 14 Rakhadilov B., Kengesbekov A., Zhurerova L., et al. Impact of electronic radiation on the morphology of the fine structure of the surface layer of R6M5 steel. *Machines*. 2021, Vol. 9(2), No. 24, pp.1-9.
- 15 Rakhadilov B., Satbayeva Z., Baizhan D. Effect of electrolytic-plasma surface strengthening on the structure and properties of steel 40kHN. *METAL 2019 - 28th International Conference on Metallurgy and Materials, Conference Proceedings*, 2019, pp. 950-955.

DOI 10.31489/2022No1/26-33

UDC 538.9;535.215; 539.23; 535.3

## INFLUENCE OF PHTHALOCYANINE NANOSTRUCTURES ON OPTICAL AND PHOTOVOLTAIC CHARACTERISTICS OF A POLYMER SOLAR CELL

Aimukhanov A.K.\*, Zeinidenov A.K., Rozhkova X.S., Akhatova Zh.Zh.

E.A. Buketov Karaganda University, Scientific Center for Nanotechnology and Functional Nanomaterials, Karaganda, Kazakhstan, [a\\_k\\_aitbek@mail.ru](mailto:a_k_aitbek@mail.ru)

*Nanocomposite polymer solar cells were obtained. Nanostructures of phthalocyanines were added to a mixture of photoactive layer at a concentration of 0.5%. The photoactive layer was applied by centrifugation at a rotation speed of 1500 rpm. Atomic force microscope images of the surface of the films were measured. Absorption spectra of composite films were measured. It was found that the introduction of phthalocyanine nanostructures into the photoactive layer leads to a broadening of the spectrum and an increase in the optical density at the absorption maximum by 2.1 times for nanorods and 1.9 times for nanoparticles. The current-voltage characteristics of composite organic solar cells were measured. To do this, an aluminum electrode with a thickness of 100 nm was sprayed onto the surface of the photoactive layer at  $10^{-3}$  Torr. It is shown that when the photoactive layer was doped with nanorods and phthalocyanine nanoparticles, the short-circuit current density of the current-voltage characteristics increased by 8% and 5%, respectively, and the efficiency value increased to 4.58% and 4.51%, respectively. The impedance spectra of composite organic solar cells were measured. Analysis of hodographs of nanocomposite films showed that doping of the photoactive layer with nanorods and phthalocyanine nanoparticles leads to an increase in the diffusion length by 2.2 times and 1.8 times, respectively, and an increase in the mobility of charge carriers by 1.4 times and 1.2 times.*

**Keywords:** semiconductor polymers, metallophthalocyanines, generation and transport of charge carriers, photovoltaics.

### Introduction

The study of the generation and transport of charge carriers in organic semiconductors is relevant today. This is due to the fact that they have a low cost and inexpensive manufacturing technology compared to traditional inorganic semiconductors. Organic semiconductors have found wide application in quantum electronics, biology, medicine, as well as in the development of sensors, sensors and converters [1-3]. These include various temperature and gas sensors, pressure sensors and electromagnetic radiation. The development of polymer nanocomposite solar cells is one of the ways to increase the efficiency of converting solar energy into electrical energy. In such films, doping of the polymer matrix with nanoscale organic materials makes it possible to create a hybrid layer in which the conductivity of the polymer material will be combined with high optical and electrical properties of organic nanostructures. It should be noted that the advantage of these composite materials is a simplified process of manufacturing a solar cell [4, 5]. However, the study of the influence of structural features of molecular clusters on the efficiency of generation, separation of charges and their transport remains relevant in the development of organic semiconductor devices. The charge transfer and semiconductor properties of polymers are very sensitive to the morphology of polymer chains and local structural ordering within the film. Thus, structural and energy disorder in conjugated polymer systems are important for describing charge transfer involving various mechanisms and electronic processes [6].

Despite the obvious progress made in the creation of polymer solar cells, there are various limitations that prevent further improvement of the efficiency of solar energy conversion. For

example, a big problem is increasing the absorption of light in the photoactive layer and reducing the recombination of charge carriers [7, 8]. Currently, various approaches are used to increase light absorption without increasing the thickness of the photoactive layer. To solve this problem, the use of nanocomposites is proposed. To create such systems, nanostructures introduced by doping into a photoactive polymer material can be used. This makes it possible to create hybrid layers in which the conductivity of polymer materials increases.

Despite a fairly large number of works devoted to composite polymer solar cells, their optical and photo-electrophysical parameters are poorly studied. The study of the mechanisms of generation and transport of charge carriers in nanocomposite structures that affect the efficiency of solar energy conversion is the subject of discussion.

## 1. Methods and materials

To create solar cells as a donor was used poly [4,8-bis(5-(2-ethylhexyl)thiophene-2-yl)benzo[1,2-b;4,5-b']dithiophene-2,6-diyl-alt -(4-(2-ethylhexyl)-3-fluorotieno [3,4-b]thiophene-)-2-carboxylate -2-6-diil] (PTB7-Th), as an acceptor – 3,9-bis(2-methylene-(3-(1,1-dicyanomethylene)indanon))-5,5,11,11-tetrakis(4-hexylphenyl)dithieno[2,3-d:2',3'-d']-s-indaceno[1,2-b:5,6-b'] dithiophene (ITIC). The preparation of the substrates was carried out according to the method [6]. Methods of physical gradient-temperature vapor deposition (TG-PVD) and laser ablation in liquid were used for the synthesis of phthalocyanine nanostructures [7, 8]. The photoactive PTB7-Th:ITIC layer was applied by centrifugation at a rotation speed of 1500 r/pm. After that, the samples were annealed in an air atmosphere at a temperature of 110°C for 10 minutes. Then, at the CY-1700x-spc-2 spraying plant (Zhengzhou CY Scientific Instruments Co., Ltd), an aluminum electrode with a thickness of 100 nm was sprayed onto the surface of the photoactive layer at a vacuum of  $10^{-5}$ Torr. The structure of the polymer solar cell is shown in Fig.1.

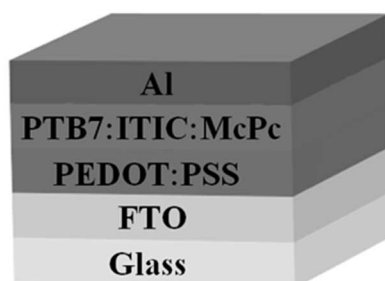


Fig.1. Solar cell structure.

Polymer and nanocomposite solar cells were obtained according to the method [9]. To create nanocomposite samples of solar cells, nanostructures of phthalocyanines were added to the prepared solution of the polymer PTB7-Th:ITIC at a concentration of 0.5% by weight of the polymer. The morphology of the surface of the obtained samples was studied using the atomic force microscope JSPM-5400 (JEOL Ltd, Japan). The optical characteristics of the films were studied using the Avantes AvaSpec-ULS2048CL-EVO spectrometer. A combined deuterium-halogen AvaLight-DHc light source with an operating range of 200-2500nm was used as a radiation source. The impedance spectra were measured using a measuring system P45X in the impedance mode. The current-voltage characteristics of photosensitive cells was determined by the Sol 3A Class AAA Solar Simulators (Newport) with PVIV-1 A I-V Test Station.

## 2. Results and discussion

AFM images of phthalocyanine nanostructures are shown in Figure 2. Nanoscale rods of phthalocyanines have an average width of 70 nm and a length of 500 nm. Phthalocyanine nanoparticles are mostly rounded in shape with an average size of about 50 nm. The same Figure 2 shows the AFM image of the PTB7-TH:ITIC film. It can be seen from the figure that the PTB7-TH:ITIC film has a homogeneous structure.

Figure 3 shows the absorption spectra of PTB7-Th:ITIC composite films doped with nanorods (a) and nanoparticles (b) of phthalocyanine and its metal complexes. The figure shows that the absorption spectrum of the PTB7-Th:ITIC film is located in the range of 450-780 nm with peaks at 642 nm and 694 nm and a half-width of 160 nm. Doping of the photoactive PTB7-Th:ITIC layer with nanorods and phthalocyanine nanoparticles leads to an increase in the optical density of the absorption spectrum. Thus, when the bulk heterojunction is doped with nanorods and ZnPc nanoparticles, the maximum increase in the optical density value in the absorption spectrum is observed (by 2.1 and 1.9 times, respectively). The half-width of the absorption spectrum increased slightly.

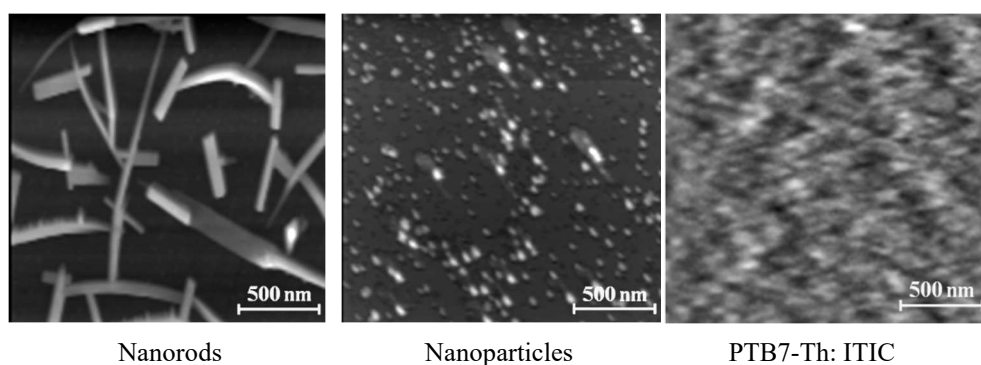


**Fig.2.** AFM images of phthalocyanine nanostructures and photoactive layer.

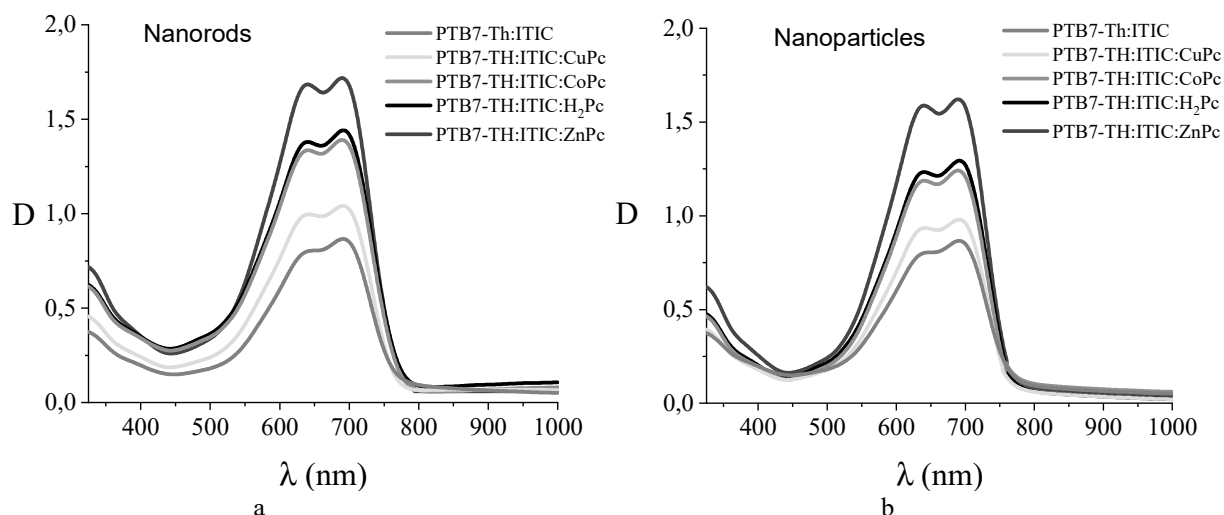


**Fig.3.** Absorption spectrum of pure polymer PTB7-TH:ITIC and absorption spectra of PTB7- TH:ITIC nanocomposites doped with nanorods (a) and nanoparticles (b) of phthalocyanines.

When doped with CuPc nanorods and nanoparticles, the optical density increased by a smaller amount (by 1.2 times). When doping with H<sub>2</sub>Pc and CoPc nanostructures, an increase in the optical density value is also observed. Table 1 shows the main optical characteristics of the obtained samples.

Thus, the introduction of nanorods and nanoparticles due to additional absorption contributes to an increase in the absorption of the photoactive layer of the polymer solar cell. One of the most important indicators of any photovoltaic devices is the efficiency of energy conversion (further EFF). The efficiency is determined by the following formula:

$$\eta = \frac{U_{OC} \cdot J_{SC} \cdot FF}{P_{IN}}, \quad (1)$$

where  $U_{OC}$  is the no-load voltage;  $J_{SC}$  is the short-circuit current density; FF is the fill factor;  $P_{IN}$  is the input power of the incident radiation.

The filling factor ( $FF$ ) determines the efficiency of the charge carrier generation process in the SC. The fill factor is determined by the ratio of the maximum power of the solar cell to the product of the no-load voltage and the short-circuit current density:

$$FF = \frac{J_{MP} \cdot U_{MP}}{J_{SC} \cdot U_{OC}}, \quad (2)$$

where  $J_{MP}$  and  $U_{MP}$  are the current density and voltage at the point of maximum power of the solar cell.

**Table 1.** Optical characteristics of PTB7-Th:ITIC thin films.

Sample	Maximum absorption		D <sub>1</sub>	D <sub>2</sub>	Half-width, nm
	$\lambda_1$ , nm	$\lambda_2$ , nm			
PTB7-Th:ITIC	642	694	0.81	0.88	160
Nanorods					
PTB7-TH:ITIC:CuPc	640	692	0.99	1.06	165
PTB7-TH:ITIC:CoPc	639	694	1.34	1.41	169
PTB7-TH:ITIC:H <sub>2</sub> Pc	641	693	1.38	1.45	168
PTB7-TH:ITIC:ZnPc	639	691	1.69	1.76	167
Nanoparticles					
PTB7-TH:ITIC:CuPc	639	691	0.94	0.99	164
PTB7-TH:ITIC:CoPc	640	693	1.19	1.24	168
PTB7-TH:ITIC:H <sub>2</sub> Pc	639	694	1.25	1.30	167
PTB7-TH:ITIC:ZnPc	640	692	1.59	1.64	166

Figure 4 shows the voltage characteristics of composite organic solar cells. The figure shows that the doping of the photoactive PTB7-Th:ITIC layer with nanorods (a) and nanoparticles (b) of phthalocyanines affects the parameters of the current-voltage characteristics cells. For example, the filling factor of a composite cell with nanorods and PTB7-Th:ITIC:CuPc nanoparticles was  $FF = 0.55$  and  $0.54$  respectively, and the value of the short-circuit current density is equal to  $J_{sc} = 10.62$  mA/cm<sup>2</sup> and  $10.53$  mA/cm<sup>2</sup>. The same changes are observed for composite cells doped with H<sub>2</sub>Pc and CoPc nanostructures.

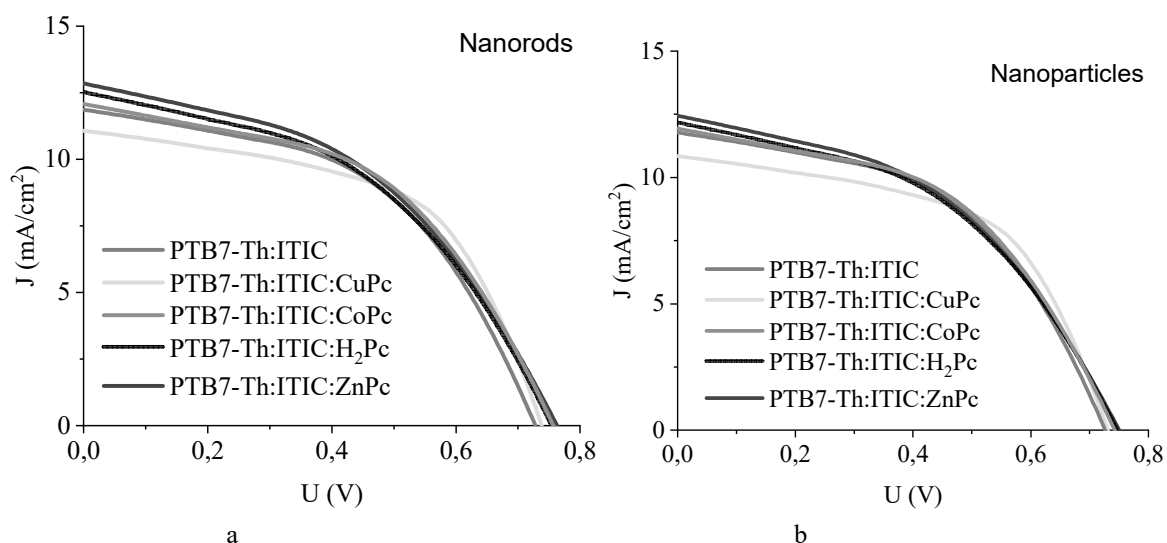


**Fig.4.** Voltage characteristics of nanocomposite solar cells based on PTB7-Th:ITIC doped with nanorods (a) and nanoparticles (b).

The maximum value of the increase in the CVC parameters is observed for a composite cell with PTB7-Th:ITIC:ZnPc nanostructures, so the short-circuit current density when doped with nanoparticles increased by 5%, the efficiency value was 4.51%, when doped with nanorods, the short-circuit current density increased by 8%, the efficiency was 4.58%. The parameters of the CVC cells are given in Table 2.

Figure 5a shows a charge carrier transfer scheme in a composite photoactive layer. The photo voltage generated in the heterojunction is determined by the difference between the quasi-fermi level of electrons in the acceptor and the quasifermi level of holes in the donor under illumination [10, 11]. It is obvious that the nanostructures of phthalocyanines in the photoactive layer will influence the position of the quasi-level of holes in PTB7-Th. As can be seen from the energy diagram (Figure 5b), the position of the bottom of the phthalocyanine conduction band is above the bottom of the ITIC conduction band.

**Table2.** Photovoltaic characteristics of organic solar cells.

Sample	$J_{sc}$ , (mA/cm <sup>2</sup> )	$J_{max}$ , (mA/cm <sup>2</sup> )	$U_{oc}$ , (V)	$U_{max}$ , (V)	FF	Efficiency, %
PTB7-TH:ITIC	11.93	8.32	0.73	0.51	0.46	4.24
Nanorods						
PTB7-TH:ITIC:CuPc	10.62	7.54	0.74	0.57	0.55	4.29
PTB7-TH:ITIC:CoPc	11.94	8.34	0.75	0.53	0.49	4.42
PTB7-TH:ITIC:H <sub>2</sub> Pc	12.43	8.77	0.75	0.51	0.48	4.47
PTB7-TH:ITIC:ZnPc	12.84	8.97	0.76	0.51	0.47	4.58
Nanoparticles						
PTB7-TH:ITIC:CuPc	10.53	7.59	0.74	0.56	0.54	4.25
PTB7-TH:ITIC:CoPc	11.94	8.28	0.74	0.52	0.49	4.31
PTB7-TH:ITIC:H <sub>2</sub> Pc	12.38	8.64	0.75	0.51	0.48	4.41
PTB7-TH:ITIC:ZnPc	12.54	8.85	0.75	0.51	0.47	4.51

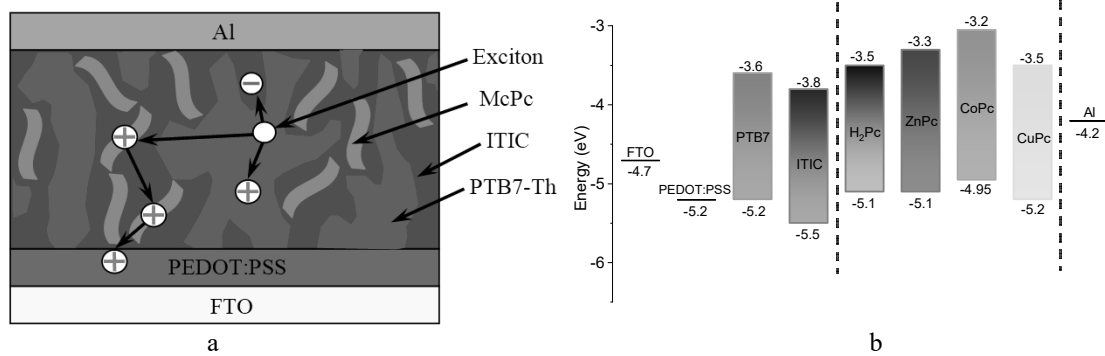


**Fig.5.** The carrier transfer scheme in the cell (a) and the energy diagram of the composite photo converter (b).

This contributes to the formation of a potential barrier for the injection of electrons from the ITIC conduction band into the conduction band of phthalocyanine nanostructures. In turn, as can be seen from the energy diagram, the upper level of the PTB7-Th valence band is slightly lower than the upper level of the phthalocyanine valence band. As a result, a built-in electric field is formed at the PTB7-Th/phthalocyanine interface, which transfers holes from the valence band of PTB7-Th to the valence band of phthalocyanine nanostructures. Also, due to the formation of nanorods and phthalocyanine nanoparticles, holes are more efficiently transported to PEDOT:PSS, which leads to an increase in photocurrent.

An increase in the value of the short-circuit current of the CVC and the efficiency of the cells can be associated with a number of reasons: a decrease in the recombination of charge carriers in the active layer, an increase in the transport of charge carriers due to an increase in the interface area [12, 13]. In order to determine the effect of phthalocyanine nanostructures on the transport and recombination of charge carriers, measurements of the impedance spectra of composite cells were carried out. To interpret the impedance spectra of solar cells, an equivalent electrical circuit was used, where  $R_1$  ( $R_w$ ) is the equivalent resistance of a multilayer film (the resistance of a photoactive layer),  $R_2$  ( $R_{rec}$ ) is the resistance of the PTB7-Th/ITIC interface, characterizing the recombination of electrons with holes (Figure 6a). The charge transport scheme in the cell is shown in Figure 6b.



**Fig.6.** Equivalent electrical circuit (a) and charge transport circuit in the cell (b).

The fitting of the spectrum parameters was carried out using the EIS-analyzer software package. The analysis of the impedance measurement results was carried out according to the diffusion-recombination model [14,15]. As a result of the analysis of the impedance spectra, the following electric transport parameters were determined:  $\tau_{eff}$  – the effective lifetime of charge carriers;  $k_{eff}$  – the effective rate of extraction of charge carriers,  $D_{eff}$  – the effective diffusion coefficient of charge carriers and  $\mu$  – the mobility of charge carriers. Analysis of hodographs (Figure 7) of nanocomposite films showed that doping of the photoactive layer with nanorods (a) and nanoparticles (b) of phthalocyanines leads to an increase in the diffusion length ( $D_{eff}$ ) and an increase in the mobility of charge carriers ( $\mu$ ) (Table 3).



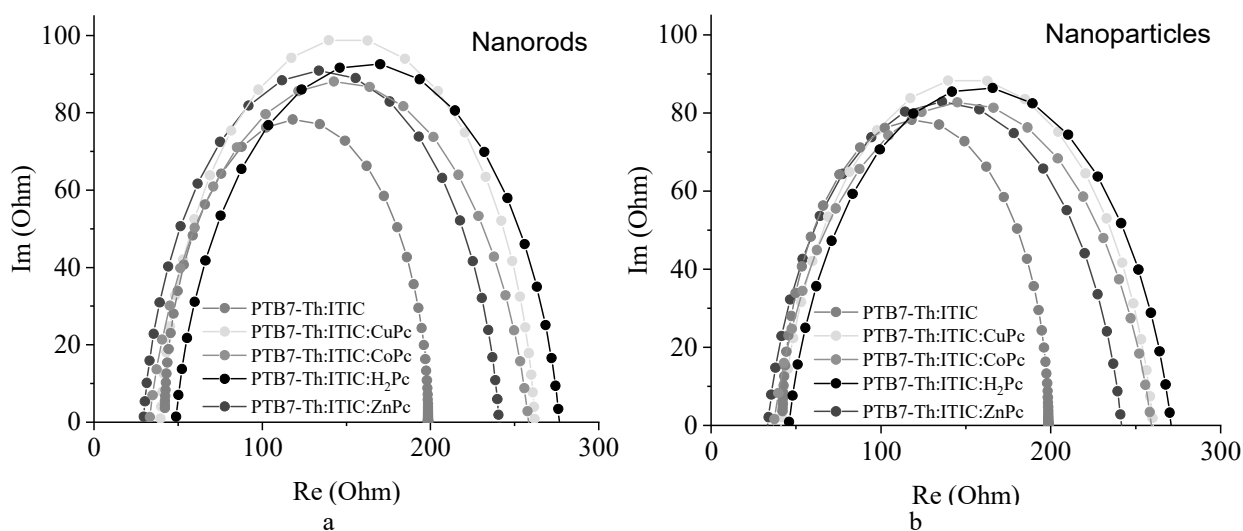


**Fig.7.** Hodographs of the impedance of solar cells based on the photoactive PTB7-TH:ITIC layer and nanocomposites doped with nanorods (a) and nanoparticles (b).

Doping of the photoactive PTB7-Th:ITIC layer with ZnPc nanorods and nanoparticles leads to a maximum 2.2 fold (for nanorods) and 1.8 fold (for nanoparticles) increase in the  $D_{eff}$  value and a decrease in the  $R_w$  value by 1.5 fold (for nanorods) and 1.3 fold (for nanoparticles).

**Table 3.** Electric transport properties of the obtained samples of nanocomposite SC with different structures.

Sample	$D_{eff}$ , ( $\text{cm}^2 \cdot \text{s}^{-1}$ )	$k_{eff}$ , ( $\text{s}^{-1}$ )	$\tau_{eff}$ , (ms)	$R_{rec}$ , (Ohm)	$R_w$ , (Ohm)	$\mu$ , ( $\text{cm}^2/\text{Vs}$ )
PTB7-TH:ITIC	$2.09 \cdot 10^{-5}$	45846	0.021	198.3	43.3	$2.82 \cdot 10^{-4}$
Nanorods						
PTB7-TH:ITIC:CuPc	$3.32 \cdot 10^{-5}$	49924	0.020	261.4	39.3	$3.12 \cdot 10^{-4}$
PTB7-TH:ITIC:CoPc	$3.87 \cdot 10^{-5}$	48835	0.020	258.4	32.6	$3.25 \cdot 10^{-4}$
PTB7-TH:ITIC:H <sub>2</sub> Pc	$2.71 \cdot 10^{-5}$	47589	0.021	276.1	48.4	$2.97 \cdot 10^{-4}$
PTB7-TH:ITIC:ZnPc	$4.54 \cdot 10^{-5}$	53486	0.019	240.2	28.3	$3.86 \cdot 10^{-4}$
Nanoparticles						
PTB7-TH:ITIC:CuPc	$3.01 \cdot 10^{-5}$	48466	0.020	258.6	41.7	$3.01 \cdot 10^{-4}$
PTB7-TH:ITIC:CoPc	$3.38 \cdot 10^{-5}$	47377	0.021	258.4	36.2	$3.14 \cdot 10^{-4}$
PTB7-TH:ITIC:H <sub>2</sub> Pc	$2.69 \cdot 10^{-5}$	46024	0.021	268.1	45.8	$2.87 \cdot 10^{-4}$
PTB7-TH:ITIC:ZnPc	$3.86 \cdot 10^{-5}$	52028	0.019	241.9	32.6	$3.49 \cdot 10^{-4}$

## Conclusion

Nanocomposite polymer solar cells containing nanostructures of phthalocyanines have been obtained. According to AFM images of the surface, using the Win SPMII Data-Processing Software package, an analysis of the surface of nanostructures and a photoactive layer was carried out. The measurement of the absorption spectra of nanocomposite cells showed that nanostructures in the photoactive PTB7-Th:ITIC layer lead to an increase in the optical density values in the maxima on average from 0.81 to 1.69 and the half-width of the absorption spectrum from 160 to 167 nm. This means that in a composite cell, when light is absorbed by a photoactive layer, the density of charge

carriers increases. Measurements of the CVC of composite cells have shown that nanostructures, minimizing the probability of charge recombination, more efficiently transport holes into PEDOT:PSS, and thus increase the short-circuit current to 12.84 mA/cm<sup>2</sup> and efficiency to 4.58%. Experiments were conducted on the effect of nanostructures on the transport and recombination of charge carriers in composite cells. It is shown that nanostructures contribute to an increase in recombination resistance at the PTB7-Th/ITIC boundary by 1.2 times and a decrease in the resistance of a multilayer film by 1.5 times. Thus, the results obtained showed the possibility of using nanostructures as promising composite materials for photovoltaic organic solar cells. The development of composite solar cells has the prospect of creating lightweight, technologically advanced and cheap in mass production autonomous power sources for a wide range of electronic devices.

#### Acknowledgments

This research is funded by the Science Committee of the Ministry of Education and Science of the Republic of Kazakhstan (Grant No. AP08856176)

#### REFERENCES

- 1 Brau A., Farges J.P. Organic Semiconductors. *Org. Conduct. Fundam. Appl. Marcel Dekker*, 1994, pp.311–357.
- 2 Hohnholz D., Steinbrecher S., Hanack M. Applications of phthalocyanines in organic light emitting devices. *Journal of Molecular Structure*, 2000, Vol. 521, pp. 231-237. doi: 10.1016/S0022-2860(99)00438-X.
- 3 Itoh E., Ohmori Y., Miyairi K. Photovoltaic Properties of Organic p-n Junction Devices Consisting of Phthalocyanine and n-Type Porphyrin Deposited on an n-Type TiO<sub>2</sub> Layer. *Japanese J. Appl. Physics. Part 1 Regul. Pap. Short Notes Rev. Pap.* 2004, Vol. 43, Is.2., pp 817-821. doi: 10.1143/JJAP.43.817.
- 4 Wagenpfahl A., Deibel C., Dyakonov V. Organic solar cell efficiencies under the aspect of reduced surface recombination velocities. *IEEE J. Sel. Top. Quantum Electron.* 2010, Vol.16, Is.6, pp. 1759-1763.
- 5 Bi X., WuZ., ZhangT., AnC., XuY., MaK., et al. Reduced Nonradiative Recombination Energy Loss Enabled Efficient Polymer Solar Cells via Tuning Alkyl Chain Positions on Pendant Benzene Units of Polymers. *ACS Appl. Mater. Interfaces.* 2020, Vol.12, pp. 24184-24191. doi: 10.1021/acsami.0c04397.
- 6 Kim K., Ihm K., Kim B. Surface Property of Indium Tin Oxide (ITO) After Various Methods of Cleaning. *Acta Physica Polonica.* 2014, Vol. 127, No. 4, pp. 1176-1179. doi: 10.12693/APhysPolA.127.1176.
- 7 Hashizume M., Kunitake T. Preparation and functionalization of self-supporting (polymer/metal oxide) composite ultrathin films. *RIKEN Rev.* 2001, Vol. 38, pp. 36–39.
- 8 Pakhomov G.L., Gaponova D.M., Lukyanov A.Yu., Leonov E. S. Luminescence in phthalocyanine thin films. *Solid state physics.* 2005, Vol.47, No.1, pp.164-167.
- 9 Zeinidenov A.K., Aimukhanov A.K., Kambar D.S., Ilyassov B.R., Zavgorodniy A.V. Effects of phthalocyanine nanostructure on photovoltaic performance of its polymer composite thin films. *Materials Chemistry and Physics.* 2021, Vol. 267, p.124680. doi: 10.1016/j.matchemphys.2021.124680.
- 10 Gregg B.A., Hanna M.C. Comparing organic to inorganic photovoltaic cells: Theory, experiment, and simulation. *Journal of Applied Physics.* 2003, Vol.93, Is.6, pp. 3605 - 3614. doi: 10.1063/1.1544413.
- 11 Ellison D.J., Kim J.Y., Stevens D.M., Frisbie C.D. Determination of quasi-fermi levels across illuminated organic donor/acceptor heterojunctions by kelvin probe force microscopy. *J. Am. Chem. Soc.* 2011, Vol.133, Is.35, pp.13802-13805. doi: 10.1021/ja2034574.
- 12 Yang H., Song Q., Lu Z., Guo C., et al. Electrochemically polymerized nanostructured poly (3,4-ethylenedioxythiophene)-poly(styrenesulfonate) buffer layer for a high performance polymer solar cell. *Energy and Environ. Science.* 2010, Vol. 3, pp.1580-1586. doi: 10.1039/C0EE00117A.
- 13 Yuan X., Song C., Wang H., Zhang J. *EIS Equivalent Circuits In Electrochemical Impedance Spectroscopy in PEM Fuel Cells.* California: Springer, 2010, doi:10.1007/978-1-84882-846-9.
- 14 Zavgorodniy A.V., Aimukhanov A.K., Zeinidenov A.K., et al. The influence of the magnetic field on the current-voltage characteristics of cupc nanostructures. *Eurasian phys. tech. j.* 2019, Vol.16, No.1(31), P.54-61.
- 15 Aimukhanov A.K., Zeinidenov A.K., Ilyassov B.R., Zavgorodniy A.V. The research of photo-electrophysical properties of cobalt phthalocyanine film. *Eurasian phys. tech. j.* 2019, Vol.16, No.2(32), P.16-20.

DOI 10.31489/2022No1/34-39

UDC: 538.9; 535.215; 539.23; 535.3; 535.3

## IMPACT OF THE ANNEALING TEMPERATURE OF $\text{In}_2\text{O}_3$ FILMS ON THE PHOTOVOLTAIC CHARACTERISTICS OF A POLYMER SOLAR CELLS

Zeinidenov A.K.<sup>1</sup>, Aimukhanov A.K.<sup>1</sup>, Omarbekova G.I.<sup>1\*</sup>, Ilyassov B.R.<sup>2</sup>

<sup>1</sup> E.A. Buketov Karaganda University, Karaganda, Kazakhstan, [gulnur\\_130983@mail.ru](mailto:gulnur_130983@mail.ru)

<sup>2</sup> Astana IT University, Nur-Sultan, Kazakhstan

*It is necessary to determine the effect of thermal annealing on morphology, absorption, and photoelectric properties for increase the efficiency of electronic transport of  $\text{In}_2\text{O}_3$  films. The paper presents the results of a study the effect of the annealing temperature of  $\text{In}_2\text{O}_3$  films obtained by spin-coating on the optical and photo-electrophysical characteristics of a polymer solar cell. It is established that an increase in the annealing temperature of films leads to an increase in the absorption and optical width of the band gap of the film. Has been determined the optimal annealing temperature of the films  $T = 300^\circ\text{C}$ , at which the electrons in the photoactive layer has the maximum lifetime of charge carriers and a low probability of recombination. At this temperature is observed, the maximum value of the efficiency of polymer solar cell.*

**Keywords:**  $\text{In}_2\text{O}_3$ , polymer solar cell, voltage characteristics, impedance spectra.

### Introduction

Currently, semiconductor complex double and triple oxides, such as  $\text{In}_2\text{O}_3$ ,  $\text{ZnO}$ ,  $\text{SnO}_2$ ,  $\text{CdO}$ ,  $\text{Ga}_2\text{O}_3$ ,  $\text{TiO}_2$ , are intensively studied. This is due to the fact that such materials have a fairly high transparency ( $\sim 90\%$ ) in the visible range and the ability to conduct electric current. Therefore, they are used in the manufacture of thin displays, organic light-emitting diodes, solar panels, thin-film transistors, gas sensors, spacecraft, etc.

Relatively have a low mobility of charge carriers films based on  $\text{ZnO}$  and  $\text{TiO}_2$ . Indium oxide ( $\text{In}_2\text{O}_3$ ) having a band gap width (3.7-3.85 eV), optical transparency and relatively high electron mobility ( $14 - 226 \text{ cm}^2 * \text{V}^{-1} * \text{s}^{-1}$ ) is an alternative [1].

There are many known methods for producing transparent conductive films based on indium oxide.  $\text{In}_2\text{O}_3$  thin films can be obtained by pulsed laser deposition (PLD) [2], magnetron sputtering [3], pyrolysis by sputtering [4], ultrasonic sputtering [5, 6], sol-gel technology [7], spin coating method. In comparison with the above methods, the spin coating method has many advantages: simplicity of technology, low cost of reagents and equipment, the use of low-temperature deposition, which allows the production of high-quality films of various shapes and sizes.

It is known that the annealing temperature affects oxygen vacancies and the defectiveness of  $\text{In}_2\text{O}_3$  films, as a result is observed of change in the structural and electrical properties of the films [8, 9]. Hence, to increase the efficiency of electronic transport, it is necessary to establish the effect of thermal annealing on the surface structure, absorption, and electrophysical and photovoltaic characteristics in  $\text{In}_2\text{O}_3$  films. In this regard, in this paper, has been studied the influence of the annealing temperature of  $\text{In}_2\text{O}_3$  films obtained by spin coating on the morphology, optical and electrical properties of the electron transport layer (ETL) in organic solar cells (OSCs).

## 1. Experimental methods

The Fluorinated Tin Oxide (FTO) -based substrates were prepared according to the methodology [10]. Indium oxide films were obtained on the FTO/glass substrates surface as follows: indium nitrate hydrate [ $\text{In}(\text{NO}_3)_3 \cdot x\text{H}_2\text{O}$ ] weighing  $m=190\text{mg}$  (Borun New Material Technology Ltd.) was dissolved in a volume of ethylene glycol  $V = 1\text{ ml}$ . The solution was stirred at room temperature for 16 hours and then kept for 24 hours at room temperature.  $\text{In}_2\text{O}_3$  films were obtained by spin-coating (SPIN150i, Semiconductor Production System) at a substrate rotation speed of 2000 rpm. After that, the films were annealed in an air atmosphere at temperatures of  $200^\circ\text{C} - 500^\circ\text{C}$  for an hour.

The surface topography of the  $\text{In}_2\text{O}_3$  films was studied by scanning electron microscopy (SEM, MIRA 3LMU, TESCAN). The absorption and reflection spectra the studied samples were recorded using the AvaSpec-ULS2048CL-EVO (Avantes) spectrometer. The impedance spectra were measured using a potentiostat-galvanostat P45X in the impedance mode. The voltage-current characteristics of photosensitive cells was determined by the Sol3A Class AAA Solar Simulators (Newport) with PVIV-1A I-V Test Station.

To obtain organic solar cells, a photoactive P3HT:ICMA layer was applied to the surface of the  $\text{In}_2\text{O}_3$  film by spin-coating (3000 rpm) (Figure 1) (P3HT 95%, ICMA 98%, Sigma-Aldrich) at a concentration of 1:0.8. After that, the film of the photoactive layer was annealed in an air atmosphere at a temperature of  $140^\circ\text{C}$  for 10 minutes, then an hole transport layer (HTL) of PEDOT:PSS ( $d \sim 30\text{ nm}$ ) was applied to the surface by spin-coating (3000 rpm), and then a current-removing electrode (Ag,  $d \sim 120\text{ nm}$ ) was sprayed by thermal deposition on the CY-1700x-spc-2 installation (Zhengzhou CY Scientific Instruments Co., Ltd).

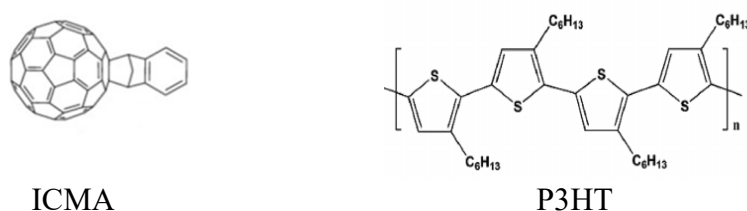


Fig.1. Structural formulas of compounds of donor-acceptor pairs P3HT: ICMA

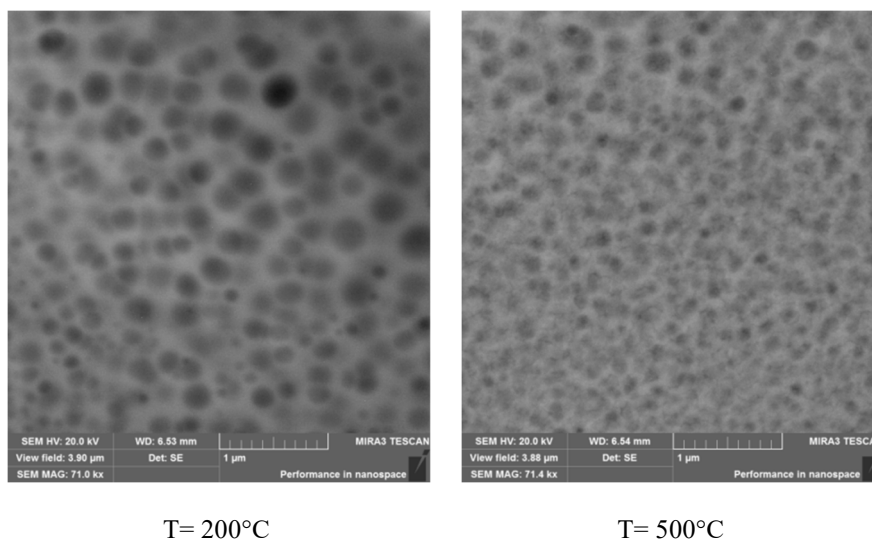
## 2. Results and discussion

Figure 2 shows SEM images of the surface of the studied films annealed at different temperatures. It can be seen from the figure that the surface of the film is a porous structure. The annealing temperature of the films affects the morphology of the surface. Thus, the pore sizes begin to decrease with an increase in the annealing temperature of the films.

To determine the effect of the annealing temperature on the optical properties of  $\text{In}_2\text{O}_3$ , the absorption and reflection spectra of films annealed at different temperatures were measured (Figure 3). The characteristics of the absorption spectra of  $\text{In}_2\text{O}_3$  films at different annealing temperatures are given in Table 1. Measurement of absorption spectra showed that the absorption of films increases with increasing annealing temperature (Figure 3, a). The annealing temperature does not affect the shape of the absorption spectrum [8].

The inset of Figure 3, a illustrates the dependences of the band gap  $\text{In}_2\text{O}_3$  at different annealing temperatures. The graph shows that at an annealing temperature at  $200^\circ\text{C}$ , the optical band gap is  $4.68\text{ eV}$  [11, 12]. An increase in the annealing temperature from  $300^\circ\text{C}$  to  $500^\circ\text{C}$  leads to an increase in the optical band gap from  $3.21\text{ eV}$  to  $3.41\text{ eV}$ . The increase in  $E_g$  is associated with a decrease in the oxygen vacancy density in the film with an increase in the annealing temperature.

Figure 3, b demonstrates the reflection spectra of thin films  $\text{In}_2\text{O}_3$ . That can be found from the figure that the film annealed at  $T = 200^\circ\text{C}$  reflects light very weakly in the short-wavelength region of the spectrum. When the annealing temperature rises to  $300^\circ\text{C}$  and above, the shape of the absorption spectrum changes.



**Fig.2.** SEM images of the surface of  $\text{In}_2\text{O}_3$  films annealed at different temperatures

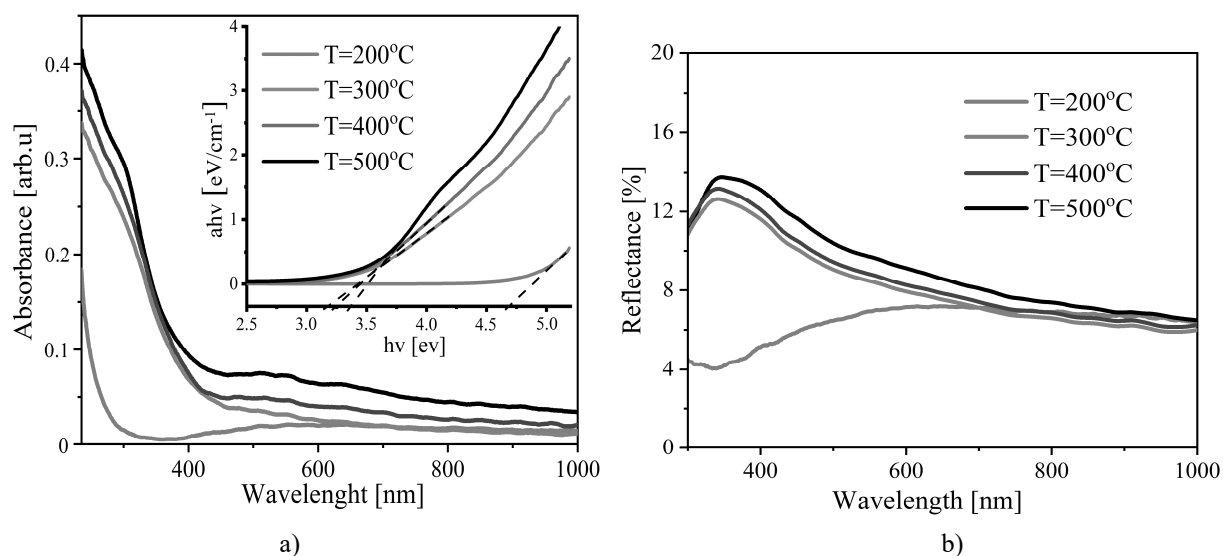


**Fig.3.** Absorption (a) and reflection (b) spectra of  $\text{In}_2\text{O}_3$  films

**Table 1.** Parameters of optical absorption spectra of  $\text{In}_2\text{O}_3$  films at different annealing temperatures

No.	Annealing temperature, $^\circ\text{C}$	Absorption, arb.u. ( $\lambda = 235 \text{ nm}$ )	Band gap, eV	Reflection, % ( $\lambda = 345 \text{ nm}$ )
1	200	0.18	4.68	4.1
2	300	0.33	3.21	12.6
3	400	0.36	3.32	13.2
4	500	0.41	3.41	13.8

The reflection of light by the film in the short-wave region of the spectrum is higher than in the long-wave region. An increase in the annealing temperature above 300°C slightly affects the reflection of the films. To determine the effect of the annealing temperature of  $\text{In}_2\text{O}_3$  films on electronic transport, an  $\text{In}_2\text{O}_3/\text{P3HT}:\text{ICMA}/\text{PEDOT}:\text{PSS}/\text{Ag}$  cell was assembled in a polymer solar cell (Figure 4).

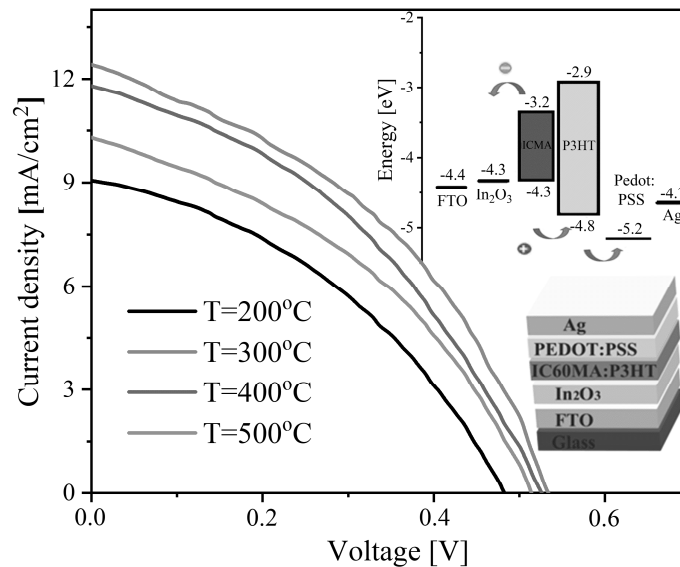


**Fig.4.** The voltage-current characteristics of FTO/ $\text{In}_2\text{O}_3$ /P3HT:ICMA/ PEDOT:PSS/Ag OSCs

When the P3HT:ICMA layer is photoexcited forms an electron-hole pair, which then forms at the interface  $\text{In}_2\text{O}_3/\text{P3HT}:\text{ICMA}$  and P3HT:ICMA/PEDOT:PSS decays into a free electron and a hole (Figure 4). Electrons are injected into the  $\text{In}_2\text{O}_3$  layer, and a hole is injected into the PEDOT:PSS layer. The volt-ampere characteristics of a polymer solar cell are shown in Figure 4.

Table 2 shows the photovoltaic parameters of the cell calculated on the basis of the voltage-current characteristics. As can be seen from Figure 4 and Table 2, the voltage-current characteristics parameters depend on the annealing temperature  $\text{In}_2\text{O}_3$ . At the annealing temperature  $T = 200^\circ\text{C}$ , the efficiency of the cell was 1.7%. When the annealing temperature rises to  $T = 300^\circ\text{C}$ , there is an increase in the values of currents, voltage and power conversion efficiency (PCE) of the cell. With an increase in the annealing temperature of  $\text{In}_2\text{O}_3$  films above  $300^\circ\text{C}$ , a decrease in the values of the voltage-current characteristics parameters is observed.

**Table 2.** Parameters of the voltage-current characteristics solar cells

Annealing temperature, °C	$V_{oc}$ , (V)	$J_{sc}$ , ( $\text{mA}/\text{cm}^2$ )	$V_{max}$ , (V)	$J_{max}$ , ( $\text{mA}/\text{cm}^2$ )	Fill factor	PCE, %
200	0.48	9.06	0.30	5.72	0.4	1.7
300	0.53	12.41	0.34	7.91	0.41	2.7
400	0.52	11.76	0.33	7.34	0.4	2.4
500	0.51	10.24	0.32	6.51	0.4	2.0

The observed changes in the voltage-current characteristics are related to the structural changes of indium oxide observed with an increase in the annealing temperature, which affect the transfer of charge carriers to OSCs. To study in detail the effect of indium oxide structure on the dynamics of charge carrier transport in OSCs, the impedance spectra of OSCs were measured. Figure 5 illustrates the impedance spectra of organic cells with indium oxide as an ETL layer annealed at different temperatures and the electrical circuit that was used to fit the impedance spectra.

Table 3 shows the electric transport parameters of cells calculated using the EIS-analyzer software package, where ( $R_w$ ) is the equivalent resistance of the  $\text{In}_2\text{O}_3$  film; ( $R_{rec}$ ) is the resistance characterizing the recombination of localized electrons with holes; ( $k_{eff}$ ) is the effective recombination rate of charge carriers; ( $\tau_{eff}$ ) is the effective lifetime of charge carriers. Table 3 shows that at the annealing temperature of  $200^\circ\text{C}$  of the  $\text{In}_2\text{O}_3$  film, the resistance of the  $R_w$  film shows the highest value compared to other films, while the recombination resistance of  $R_{rec}$  is the lowest value. This leads to a deterioration in the transport of injected electrons into the FTO electrode. When the annealing temperature of the  $\text{In}_2\text{O}_3$  film increases to  $300^\circ\text{C}$ , the resistance  $R_w$  decreases to the lowest value compared to other films, while the resistance  $R_{rec}$  increases and reaches the highest value among all. As a result, the electric transport characteristics of the film are improved, this leads to an increase in efficiency (2.7%).

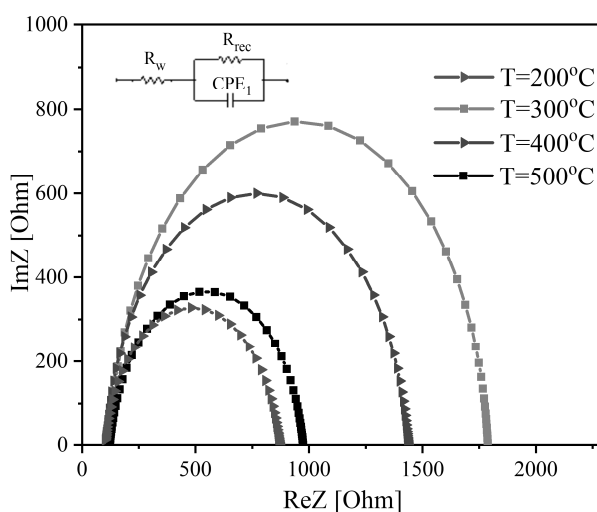


**Fig.5.** Impact of annealing temperature of  $\text{In}_2\text{O}$  films on the impedance spectra of OSCs

**Table 3.** The value of electrophysical parameters of films.

Annealing temperature, $^\circ\text{C}$	$R_w$ , (Ohm)	$R_{rec}$ , (Ohm)	$R_{rec}/R_w$ , (Ohm)	$\tau_{eff}$ , (ms)	$k_{eff}$ , ( $\text{s}^{-1}$ )
200	121	769	6.35	1.1	948
300	99	1667	16.84	2.1	476
400	102	1331	13.05	1.7	561
500	105	952	9.07	1.3	782

The analysis of the cell impedance spectra shows that the  $\text{In}_2\text{O}_3$  film at an annealing temperature of  $300^\circ\text{C}$  is optimal for OSCs, at which an increase in the efficiency of charge carrier transport is observed. In this case, the electrons in the photoactive layer have the maximum lifetime of charge carriers and a low probability of recombination.

## Conclusion

In this paper has been studied, the influence of the  $\text{In}_2\text{O}_3$  annealing temperature on morphology, structure and optical properties. It is established that with increasing annealing temperature, the porosity of the film begins to decrease. It is shown that an increase in the annealing temperature leads to an increase in the optical band gap by 0.2 eV. It is shown that the parameters of the voltage-current characteristics depend on the annealing temperature  $\text{In}_2\text{O}_3$ . It is established that the annealing temperature of  $300^\circ\text{C}$  of  $\text{In}_2\text{O}_3$  films is optimal for OSCs. At this temperature,

observed an increase in efficiency up to 2.7%, the maximum lifetime of charge carriers and a low probability of recombination in the OSCs. The obtained experimental data will have a perspective for the creation of electron transport layers of an organic photoconverter, providing a high conversion rate of light energy into electrical energy. This will help in the development of lightweight, technologically advanced and inexpensive in mass production, autonomous power supply sources for a wide range of electronic appliances and devices.

## REFERENCES

- 1 Huang W., Zhu B., Chang Sh.Y., et al. High Mobility Indium Oxide Electron Transport Layer for an Efficient Charge Extraction and Optimized Nanomorphology in Organic Photovoltaics. *Nano Letters*, 2018, Vol.18(9), pp. 5805–5811.
- 2 Stankiewicz J., Torrelles X. Structural and electrical properties of indium oxide thin films grown by pulsed laser deposition in oxygen ambient. *J. Alloy. Compd.*, 2017, Vol. 694, pp. 1280 – 1286.
- 3 Binas V., Kortidis I. Ageing resistant indium oxide ozone sensing films. *Sens. Lett.*, 2016, Vol. 14, pp. 563–566. <https://doi.org/10.1166/sl.2016.3665>
- 4 Attaf A., Bouhdjer A. On tuning the preferential crystalline orientation of spray pyrolysis deposited indium oxide thin films. *Thin Solid Films*, 2017, Vol. 625, pp. 177–179. <https://doi.org/10.1016/j.tsf.2017.01.055>
- 5 Bouhdjer A., Attaf A. Influence of annealing temperature on In<sub>2</sub>O<sub>3</sub> properties grown by an ultrasonic spray CVD process. *Optik*, 2016, Vol. 127, pp. 6329–6333. <https://doi.org/10.1016/j.ijleo.2016.04.100>
- 6 Bouhdjer A., Saidi H. Structural, morphological, optical, and electrical properties of In<sub>2</sub>O<sub>3</sub> nanostructured thin films. *Optik*, 2016, Vol. 127, pp. 7319–7325. <http://doi.org/10.1016/j.ijleo.2016.05.035>
- 7 Ilican S., Caglar M., Caglar Y. Structural, morphological and optical properties of indium oxide film by sol gel spin coating. *J. Mater. Electron. Dev.*, 2016, Vol 1, pp. 19 – 23.
- 8 Yuan Z., Zhu X., Wang X., Cai X., Zhang B., Qiu D. Annealing effects of In<sub>2</sub>O<sub>3</sub> thin films on electrical properties and application in thin film transistors. *Thin Solid Films*, 2011, Vol. 519(10), pp. 3254–3258.
- 9 Gan J., Lu X. Oxygen vacancies promoting photoelectrochemical performance of In<sub>2</sub>O<sub>3</sub> nanocubes. *Sci. Rep.* 2012, Vol. 3, pp. 1021. <https://doi.org/10.1038/srep01021>
- 10 Farrag A.A., Balboul M.R. Nano ZnO thin films synthesis by sol–gel spin coating method as a transparent layer for solar cell applications. *J. Sol-Gel Sci. Technol.*, 2017, Vol. 82, pp. 269–279.
- 11 Ismail R.A. Preparation of colloidal In<sub>2</sub>O<sub>3</sub> nanoparticles using nanosecond laser ablation in water. *Micro & Nano Letters*, 2011, Vol. 6, pp. 951–954. <https://doi.org/10.1049/mnl.2011.0459>
- 12 Yahiaa A., Attafa A. Structural, optical, morphological and electrical properties of indium oxide thin films prepared by sol gel spin coating process. *Surfaces and Interfaces*, 2019, Vol. 14, pp. 158–165.



DOI 10.31489/2022No1/40-49

UDC 620.9

## THERMAL POWER PLANT BASED ON A FREE PISTON ENGINE AND A RECIPROCATING GENERATOR

Kaluzhsky D.L.<sup>1</sup>, Mekhtiyev A.D.<sup>2,3</sup>, Neshina Y.G.<sup>4\*</sup>, Alkina A.D.<sup>4</sup>, Sarsikheyev Y.Z.<sup>2</sup>

<sup>1</sup> Novosibirsk State Technical University, Novosibirsk, Russia

<sup>2</sup> S. Seifullin Kazakh Agrotechnical University, Nur-Sultan, Kazakhstan

<sup>3</sup> National Research Tomsk Polytechnic University, Tomsk, Russia

<sup>4</sup> Karaganda Technical University, Karaganda, Kazakhstan, 1\_neg@mail.ru

*The article discusses an autonomous power supply system based on a Stirling engine and a reciprocating generator. There are analyzed the conditions of its operation, the choice of an external combustion engine and a linear synchronous generator. In the course of solving the problem of supplying autonomous consumers with thermal and electric energy remote from the city infrastructure, a power plant with the capacity of up to 100 VA was developed and manufactured. Its experimental study, as well as the analysis of the patent-information array, made it possible to determine the boundaries of using this technical object. The reciprocating generator is driven by a free-piston engine with an external heat supply. For carrying out field experiments, a prototype laboratory model of a free-piston engine with an external heat supply with a linear alternator has been developed. Its main difference from the known types of Stirling engines is the absence of a massive flywheel with a crankshaft and a crank mechanism, which makes it possible to achieve greater tightness and significantly increases the power on output shaft while limiting the outer dimensions. Air is used as the working medium with addition of a small percentage of water, which makes it possible to develop pressure up to 10 MPa. The technical calculation of the generator design has been given, the force required to develop the needed power during the movable element reciprocating movement has been determined. Solutions have been adopted to suppress acoustic noise causing discomfort to consumers. This can in particular be done by placing vibration dampers and designing a generator with a high efficiency. The design of the moving element should minimize mechanical stress on the windings or magnets. The proposed generator can be competitive and can successfully replace traditional low-power sources of electricity with diesel or gasoline engines.*

**Keywords:** : micro power plant, Stirling engine, reciprocating generator, alternative source.

### Introduction

At present, in the Republic of Kazakhstan, there exists an extremely acute problem associated with the effective power supply of small business focused on the production of agricultural products and residents of small settlements. The fact is that even in hard-to-reach areas there are abundant power lines with voltages of 10 and 35 kV that were inherited from the USSR. At the same time, the possibility of building step-down substations is often simply not considered, due to their low profitability, although in these areas electricity tariffs can be 2-3 times higher than the national average. A way out of this situation can be the development of decentralized energy sources of low power, which will allow producing electrical and thermal energy on site, without transport losses and in the required amount. It is known that the most widespread in this technical segment are power plants, in which diesel engines and internal combustion engines (ICE) are used as driving mechanisms. Diesel electric generators are more economical in terms of fuel consumption. They consume 280-350 g of fuel per kWh of generated energy depending on operating conditions.

Knowing this feature, manufacturers deliberately raise the price of diesel units in comparison with generating systems that run on gas or petrol. But there are two problems here:

- supplying gasoline, diesel fuel (and even more so gas) to districts remote from cities is often very expensive undertaking. Delivery of any of the listed types of fuel is always associated with significant transport costs, which makes it 2.5-3 times more expensive for a resident of a remote village than for an urban consumer, as statistics show, for farms of distant pasture cattle breeding the tariff can be even higher;

- for autonomously living consumers, in addition to electricity, heat energy is also needed, which is used to heat the premises. From this point of view, a diesel engine is less efficient, as it warms up more slowly than a gasoline engine.

As studies have shown, the solution to this problem can be the use of autonomous generation systems based on a Stirling engine (SE) and a multi-pole generator with combined excitation [1]. They are favorably distinguished by their ability to operate on various types of fuel including gas, coal, fuel oil and biological resources; high efficiency reaching 41-43 % (excluding power losses on sliding contacts) [2]; a low noise level and high environmental parameters that are superior to diesel engines, according to a number of literary sources [3, 4]; the simplicity of the generator design, which affects its low cost; high frequency of the output voltage, which is known to be proportional to power; the ability to operate the generating system in a wide range of rotational speeds of the Stirling engine output shaft, an extremely low level of use of semiconductor elements in the system, which makes it available to the mass consumer. With an excess of local fuel (sawdust, straw, meat/fish/poultry farms waste, etc.), as well as a sufficient efficiency of decentralized sources, they can be used not only by residents of remote areas but also by consumers connected to centralized electricity and heat supply systems [5, 6]. At the same time, the efficiency of a system with a power from 1 to 100 kW (taking into account the effect of heating the premises) can reach 80 %.

The Stirling engine (SE) has long been known and described in detail both in theoretical and practical aspects [4, 7]. The SE design has undergone various improvements and modernizations; one of the options of this engine can be a free piston engine. A mathematical model describing the principle of its operation is presented in [8]. Methods of studying the SE used in this work are taken from [9]. There are a number of works dealing with studying free piston diesel engines as a rather promising type of these heat engines; there is a mathematical description of the power plant based on them, and the results of laboratory studies are presented in [10-12]. Based on the material studied [9-12], the free piston SE was adopted for developing due to a number of advantages over other types of SEs, first of all, due to its high tightness and the ability to reach pressure of 20 MPa without the technical difficulties inherent in other SE designs. The higher the working fluid pressure, the higher the power of the SE and its efficiency. That is why the purpose of studies in the proposed work is a generation system built on the basis of a free piston engine with an external heat supply that was invented by Professor Beale. In the 50-s of the last century in the United States, the Sunpower Company manufactured an industrial design [4]. This design is the most successful of the entire SE family. The NASA engineers developed several options for use in spacecrafts. Its resource is about 100,000 hours of continuous operation. There is a well-known version of the free piston type SE developed by the NASA engineers; the details of their operation principle can be found in works [13-16].

Works [17-19] provide a mathematical description of thermodynamic, electromechanical and thermal processes occurring in the considered free piston EHSE. To carry out field studies, a laboratory model of a cogeneration-type power plant was developed on the basis of a free piston EHSE.

Scientists studied the effect of the variable purge time technology implemented in a generator with a free piston engine [10-13]. In the case where a free piston generator has different compression ratios, cycling and frequency, variable purge time technology has improved purge quality and productivity. The presented numerical model of a generator with a free piston engine was developed in the Simulink and BOOST software. Changing the characteristics of generators with a free piston engine under various unsteady conditions was also discussed. A free piston SE works on the same principle as other SE designs with a drive mechanism [10-11]. Under the action of gas pressure in the working cavities the pistons move, and the movement in the opposite direction occurs due to the elastic forces of the mechanical spring. There is no rigid kinematic connection between the pistons. The displacer, in comparison with the working piston, has a lower mass. As a consequence, it advances the working piston by a certain phase angle. This condition is necessary to obtain useful work in engines operating on the Stirling cycle [10-11].

## 1. Materials and methods

To carry out field experiments, a prototype laboratory model of a free-piston engine with an external heat supply (EHSE) with a linear alternator on a permanent magnet has been developed. An experimental laboratory power plant with a free piston SE is shown in Figure 1. Its main difference from the known types of SEs is the absence of a massive flywheel with a crankshaft and a crank mechanism. In addition, the design makes it possible to achieve greater tightness, which significantly increases the power on the output shaft while limiting the outer dimensions [4,7]. Air is used as a working fluid with addition of a small percentage of water, which makes it possible to develop pressure up to 10 MPa. The EHSE design is shown in Figure 2, a description of the principle of operation and the physical laws of its operation can be found in works [4, 6, 7].

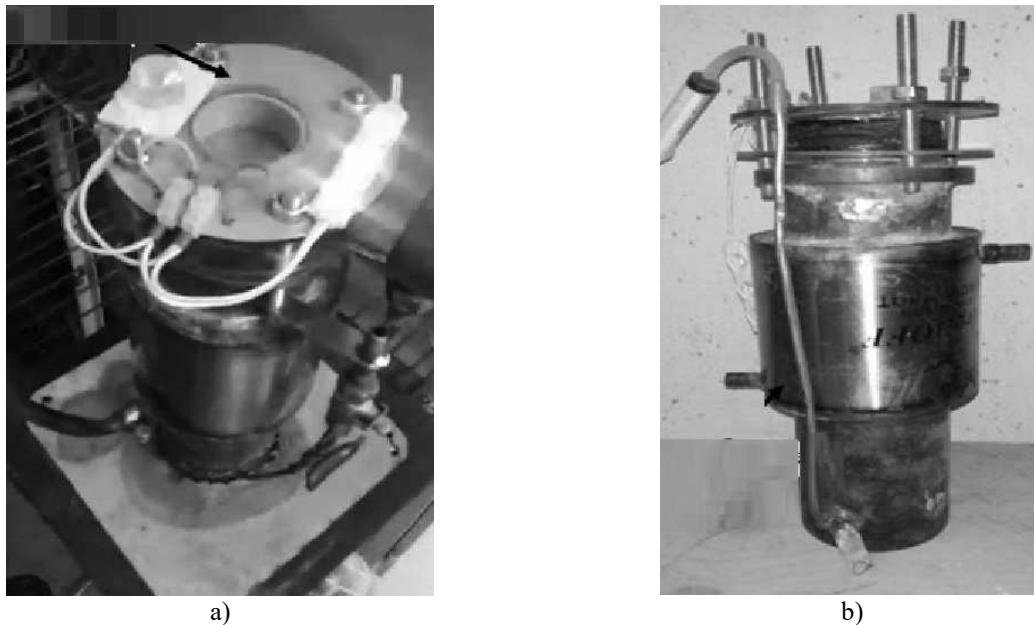


**Fig.1.** Experimental laboratory setup with the power of 100 W: a) – linear generator; b) – cooling system.

When developing the EHSE design, theoretical information presented in works [4, 6, 7] was used and the recommendations of the free piston EHSE researchers [10, 11] were taken into account. In the lower part of the body, the working fluid located in the inner part of the EHSE is heated with a gas burner. Displacer 4 is made of an aluminum alloy and is hollow, since it must have a lower mass compared to permanent magnet 6. When heated, the working fluid expands and pushes the displacer upwards. The undercarriage contains an elastic membrane that rises upwards together with permanent magnet 6. The displacer and the permanent magnet are interconnected through the undercarriage elements. The magnet moves from the bottom to the top. Its movement inside the coil of an electric generator induces EMF in it.

Then the working fluid is cooled in cooler 2, after which it is compressed and the piston is lowered down under the impact of the magnet weight and the force of the pre-compressed spring. Cooler 2 is a reservoir through which coolant circulates. Then the working fluid is heated again at the bottom. The developed EHSE operates according to the Stirling thermal cycle [4, 6, 7] and belongs to the free piston type [10, 11]. The difference from the known designs consists in the fact that the working piston is moved outside the housing and replaced by the permanent magnet. This simplifies the design and makes it easier to adjust the EHSE, and reduces its cost. The proposed EHSE has a disadvantage of a lower efficiency compared to analogs [10, 11], but its advantage is the lower cost and simplicity of design.

The reason for this is the unique thermo-physical characteristics of water vapor [20]. As follows from the tabular data obtained by Professor M.P. Vukalovich, at the saturated steam temperature  $T = 330\text{ }^{\circ}\text{C}$ , its pressure reaches 12.8 MPa (128 atm.). In contrast to the well-known foreign samples of free piston SEs, the transition was made from helium to the mixture of air with saturated water vapor that is obtained upon heating. The volume of injected distilled water added is 3-5 cm<sup>3</sup> per one liter of the SE working volume. This will make it possible to achieve the following calculated parameters of the dry saturated steam: at  $T = 150\text{ }^{\circ}\text{C}$  pressure  $P = 0.5\text{ MPa}$ , at  $T = 200\text{ }^{\circ}\text{C}$  pressure  $P = 1.5\text{ MPa}$ , at  $T = 300\text{ }^{\circ}\text{C}$  pressure  $P = 8.5\text{ MPa}$ , at  $T = 330\text{ }^{\circ}\text{C}$  pressure  $P = 12.8\text{ MPa}$ . The design of a laboratory sample of a free piston SE is intended for maximum initial pressure of 2.5 MPa; for operation at higher pressures, serious changes in the design are required. Heating is carried out from below with a 1 kW gas burner. Outside the cylinder is a water-cooled jacket. The design parameters of the set are as follows: electrical power of alternating current up to 100 VA and thermal power up to 300 W.

The pressure inside the cylinder depends on the power of the burner flame and the temperature of the heater, as well as on the temperature of the working fluid. During the experiment, the pressure was varied from 0.5 to 2.5 MPa. The working pressure was selected to be 1.5 MPa. At the maximum pressure above 2.5 MPa, there is a risk of destruction of the EHSE cylinder. The temperature was measured with two instruments using a laser temperature meter Fluke 51 (Fluke, USA) to identify the hottest areas of the cylinder. Continuous control of the heating temperature was performed using a 4-channel digital

thermometer HT-9815 (Xintest, China). The pressure was measured using a pressure gauge with the measurement limit of 10 MPa.

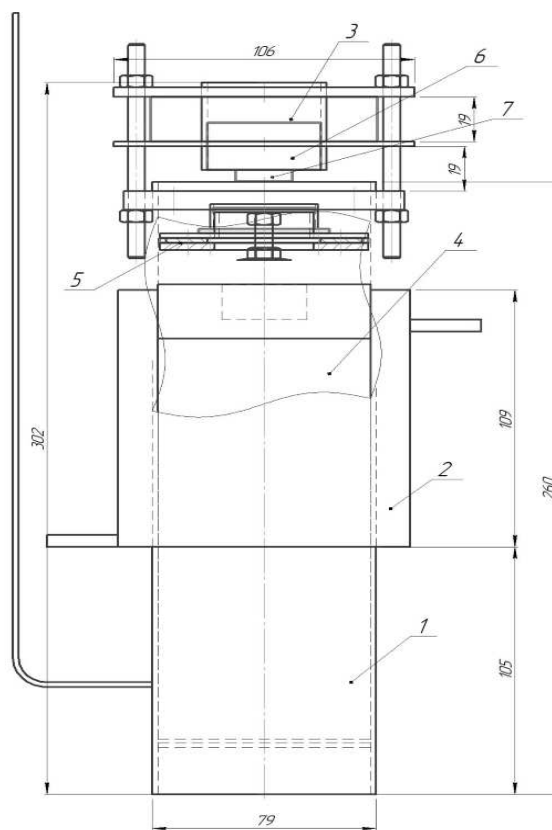


**Fig.2.** The EHSE arrangement:

- 1 - housing, 2 - cooler, 3 - electric generator, 4 - displacer, 5 - undercarriage, 6 - permanent magnet of electric generator, 7 - permanent magnet for communication with undercarriage, 8 - M6 bolt with return spring, 9 - M6 nut, 10, 11 - washer

In the course of studies [6-9], an extremely interesting feature of Stirling engines was revealed. It turned out that at the power that is lower than 2 kW, the conversion of thermal energy into mechanical energy occurs with a high efficiency if the movable element performs reciprocating movement (most of the known structures are oriented to rotation). That is why the purpose of research in the proposed work is a generation system built on the basis of a free-piston engine with an external heat supply invented by Professor Beale. In the 50-s of the last century in the United States, the Sunpower Company manufactured industrial prototypes. Their design turned out to be so successful among the entire Stirling family that the NASA engineers developed several options for using them on spacecraft. Their resource is about 100,000 hours of continuous operation. There is a well-known version of the SE of a free piston type developed by the NASA engineers; the details of their operation principle can be found in source [2].

A free piston Stirling engine works on the same principle as a Stirling engine with a drive train. Under the action of gas pressure in the working cavities, the pistons move, and the movement in the opposite direction occurs due to the elastic forces of the mechanical spring. There is no rigid kinematic connection between the pistons. The displacer, in comparison with the working piston, has a lower mass. As a consequence, it advances the working piston by a certain phase angle. This condition is necessary to obtain useful work in engines operating on the Stirling cycle. For carrying out field experiments, a prototype laboratory model of a free-piston engine with an external heat supply (EHSE) with a linear alternator has been developed. Its main difference from the known types of SE is the absence of a massive flywheel with a crankshaft and a crank mechanism. In addition, the design allows for greater tightness, which significantly increases the output shaft power while limiting the outer dimensions. Air is used as the working medium with addition of a small percentage of water, which makes it possible to develop pressure up to 10 MPa. A

diagram of the cogeneration thermal power plant (TPP) with a linear generator with reciprocating motion is shown in Figure 3.

The proposed TPP is capable of operating in the cogeneration mode and producing electric and thermal energy in a complex manner. The main parameters of a free piston engine with external heat supply are shown in Table 1 below. The main parameters of a free piston engine with an external heat supply are shown in Table 1. The reason for this is the unique thermo-physical characteristics of water vapor [17].

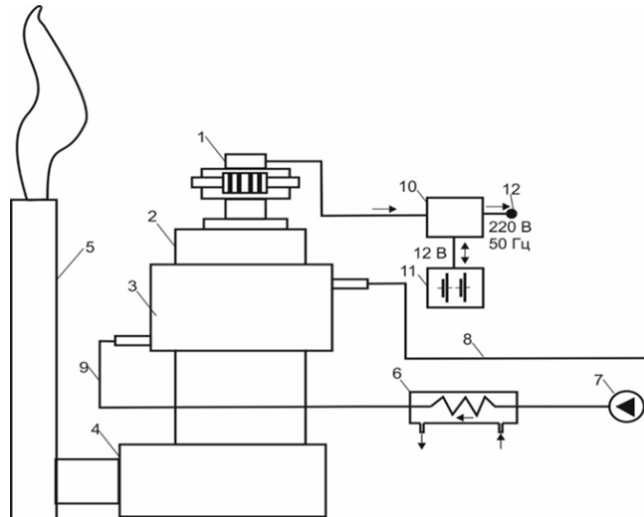


**Fig.3.** Diagram of the cogeneration power plant with a linear generator of a reciprocating type:  
 1 - linear generator; 2 - free piston EHSE; 3 - liquid cooling system; 4 - heating source (furnaces with a firebox);  
 5 - chimney; 6 - heat exchanger of the cooling system; 7 - circulation pump; 8 - supply pipeline; 9 - return  
 pipeline; 10 - electrical control and conversion unit; 11 - drive; 12 - device for connecting an external electrical load

**Table 1.** The main parameters of a free piston engine with EHSE

No.	Parameter	Value
1.	Pressure at the temperature 150 <sup>0</sup> C, MPa	0.5
2.	Pressure at the temperature 200 <sup>0</sup> C, MPa	1.5
3.	Pressure at the temperature 300 <sup>0</sup> C, MPa	8.5
4.	Liquid temperature at the outlet of the cooling system, <sup>0</sup> C	50-80
5.	Liquid temperature at the inlet to the cooling system, <sup>0</sup> C	25-30
6.	Pump capacity, l/min	4
7.	Maximum overall efficiency, no more, %.	80
8.	Maximum electrical power of the generator, W.	До 100

Experiments have been carried out to construct a PV diagram of a closed Carnot heat cycle and to consider the dependence of pressure and volume on different positions of the pistons. The results are shown in Figure 4. The studies carried out allow finding the optimal parameters of the structural parts of the heat engine, to establish precise geometric dimensions of the piston and the displacer, as well as the magnitude of their stroke with the optimal value of the phase shift. If the phase shift changes from 90<sup>0</sup> to 0<sup>0</sup>, then the EHSE stops working. In this case, the displacer must be at least three times lighter than the working piston, and its stroke is many times greater; this statement was noted earlier [4, 10, 11]. The obtained characteristics of the EHSE have low efficiency indicators compared to the ideal Carnot cycle, the area of which is shaded. Accordingly, there is needed the EHSE specimen refinement in order to reduce heat losses and to increase its efficiency.

To calculate the efficiency, there was used the following formula:

$$\text{Efficiency} = A/Q \cdot 100\%,$$

where A is the useful work (power), W; Q is the power spent for performing the work, W.

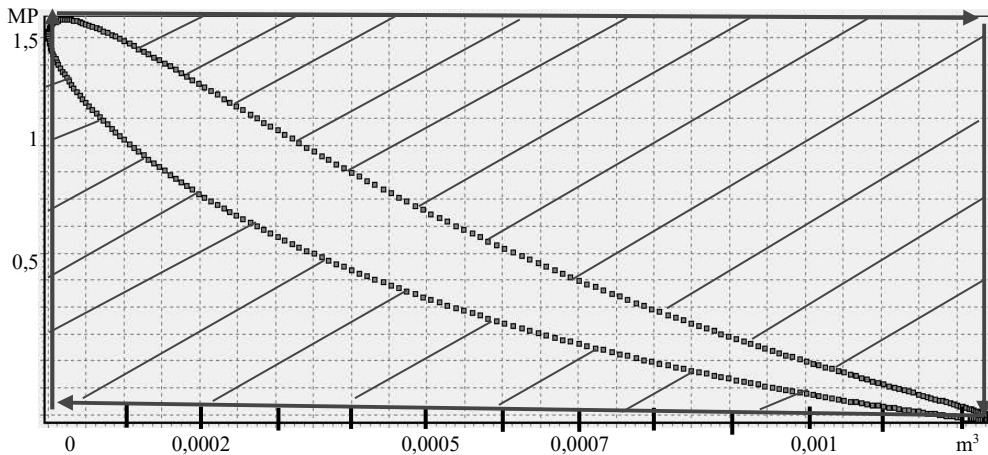


**Fig.4.** Free piston engine main parameters dependences when operating with the heater temperature of 2000C and the cooler temperature of 300C.

With the burner power of 1000 W, the maximum power developed by the electric generator reached 100 W, the efficiency did not respectively exceed 10%. In this case, the measurement errors made 11% due to the significant scattering of the data and the difficulty of stabilizing the heating and cooling modes. Unstable operation of the electric generator was observed, which caused the output power to fluctuate from 80 to 100 W. The EHSE power depends on the operation of the cooling system: the higher the temperature between the heater and the cooler, the higher the efficiency. According to the theoretical information [4, 10,11], the EHSE thermal power should be 300 W. The overall efficiency can reach 40-50% [4, 10, 11]. The resulting heat energy can be used for heating and hot water supply.

## 2. Deriving the equations and technical solutions accepted

To select the generator design, it is necessary to determine the force required to develop the needed power, with the reciprocating movement of the movable element by 4.21 mm. At the start and end points, the stem speed is zero. Neglecting the higher harmonics, the dependence of the speed on time  $t$  can be represented as follows:

$$v(t) = v_{\max} \sin\left(\frac{2\pi t}{T}\right). \quad (1)$$

Accordingly, within half the period  $T$  with frequency that is close to 50 Hz, the stem is to run:

$$L = \int_0^{T/2} v_{\max} \sin\left(\frac{2\pi t}{T}\right) dt = \frac{T v_{\max}}{2\pi} \int_0^{\pi} \sin \alpha d\alpha = \frac{v_{\max} T}{\pi} = 4.21 \quad \text{mm.}$$

From here it follows that the maximum speed  $v_{\max} = \frac{L\pi}{T} = 661.3$  mm/s.

Mechanical power converted into electrical power is determined by the known formula:

$$N = \vec{F} \cdot \vec{v} = P = m E_1 I_1 \cos \psi, \quad (2)$$

where  $\vec{F}$  is the vector of one component of the vibro-acoustic force of the Stirling engine at the time moment considered that is involved in the process of electro-mechanical energy conversion;  $P$  is active power;  $m$  is the number of phases;  $E_1$  is the EMF first harmonic in the phase;  $I_1$  is current in the phase;  $\psi$  is the difference of phases between current and EMF.

Neglecting the higher harmonics, the force component involved in the electro-mechanical conversion of energy can be represented as follows:

$$F(t) = F_{\max} \sin\left(\frac{2\pi t}{T} - \varphi\right)$$

Then, the net power, or the average power for the period will be equal to:

$$P = \frac{1}{T} \int_0^T F(t) \cdot v(t) dt = \frac{F_{\max} v_{\max}}{2} \cos \varphi$$

at the maximum output power  $\varphi = 0$  and  $F_{\max} = \frac{2P}{v_{\max}} = 302.4$  H.

The obtained value of the force at the relatively small value of  $W$ , speaks of serious difficulties arising in designing power plants of this type. Firstly, it is necessary to pay increased attention to suppression of acoustic noise that creates discomfort for consumers. This can be done, in particular, by placing vibration dampers and designing a generator with a high efficiency. Secondly, the design of the moving element should minimize mechanical stress on the windings or magnets. The results of calculating the full power of the generator at an active load are summarized in Table 2.

**Table 2.** The results of calculating the full power of the generator at an active load

$I_1, A$	1	2	3	3.5	4.0	4.5	5
$I_1 x_\phi$	3.58	7.16	10.74	12.53	14.32	16.11	17.90
$\sqrt{E_{xx}^2 - (I_1 x_\phi)^2}$	34.82	34.26	33.31	32.68	31.94	31.07	30.08
$I_1 r_\phi$	1.52	3.04	4.56	5.32	6.08	6.84	7.6
$U_1, B$	33.3	31.32	28.75	27.36	25.86	24.13	22.48
$S1, BA$	33.3	62.44	86.25	95.76	103.44	109.0	112.4

The analysis of the information array made it possible to propose a linear generator for the TPP under consideration shown in Figures 5, 6. Its rotor (the movable element) contains a shaft (Fig. 5a); a square permanent magnet with an inner hole that is magnetized along the horizontal axis; two bushings made of 45 steel along the edges of the magnet fitted on the shaft and having a rectangular outer profile; rectangular sheets (Figure 5b) made of electrical steel 2013 with the thickness of 0.5 mm.

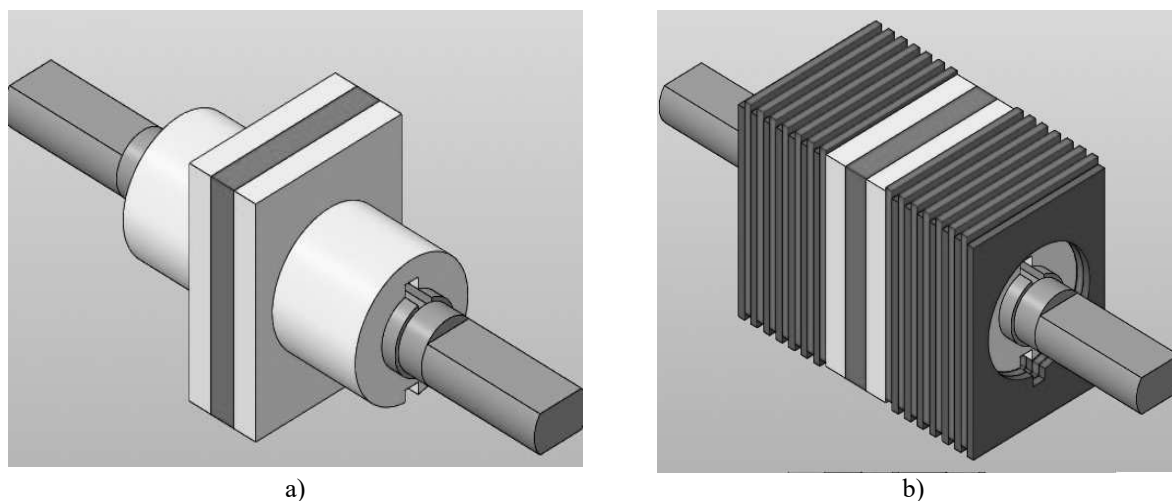


**Fig.5.** Moving elements of the linear generator: a) shaft with bushings and a permanent magnet; b) toothed rotor.

The ends of the shaft have a circular cross-section with a sawn-off outer part bounded by two parallel surfaces passing through two identical chords. This is needed to avoid rotation of the movable element in the bearing units. The bushings sit on the shaft along the key. The sheets are made with the offset relative to the central hole, either down or up. By alternating different types of sheets, four of each type, during blending teeth are obtained on the outer working surface, the distance between the axes of which is 4.21 mm with the filling factor of the package with steel 0.95. The non-working part of the packages is made without teeth, the section in this part is designed to redistribute the variable flow from the upper part of the rotor to the lower part and vice versa. Along the edges, the packages are pulled together by pressure washers and nuts, which are tightened along the thread made on a non-magnetic shaft (X19H10T).

The generator works as follows. In the initial position, the axes of the teeth of the upper stator package (Fig. 6a) coincide with the axes of the teeth of the rotor located on its outer upper part. In the lower stator package, the axes of the teeth coincide with the axes passing through the slots of the rotor in its outer lower part. Thus, the flux developed by the magnet, passing through the left sleeve, enters the rotor package and, then along the path with the least reluctance moves to the upper part of the rotor package and enters the upper stator package. Penetrating the coil, the magnetic lines of force pass into the right side of the stator package, enter the rotor package and close at the south pole of the magnet. It should be noted that in the initial position, the flux passing through the lower stator package is small, since it follows the path with high reluctance.

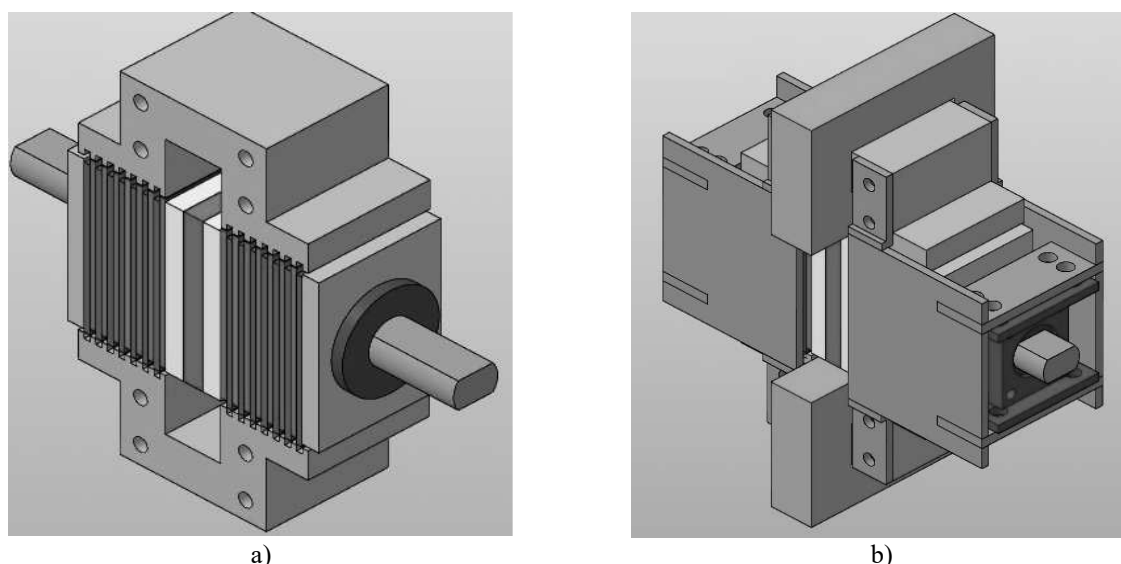


**Fig. 6.** Linear generator: a) rotor with the stator packages; b) generator assembled.

Electromagnetic and strength calculations of the generator have been performed using the ANSYS software application. The main parameters of the power plant are shown in Table 3. Below, Figure 7 shows experimental values of the total power and output voltage of the generator depending on the current strength. In the numerical experiments, the load is active.

**Table 3.** The main parameters of the power plant

Parameter	Value
Net power, W	100
Nominal voltage on the battery, V	24
Maximum linear speed, mm/s	661.3
Minimum linear speed, mm/s	420.7
Maximum force on S1, N	302.4
Maximum current, no more, A	4.2
Number of phases	1
Number of stator teeth per pole	8
Electrical losses in the stator winding, W	74
Inductive resistance of the winding, Ohm	3.58
Losses in stator steel, no more, W	3.6
Permanent magnet type Ne-Fe-B	45 SH



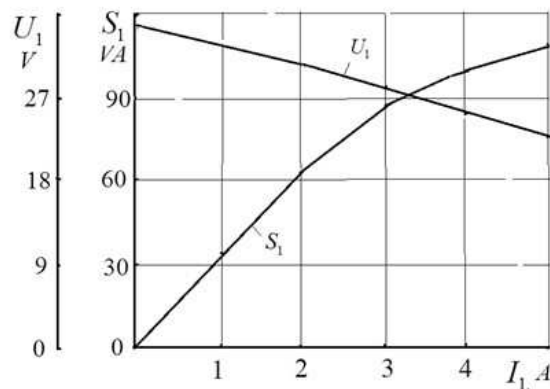


Fig.7. Output voltage and full generator power dependence on load current

## Conclusions

1. This paper shows the principal possibility of designing a power plant based on a reciprocating Stirling engine and a linear generator.
2. Ne-Fe-B 45SH is capable of delivering the full power of 110 VA. With its scaling and proportional increasing the cylinder volume of a free piston EHSE, the power of 1-2 kVA can be achieved, but further increasing the power is not advisable, due to the high increasing of the electric generator cost.
3. The analysis of the power plant technical parameters shows that this technical facility is competitive and can successfully replace traditional low-power sources of electricity with diesel or gasoline engines. Comparison of the developed thermal power plant and the electricity generation system based on a generator with a rotating rotor [1] characteristics suggests that at the power that is lower than 2.0 - 2.5 kVA, the conversion of thermal energy into mechanical energy of reciprocating motion is more profitable from the economic point of view. If an autonomous consumer requires power of 3.0-12 kVA, then there is no alternative to the use of a Stirling engine and a generator with combined excitation of the rotating type.
4. A thermal power plant based on a free piston engine and a reciprocating generator is capable of producing simultaneously electrical and thermal energy, which allows it being used to supply power to remote consumers in rural areas, while this unit is capable of operating with almost any type of fuel and agricultural waste.

## Acknowledgments

The article was prepared within the framework of the project AP05131751 "Micro thermal power plant of the cogeneration type with heat recovery".

## REFERENCES

- 1 Kaluzhsky D.L., Mekhtiev A.D., Dashinimaev A.O., Filippov D.A., Kharitonov A.S. An autonomous power generation system based on a Stirling engine and a multi-pole synchronous machine. *Reports of the Academy of Sciences of the Higher School of the Russian Federation*. 2019, No.1(42), pp. 31-43. [in Russian]
- 2 Miguel Torres García, Elisa Carvajal Trujillo, José Antonio Vélez Godiño, David Sánchez Martínez. Thermodynamic Model for Performance Analysis of a Stirling Engine Prototype. *Energies*. 2018, No.11(10), pp.2655-2665. <https://doi.org/10.3390/en11102655>
- 3 Lee Myungkee, Choi Seungchul. *Vibration motor for an electric hand-held appliance*. European patent. EP 3 327 910 A1. Bulletin 2018/22. Publ. 05/30/2018, 10 p.
- 4 Reeder G. *Stirling Engines*. Moscow, 1986, 464 p. [in Russian]
- 5 Menzhinsky A., Malashin A.N., Sukhodolov Yu. Development and analysis of mathematical models of generators of linear and reciprocating types with electromagnetic excitation. *Proceedings of higher educational institutions and energy associations of the CIS. Energy*. 2018, No. 2, pp. 118 – 128. [in Russian]
- 6 Henry Jr., Brandhorst W., Peter Jr., Chapman A. New 5kW free-piston Stirling space convertor developments. *Science Direct, Acta Astronautica*, 2008, No. 63, pp. 342 – 347.
- 7 Walker G. *Stirling Engines* / Per. from English. Moscow, Mir, 1985, 408 p.
- 8 Bobylev A.V., Zenkin V.A. Mathematical model of a free-piston Stirling engine. *Technique. Technology. Engineering*. 2017, No.1, pp. 22-27.

- 
- 9 Belozertsev V.N., Gorshkalev A.A., Nekrasov S.O., et al. *Calculation methods and experimental research of Stirling's heat engines*: textbook. Allowance. Samara: SSAU Publishing House, 2015, 76 p.
- 10 Safin A.R., Ivshin I.V., Gracheva E.I., Petrov T.I. Development of a mathematical model of an autonomous power supply with a free piston engine based on a synchronous reciprocating electric machine with permanent magnets. *Proceedings of higher educational institutions. Energy Problems*. 2020, No.22(1), pp. 38-48. <https://doi.org/10.30724/1998-9903-2020-22-1-38-48> [in Russian]
- 11 Ziwen Cheng, Boru Jia, Zhenfang Xin, Huihua Feng, Zhengxing Zuo, Andrew Smallbone, Anthony Paul Roskilly. Investigation of performance of free-piston engine generator with variable-scavenging-timing technology under unsteady operation condition. *Applied Thermal Engineering*. 2021, No. 196, pp. 1359-4311. <https://doi.org/10.1016/j.applthermaleng.2021.117288>.
- 12 Shuangshuang Liu, Zhaoping Xu, Leiming Chen, Liang Liu, Comparison of an opposed-piston free-piston engine using single and dual channel uniflow scavenging, *Applied Thermal Engineering*. 2021, No. 201, pp.1359-4311, <https://doi.org/10.1016/j.applthermaleng.2021.117813>.
- 13 Langlois J. *Dynamic computer model of a Stirling space nuclear power system*. Trident Scholar project report no. 345. Annapolis: US Naval Academy. 2006, 348 p.
- 14 Thermoacoustic Stirling Heat Engine (TASHE) for Space Power and Cooling SBIR Phase 3. Presentation to Stirling Technical Interchange Meeting NASA Glenn Research Center June 29, 2015. Available at the: <https://technology.nasa.gov/patent/LEW-TOPS-80>.
- 15 Bobylev A.V., Zenkin V.A. Mathematical model of a free piston Stirling engine. *Technics. Technologies. Engineering*. 2017, No. 1, pp. 22-27. [in Russian]
- 16 Wanks V.A., Leskov L.V., Lukyanov A.V. *Space power systems*. Moscow, 1990, 144 p.
- 17 Mekhtiev A.D., Bekbaeva B.T., Beltaev A.B., et al. Micro-CHP for power supply of objects remote from the power plant. *Proceedings of the XI Intern. Scientific and Practical Conference "Perspective Issues of World Science - 2017"*. Bulgaria, Sofia. 2017, pp. 41 – 43. [in Russian]
- 18 Mekhtiev A.D., Yugay V.V. Alkina A.D., et al. *Mini CHP with a linear current generator with a recuperator for the disposal of waste subject to combustion*. Certificate of state registration of rights to the copyright object of the Republic of Kazakhstan, publ. 23.05.2016. No. 0956. [in Russian]
- 19 Mekhtiyev A.D., Sarsikyevev Y.Z., Yugay V.V., Neshina Y.G., Alkina A.D. Thermoacoustic engine as a low-power cogeneration energy source for autonomous consumer power supply. *Eurasian Physical Technical Journal*. 2021, Vol.18, No.12 (36), pp. 60 – 66.
- 20 Vukalovich M.P., Novikov I.I. *Thermodynamics*: Textbook. Moscow, Mechanical Engineering, 1972, 670 p. [in Russian]

## SYNTHESIS OF URANIUM-THORIUM OXIDE POWDERS IN LOW-TEMPERATURE PLASMA OF HIGH FREQUENCY TORCH DISCHARGE

Novoselov I.Yu.<sup>1\*</sup>, Shrager E.R.<sup>2</sup>, Tikhonov A.<sup>1</sup>

<sup>1</sup>National Research Tomsk Polytechnic University, Tomsk, Russia, [inovoselov@tpu.ru](mailto:inovoselov@tpu.ru)

<sup>2</sup>National Research Tomsk State University, Tomsk, Russia

*The article discusses the process of plasma chemical synthesis of uranium-thorium oxide powders for a new generation dispersion nuclear fuel. In the course of research, the combustion parameters of the precursors were calculated. Precursors were water-organic nitrate solutions based on uranyl nitrate and thorium nitrate (fissile components), as well as magnesium nitrate (matrix material). The organic component of the solutions was acetone due to the sufficiently high calorific value and good mutual solubility. In the course of thermodynamic calculations, the optimal modes of processing of the water-organic nitrate solutions in low-temperature plasma were determined. These modes ensured the synthesis of oxide powders of the necessary stoichiometry without impurities of unoxidized carbon (soot). Experiments to obtain the samples of powders were carried out with the model solutions in which uranyl and thorium nitrates were replaced by neodymium and cerium ones, which are in the same group of the periodic table. The synthesis was carried out with the use of a plasma chemical unit based on a high frequency torch plasmatron. The synthesized powders were subjected to a number of analyzes including electron microscopy, particle size analysis, X-ray phase analysis and BET analysis. The results showed that the powders can be classified as nanosized.*

**Keywords:** high frequency torch discharge, plasma, powder, nuclear fuel, uranium, thorium, analysis.

### Introduction

Most of the operating nuclear power plants use ceramic nuclear fuel from uranium dioxide enriched in the isotope uranium-235. Such fuel along with its undoubted advantages also has significant disadvantages which are low thermal conductivity limiting the specific power of the reactor in terms of melting temperature, fragility, tendency to cracking, short cycle of use (3–5 years), high costs for the disposal of spent fuel and finally limited resource of the uranium-235 isotope. In case of uranium-238 and thorium-232 isotopes, there is no need for expensive isotopic enrichment, and the cycle of use of such nuclear fuel can be brought up to 10–15 years. Moreover, the predicted reserves of thorium in the earth's crust are 3–5 times greater than that of uranium [1–6]. One of the promising directions for the further development of nuclear power is the use of dispersion nuclear fuel, in which inclusions of fissile materials (e.g. uranium, thorium) in the form of granular oxide compounds (OC) are placed in a matrix with a high thermal conductivity coefficient. The use of a matrix made of metal powders (aluminum, molybdenum, tungsten, stainless steel, etc.) increases the thermal conductivity, but leads to a deterioration in the neutron balance due to the high resonance absorption of neutrons. In addition, the use sol-gel process to obtain microspheres from mixed water nitrate solutions is associated with the following disadvantages: multistage, long duration, low productivity, the need to use a large number of chemical reagents, the need for additional hydrogen reduction. In addition, separate production and further mechanical mixing of fissile and matrix materials do not provide a homogeneous phase distribution in such dispersion nuclear fuel. Table 1 shows some advantages and disadvantages of some prospective methods to obtain oxide powders.

The undoubted advantages of using plasma for the OC plasma chemical synthesis from water nitrate solutions in comparison with another methods include one-stage, high process rate, the ability to actively influence the particle size and morphology and compactness of technological equipment. It should be noted that the addition of an organic component (alcohol, acetone, etc.) to the nitrate solution will reduce the specific energy consumption, thus, the use of water-organic nitrate solutions (WONS) is preferable [7].

The work objective is to study the process of synthesis of oxide compositions for uranium-thorium nuclear fuel under conditions of non-equilibrium air plasma of a high frequency torch discharge.

**Table 1.** Pros and cons of some prospective methods to obtain oxide powders.

	Method	Advantages	Disadvantages
1	Ultrasound dispersion	Powders are distinguished by the uniformity of particle sizes of the dispersed phase	Long process duration
2	Mechanical synthesis	Low process temperature	Long process duration, high energy intensity
3	Chemical sedimentation	Accessibility	Wide distribution of particle size values
4	Hydrothermal method	Accessibility	High cost and complexity of equipment
5	Electric explosion of metal wires	Small particle size	High energy intensity, low productivity

## 1. Theoretical part

In this work, uranium and thorium oxides were considered as a fissile component of dispersion nuclear fuel, and magnesium oxide was considered as a matrix material. The initial precursors were nitrates of uranyl, thorium and magnesium nitrates, and acetone was an organic component, which has a sufficiently high calorific value and good mutual solubility. Thus WONS was considered as a mixture of water solutions of  $\text{UO}_2(\text{NO}_3)_2 \cdot 6\text{H}_2\text{O}$ ,  $\text{Th}(\text{NO}_3)_4 \cdot 6\text{H}_2\text{O}$ ,  $\text{Mg}(\text{NO}_3)_2 \cdot 6\text{H}_2\text{O}$ , and  $\text{C}_2\text{H}_6\text{O}$ . Firstly, to determine the optimal WONS composition, the net calorific value  $Q_l$  of the solutions was calculated according to the equation [8]:

$$Q_l = \frac{(100 - W - A)Q_{lc}}{100} - \frac{2.5W}{100},$$

where  $Q_{lc}$  is lower heat value of combustible component of WONS, MJ/kg;  $W$  and  $A$  are content of water and noncombustible components, wt.%; 2.5 is the value of latent heat of vaporization for water at 0 °C, MJ/kg. It was shown that WONS Shaving  $Q_l \geq 8.4$  MJ/kg can provide a significant reduction in energy consumption for the plasma chemical synthesis of oxide compounds [8, 9]. Thus, for the synthesis of OC of various compositions, the optimal compositions of WONS having  $Q_l \geq 8.4$  MJ/kg were determined and are given in Table 2. In the course of calculations, the ratio of fissile components was taken  $\text{UO}_2/(\text{ThO}_2 + \text{UO}_2) = 0.1$ , and the proportion of the matrix varied from 1 to 10% [3].

Further, a thermodynamic calculation of the process of plasma chemical synthesis of oxide compositions from WONS was carried out in the program "TERRA". This program provides an opportunity to make thermodynamic calculations of the phase compositions of heterogeneous systems. The calculations were carried out at atmospheric pressure, in a wide temperature range (300–5000 K) and mass fractions of air plasma coolant (0.1–0.9). Figure 1 shows the temperature dependence of the mass fraction of formed oxide products obtained after plasma treatment of WONS-1 at a mass fraction of air of 67% (a) and 70% (b).

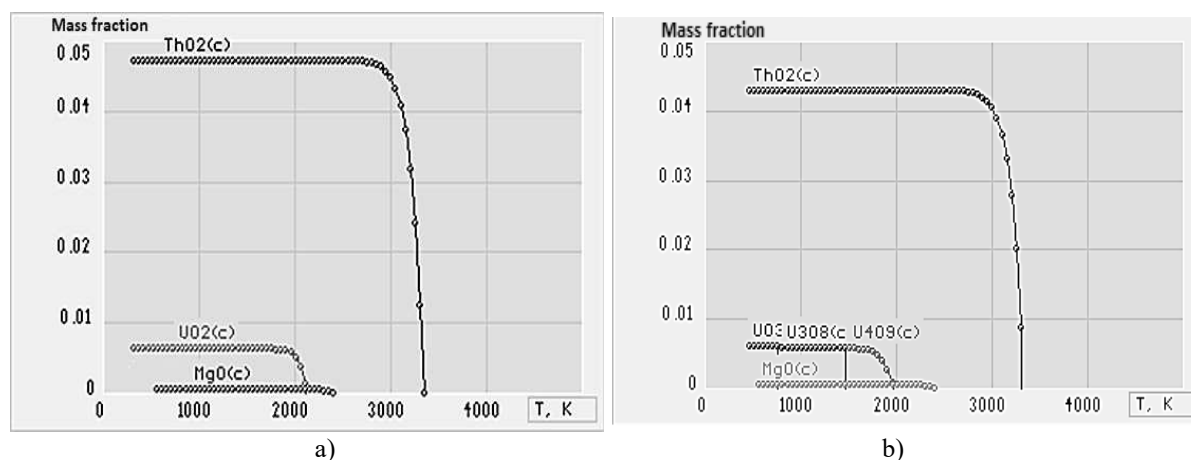


**Fig.1.** Temperature dependence of the mass fraction of formed oxide products obtained after plasma treatment of WONS-1 at a mass fraction of air of 67% (a) and 70% (b).

**Table 2.** Calculations of WONS compositions.

OC composition	WONS composition, wt. %.				
	H <sub>2</sub> O	C <sub>2</sub> H <sub>6</sub> O	UO <sub>2</sub> (NO <sub>3</sub> ) <sub>2</sub> ·6H <sub>2</sub> O	Th(NO <sub>3</sub> ) <sub>4</sub> ·6H <sub>2</sub> O	Mg(NO <sub>3</sub> ) <sub>2</sub> ·6H <sub>2</sub> O
WONS-1					
89.1%ThO <sub>2</sub> – 9.9%UO <sub>2</sub> – 1.0%MgO	28.4	29.0	3.5	37.9	1.2
WONS-2					
87.8%ThO <sub>2</sub> – 9.7%UO <sub>2</sub> – 2.5%MgO	28.4	29.0	3.4	36.3	2.9
WONS-3					
85.5%ThO <sub>2</sub> – 9.5%UO <sub>2</sub> – 5.0%MgO	28.4	29.0	3.1	33.8	5.7
WONS-4					
83.3%ThO <sub>2</sub> – 9.2%UO <sub>2</sub> – 7.5%MgO	28.4	29.0	2.9	31.5	8.2
WONS-5					
81.0% ThO <sub>2</sub> – 9.0% UO <sub>2</sub> – 10.0%MgO	28.4	29.0	2.7	29.4	10.5

An analysis of the equilibrium compositions shows that plasma treatment of WONS-1 at a mass fraction of air of 67% and temperatures up to 2000 K (Figure 1a) leads to the plasma chemical synthesis of the required OC “89.1% ThO<sub>2</sub>– 9.9% UO<sub>2</sub>– 1.0% MgO”. An increase in the air fraction above 69% in the temperature range 1000–1600 K leads to the formation of oxide U<sub>3</sub>O<sub>8</sub> instead of the required UO<sub>2</sub> (Figure 1b). A decrease in the proportion of air below 67% leads to the formation of carbon in the condensed phase (soot) in the composition of the products, which contaminates the synthesis products. Similar results were obtained for the rest WONS.

## 2. Experimental technique

Experimental studies with the purpose of producing samples of oxide powders were carried out using a plasma chemical unit based on a high-frequency torch plasmatron (Figure 2).

The unit is designed to carry out the processes of plasma treatment of dispersed water-salt solutions of various compositions. The torch plasmatron generates a low-temperature (mass-average temperature up to 3000 °C) nonequilibrium air plasma. The auto electronic type of emission, which is realized in this case, excludes the erosion of the electrode and thus prevents the contamination of the synthesized products. Due to the absence of an opportunity to deal with uranium and thorium at the university laboratory all experiments were carried out with model WONS. Fissile materials UO<sub>2</sub>(NO<sub>3</sub>)<sub>2</sub>·6H<sub>2</sub>O, Th(NO<sub>3</sub>)<sub>4</sub>·6H<sub>2</sub>O in the course of the experiments were replaced by metal salts respectively Nd(NO<sub>3</sub>)<sub>3</sub>·6H<sub>2</sub>O and Ce(NO<sub>3</sub>)<sub>3</sub>·6H<sub>2</sub>O that are in the same group of chemical elements with uranium and thorium. The prepared WONS (Table 1) was dispersed using a mechanical atomizer into a plasma-chemical reactor, where it was treated with a plasma jet and oxide powder was synthesized during thermolysis.

## 3. Results and discussion

The synthesized powders were subjected to a number of analyzes. Scanning (SEM) and transmission (TEM) electron microscopy were performed to analyze particle size and morphology, X-ray phase analysis, particle size analysis to study the particle size distribution, and BET analysis to determine the specific surface area [10]. The morphological characteristics were qualitatively assessed using electron microscopy.

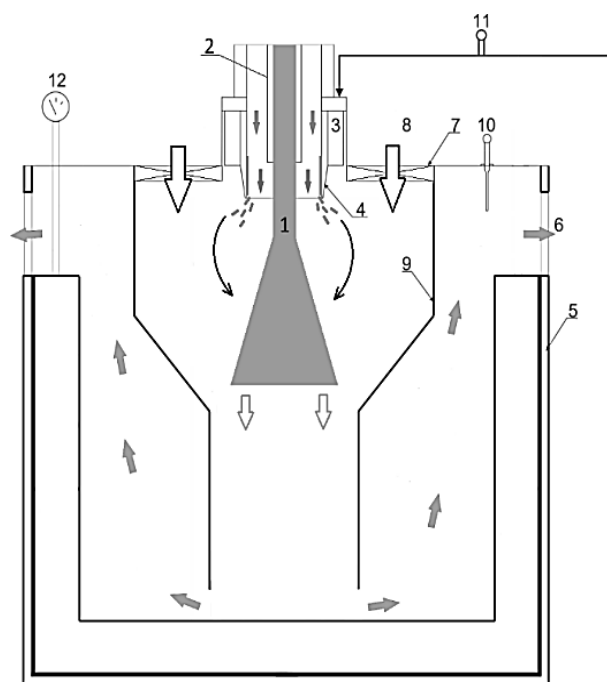
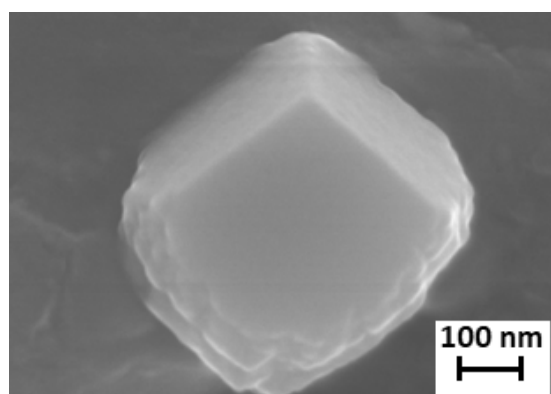
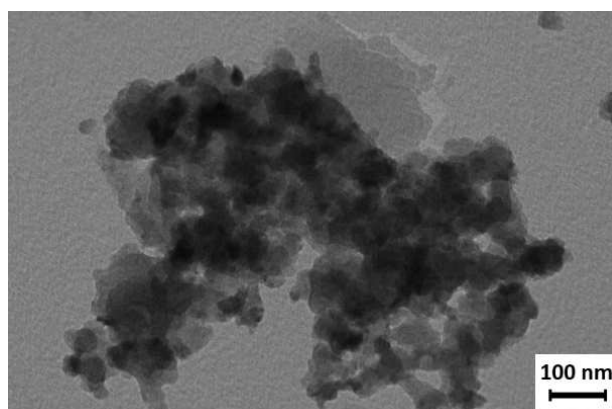


**Fig.2.** Plasmachemical unit based on a high-frequency torch plasmatron: 1 – plasma generated by high-frequency torch plasmatron; 2 – quartz discharge chamber; 3 – sleeve; 4 – mechanical atomizer; 5 – reactor case; 6 – exhausted gases; 7 – sliding shutter; 8 – air entraining; 9 – reactor; 10, 11 – thermal couples; 12 – manometer.

SEM was performed using JSM-7500FA microscope (Figure 3a), TEM was performed using a Philips CM30 microscope (Figure 3b). An analysis of the SEM image results suggests that the powder has agglomerated into dense bulk structures 400–500 nm in size. The TEM image, on the other hand, allows to examine individual polydisperse powder particles in agglomerates. The particle size varies in the range of 30–120 nm, the shape of the particles is round. The X-ray phase analysis (Figure 4) showed the presence of the target oxides  $\text{Nd}_2\text{O}_3$ ,  $\text{CeO}_2$ , and  $\text{MgO}$  in the powder sample. The size of the coherent scattering region, identified with the particle size, according to the analysis results is 87 nm.



a)



b)

**Fig.3.** Micrographs of the powder obtained from WONS-1: SEM (a) and TEM (b).

Results demonstrates that all major peaks correspond to target oxides, indicating pureness of powder. The specific surface area of the powder was determined by the Brunauer-Emmett-Teller (BET) method and is  $11 \text{ m}^2/\text{g}$ . The resulting area value was recalculated into the size of the particles, based on the assumption of their spherical geometry. Thus, the BET particle size is 82 nm.

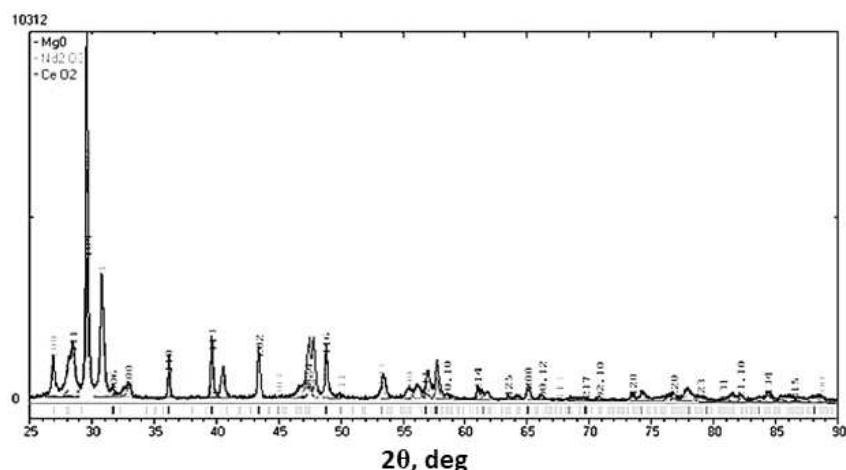


Fig.4. X-ray phase analysis of powder synthesized from WONS-1.

The results of the analyzes are in satisfactory agreement with each other without any conflicting, and make it possible to classify the powder synthesized in plasma as a nanosized

## Conclusions

As a result of the studies, it was established the possibility of carrying out the process of plasmachemical synthesis of oxide compounds for dispersion nuclear fuel of the uranium-thorium cycle. It is shown that the optimal proportion of air plasma coolant for the synthesis of a composition of the required stoichiometry is 67%. Analysis of the obtained powders in the course of experimental studies shows that the average size of particle agglomerates is 500 nm, while the powder particles themselves have a size of 30–120 nm and a round shape. The size of coherent scattering region of the powder is 87 nm, the particle diameter determined by the BET method is 82 nm, and the specific surface area is 11 m<sup>2</sup>/g. The results of the analyzes are in satisfactory agreement with each other, and make it possible to classify such a powders as a nanoscale.

It is important to note that the nanoscale dimensionality of the powder can provide an increase in the density of the pellets produced on their basis; in addition, it can provide a decrease in the compacting pressure and sintering temperature of fuel pellets. The described plasmachemical synthesis technology can be used to obtain other simple and complex oxide powders for fabricating promising types of nuclear fuel.

## REFERENCES

- 1 Skorov D.M., Bychkov Yu.F., Dashkovsky A.M. *Reactor material science*. Moscow, 1979, 344 p. [in Russian]
- 2 SongT., WangY., ChangZ., GuoL. In-situ fabrication of dispersion nuclear fuel pellets with core-shell structure. *Ann.Nucl. Energy*. 2019, Vol. 35, pp. 258 – 262.
- 3 Alekseev S.V., Zaytsev V.A., Tolstoukhov S.S. *Dispersion Nuclear Fuel*. Moscow, 2015, 248 p.
- 4 Shelke A.V., Gera, B., Maheshwari N.K., Singh R.K. Theoretical studies on fuel dispersion and fireball formation associated with aircraft crash. *Combust. Sci.Technol*. 2018, Vol. 19, Iss. 12, pp. 2134 – 2163.
- 5 Kushtym A.V., Belash M.M., Zigunov V.V., Slabospitska O.O., Zuyok V.A. Dispersion fuel for nuclear research facilities. *Probl. At. Sci. Technol*. 2017, Vol. 108, Iss. 2, pp. 124 – 130.
- 6 Degueldre C., Paratte J.M. Concepts for an inert matrix fuel: An overview. *J. Nucl. Mater*. 1999, Vol.274, pp. 1–6.
- 7 Karengin A.G., Karengin A.A., Novoselov I.Y., Tikhonov A.E. Investigation of plasmachemical synthesis of oxide compositions for plutonium-thorium dispersion nuclear fuel. *J. Phys. Conf. Ser*. 2021, Vol. 1989, Article number 012005, pp. 1 – 5.
- 8 Bernadiner M.N., Shurygin A.P. *Fire processing and disposal of industrial waste*. Moscow, 1990, 304 p.
- 9 Novoselov I.Y., Karengin A.G., Shamanin I.V., Alyukov E.S., Gusev A.A. Plasmachemical synthesis of nanopowders of yttria and zirconia from dispersed water-salt-organic mixtures. *AIP Conf. Proc*. 2018, Vol. 1938, Article number 020010, pp. 1 – 7.
- 10 Kosmachev P.V., Abzaev Y.A., Vlasov V.A. Quantitative phase analysis of plasma-treated high-silica materials. *Rus. Phys. J*. 2018, Vol. 61, Iss. 2, pp. 264 – 269.

## A NEW METHOD FOR DETERMINING PARAMETERS OF PHOTOVOLTAIC MODULE BASED ON THE DATA FROM TECHNICAL SPECIFICATION

Obukhov S.G., Plotnikov I.A.\* , Klimova G.N.

National Research Tomsk Polytechnic University, Tomsk, Russia, igorplt@tpu.ru

*In the given article the methodology of making a photovoltaic module mathematical model is presented, which lets reproduce its energy characteristics in real operating conditions. Also, the major types of mathematical models of photovoltaic converters are discussed and most well-known estimation methods of their parameters are analyzed. An original and simple way of parameters definition of photovoltaic module is introduced based on the technical specification data without using programming and developing numerical estimation algorithms. The suggested method is easily realized in the tabular program Excel with installed tool «Search for solutions». The simulation results of volt-ampere characteristic (V-I curve) of photovoltaic module Kyocera KC200GT are presented in a wide variation range of temperature and illumination. In addition, an accuracy evaluation is made by comparing the model characteristics and experimental data. The model was tested on a number of photovoltaic modules and proved good modeling results compliance with manufacturer's data. The model provides a high modeling accuracy around MPP (maximum power point). This fact allows to use it for development of effective algorithms for photovoltaic power stations controllers, circuit design advancement of converting devices, prediction of power generation, operating modes analysis and optimization for photovoltaic systems.*

**Keywords:** photovoltaic module, solar cells, single diode model, parameters extraction photovoltaic panel.

### Introduction

A rapid development of photovoltaic market creates a necessity of research connected with design, development and analysis of photovoltaic system operating modes. The main component of photovoltaic power stations is a solar panel which consists of photovoltaic modules (PM). Their operating mode modeling in real operating conditions provides a reasonable choice of main PV stations energy components, output predictions and operating mode optimization. One of the major tasks of PM mathematical modeling is authentic parameters definition which defines the modeling accuracy of the power station operating modes.

There are a lot of scientific papers and research connected with the problem of mathematical models development of photovoltaic converters. However, scientifically, the question is still unanswered. The reason of that can be the complexity and diversity of physical processes taking place in the semiconductor during solar energy conversion into electricity. Many of these processes do not correspond the physical laws and can be described only with empirical equations. One more problem is instability of main parameters of photovoltaic converters, its dependence on external climatic conditions, fabrication methods and interference on each other. For solving this problem more complicated models are introduced, special calculative algorithms, however, a «perfect» model of photovoltaic converter is not created yet.

What is remarkable, is that in many cases the tendency to increase the model accuracy leads to unjustified raise in complexity. Moreover, for many practical tasks connected with operating mode examination for photovoltaic systems it is enough to provide the reproduction of main electrical characteristics of PM with engineering accuracy. For such cases the first priorities are simplicity, universality and usability of the model.

The main goal of this paper is to develop a mathematical model of photovoltaic module according to the technical specification data given by manufacturer, which lets reproduce the module's energy characteristics considering the changes in operating conditions. The basic principles are maximal simplicity and usability for the end user. Thus, using only PM catalogue data it is possible obtain a full solar panel model of arbitrary configuration.



## 1. Solar cell model

The simplest solar cell (SC) consists of two semiconductor plates of p and n types, which generate electrical current with the influence of the sun. The working principle of SC, its construction and major physical processes are described in details in [1, 2]. The exact SC theoretical model can be obtained from equations of solid state physics, describing the rectifying effects of p-n junction [2].

The theoretical model of SC is quite cumbersome and is mainly used by photovoltaic converters developers. Simplified SC mathematical models based on the equivalent electrical circuits are widely used for analysis of the PV-systems operating modes. The idealized model of the solar cell is presented on the fig. 1, a.

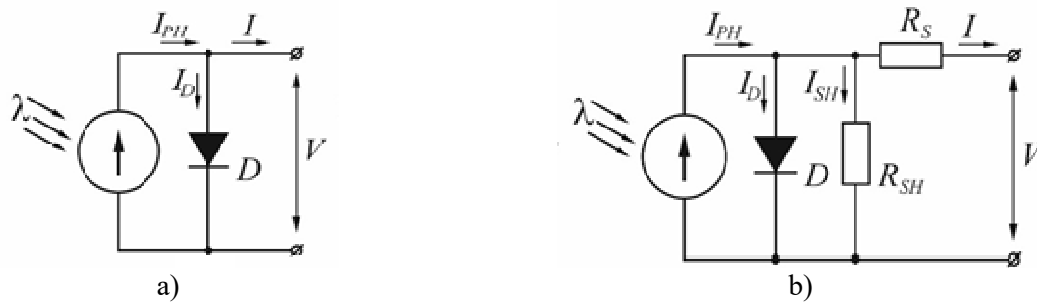


Fig. 1. Solar cell equivalent circuits: a – idealized; b– real with one diode

In this model the output current  $I$  and output voltage  $V$  of the solar cell are in the following relation [2]:

$$I = I_{PH} - I_D = I_{PH} - I_0 \cdot \left[ \exp\left(\frac{q \cdot V}{k \cdot T}\right) - 1 \right] \quad (1)$$

The idealized model consists of the current source creating photocurrent  $I_{PH}$  and an ideal diode. The current  $I_D$  which runs through this diode is defined with the Shockley diode equation and depends on the absolute temperature  $T$  and SC output voltage  $V$  ( $q = 1.602 \cdot 10^{-19}$  – electron charge;  $k = 1.38 \cdot 10^{-23} \text{J/}^\circ\text{K}$  – Boltzmann's constant;  $I_0$  – diode reverse current)

The equation (1) includes 2 undefined parameters  $I_{PH}$  and  $I_0$  which depend on the magnitude of the solar insolation  $\lambda$  and SC operating temperature. With general assumptions they can be found in the form of:

$$I_{PH} = [I_{SC\_STC} + k_I \cdot (T - T_{STC})] \cdot \lambda, \quad (2)$$

where  $I_{SC\_STC}$  – short-circuit current of photovoltaic converter in standard conditions;  $k_I$  – temperature coefficient of short-circuit current;  $T_{STC}$  – cell temperature in standard conditions;  $\lambda$  – solar insolation,  $\text{kW/m}^2$ .

$$I_0 = \left[ \frac{I_{SC\_STC}}{\exp\left(\frac{q \cdot V_{OC\_STC}}{A \cdot k \cdot T_{STC}}\right) - 1} \right] \cdot \left(\frac{T}{T_{STC}}\right)^3 \cdot \exp\left[\frac{q \cdot E_G}{k \cdot A} \left(\frac{1}{T_{STC}} - \frac{1}{T}\right)\right], \quad (3)$$

where  $E_G$  – band gap width of semiconductor (depends on the solar cell type).

The equations (1)-(3) let calculate the volt-ampere characteristic of the solar cell, however, the model accuracy will be not high. In real solar cells power losses are inevitable, and for the accuracy increasing the equivalent circuit on fig. 1, b is used. The volt-ampere characteristic for this model can be described as:

$$I = I_{PH} - I_D - I_{SH} = I_{PH} - I_0 \cdot \left[ \exp\left(\frac{q(V + I \cdot R_S)}{A \cdot k \cdot T}\right) - 1 \right] - \frac{V + I \cdot R_S}{R_{SH}}, \quad (4)$$

where  $A$  – ideality factor;  $R_S$  and  $R_{SH}$  – serial and parallel solar cell resistance, accordingly.

The equation (4) includes five unknown parameters ( $I_{PH}$ ,  $I_0$ ,  $A$ ,  $R_S$ ,  $R_{SH}$ ). To define them it is necessary to solve a complicated mathematical problem. It should be noted, that there are some more complicated SC models, e. g. models with two or three diodes in the equivalent circuit [3,4], which raise the

modeling accuracy. At the same time many authors use simple models neglecting parasitic drags [5,6] or influence of a shunt resistor ( $R_S$ -model) [5,7]. This paper considers a model with one diode and two resistors ( $R_p$ -model), which is a good trade-off between simplicity and accuracy. That is why it became popular in similar studies [8-10].

## 2. Model of photovoltaic module

Photovoltaic module consists of many identical solar cells connected into serial-parallel circuits to increase its voltage and output power. The equation (4) for PM including  $N_s$  serial and  $N_p$  parallel solar cells transform into [5]:

$$I = N_p \cdot I_{PH} - N_p \cdot I_0 \cdot \left[ \exp\left(\frac{q(V + I \cdot R_S)}{N_s \cdot A \cdot k \cdot T}\right) - 1 \right] - \frac{V + I \cdot R_S}{R_{SH}} \quad (5)$$

where  $I$ ,  $V$  – current and voltage at the terminals of PM;  $R_S$  and  $R_{SH}$  – equivalent serial and shunt resistance of PM, accordingly.

The equation (5) defines the PM volt-ampere characteristic which is presented in the fig. 2.

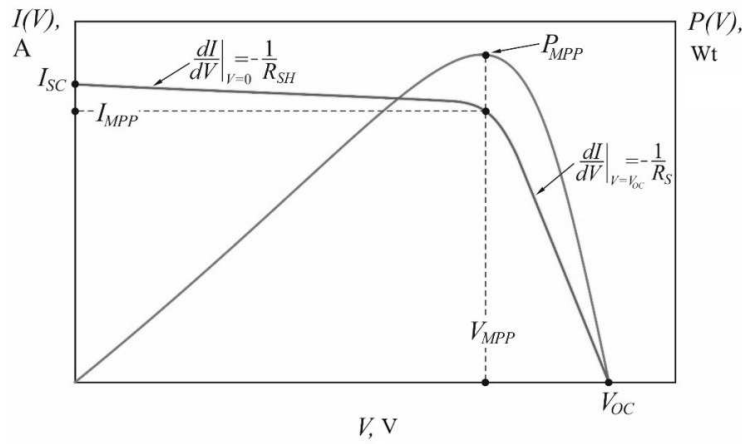


**Fig.2** Volt-ampere and volt-watt characteristics of a photovoltaic module

To some extent of approximation, it can be said that the PM volt-ampere characteristic is a superposition of module's photocurrent and a dark volt-ampere characteristic of diode (unless  $R_S > 0$ ). When the PM is irradiated, it behaves like a current source. When it is shaded, its volt-ampere characteristic is similar to the diode's one. Spectrum, intensity of solar insolation, temperature and parameters of PM depending on its type and design – all they have direct influence on the volt-ampere characteristic. Several characteristic points of the volt-ampere curve can be used for its description (fig. 2). It lets one define a number of parameters of PM equivalent circuit and evaluate the quality of the photovoltaic converter.

If make PM output terminals short-circuited, current  $I_{SC}$  will appear. Analytic form for this short-circuit current can be obtained from (6) considering  $V=0$ ,  $I = I_{SC}$  (here and below  $N_p = 1$  and is not written as most PMs consist only of SCs connected in series):

$$I_{SC} = I_{PH} - I_0 \cdot \left[ \exp\left(\frac{I_{SC} \cdot R_S}{A \cdot V_T}\right) - 1 \right] - \frac{I_{SC} \cdot R_S}{R_{SH}}, \quad (6)$$

where  $V_T = \frac{N_s \cdot k \cdot T}{q}$  – heat stress of PM.

Short-circuit current appears because of generation and disjunction of charge carries generated by light and depends on intensity and spectrum of solar insolation, area of SC and optical properties of PM. In case of disconnected exterior circuit ( $I=0$ ) voltage on the terminals of PM will be equal to open-circuit voltage  $V=V_{OC}$ :

$$0 = I_{PH} - I_0 \cdot \left[ \exp\left(\frac{V_{OC}}{A \cdot V_T}\right) - 1 \right] - \frac{V_{OC}}{R_{SH}} \quad (7)$$

Open-circuit voltage is equal to forward bias corresponding to  $p-n$  junction voltage change due to photocurrent, and characterizes recombination velocity in the photovoltaic converter. Open-circuit voltage mostly depends on SC saturation current.

One of the most important PM characteristics is load operation mode corresponding to maximum power point (MPP). In this case  $I=I_{MPP}$ ,  $V=V_{MPP}$  and equation (5) changes into:

$$I_{MPP} = I_{PH} - I_0 \cdot \left[ \exp\left(\frac{V_{MPP} + I_{MPP} \cdot R_S}{A \cdot V_T}\right) - 1 \right] - \frac{V_{MPP} + I_{MPP} \cdot R_S}{R_{SH}} \quad (8)$$

On the volt-ampere curve MPP lets define the magnitude of fill factor ( $FF$ ). Graphically it is equal to the maximum area of the rectangle, which can be inscribed in the volt-ampere characteristic (fig. 2):

$$FF = \frac{I_{MPP} \cdot V_{MPP}}{I_{SC} \cdot V_{OC}} \quad (9)$$

Physically fill factor defines the maximum power, which can be obtained from the photovoltaic converter and characterizes its quality. From fig. 2 it becomes clear that the numerical value of  $FF$  is determined by the volt-ampere curve shape which depends on the PM interior parameters:  $A$ ,  $R_S$  and  $R_{SH}$ . The magnitude of  $R_S$  is defined by the SC type and geometry and depends on emitter and contact resistances. The analysis of equations (5) and (7) shows that the serial resistance does not influence on the PM characteristics in case of open-circuit. However, it defines the volt-ampere characteristic shape around the point of the open-circuit voltage. This property of  $R_S$  is often used for its direct definition by the volt-ampere characteristic inclination in the point of the open-circuit voltage.

The  $R_{SH}$  exists due to production defects of the solar cell which create alternative canals for photocurrent. Parallel resistance has significant influence on the volt-ampere characteristic shape in case of low intensity of insolation when the magnitude of the photocurrent is small. The magnitude of  $R_{SH}$  defines the volt-ampere curve inclination near the short-circuit point, thus, it is possible to estimate its numerical value. From the fig.2 it is clear that the inclination of the volt-ampere curve in the open-circuit point is bigger than in the short-circuit point. Consequently, the magnitude of  $R_S$  is much smaller than  $R_{SH}$ , and the magnitude of serial resistance has a major influence on the curve shape.

Ideality factor  $A$  determines the correlation between the volt-ampere curve of a real diode and an ideal one. Its magnitude characterizes quality of  $p-n$  junction and recombination type in the SC. In case of usual recombination mechanisms  $A=1$ , however, in real SCs other recombination mechanisms take place. As a consequence, for different SC types the magnitude of  $A$  can take on the value from 1 to 5, table 1 [11]. Due to the fact that  $A$  is an absolutely empirical value and it is impossible to define it from physical laws, in many cases the magnitude of ideality factor is chosen from table 1, also the assumption about absence of dependence from temperature and parasitic drags is made. This approach is valid as  $A$  has a minor influence on the V-I curve shape comparing to  $R_S$  и  $R_{SH}$ , and there are recommendations for choosing  $A$  based on numerous experiments with different PM types. For example, for silicic PMs the recommended diapason of  $A$  is 1-1.5 [9,12].

**Table 1.** Average values of ideality factor depending on PM production technology.

Technology	$A$
Si-mono	1.2
Si-poly	1.3
A-Si:H	1.8
A-Si:H tandem	3.3
A-Si:H triple	5
CdTe	1.5
CTS	1.5
AsGa	1.3

### 3. Parameters definition of the PM equivalent circuit

For making a worthwhile PM model it is necessary to define parameters of the equivalent circuit authentically. Due to the fact that most of the parameters depend on the module type, production technology and quality, it is rational to use technical specification data given by manufacturer for the parameters definition. However, in PM technical specification there are no parameters of the equivalent circuit given, which let one find volt-ampere characteristic directly. There are only few experimental data about electrical and thermal characteristics of photovoltaic converters, which was obtained in standard test conditions, insolation intensity  $\lambda=1000 \text{ Wt/m}^2$ , solar spectrum AM 1.5, temperature  $T=25^\circ\text{C}$ . For the given PM model it is necessary to define five unknown parameters of equivalent circuit which are included in equation (6). This equation is non-linear and transcendental, so it does not have direct analytical solution. At the current moment, there are many methods of parameters definition for PM equivalent circuit which can be classified as analytical [13,14] and numerical [15,16] ones. Among numerical methods the most popular ones are evolutionary algorithms, for example, genetic algorithms [17], fish shoal [18], cuckoo [19], mine explosion [20] and many others. Detailed review of parameters definition methods can be found in [20]. Popular ones can considerably differ with assumptions, accuracy, calculation algorithm. Many methods are quite complicated and require additional mathematical knowledge and programming skills.

For making the process of PM parameters calculation easier, combined methods can be used. Some parameters ( $I_{PH}$  and  $I_0$ ) are defined with analytical forms, for the rest ones ( $R_S$ ,  $R_{SH}$ ,  $A$ ) iterative procedures are used [8,10,12]. Original combined method of PM parameters definition was suggested by M. Villalva in paper [22]. Technical specification data of PM obtained in standard test conditions (STC) is used as given data. Photocurrent and diode reverse current for STC are defined with analytical formulas:

$$I_{PH\_STC} = \frac{R_{SH} + R_S}{R_{SH}} I_{SC\_STC}. \quad (10)$$

$$I_{0\_STC} = \frac{I_{SC\_STC}}{\exp\left(\frac{V_{OC\_STC}}{A \cdot V_{T\_STC}}\right) - 1}. \quad (11)$$

Ideality factor  $A$  is chosen from table 1, assumed to be constant and independent from PM temperature.

Numerical values of serial  $R_S$  and parallel  $R_{SH}$  resistances are defined using iterative method, considering condition of equality of maximum power obtain experimentally  $P_{MPP\_exp}$  and as a result of calculations  $P_{MPP\_calc}$  [22]:

$$P_{MPP\_calc} = V_{MPP} \left\{ I_{PH} - I_0 \cdot \left[ \exp\left(\frac{V_{MPP} + I_{MPP} \cdot R_S}{A \cdot V_T}\right) - 1 \right] - \frac{V_{MPP} + I_{MPP} \cdot R_S}{R_{SH}} \right\} = P_{MPP\_exp} \quad (12)$$

For definition of parasitic drags it is necessary to perform a number of iterative calculations with different fixed values of  $R_S$ , starting from  $R_S=0$  and after that introduce increment with definite step. The condition of iteration convergence is:

$$\left| P_{MPP\_calc} - P_{MPP\_exp} \right| < \varepsilon, \quad (13)$$

where  $\varepsilon$  – allowable error.

Minimal (initial) value of parallel resistance is set by the following expression:

$$R_{SH\_min} = \frac{V_{MPP}}{I_{SC\_STC} - I_{MPP}} - \frac{V_{OC\_STC} - V_{MPP}}{I_{MPP}}. \quad (14)$$

The authors of this paper prove that the dependence  $P_{MPP\_calc}=f(R_S)$  obtained from a number of iterative calculations has explicit extremum. This fact lets one find a pair of resistances  $R_S$  and  $R_{SH}$  without complicated graphic construction. The suggested method was tested by authors on several PM models and demonstrated good correlation between calculation results and experimental ones. Simplicity and clearness made this method popular among other researchers of photovoltaic systems. This conclusion can be made from many references to this paper in scientific periodicals [5,6,8,10,13,19 and others]. Disadvantage of this method is quite complicated process of  $R_S$  and  $R_{SH}$  definition, which requires certain programming skills and competence in applied mathematical software.

#### 4. Suggested method of PM parameters definition

In this paper an alternative and easy way of PM parameters definition for equivalent circuit is suggested. It lets user solve this problem within minimal time providing engineering accuracy. In this method combined algorithm is used which is easily realized in tabular program Excel with installed tool «Search for solutions». The idea is the following: using chosen and fixed value of  $A$ , the condition of equality of calculated  $I_{MPP\_calc}$  and experimental  $I_{MPP\_exp}$  PM currents in MPP is considered.

After putting equations (10), (11) in (8) the result is:

$$\frac{R_{SH} + R_S}{R_{SH}} I_{SC\_STC} - \left[ \frac{I_{SC\_STC}}{\exp\left(\frac{V_{OC\_STC}}{A \cdot V_{T\_STC}}\right) - 1} \right] \cdot \left[ \exp\left(\frac{V_{MPP} + I_{MPP} \cdot R_S}{A \cdot V_{T\_STC}}\right) - 1 \right] - \frac{V_{MPP} + I_{MPP} \cdot R_S}{R_{SH}} - I_{MPP} = 0, \quad (15)$$

where  $V_{T\_STC} = \frac{N_S \cdot k \cdot T_{STC}}{q}$  – heat stress of PM in STC.

Equation (15) includes only two unknown parameters and it can be considered as objective function with two variables  $R_S$  and  $R_{SH}$ . Then the procedure of PM parameters definition comes to creation of Excel list where should be a table for input of PM technical specification data and formulas (10), (11) and (15). After launching the tool «Search for solutions», it is necessary to choose a cell with formula (15) as an objective function. Cells with unknown parameters  $R_S$  and  $R_{SH}$  should be set as variables.

Upper and lower variation limits of the variables can be in diapason:

$$\begin{aligned} 0.002 \frac{N_S}{N_p} \leq R_S \leq 0.005 \frac{N_S}{N_p} \\ 1 \frac{N_S}{N_p} \leq R_{SH} \leq 15 \frac{N_S}{N_p} \end{aligned} \quad (16)$$

For getting a final result, it is not necessary to develop new programs and computational algorithms. What is necessary is to set calculation parameters in the dialog box: accuracy limits, maximum number of iterations, maximum calculation time, etc. and start the performance. An obvious advantage of the suggested method is maximum simplicity and universality. Once created calculation form can be used many times for parameters definition of different PM types.

#### 5. Modeling of PM energy characteristics

Almost all PM parameters depend on temperature and insolation intensity. For parameters such as  $A$ ,  $R_S$  and  $R_{SH}$  these dependences are less significant and can be neglected, however, for  $I_{PH}$  and  $I_0$  they should be taken into account. In this paper for finding the values of  $I_{PH}$  and  $I_0$  in case of changing climate conditions during operation, the following equations were used [2]:

$$I_{PH} = \left[ \frac{R_{SH} + R_S}{R_{SH}} I_{SC\_STC} + k_I \cdot (T - T_{STC}) \right] \cdot \frac{\lambda}{\lambda_{STC}} \quad (17)$$

$$I_0 = \frac{I_{SC\_STC} + k_I \cdot (T - T_{STC})}{\exp\left(\frac{V_{OC\_STC} + k_V \cdot (T - T_{STC})}{A \cdot V_T}\right) - 1} \quad (18)$$

Having the values of temperature and insolation for energy characteristic modelling it is necessary to solve equation (5). For its solving Newton-Raphson method was used: algorithm of finding a numerical solution of equation  $f(x)=0$  yields iterative calculation procedure:

$$x_{n+1} = x_n - \frac{f(x_n)}{f'(x_n)}, \quad (19)$$

where  $f'(x)$  is function derivative.

Equation (6) transforms into:

$$f(I) = I_{PH} - I - I_0 \cdot \left[ \exp\left(\frac{V + I \cdot R_S}{A \cdot V_T}\right) - 1 \right] - \frac{V + I \cdot R_S}{R_{SH}} = 0 \quad (20)$$

Taking into account the equation (41) gives:

$$I_{n+1} = I_n - \frac{I_{PH} - I_n - I_0 \left[ \exp\left(\frac{V + I_n \cdot R_S}{A \cdot V_T}\right) - 1 \right] - \frac{V + I_n \cdot R_S}{R_{SH}}}{-1 - I_0 \cdot \frac{R_S}{A \cdot V_T} \cdot \exp\left[\frac{V + I_n \cdot R_S}{A \cdot V_T}\right] - \frac{R_S}{R_{SH}}} \quad (21)$$

Equations (17)-(21) are basic for making a PM mathematical model. This algorithm of energy characteristics calculation can be realized using MS Excel as well as other mathematical software [23, 24]. For model testing the data from technical specification of PM Kyocera KC200GT was used [25]. The modelling results were compared to experimental volt-ampere characteristics and results of other published studies [10, 12, 19, 22]. Table 2 presents technical specification data of PM Kyocera KC200GT; table 3 presents calculated parameters of equivalent circuit obtained from mathematical modelling.

**Table 2.** Technical specification data of PM Kyocera KC200GT in standard test conditions

Technology	Si-poly
$P_{MPP}$	200.143 W
$V_{MPP}$	26.3 V
$I_{MPP}$	7.61 A
$V_{OC}$	32.9 V
$I_{SC}$	8.21 A
$k_V$	-0.123 V/°K
$K_I$	0.00318 A/°K
$N_S$	54
$N_P$	1

**Table 3.** Calculated parameters of equivalent circuit of PM Kyocera KC200GT

Parameter/ Method (publication)	Suggested method	Simplified analytical method ( $R_S$ -model)	Analytical method with fixed $A$ ( $R_P$ -model) [10]	Combined method ( $R_P$ -model) [22]	Numerical method ( $R_P$ -model) [12]	Numerical method, evolutionary algorithm [19]
$I_0$ , A	$9.891 \cdot 10^{-8}$	$7.712 \cdot 10^{-8}$	$9.763 \cdot 10^{-8}$	$9.825 \cdot 10^{-8}$	$4.812 \cdot 10^{-8}$	$5.12 \cdot 10^{-10}$
$I_{PH}$ , A	8.214	8.210	8.213	8.214	8.215	8.215
$A$	1.3	1.283	1.3	1.3	1.235	1.017
$R_S$ , Ohm	0.223	0.255	0.231	0.221	0.247	0.257
$R_{SH}$ , Ohm	446.293	$\infty$	597.386	415.405	414.89	117.922

Analysis of data from table 3 demonstrates good correlation between equivalent circuit parameters of suggested PM model and results of published studies. For testing the ability of model to display the volt-ampere curve in real operating conditions calculation of model characteristics with changing insolation and module temperature was conducted, fig. 3, 4. The curves correspond to calculated characteristics and experimental data is marked on the curves. From fig. 3 and 4 it can be seen that PM model characteristics are in a good correlation with experimental ones in a wide range of temperature and insolation. Conducted calculation experiments proved that the modelling results of the volt-ampere characteristic are identical to ones presented in papers [10,12,22]. The explanation is that all models of these studies were based on the same initial equations, and the difference is only in definition methods of the equivalent circuit parameters. Absolute error of the model in comparison to experimental data for PM Kyocera KC200GT for various insolation is shown on the fig. 5.

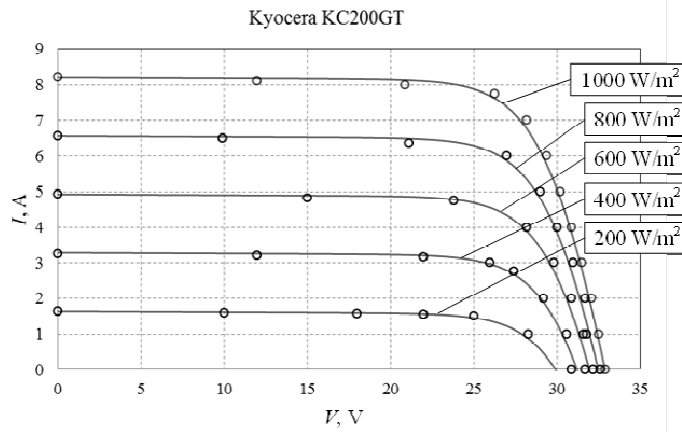


**Fig.3.** Calculated and experimental volt-ampere characteristics of PM Kyocera KC200GT with changing insolation ( $T=25\text{ }^\circ\text{C}$ ).

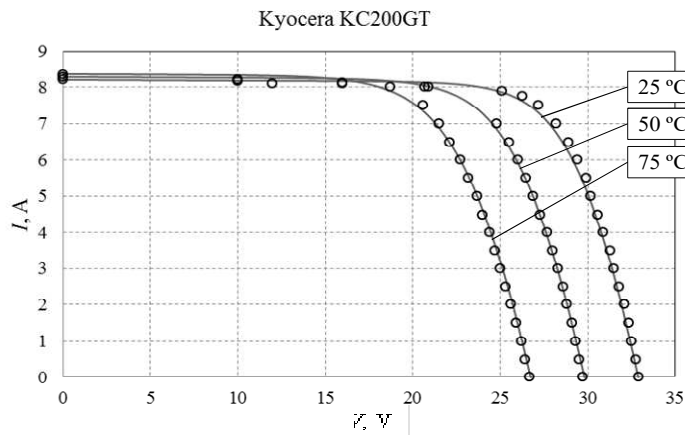


**Fig.4.** Calculated and experimental volt-ampere characteristics of PM Kyocera KC200GT with changing module temperature ( $\lambda=1000\text{ }W/m^2$ ).

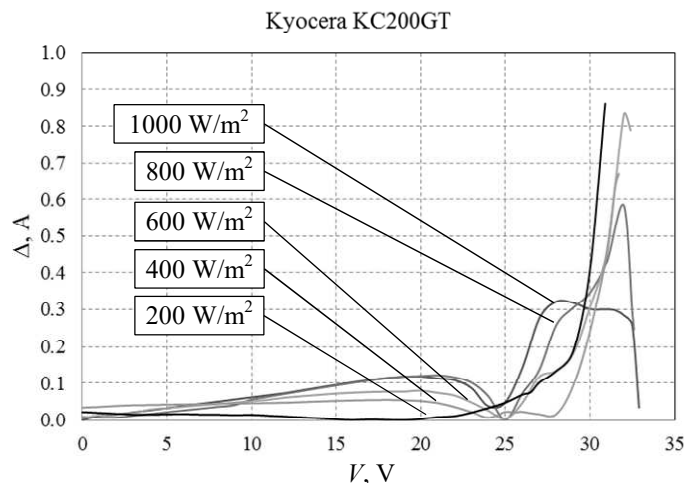


**Fig.5.** Absolute errors of suggested model of PM Kyocera KC200GT in case of changing insolation ( $T=25\text{ }^\circ\text{C}$ ).

Analysis of the results shows that the magnitude of the absolute error of the model in all insolation diapason does not exceed 0.85 A. Maximal error appears in modes which are close so open-circuit operation. Due to the fact that most photovoltaic power stations work with MPPT controllers, relatively high error in these modes is no critical. It is far more important to provide high modelling accuracy in modes which are close to MPP. The suggested model demonstrates desired results. For accuracy estimation of the model, data

of the PM comparison analysis from [26] was used. Regarding this analysis it can be said, that the model provides accuracy which is comparable with other known  $R_p$ -models, exceeds  $R_s$ -models in accuracy and is slightly inferior to more complicated models based on two diodes. An important advantage of the model is high accuracy of PM energy characteristics modelling in case of changing temperature. It can be provided due to the fact that for definition of diode reverse current instead of frequently used equation (3) in the suggested model a more precise analytical formula (18) is used, first suggested in paper [22].

The suggested model was tested on a number of popular photovoltaic modules of poly- and monocrystalline type and demonstrated satisfactory results: relative error for all the tested PMs around MPP does not exceed 5%.

## Conclusions

In the paper results of research about enhancement of photovoltaic modules modelling are presented. Based on the conducted comparison analysis of wide spread mathematical models types of photovoltaic converters, a base structure of exponential model with one diode was chosen.

Application of given model with preliminarily chosen and fixed value of ideality factor lets noticeably simplify mathematical description of the studied object. Thus, combined method can be used for PM parameters definition, where photocurrent and diode saturation current are found with analytical expressions and for parasitic drags numerical method is used. Advantage of this approach is ability to define all unknown PM parameters using only technical specification data as initial data. And for parasitic drags definition tabular program Excel with installed tool «Search for solutions» can be used. This tool lets one easily calculate the values of serial and parallel resistances without programming and calculating algorithms. The suggested method of PM parameters definition provides high automation of calculation using universal form on the Excel list, which can be repeatedly used for parameters definition of various PMs.

The suggested model was tested on a number of photovoltaic modules and showed good correlation of modelling results with data given by manufacturer. The model provides high modelling accuracy around maximum power point. Thus, it can be used for making effective algorithms for photovoltaic power stations controllers, enhancement of circuit technology of converting devices, prediction of electrical energy generation by photovoltaic systems, analysis and optimization their operating modes.

The direction of further research is the development of a complex mathematical model of photovoltaic power plants and hybrid energy systems based on them in order to study their modes and optimize the composition of the equipment.

## Acknowledgments

The research is carried out at Tomsk Polytechnic University within the framework of Tomsk Polytechnic University Competitiveness Enhancement Program grant.

## REFERENCES

- 1 Handbook of photovoltaic science and engineering / edited by Antonio Luque and Steven Hegedus. John Wiley & Sons Ltd, The Atrium, Southern Gate, Chichester, West Sussex PO19 8SQ, England, 2003, 1117p.
- 2 Practical handbook of photovoltaics: fundamentals and applications / edited by Tom Markvart and Luis Castafier. Elsevier Advanced Technology, The Boulevard. Langford Lane, Kidlington Oxford OX5 1GB, UK, 2003
- 3 Wang S., Zhang Y., Hao P., Lu H. An improved method for PV output prediction using artificial neural network with overlap training range. *Journal of Renewable and Sustainable Energy*. 2021, Vol. 13, article number 063502. doi: 10.1063/5.001951
- 4 Khanna V., Das B.K., Bisht D., Vandanac, Singh P.K. A three diode model for industrial solar cells and estimation of solar cell parameters using PSO algorithm. *Renewable Energy*. 2015, Vol. 78, pp. 105-113. doi: 10.1016/j.renene.2014.12.072
- 5 Masmoudi F., Salem F.B., Derbel N. Identification of Internal Parameters of a Mono-Crystalline Photovoltaic Cell Models and Experimental Ascertainment. *International journal of renewable energy research*. 2014, Vol. 4, No.4, pp. 840-848.
- 6 Bal S., Anurag A., Nanda M., Sourav S. Comprehensive Analysis and Experimental Validation of an Improved Mathematical Modeling of Photovoltaic Array. *Advances in Power Electronics*. 2015, 654092, doi: 10.1155/2015/654092
- 7 Jakhrani A.Q., et al. An Improved Mathematical Model for Computing Power Output of Solar Photovoltaic Modules. *International Journal of Photoenergy*. 2014, 346704. doi: 10.1155/2014/346704



- 8 Abbassi A., Gammoudi R., Dami M.A., Hasnaoui O., Jemli M. An improved single-diode model parameters extraction at different operating conditions with a view to modeling a photovoltaic generator: A comparative study. *Solar Energy*. 2017, Vol. 155, pp. 478-489. doi: 10.1016/j.solener.2017.06.057
- 9 Hmamou D.B., Elyaqouti M., Arjdal E., et al. Parameters identification and optimization of photovoltaic panels under real conditions using Lambert W-function. *Energy Reports*. 2021, Vol.7, pp. 9035-9045. doi: 10.1016/j.egyr.2021.11.219
- 10 Cubas J., Pindado S., Victoria M. On the analytical approach for modeling photovoltaic systems behavior. *Journal of Power Sources*. 2014, Vol. 247, pp. 467-474. doi: 10.1016/j.jpowsour.2013.09.008
- 11 Said S., Massoud A., Benammar M., Ahmed S. A Matlab/Simulink-Based Photovoltaic Array Model Employing Sim Power Systems Toolbox. *Journal of Energy and Power Engineering*. 2012, Vol. 6, pp. 1965-1975.
- 12 El Tayyan A.A. PV system behavior based on datasheet. *Journal of Electron Devices*. 2011, Vol. 9, pp. 335-341.
- 13 Cubas J., Pindado S., de Manuel C. Explicit Expressions for Solar Panel Equivalent Circuit Parameters Based on Analytical Formulation and the Lambert W-Function. *Energies*. 2014, Vol.7, pp. 4098-4115. doi: 10.3390/en7074098
- 14 Aoun N., Chenni R., Nahman B., Bouchouicha K. Evaluation and Validation of Equivalent Five-Parameter Model Performance for Photovoltaic Panels Using Only Reference Data. *Energy and Power Engineering*. 2014, Vol. 6(9), pp. 235-245. doi: 10.4236/epe.2014.69021
- 15 Houssein E.H., Nageh G., AbdElaziz M., Younis E. An efficient Equilibrium Optimizer for parameters identification of photovoltaic modules. *PeerJ Computer Science*. 2021, 7:e708. doi: 10.7717/peerj-cs.708.
- 16 Premkumar M., Jangir P., Ramakrishnan C., et al. Identification of Solar Photovoltaic Model Parameters Using an Improved Gradient-Based Optimization Algorithm With Chaotic Drifts. *IEEE Access*. 2021, Vol. 9, pp. 62347-62379. doi: 10.1109/ACCESS.2021.3073821.
- 17 Patel S.J., Pancha A.K., Kheraj V. Solar Cell Parameters Extraction from a Current-Voltage Characteristic Using Genetic Algorithm. *Journal of nano- and electronic physics*. 2013, Vol. 5(2), 02008.
- 18 Han W., Wang H.H., Chen L. Parameters Identification for Photovoltaic Module Based on an Improved Artificial Fish Swarm Algorithm. *Hindawi Publishing Corporation the Scientific World Journal*. 2014, 859239. doi: 10.1155/2014/859239
- 19 Ma J., et al. Parameter Estimation of Photovoltaic Models via Cuckoo Search. *Journal of Applied Mathematics*. 2013, 362619. doi: 10.1155/2013/362619
- 20 El-Fergany A. Efficient Tool to Characterize Photovoltaic Generating Systems Using Mine Blast Algorithm. *Electric Power Components and Systems*. 2015, Vol.43, pp. 890-901. doi: 10.1080/15325008.2015.1014579
- 21 Abbassi R., Abbassi A., Jemli M., Chebbi S. Identification of unknown parameters of solar cell models: A comprehensive overview of available approaches. *Renewable and Sustainable Energy Reviews*. 2018, Vol. 90, pp. 453-474. doi: 10.1016/j.rser.2018.03.011
- 22 Villalva M.G., Gazoli J.R., Filho E.R. Comprehensive Approach to Modeling and Simulation of Photovoltaic Arrays. *IEEE Transactions on Power Electronics*. 2009, Vol. 24, pp. 1198-1208. doi: 10.1109/TPEL.2009.2013862
- 23 Obukhov S.G., Plotnikov I.A., Surzhikova O.A., Savkin K.D. Method for prediction of the power output from photovoltaic power plant under actual operating conditions. *IOP Conf. Ser.: Materials Science and Engineering*. 2017, Vol. 189, 012008. doi: :10.1088/1757-899X/189/1/01200
- 24 Obukhov S.G., Plotnikov I.A., Kryuchkova M. Simulation of Electrical Characteristics of a Solar Panel. *IOP Conf. Ser.: Materials Science and Engineering*. 2016, Vol. 132, 012017. doi: 10.1088/1757-899X/132/1/012017
- 25 KC200GT High Efficiency Multicrystal Photovoltaic Module Datasheet Kyocera. <https://www.energy-matters.com.au/images/kyocera/KC200GT.pdf>
- 26 Ishaque K., Salam Z., Taheri H., Syafaruddin. Modeling and simulation of photovoltaic (PV) system during partial shading based on a two-diode model. *Simulation Modelling Practice and Theory*. 2011, Vol. 19, pp. 1613-1626. doi: 10.1016/j.simpat.2011.04.005

## RESEARCH ON THE STRUCTURE OF THE MATERIAL BASED ON NANO- AND MICRO-SIZED CUBIC BN SYNTHESIZED FROM MECHANICALLY ACTIVATED GRAPHITE-LIKE BN WITH THE ADDITION OF ALUMINUM UNDER HPHT CONDITIONS

Senyut V.T.

Joint Institute of Mechanical Engineering of NAS of Belarus, Minsk, Belarus, [vsenyut@tut.by](mailto:vsenyut@tut.by)

*In the article the structure and phase composition of the material based on nano- and micro-sized cubic boron nitride (cBN) obtained under high pressure and high temperature conditions from mechanically activated graphite-like boron nitride (hBN) in the presence of aluminum (Al), which plays the role of an initiator for the phase transformation  $hBN \rightarrow cBN$ , are investigated. It has been shown that the use of mechanical activation contributes to the formation of cBN nuclei in hBN, which makes it possible to increase the dispersion of the final product. The technological parameters of the cBN synthesis and the amount of Al have a significant effect on the structure of the material as well as the content of the cubic BN phase in it. The increase in the pressure for the hBN (MA) -10% Al system from 2.5 to 5.5 GPa and the temperature from 1550 °C to 1750 °C contributes to the increase of the content of the cBN phase from 10-15% to 90%. In this case, the size of cBN grains synthesized at pressures of 2.5 and 5.5 GPa is in the range of 200-500 nm and 40-120 nm, respectively. The increase in the amount of Al, temperature and duration for the cBN synthesis leads to the formation of large cBN grains with a size of about 10-50  $\mu\text{m}$ .*

**Keywords:** mechanical activation, phase transformation, nanostructured cubic boron nitride, high pressure and temperature, synthesis.

### Introduction

At the present time cubic boron nitride (cBN) is used in the production of tools for highly efficient abrasive and blade machining of a wide class of machine-building materials [1]. Cubic BN is of a lower hardness to diamond, but has a higher thermal stability and chemical inertness, which makes it indispensable for processing alloy steels, cast irons, as well as nickel and titanium alloys, heat-resistant wear-resistant coatings, surfacing, etc. [2].

The industrial production of cBN is based on the phase transformation of graphite-like boron nitride (hBN) into cubic BN under high pressure and high temperature (HPHT) conditions in the presence of catalysts (initiators) [3]. As a rule, the spontaneous crystallization method used in industry makes it possible to synthesize cBN powders from units to several hundred micrometers efficiently. However, the synthesis of cBN nano- and submicro- and micro-powders is associated with a sharp rise in the cost of the production process and, accordingly, their cost on the market. At the same time, an increase in the level of physical, mechanical and operational characteristics of blade and abrasive tools is associated with the use of highly dispersed (nano- and submicron) cBN powders in their production. Therefore, the development of technological processes for the synthesis of both cBN powders and cBN containing materials is an urgent task today.

### 1. Effect of mechanical activation on structural and phase transformations in hBN

One of the most effective ways to increase the dispersion of the synthesized cBN is mechanical activation (MA) of the initial reaction mixture. It is known that the use of mechanically activated hBN as a starting material leads to an increase in the number of crystallization centers and a decrease in the size of cBN crystals during subsequent HPHT treatment [4, 5]. In a number of experimental studies [6-8], it has been shown a strong effect of MA on the structure of hBN as well as the dispersion and phase composition of the synthesized material.

For example, milling of hBN particles is observed after mechanical treatment of the hBN powder in a ball mill. At the same time there is a decrease in the size of the coherent scattering regions (CSR) hBN from 120 nm for the initial hBN powder to 100 nm for the processed one during 7.5 h and up to 63 nm for the

processed one for 15 h. There is also a decrease in the lattice parameters and, as a consequence, a decrease in the volume of the unit cell in the first case by 0.059% and in the second case by 0.171%. With increasing duration of milling, the shift of hBN reflections towards larger angles and their broadening indicates the development of a defect structure of hBN. In this case, the phase composition of the powder does not change [9]. Intensive activation in a planetary ball mill (PBM) leads to the formation of BN particles with a crystallite size of 4-10 nm, while the specific surface area of BN powder activated in a PCM increases 3-6 times as compared with attritor treatment. After activation, BN powder is in an aggregated state and represents aggregates with a size of 0.5-2  $\mu\text{m}$ , consisting of individual particles with a size of 50-200 nm. With an increase in the MA treatment duration, the transformation of the hBN substructure from crystalline to nanocrystalline and amorphous is observed [10].

It is shown in [11] that as a result of prolonged MA (180 h) of graphite-like BN in a PBM, a product is formed based on nanocrystalline and amorphous hBN with a turbostratic structure with a nanocrystal grain size less than 3 nm. In the resulting amorphous a-BN, along with  $\text{sp}^2$ -hybridized interatomic bonds, there is a-BN with  $\text{sp}^3$ -type bonds. In [12], the transformation of hBN into diamond-like high-pressure phases (wurtzite BN and cBN) is established in the process of MA in a PBM. After 12-hour MA treatment, the yield of these phases is about 20% and does not change with an increase in duration. It indicates the reversible nature of the phase transformation. The reverse transition of the cBN phase into hBN with recrystallization of the latter during the MA of hBN is observed in [13]. Thus, the results of the above researches point out to the formation of high-pressure diamond-like phases during MA of hBN. They serve as crystallization centers, and this stimulates the formation of cBN crystals.

## 2. HPHT treatment of mechanically activated hBN

It is known that thermobaric HPHT treatment of mechanically activated hBN powder without activating additives under high pressures of 6.0-10.0 GPa and temperatures of the order of 2000 °C makes it possible to form a polycrystalline superhard material (PSHM) mainly based on the cBN phase with a grain size within 0.4-1.1 microns. In turn, cBN grains are characterized by a fragmented substructure with a subgrain size of 25-50 nm [10]. At lower pressures of 2.5-4.5 GPa, a nanostructured material is formed on the basis of mechanically activated hBN, its phase composition is predominantly represented by the hexagonal BN phase [14]. Additional stimulation of the cBN formation takes place due to the use of initiators (catalysts) for the transformation of graphite-like BN into the cubic BN phase [15]. Thus, in the presence of initiators, the degree of conversion hBN  $\rightarrow$  cBN during the synthesis of coarse-grained (40-315  $\mu\text{m}$ ) cBN powders from mechanically activated hBN increases from 40 to 70 wt. % [16]. However, in this case, the addition of catalysts leads to an increase in the size of cBN grains as a result of their recrystallization [17, 18]. To exclude grain growth, it is necessary to increase the pressure of HPHT treatment, but this significantly increases the cost of the final product.

However, in practice, at present the task is to increase the content of nano- and micro-sized cBN grains in the synthesized product with economically justified parameters of cBN synthesis. The aim of this work is to study the possibility of synthesizing a material based on nano- and micro-sized cBN grains under relatively low pressures of HPHT treatment of mechanically activated hBN in the presence of an initiator of the hBN  $\rightarrow$  cBN phase transformation and to study the structure and phase composition of the obtained material.

## 3. Initial materials and research methods

The hBN produced by PJSC "Zaporozhabraziv" (Ukraine) with a hexagonal phase content of 97-98% with a particle size of 5 to 100  $\mu\text{m}$  is used as the initial powder. Mechanical activation of hBN powders is carried out in a PBM "Aktivator-2S" (Russia) at a drum rotation speed of 1820 rpm and a centrifugal acceleration of milling bodies of 600  $\text{m/s}^2$  for 10 min. The ratio of the masses of milling bodies to the mass of the processed powder = 10. The size of the hBN powder particles after MA is 0.05-0.2  $\mu\text{m}$ , the specific surface area, measured by the BET method, is 27  $\text{m}^2/\text{g}$ . Aluminum is used as the initiator of the transformation, which is effectively used to activate the phase transformation in BN in the synthesis of polycrystalline cBN [19].

HPHT treatment of mechanically activated hBN powders is carried out in a high-pressure apparatus "anvil with a hole" at pressures of 2.5 and 5.5 GPa and temperatures from 1400 to 1950 °C for 15-60 s. The morphology of surface and fracture of the sintered samples is investigated on an atomic force microscope (AFM) NT-206 (Micro Test Machines Co, Belarus) in the contact mode. The microstructure of the obtained materials is studied with a high-resolution scanning electron microscope (SEM) "Mira" ("Tescan", Czech

Republic). X-ray studies of the powders are performed on a Bruker D8 ADVANCE diffractometer in Cu-K $\alpha$  radiation in an automatic recording mode. Phase analysis of diffraction patterns is performed using the ICDD PDF2 X-ray standards database. The structural parameters are calculated by the least squares method with a full-profile analysis of diffractograms in TOPAS software using the Pawley iterative procedure. Semi-quantitative phase analysis (S-Q) is performed using the RIR (Reference Intensity Ratio).

The technology for obtaining material containing nano- and micro-sized cubic BN consists of the following operations. At the first stage of material preparation, hBN powder was mechanically activated in a planetary ball mill. Then, a phase transformation initiator aluminum (Al) was applied onto the powder by a chemical-thermal method. It has been previously shown that the formation of an Al film on the surface of the hBN powder (i.e., the modification of hBN with aluminum) leads to an increase in the content of dispersed cBN and a decrease in the technological parameters of the hBN  $\rightarrow$  cBN phase transition [20]. In this paper, Al in the amount of 10 and 40 wt. % is applied directly to the mechanically activated hBN powder by the method of chemical thermal deposition [20].

Technology for applying aluminum to hBN powder is as follows. Al powder was added to a weighed portion to hBN powder in an amount of 10 or 40 wt. % and stirred. Then the mixture was annealed in a sealed container in the aluminum halides atmosphere at the temperature of 900°C for 1.5–3.0 h. As a result, a fine-grained (nanocrystalline) coating is formed on the hBN powder in the form of an “island-type” film.

After that the hBN powder was pressed with a force of 3–5 tons/cm<sup>2</sup>, and pressed samples were obtained in the form of tablets with a diameter of 5–10 mm and a height of 6–8 mm. The tablets were sintered under conditions of high pressures and temperatures on a DO-138 press unit with a force of 6.3 MN (630 tons) in special high-pressure apparatuses. The samples were heated by direct current passing through a tubular graphite heater containing a sample inside. Duration of temperature increase to operating values was 10–15 s.

## 4. Experimental part. Discussion of the results

### 4.1 hBN<sub>MA</sub> - 10% Al system, pressure 2.5 GPa

X-ray diffraction analysis of the material samples obtained at a pressure of 2.5 GPa, in a temperature range of 1400–1550 °C for 15-30 s with the addition of 10% aluminum (Fig.1) shows the presence of boron nitride phases, graphite-like and cubic BN, in the material, as well as aluminum compounds –  $\alpha$ -Al<sub>2</sub>O<sub>3</sub>, AlB<sub>2</sub> and AlN.

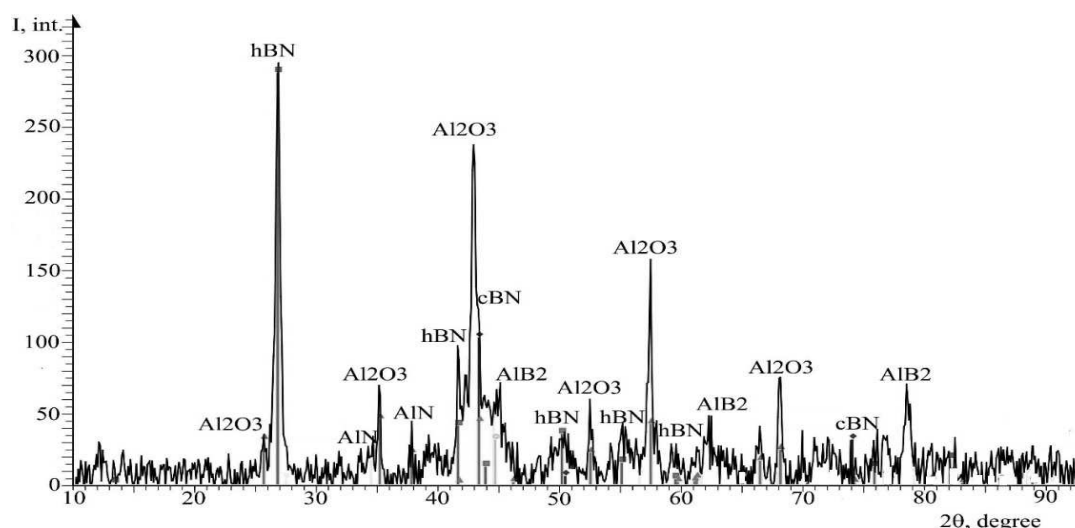


**Fig. 1.** X-ray diffraction pattern after HPHT treatment: at a pressure of 2.5 GPa, a temperature of 1550 °C, a holding time of 15 s. Additive - 10 wt% Al

The formation of corundum  $\alpha$ -Al<sub>2</sub>O<sub>3</sub> in the material can be associated with the presence of oxygen (oxygen-containing compounds) adsorbed on the surface of the initial hBN and aluminum powders. As a result of the research on the fine structure of the material, it is defined that the size of the CSR of the cBN phase is 20 nm, the lattice parameter is increased and equal to  $a = 0.3679$  nm, it may be associated with the formation of solid solutions of Al in cBN [19]. The content of the cBN phase in the resulting material is about 10–15%. For the hBN phase, the CSR size is 30 nm, the lattice parameters are  $a = 0.2498$  nm,  $b = 0.2504$  nm,  $c = 0.6651$  nm.

nm, and it practically coincides with the tabular values from the used base of X-ray diffraction standards ICDD PDF2. The CSR sizes of  $\alpha$ -Al<sub>2</sub>O<sub>3</sub> corundum and aluminum boride AlB<sub>2</sub> are 280 and 35 nm, respectively. At a higher synthesis temperature at a pressure of 2.5 GPa, graphite-like BN is predominantly formed, and its content increases with increasing holding time

#### 4.2 hBN<sub>MA</sub> - 10% Al system, pressure 5.5 GPa

X-ray diffraction analysis of the samples with 10% aluminum obtained at a synthesis pressure of 5.5 GPa in a temperature range of 1550-1750 °C and holding for 15-30 s shows the presence of a cubic BN phase mostly and a relatively small (up to 10%) the amount of graphite-like BN in them (Fig. 2). Analysis of the fine structure shows that the size of the CSR in the cBN phase is about 40 nm, the lattice parameter is  $a = 0.361696$  nm. The content of the cBN phase in the resulting material is estimated at 90%. For the hBN phase, the CSR size is about 50 nm.

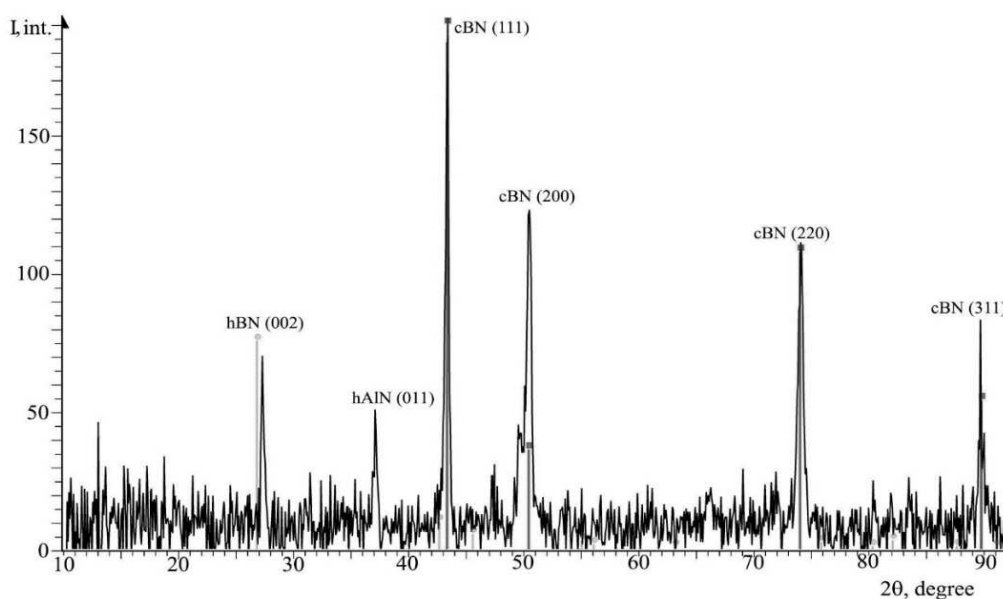


**Fig. 2.** X-ray diffraction pattern of the sample after HPHT treatment at a pressure of 5.5 GPa, temperature 1750 °C, synthesis time 15 s. Additive - 10 wt% Al

Fig. 3 shows the structure of the samples obtained with the addition of 10% Al at pressures of 2.5 and 5.5 GPa and temperatures of 1550 °C and 1750 °C, respectively. The grain size of cBN, estimated by scanning and atomic force microscopy, is within 200-500 nm and 40-120 nm for the samples synthesized at pressures of 2.5 and 5.5 GPa, respectively, and at the temperatures indicated above. Large (micron) hBN particles with a characteristic layered structure are not detected in the samples of the cBN-based material at the given HPHT parameters.

In this case, the preservation of the nano- and submicron-grained structure of cBN synthesized with the addition of 10% Al may be due to a number of structural and technological factors. First, in the process of the synthesis, the nanostructured refractory compounds  $\alpha$ -Al<sub>2</sub>O<sub>3</sub> and AlB<sub>2</sub> are formed, their presence along the grain boundaries of cBN prevents growth of cBN. Secondly, technological modes (high pressure and short synthesis time) also contribute to the stabilization of the cBN grain size.

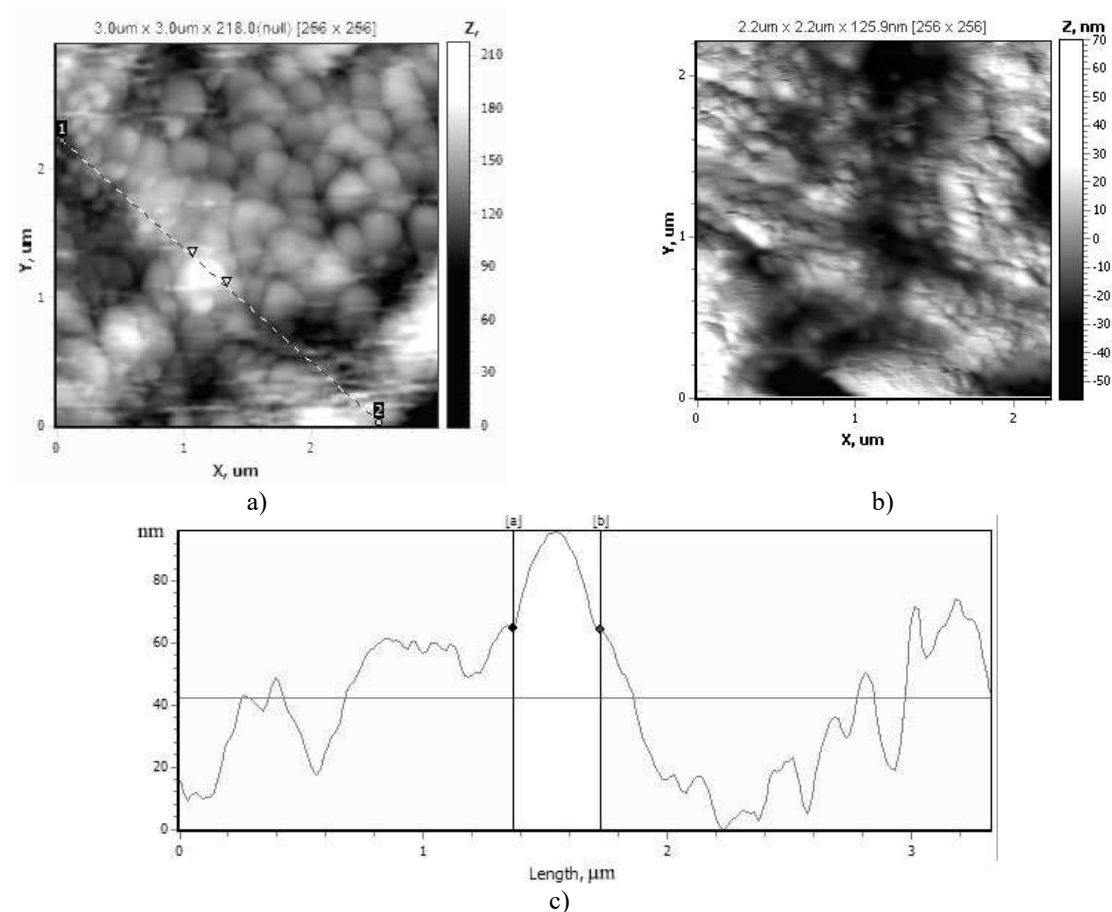


**Fig. 3.** The fracture of the samples obtained in the hBN MA - 10% Al system after synthesis for 30 s: a - pressure 2.5 GPa, temperature 1550 °C; b - pressure 5.5 GPa, temperature 1750 °C; c - surface roughness of the structure shown in Fig. 3a

#### 4.3 hBN<sub>MA</sub> - 40% Al system, pressure 2.5 GPa

Fig. 4 shows the microstructure of the obtained samples (pressure 2.5 GPa, time 30 s, temperature 1550 °C, amount of Al 40 wt.%). In this case, technological additives of boron and silicon are also introduced into the reaction mixture in an amount of 1-2 wt. % to eliminate the negative effect of oxygen on the crystallization process and to improve the fluidity of the melt.

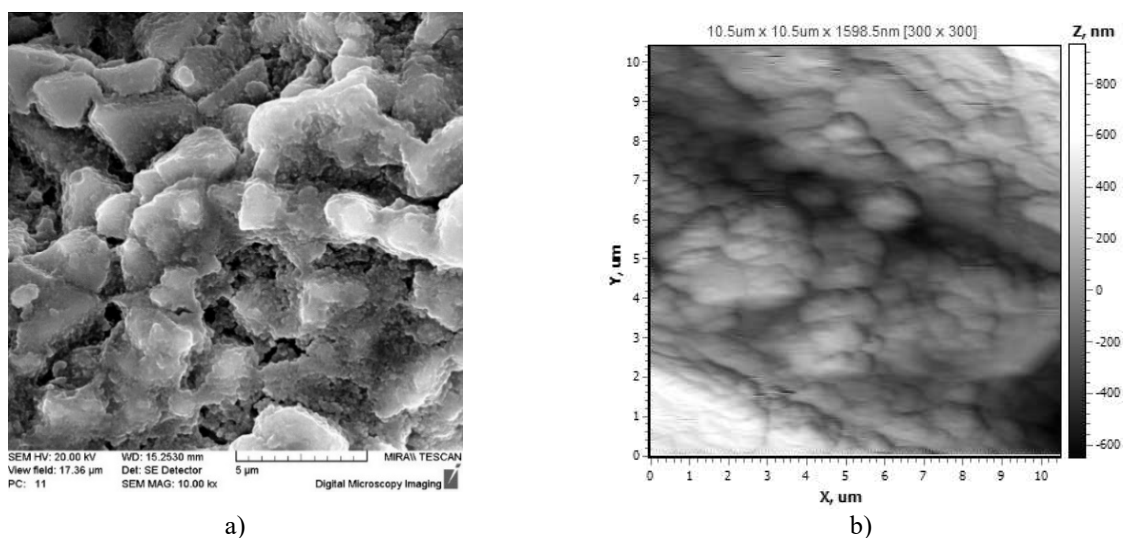


**Fig. 4.** The structure of the material after HPHT treatment at a pressure of 2.5 GPa, exposure time 30 s, temperature 1550 °C: a - general view of the fracture surface, SEM; b - aggregate structure, AFM

Thus, the material obtained at a pressure of 2.5 GPa for 30 s represents individual loose agglomerates up to 5  $\mu\text{m}$  in size, consisting of submicron cBN particles, as well as individual cBN particles of the order of 500 nm. AFM analysis also confirms the presence of polyhedral cBN particles with a size of 200-800 nm, collected in porous agglomerates.

#### 4.4 hBN<sub>MA</sub> - 40% Al system, pressure 5.5 GPa.

A different structure is observed in the samples obtained by HPHT treatment at a pressure of 5.5 GPa, temperatures of 1850-1950  $^{\circ}\text{C}$  for 30-60 s. The studies by the SEM method have shown that in this case the particles of two types are observed in the material (Fig. 5): the large polycrystalline particles of cBN with a size of 10-50  $\mu\text{m}$  (Fig. 5, a, b) and smaller faceted cBN grains of cubic habit with a size of 1-4  $\mu\text{m}$  (Fig. 5, c).

The large polycrystalline particles of cBN are formed as a result of sintering of smaller grains. AFM analysis shows that cBN grains in the indicated size range are both poly- and single crystals. In this case, micron cBN grains are surrounded by fine cBN grains 100-800 nm in size with a characteristic tetrahedral habit (Fig. 5, d-f).

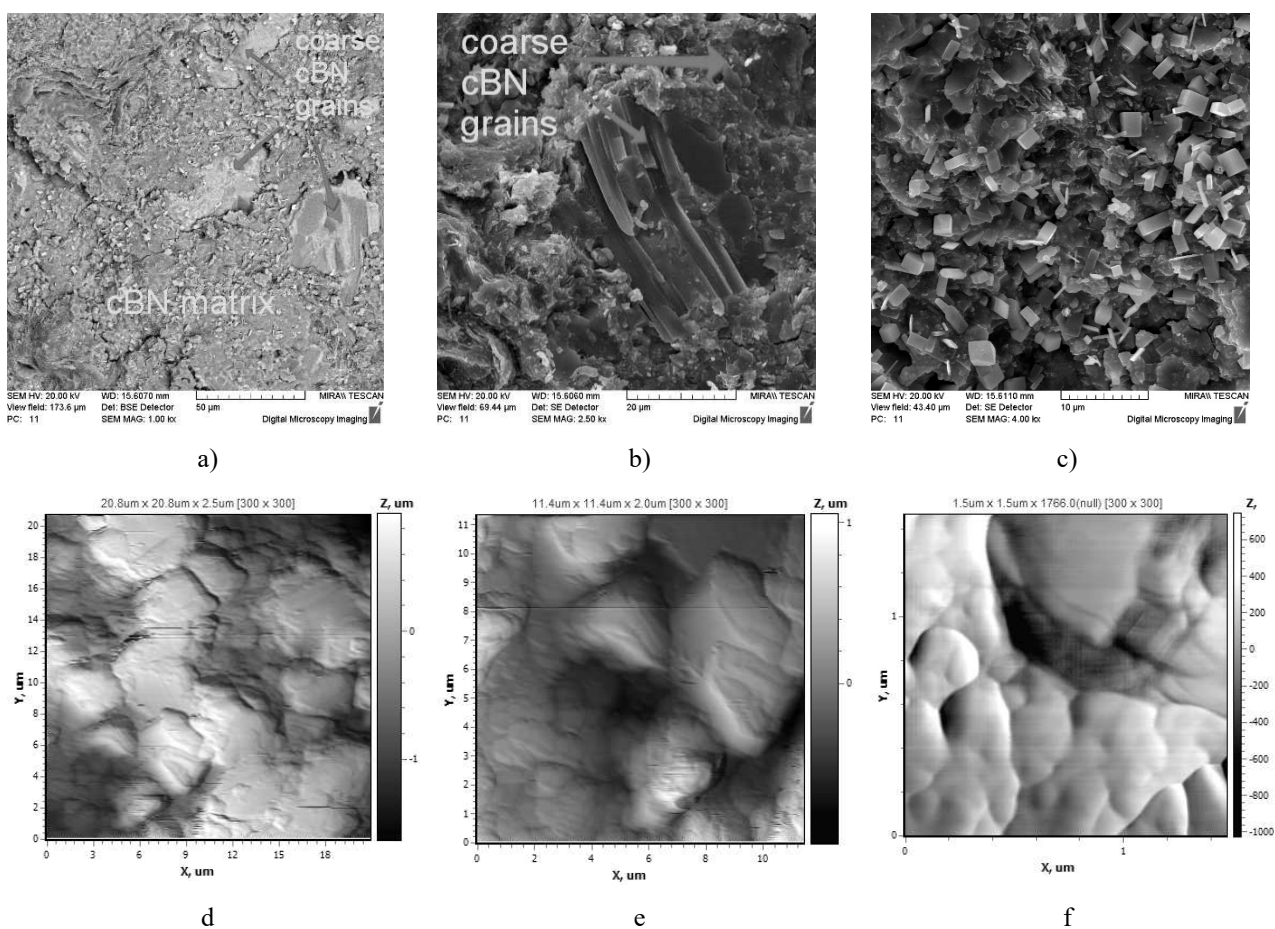


**Fig. 5.** The structure of the material after HPHT treatment at a pressure of 5.5 GPa, a temperature of 1950  $^{\circ}\text{C}$ , synthesis time 60 s: a-c- general view of the fracture surface, SEM; d-f - the structure of cBN crystals (polycrystals), AFM

According to the data of X-ray analysis (Fig. 6), the main phases in the synthesized material are cBN (up to 60%), corundum  $\text{Al}_2\text{O}_3$  (up to 20%), residual (unreacted) aluminum Al and the boron nitride phase  $\text{B}_{50}\text{N}_{1.87}$ . In this case, an increase in the aluminum content to 40%, the synthesis temperature and a longer holding time lead to the growth of cBN grains and their sintering into polycrystals, despite the presence of refractory compounds that play the role of a stabilizer of the grain structure of cBN.

We can see a certain sequence for the morphological changes in the structure of the obtained material. At high pressures and temperatures in the stability region of cBN, the transition of graphite-like BN to the cubic modification of BN takes place. In this case, mechanical activation and the introduction of aluminum stimulate

additionally the phase transformation of the layered structure of graphite-like BN into a cBN modification with a close-packed lattice and a different grain morphology.

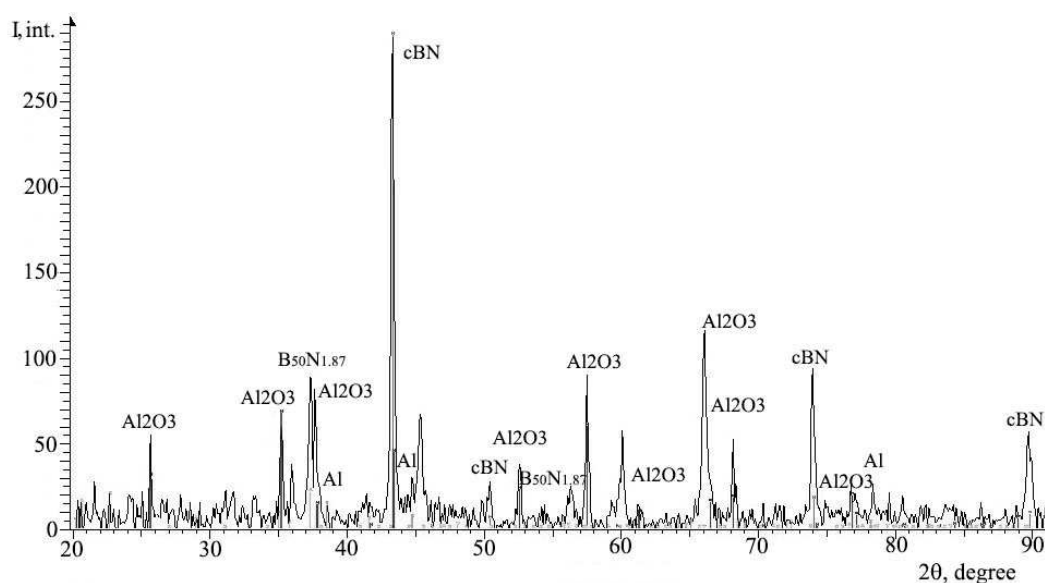


**Fig. 6.** X-ray diffraction pattern of the material after HPHT treatment at a pressure of 5.5 GPa, a temperature of 1950 °C, and a synthesis time of 60 s. Additive - 40 wt.% Al

Thus, the formation of cBN grains of tetrahedral or cubic habit takes place. At higher temperatures, a collective recrystallization in cBN and the formation of large polycrystalline grains based on smaller primary cBN grains are observed.

## Conclusion

The use of MA of hBN leads to formation of cBN nuclei in hBN, and this makes it possible to increase the dispersion of the cBN grains and to reduce the parameters of the hBN → cBN phase transformation under HPHT conditions. Aluminum deposited as a coating on the surface of mechanically activated hBN as an initiator of the synthesis process contributes to the phase transformation of mechanically activated graphite-like BN into cBN in the pressure range of 2.5–5.5 GPa. With the use of Al additive in an amount of 10 wt. %, the material mainly consists of highly dispersed cBN (nano- and submicro-sized), and its amount increases from 10-15% to 90% with an increase in pressure from 2.5 to 5.5 GPa. An increase in the content of the initiator (Al) from 10 to 40 wt. % with an increase in the holding time from 15 to 60 s in the investigated range of pressures and temperatures stimulates the formation of large single cBN particles and their sintering into polycrystals.

## Acknowledgements

The work is supported by the State Program of Scientific Research “Materials Science, New Materials and Technologies” (“Nanostructured materials, nanotechnology, nanotechnique (“Nanostructure”)”), task 2.11.3

## REFERENCES

- 1 Novikov N.V., Klimenko S.A. *Tools made of superhard materials*. Moscow, 2014, 608 p. [in Russian]
- 2 Shulzhenko A.A., Bozhko S.A., Sokolov A.N., et al. *Synthesis, sintering and properties of cubic boron nitride*. Kiev, Naukovadumka Publ., 1993, 255 p. [in Russian]
- 3 Novikov. N.V. *Superhard materials. Obtaining and application*: In Vol. 1: *Synthesis of diamonds and similar materials*. Ed. A.A. Shulzhenko. Kiev: V. Bakul Institute for Superhard Materials, IPC "ALKON" of NAS of Ukraine, 2003, 320 p. [in Russian]
- 4 Sokolov A.N., Shulzhenko A.A., Tkach V.N., Budyak A.A. Investigation of the effect of mechanical activation of hexagonal boron nitride on the phase transformation into cubic modification. *Rock-cutting and metal-working tools – equipment, technology for its manufacture and use*. Kiev: V. Bakul Institute for Superhard Materials, 2005, No. 8, pp. 149-154. [in Russian]



- 5 Gameza L.M., Vityaz P. A., Antonovich Ya.V., Mosunov E.I., Senyut V.T., Uniarkha L.S. Synthesis of cubic boron nitride in the BN–NaN<sub>3</sub> system. *Powder metallurgy*. Minsk, 2015, No. 38. pp. 115–118. [in Russian]
- 6 Du Yong-hui, Zhang Bo-bo, Wang Shao-wei, Zhang Tie-chen. Synthesis of Cubic Boron Nitride Using Ball Milling Hexagonal Boron Nitride. *J. of Synthetic. Crystals.*, 2016, Vol. 45, No. 10, pp. 2441–2445. doi:10.16553/j.cnki.issn1000-985x.2016.10.016
- 7 Streletsky A.N., Permenov D. G., Streletsky K. A. Mechanochemistry of a hexagonal boron nitride. 1. Destruction and amorphization during mechanical treatment. *Colloid J.*, 2010, Vol. 72, No. 4, pp. 532–541 [in Russian]
- 8 Senyut V.T., Vityaz P.A., Kovaliova S.A., Grigorieva T.F. Effect of mechanical activation of powders BN – (TiN, AlN) on the structure of composite material obtained by ultrahigh pressure sintering. *Mater. Today: Proceedings*, 2019, No. 12, pp.102–105. <https://doi.org/10.1016/j.matpr.2019.03.074>
- 9 Vityaz P.A., Senyut V.T. Synthesis and application of nanostructural superhard materials of tool appointment. *Proceedings of the National Academy of Sciences of Belarus. Physical-technical series*, 2015, No. 3, pp. 60-76. [in Russian]
- 10 Senyut V.T., Kovaleva S.A., Gamzeleva T.V., Grigorieva T.F. Investigation of the structural features of boron nitride after mechanical activation in attritor and planetary mill followed by agglomeration at high pressure and temperature. *Chemistry for sustainable development*, 2016, Vol. 24, No. 2, pp.169–175. <https://doi.org/10.15372/KhUR20160208>
- 11 Huang J.Y., Yasuda H., Mori H. HRTEM and EELS Studies on the Amorphization of Hexagonal Boron Nitride Induced by Ball Milling. *J. Am. Ceram. Soc.*, 2000, Vol. 83, No. 2, pp. 403–409. <https://doi.org/10.1111/j.1151-2916.2000.tb01204.x>
- 12 Batsanov S.S., Gavrilkin S.M., Bezduganov S.V., Romanov P.N. Reversible phase transformation in boron nitride upon pulsed mechanical action. *Inorganic materials*, 2008, Vol.44, No.11, pp.1332–1334. [in Russian]
- 13 Senyut V.T., Kovaleva S.A., Mosunov E.I., Stefanovich A.A. Structural and phase transformations in boron nitride during attritor treatment. *Chemistry for sustainable development*, 2009, Vol. 17, No. 6, pp. 647–652.
- 14 Senyut V.T., Kovaleva S.A., Valkovich I.V., et al. Effect of mechanical activation and high pressure high temperature treatment on the synthesis of the material based on nanostructured boron nitride. *Mechanics of Machines, Mechanisms and Materials*, 2019, No. 3 (48), pp. 69–76.
- 15 Golubev A.S., Kurdyumov A.V., Pilyankevich A.N. *Boron nitride: structure, properties, production*. Kiev, Naukovadumka Publ., 1987, 200 p. [in Russian]
- 16 Shulzhenko A.A., Borimsky I.A., Borimsky A.I., et al. Effect of the intensity of mechanical activation on the structure of the hexagonal boron nitride. *Rock-cutting and metal-working tools – equipment, technology for its manufacture and use*. Kiev: V. Bakul Institute for Superhard Materials, 2011, No. 14. pp. 370-376. [in Russian]
- 17 Vityaz P.A., Senyut V.T., Kheifets M.L., Kolmakov A.G. Production of alumo-matrix composite material modified by nanostructured cubic boron nitride. *Proceedings of the National Academy of Sciences of Belarus. Physical-technical series*, 2018, Vol. 63, No.3, pp. 271–279. doi.org/10.29235/1561-8358-2018-63-3-271-279 [in Russian]
- 18 Senyut, V.T. Study of synergistic effect of mechanical activation and high pressure and high temperature sintering on the structure of the material based on boron nitride. *Eurasian Phys. Tech. J.* 2020, Vol, 17, No.1(33), pp. 19–25. doi: 10.31489/2020No1/19-25
- 19 Butylenko, A.K., Bartnitskaya, T.S., Lugovskaya, E.S., Timofeeva, I.I. Annealing of cubic boron nitride by aluminum. *Pis'ma Tekhn. Fiz.*, 1977, Vol. 3 (20), pp. 1094–1095. [in Russian]
- 20 Senyut V.T., Vityaz P.A., Kovaleva S.A., et al. Synthesis of polycrystalline cubic boron nitride from hexagonal boron nitride after mechanical activation and modification with aluminum. *Inorganic Materials: Applied Research*, 2016, Vol. 7, No.1, pp. 53–57. doi: 10.1134 / S2075113316010238.

## MICROSTRUCTURE EVOLUTION OF STEEL-ALUMINUM WIRE DURING DEFORMATION BY "EQUAL-CHANNEL ANGULAR PRESSING-DRAWING" METHOD

Volokitina I.E.<sup>1\*</sup>, Volokitin A.V.<sup>2</sup>, Panin E.A.<sup>2</sup>, Latypova M.A.<sup>2</sup>, Kassymov S.S.<sup>3</sup>

<sup>1</sup> Rudny Industrial Institute, Rudny, Kazakhstan, [irinka.vav@mail.ru](mailto:irinka.vav@mail.ru)

<sup>2</sup> Karaganda Industrial University, Temirtau, Kazakhstan

<sup>3</sup> E.A. Buketov Karaganda University, Karaganda, Kazakhstan

*During experimental studies of the equal-channel angular pressing-drawing effect on the microstructure evolution and mechanical properties change, the principal possibility and effectiveness of using the proposed continuous method for forming an ultrafine-grained structure and increasing the strength properties of steel-aluminum wire was proved. The deformation was carried out at ambient temperature in three passes. It is shown that both layers of bimetallic wire are processed unevenly. An aluminum shell with an initial grain size of 22 microns was processed up to 2 microns. The steel core has a different grain size in the transverse and longitudinal sections. With an initial grain size of 18 microns, after deformation the grain size is about 10 microns in the longitudinal section and 8 microns in the transverse section.*

**Keywords:** severe plastic deformation, microstructure, bimetallic wire, steel, aluminum, mechanical properties.

### Introduction

Currently, bimetallic materials representing a combination of metals or alloys with different physical and mechanical properties are widely used in various industries around the world [1-3]. The metal products obtained from these materials, including rods and wire, determine the safety and reliability of the functioning of railways, telephone wires, cables, objects of the defense industry, aviation, etc. For example, in the cable industry, the material for a conductive core is used by volume, not by weight. This means that 1 ton of aluminum can be used to make 3.2 times the length of a wire of the same diameter than 1 ton of copper. Another important point is the price per unit of mass. Aluminum is much cheaper than copper. The price difference is constantly changing depending on the demand for materials and their availability, not to mention speculation in the metal markets, but aluminum is always about 2-3 times cheaper than copper. Therefore, the use of bimetallic wire in the production of high-frequency cables is most advantageous [4-5]. Due to the surface effect, the current flows only in a very thin part of the wire near the outer surface. The thickness of this layer depends on the frequency at which the cable is operated.

Currently, due to the large difference in the prices of copper and aluminum, the transmission of electricity through cable products with a conductive core made of bimetallic wire is of increasing interest. In recent years, the following types of bimetallic wire have been widely used in industry:

- steel-copper wire, which is used for overhead lines of weak and strong current and the manufacture of wires;

- steel-aluminum wire used for the manufacture of heating elements.

Bimetallic rods are also widely used, including, for example, copper-aluminum current-carrying rods. The replacement of copper in the production of current-carrying wires with aluminum clad with a thin layer of copper makes it possible to reduce the metal consumption of products while maintaining high electrical conductivity. The main quality indicators of bimetallic wire and rods are the combination of their strength and plastic properties. At the same time, the main properties of the bimetallic material of wire and rods, as a structural material, are structurally sensitive, that is, they can be controlled by purposeful changes in the structure during pressure treatment [6-8].

In conditions of a shortage of energy and raw materials, the development of resource-saving methods for obtaining bimetallic materials with properties that combine high strength and plasticity at the same time, using

relatively simple and inexpensive devices that allow spending the minimum possible amount of time when processing products, is very relevant.

One of the most promising directions for improving the strength and plastic properties of bimetallic wire is the formation of an ultrafine-grained (UFG) structure in materials by deformation methods. In this regard, severe plastic deformation (SPD) methods are actively developing, mainly implementing a simple shear scheme under conditions of multi-cycle processing [9-15]. Obtaining this type of structure makes it possible to significantly increase the strength characteristics of metal materials [16-19]. Therefore, the search for high-performance schemes for the formation of UFG structures in metals based on traditional metal forming processes is an important stage in the further development of SPD processes. A special place among these methods is occupied by the "equal-channel angular pressing-drawing" (ECAP-drawing) combined process [20-22]. Its key feature is that, unlike other combined methods, there is no rolling stage here. The continuity of deformation is ensured by the drawing process, which takes place immediately after the ECAP process. In connection with the above, the task of studying the regularities of structural changes in bimetallic steel-aluminum wire during deformation by the "ECAP-drawing" method, as well as establishing a connection between the structural state of the material before and after deformation, is urgent. This will make it possible to significantly advance in understanding the ongoing processes and predict the complex of mechanical properties of such blanks.

## 1. Experimental part

Based on the modeling given in [23-24], the design of tools and accessories for the stand implementing the "ECAP-drawing" combined process was carried out. A matrix for equal-channel angular drawing is designed, consisting of upper and lower segments, repeating the bend of the channel (Figure 1a). The geometric dimensions of the matrix are taken, according to the results obtained during modeling in the Deform software package. The design of all component parts is carried out in the KOMPAS-3D software package (Figure 1b). To check the correctness of the geometric dimensions, as well as the fitting and docking of all the components of the matrix, the tools and accessories were assembled in the KOMPAS-3D software package (Figure 2).

According to the drawing shown in Figure 1a, the matrix was made in the metal structures workshop of Kurylysmet LLP. The matrix segments are made of 5HV2S stamp steel. After manufacturing, the matrix was subjected to heat treatment to increase the hardness and strength. Based on the results of the simulation, the inclination angle between the channels of the matrix was assumed to be equal to  $135^\circ$ . This angle ensures the dominance of shear (non-destructive) stresses over normal (destructive) stresses. There are no rounding at the joints of the matrix channels in order to intensify shear deformations.

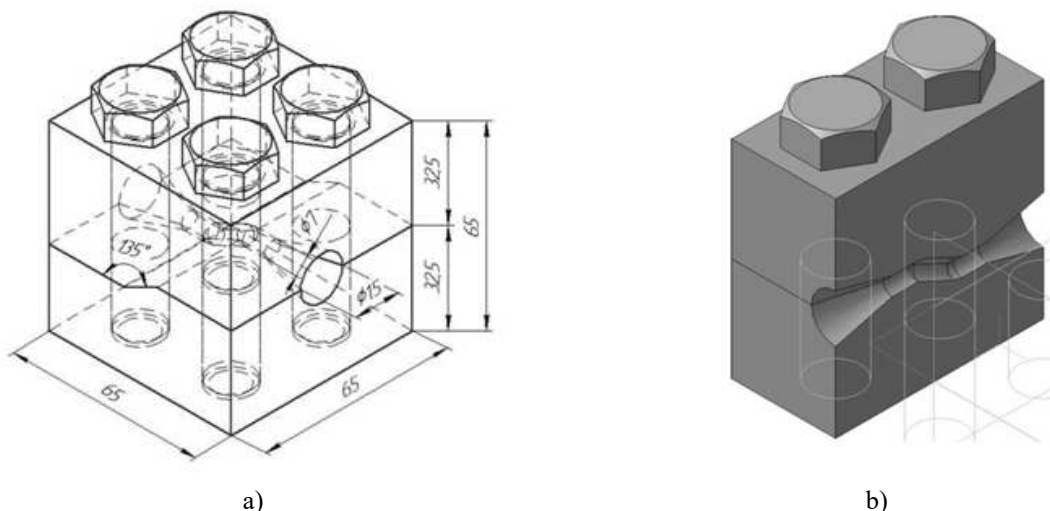


**Fig.1.** Matrix for equal-channel angular drawing: a) - matrix scheme, b) - 3D model

A bimetallic wire consisting of a core of 65G steel and an outer layer of AL6063 aluminum with a diameter of 8 mm was used as the initial billet, the diameter of the steel core was 6.5 mm. The laboratory experiment was carried out on an industrial drawing mill B-I/550 M. An equal-channel step matrix with a channel diameter of 10.0 mm and a junction angle of the matrix channels of  $135^\circ$  was fixed before the drawing

tool. The matrix was located in a lubrication container. The deformation was carried out in three passes. The initial diameter of the blank was 8.0 mm. Hard-alloy drawing tools with polished channels, reduced taper angles of the working zone and smooth transitions from one zone to another were used for drawing stage. Bimetallic wire surface preparation for drawing was carried out according to the usual technology for steel wire, a mixture of soap and sulfur powders was used as a lubricant. The speed of the wire was 10.0 mm/s through the matrix, and 13.6 mm/s through the drawing die.

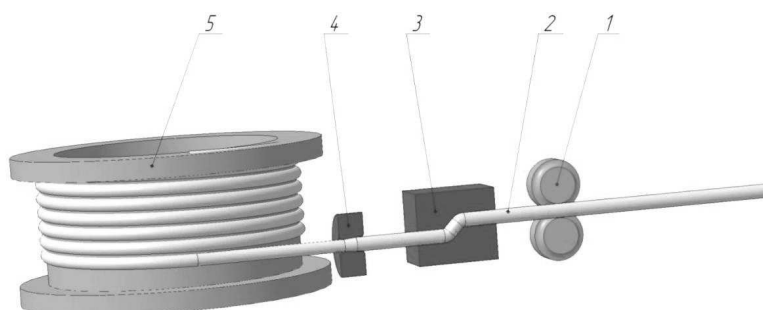


**Fig.2.** Tool assembly: 1 - setting device; 2 - wire; 3 - equal-channel step matrix; 4 – drawing tool in holder; 5 - winding drum

For the study the samples with a length of 15 mm of steel-aluminum wire were cut out, then micro-sections were prepared on the end sides of these blanks. For the preparation convenience and the blockages absence, the plane slots were fixed in a clamp. To prevent the removal of the aluminum layer, depressions with a cylindrical surface were made in the clamp, the radius of which corresponded to the radius of the wire.

To identify the structural elements of 65G steel, the micro-sections were etched in an alcoholic solution of nitric acid (4 cm<sup>3</sup> of nitric acid and 96 cm<sup>3</sup> of ethyl alcohol) for 5-10 seconds. Etching of the aluminum surface was performed with a 5% NaOH solution at a temperature of 70-80°C for 1.5 minutes.

The samples preparation for metallographic analysis was carried out at the Struers electrolytic sample preparation unit. All samples were examined in the middle plane of the sample to avoid the influence of peripheral areas. The obtained samples were considered in transverse and longitudinal sections. The structure and phase composition were analyzed using optical microscopy. Qualitative and quantitative analysis of the main mass microstructure and primary phases was carried out using a LEICA optical microscope equipped with a nozzle for determining the microhardness of individual phases, as well as software for determining the degree of granularity and the number of phases on mechanically polished and etched samples.

## 2. Results and discussion

Figure 3 shows photos of the microstructure of bimetallic wire in the initial state and after three passes of deformation by the "ECAP-drawing" method in longitudinal and transverse sections. The initial grain size of the aluminum shell before deformation was 22 microns, the grain size of steel core was 18 microns (Figure 3a). The structural heterogeneity formed as a result of diffusion processes at various stages of technological operations for the production of bimetallic wire is revealed at the boundary of the connection of steel and aluminum. Metallographic studies have shown that the "ECAP-drawing" process leads to a significant change in the bimetallic wire structure. The most significant changes occur in the surface layers of the aluminum shell (Figure 3b-c). After 3 deformation cycles, a fragmented structure with equiaxed grains is formed in the steel core in both transverse and longitudinal sections. Moreover, in the longitudinal section, the grain size is about 10 microns (Figure 3 d), and 8 microns in the transverse section (Figure 3 e).

In addition, there is a fragmentation of pearlite areas. The thickness of the crushed aluminum layer continuously increases with the number of passes, and after the third pass, the structure becomes almost uniform. The grain size formed after 3 deformation cycles is 2 microns. The results of tensile tests showed that the strength properties of the wire, even after three deformation passes significantly increase compared to the initial state. The tensile strength was increased from 370 MPa in the initial state to 765 MPa after the third pass. The yield strength increased from 260 MPa up to 515 MPa after the third pass.

At the same time, the relative elongation was 22%, while the initial one was 32%. A slight drop in the plastic properties of steel-aluminum wire can be explained by the formation of an ultrafine-grained structure with large-angle nonequilibrium boundaries capable of shear [25].

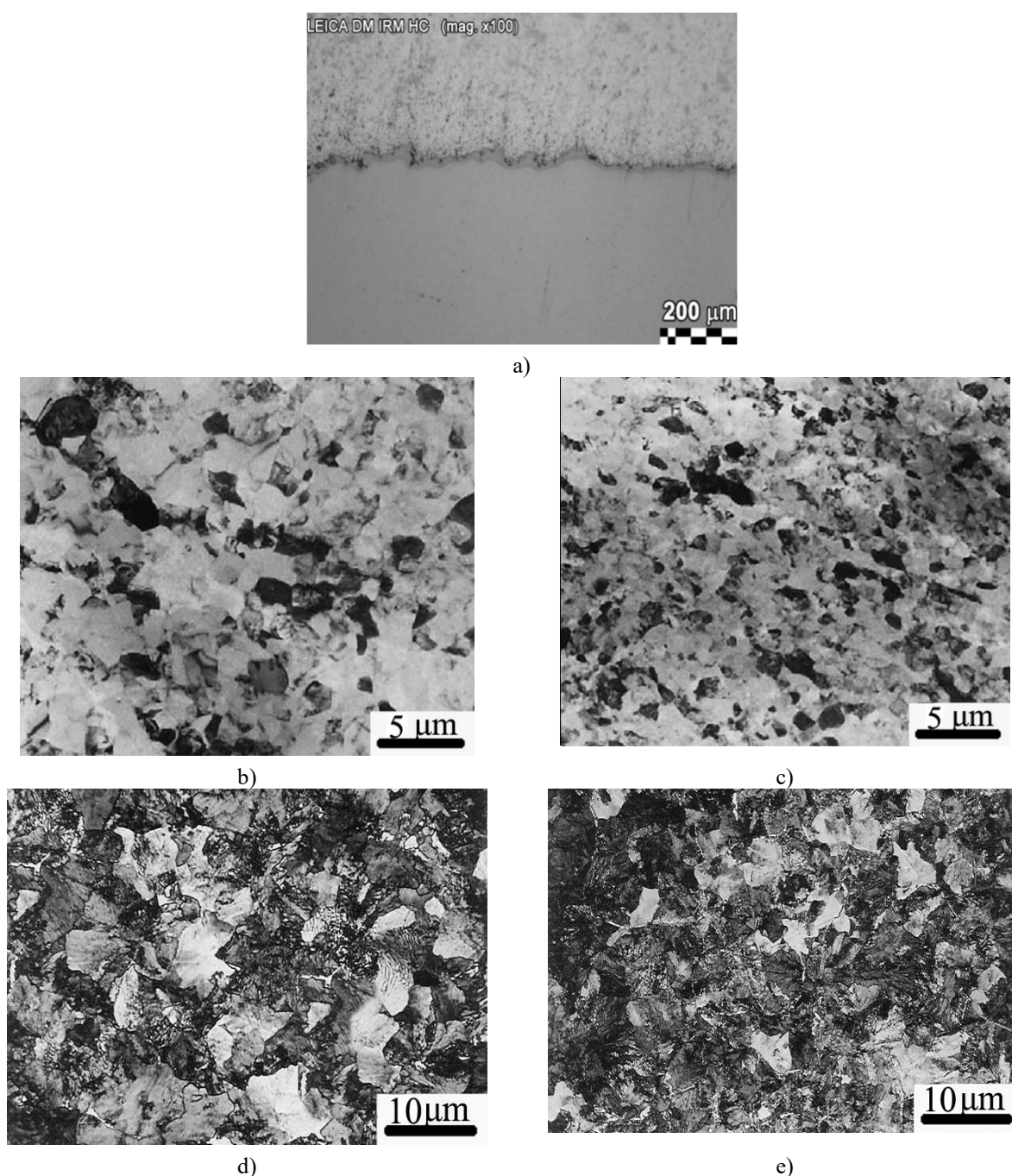


**Fig.3.** Microstructure of bimetallic steel-aluminum wire: a) – initial state; b - aluminum shell (longitudinal section); c) - aluminum shell (transverse section); d) - steel core (longitudinal section); e) – steel core (transverse section)

## Conclusion

The study confirmed the regularity of deformation hardening of bimetallic wire. A significant change in the microstructure, initiated by the combination of equal-channel angular pressing with drawing of steel-aluminum wire, allowed achieving the following most important results:

1. During the deformation of the steel core, which determines the strength properties of the steel-aluminum wire, there is fragmentation of ferrite and crushing of pearlite sections in the longitudinal section up to 10 microns, and up to 8 microns in the transverse section.

2. The strength properties of the wire after three passes of deformation significantly increase compared to the initial state. The tensile strength was increased from 370 MPa to 765 MPa. The yield strength was

increased from 260 MPa to 515 MPa. At the same time, the relative elongation was reduced to 22% from the initial 32%.

3. The combination of equal-channel angular pressing with drawing allows not only the composition strengthening, but also at the same time to increase the plastic properties of products regulated by a number of standards. This circumstance favorably distinguishes the investigated method from other traditional types of wire metal forming.

### Acknowledgments

This research was funded by the Science Committee of the Ministry of Education and Science of the Republic of Kazakhstan (Grant No. AP08052852).

### REFERENCES

- 1 Chukin M.V., Polyakova M.A., Emaleeva D.G., Gulina A.E. Creating Ultrafine Grain Structure in High Strength Bimetallic Steel–Copper Products. *Steel in Translation*. 2014, Vol. 44, No. 4, pp. 320–323.
- 2 Lee K.S., Jun H.J., Lee Y.S. Fabrication of bimetallic rods consist of a Zr-based BMG and a crystalline copper by co-extrusion. *Intermetallics*. 2010, Vol. 18, pp. 1958-1963.
- 3 Llorca-Isern N., Escobar A.M., Roca A., Cabrera J. Equal Channel Angular Pressing of Cu-Al Bimetallic Rod. *Materials Science Forum*. 2012, Vol. 706-709, pp. 1811-1816.
- 4 Acarer M. Electrical, corrosion, and mechanical properties of aluminum-copper joints produced by explosive welding. *Journal of Materials Engineering and Performance*. 2012, Vol. 21, pp. 2375–2379.
- 5 Alizadeh M., Samiei M. Fabrication of nanostructured Al/Cu/Mn metallic multilayer composites by accumulative roll bonding process and investigation of their mechanical properties. *Materials and Design*. 2013, Vol.56, pp. 680-684.
- 6 Eivania A.R., et al. Investigation of joint interface and cracking mechanism of thick cladding of copper on aluminum by equal channel angular pressing (ECAP). *Journal of Materials Research and Technology*. 2020, Vol. 9(3), pp. 3394–3405.
- 7 Chen C.-Y., Chen H.-L., Hwang W.-S. Influence of interfacial structure development on the fracture mechanism and bond strength of aluminum/copper bimetal plate. *Materials Transaction*. 2006, Vol. 47, pp.1232-1239.
- 8 Volokitina I., Volokitin A., Naizabekov A., et al. Microstructure of bimetallic wire in the “ECAP-drawing» process. *Journal of Chemical Technology and Metallurgy*. 2021, Vol. 56, No. 4, pp.857-866.
- 9 Lezhnev S., Panin E., Volokitina I. Research of combined process rolling-pressing influence on the microstructure and mechanical properties of aluminium. *Advanced Materials Research*. 2013, Vol.814, pp. 68-75.
- 10 Valiev R.Z., Estrin Y., Horita Z., et al. Producing bulk ultrafine-grained materials by severe plastic deformation: ten years later. *JOM*. 2016, Vol. 68, pp.1216-1226.
- 11 Furukawa M., Horita Z., Langdon T.G. Application of equal-channel angular pressing to aluminum and copper single crystals. *Materials Science Forum*. 2007, Vols. 539-543, pp. 2853-2858.
- 12 Surzhikov A.P., Lysenko E.N., Malyshev A.V., et al. Phase transformations in ferrites during radiation-thermal sintering. *Eurasian Physical Technical Journal*. 2020, Vol. 17, No.1, pp. 26-34.
- 13 Haddad M., Ivanisenko Y., Fecht H.J. Behavior of C45 steel Subjected to Different High Pressure Torsion (HPT) Procedures. *International Journal of Applied Science and Technology*. 2015, Vol. 5, No. 1, pp. 144-153.
- 14 Naseri R., et al. An experimental investigation of casing effect on mechanical properties of billet in ECAP process. *International Journal of Advanced Manufacturing Technology*. 2017, Vol. 90, pp. 3203–3216.
- 15 Polyakov A.V., Semenova I.P., Raab G.I. Peculiarities of ultrafine-grained structure formation in Ti Grade-4 using ECAP-Conform. *Advanced Materials Science*. 2012, Vol.31, pp. 78-84.
- 16 Xiao W., Wang B., Wu Y., Yang X. Constitutive modeling of flow behavior and microstructure evolution of AA7075 in hot tensile deformation. *Materials Science and Engineering A*. 2018, Vol. 712, pp.704-713.
- 17 Kasenov B.K., Kasenova Sh.B., Sagintaeva Zh.I., et al. Synthesis and X-ray investigation of novel nanostructured copper-zinc manganites of lanthanum and alkali metals. *Eurasian Physical Technical Journal*. 2021, Vol. 18, No.1, pp.29-33.
- 18 Chung K., Ahn K., Yoo D.-H., et al. Formability of TWIP (twinning induced plasticity) automotive sheets. *International Journal of Plasticity*. 2011, Vol. 27, No. 1, pp. 52-81.
- 19 Alizadeh M., Samiei M. Fabrication of nanostructured Al/Cu/Mn metallic multilayer composites by accumulative roll bonding process and investigation of their mechanical properties. *Materials & Design*. 2014, Vol. 56, pp. 680–684.
- 20 Volokitina I.E., Volokitin A.V. Evolution of the Microstructure and Mechanical Properties of Copper during the Pressing–Drawing Process. *Physics of Metals and Metallography*. 2018, Vol. 119, pp. 917-921.
- 21 Lezhnev S.N., Naizabekov A.B., Volokitin A.V., Volokitina I.E. New combined process pressing-drawing and impact on properties of deformable aluminum wire. *Procedia Engineering*. 2014, Vol. 81, pp. 1505–1510.
- 22 Naizabekov A., Volokitina I., Volokitin A., Panin E. Structure and mechanical properties of steel in the process "pressing-drawing. *Journal of Materials Engineering and Performance*. 2019, Vol. 28, No. 1, pp. 1762-1771.
- 23 Volokitina I., Volokitin A., Naizabekov A., Panin E. FEM-study of bimetallic wire de-formation during combined ECAP-drawing. *Journal of Chemical Technology and Metallurgy*. 2021, Vol.56, No. 2, pp.410-416.
- 24 Volokitina I., Volokitin A., Naizabekov A., Lezhnev S., Panin Ye. Deformation of bimetallic wire during combined ECAP-Drawing. *Proceeding of the 29th Intern. Conf. on Metallurgy and Materials*, Brno, 2020, pp. 183-189.
- 25 Valiev R. Nanostructuring of metals by severe plastic deformation for advanced properties. *Nature Materials*. 2004, Vol.3, pp.511–516.

## TRIBOLOGICAL CONTACT IN MATERIALS SYSTEMS "CuCrNiZrTi - M500", "CuCrNiZrTi - 5140H", "CuCrNiZrTi - 3310H"

Kubich V.I.<sup>1</sup>, Cherneta O.G.<sup>2</sup>, Yurov V.M.<sup>3</sup>, Baltabekov A.<sup>4</sup>, Guchenko S.<sup>4</sup>

<sup>1</sup>National University "Zaporizhzhya polytechnic", Zaporizhia, Ukraine, [schmirung@gmail.com](mailto:schmirung@gmail.com)

<sup>2</sup>Dniprovsk State Technical University, Kamenskoye, Ukraine, [ocherneta@gmail.com](mailto:ocherneta@gmail.com)

<sup>3</sup>Karaganda Technical University, Karaganda, Kazakhstan, [1\\_neg@mail.ru](mailto:1_neg@mail.ru)

<sup>4</sup>E.A. Buketov Karaganda University, Karaganda, Kazakhstan, [exciton@list.ru](mailto:exciton@list.ru)

*The limited information on the manifestation of the parameters of the molecular component of friction - the shear strength of the adhesive bond  $\tau_0$  and the piezoelectric coefficient  $\beta$  of the molecular component for each specific study predetermines the use of purposeful determination of parameters by modeling shear on small-sized samples in order to increase the objectivity and accuracy of the result assessment. The article poses the task of conducting definitive tribotechnical tests of the high-entropy alloy to assess its adaptability to loading and lubrication conditions during contact with steel, cast iron and to establish the nature of the manifestation of the parameters of adhesion properties by modeling shear on small samples. It was found that under conditions of drop lubrication, the surfaces of the samples of the studied materials appear to be compatible and are satisfactorily run-in. In this case, the parameters of high-speed and force loading determine the manifestation of boundary lubrication. The time reaching the steady-state friction mode is practically the same for all systems, and is observed after 7.5 minutes. The obtained graphic patterns and parameters of their mathematical approximation made it possible to determine the nature of the change in the adhesive properties of a high-entropy alloy with a change in shear rates.*

**Keywords:** system of materials, coefficient of friction, piezo coefficient, shear, tangential strength, lubrication formation

### Introduction

This work is a continuation of work [1], which shows the importance of having numerical values of the parameters of adhesion properties directly for the surfaces of metals of full-scale operational friction units of machines and mechanisms with reversible movement, i.e. in which there is a shear with a certain speed of movement, when the manifestation of the molecular (adhesive) component of the friction force has time to manifest itself. According to the authors of [2], a distinctive feature of high-entropy alloys (HEA) from traditional alloys is that these alloys have a high entropy of mixing, which affects the formation of structures based on solid solutions. A little over 15 years have passed since the discovery of high-entropy alloys.

### 1. Analysis of publications

The first review is made in the form of a complete materials science cycle "production - structure - properties" for a new class of vacuum-plasma coatings - nitrides of multi-element high-entropy metal alloys, information is given in [3]. The analysis of the current state of production of such coatings, their morphology, elemental and phase composition, structure, substructure, stress state and functional properties, depending on the main parameters of the formation: substrate temperature during deposition; the value of the applied bias voltage; substrate, as well as the composition of the gas atmosphere. Then there were many articles on the synthesis and study of various high-entropy alloys [4-10].

The last review of HEA was made in [11]. Analysis of more than 200 obtained high-entropy alloys (HEAs) made it possible to establish the relationship between the electron concentration, phase composition, lattice parameter, and properties of solid solutions based on bcc, fcc lattices. The main conditions for the appearance of high-entropy chemical compounds - the Laves phase,  $\sigma$ - and  $\mu$ -phases, have been identified. For the formation of a 100% high-entropy  $\sigma$ -phase, it is necessary that all the elements that make up high-entropy alloys form the  $\sigma$ -phase in two-component alloys in a different combination, and the electron concentration of the alloy should be in the range of 6.7-7.3 electron/atom.

For the formation of a 100% high-entropy Laves phase, the following conditions are necessary [11]:

- total negative enthalpy of mixing of the alloy at the level of -7 kJ/mol and below;
- the presence of a pair with an atomic difference of more than 12 %;
- in the presence of two elements in the alloy with the enthalpy of mixing less than 30 kJ/mol, the average concentration of electrons should be in the range of 6-7 electron/atom.

In [11] it is shown that the ratio of the lattice parameters of a solid-state HEA, determined in the experiment, to the lattice parameter of the most refractory metal of the HEA determines the value of the elastic modulus. The values of the modulus of elasticity predetermine the manifestation of the mechanical properties of the HEA in contact with other structural materials. Revealing the features of the manifestation of the service properties of newly created materials, which include HEAs, is relevant in the development of materials science and tribological aspects of ensuring the reliability of friction pairs of various mechanical engineering objects. As an option, it is proposed to consider the feasibility of using HEAs in the manufacture and repair of parts, for example, such mechanical engineering objects as cars, tractors and others.

The purpose of this work is to conduct definitive tribotechnical tests of the high-entropy CuCrNiZrTi alloy to assess its adaptability to loading and lubrication modes during contact interaction with steel, cast iron and the manifestation of the parameters of adhesion properties by modeling shear on small samples.

## 2. Research methodology

To prepare the CuCrNiZrTi target, micropowders of the corresponding metals were taken and mixed in equiatomic proportions. Then the prepared powder mixture was placed in a grinding jar of a planetary ball mill made of tungsten carbide, and grinding bodies were added. Grinding bodies are balls with a diameter of 5-10 mm, also made of tungsten carbide, the mass of which was equal to 10 masses of the powder mixture.

Then the grinding bowl was filled with a gasoline galosh, the lid was tightly closed, and the planetary ball mill was turned on (rotation speed  $500 \text{ min}^{-1}$ , operating time 5 hours). The resulting homogenized composition was dried under vacuum and pressed to form the composition into a flat disc 100 mm in diameter and 5 mm thick. Then the disk was placed in a vacuum thermal furnace and baked in it for 3 hours. Next, the fabricated target of CuCrNiZrTi (Fig. 1a) was used to deposit a magnetron coating on an NNV-6.6I1 setup. The coating was carried out on prepared substrates of AISI-201 steel (hexagons with a side length of 22 mm and a thickness of 5 mm). The vacuum chamber was evacuated to a pressure of 0.003 Pa, then a hot cathode plasma source (PSWHC) was turned on, argon was injected to a pressure of 1 Pa, a negative bias potential of 1000 V was applied to the substrate, and the substrate surface was cleaned and heated for 10 minutes. After that, the argon pressure was lowered to 0.1 Pa and the magnetron was turned on. The bias potential on the substrate was reduced to 150 V, the magnetron current was kept constant at a level of 3 A. The substrate was placed in the chamber at a distance of 15 cm, and the deposition time was 1 hour.

The phase composition and structural parameters of the samples were studied on an XRD-6000 diffractometer using  $\text{CuK}_\alpha$  radiation (Fig. 1b). Phase composition of CuCrNiZrTi coating (table 1). Let's discuss this composition.

The first is  $\text{Cu}_{1.5}\text{ZrNi}_{3.5}$  with a phase content of 10 at. % and with a lattice constant  $a = 6.7671 \text{ \AA}$ . According to [12, 13],  $\text{Cu}_{1.5}\text{ZrNi}_{3.5}$  has the B2 structure, a high-temperature austenite phase ordered according to the CsCl type (Pm3m-fcc).

In second place is Cu with a phase content of 7.8 at. % and lattice constant  $a = 3.6178 \text{ \AA}$ . Unit cell of fcc copper.

In third place is  $\text{Zr}_{0.02}\text{Ni}_{0.98}$  with a phase content of 19.8 at. % and lattice constant  $a = 3.3406 \text{ \AA}$ . According to X-ray spectral analysis, the main component of the eutectic is a combination of nickel and zirconium. The eutectic component is identified as a ZrNi intermetallic compound with an fcc lattice corresponding to the space group F43m (sphalerite type).

The fourth place is occupied by  $\text{TiCr}_2$  with a phase content of 29.5 at. % and lattice constant  $a = 4.9076 \text{ \AA}$  and  $c = 15.9700 \text{ \AA}$ . Intermediate phases with a Laves structure are formed near the  $\text{TiCr}_2$  composition [14].

In fifth place is NiTi with a phase content of 33 at. % and the lattice constant  $a = 2.8007 \text{ \AA}$ ,  $b = 4.6192 \text{ \AA}$ ,  $c = 4.1824 \text{ \AA}$ ,  $\beta = 97.5793$ . According to [15], the results of neutron diffraction studies of quenched alloys in the initial austenitic and martensitic states show that the  $\text{Ti}_{49.5}\text{Ni}_{50.5}$  alloy is in the austenitic state at room temperature.



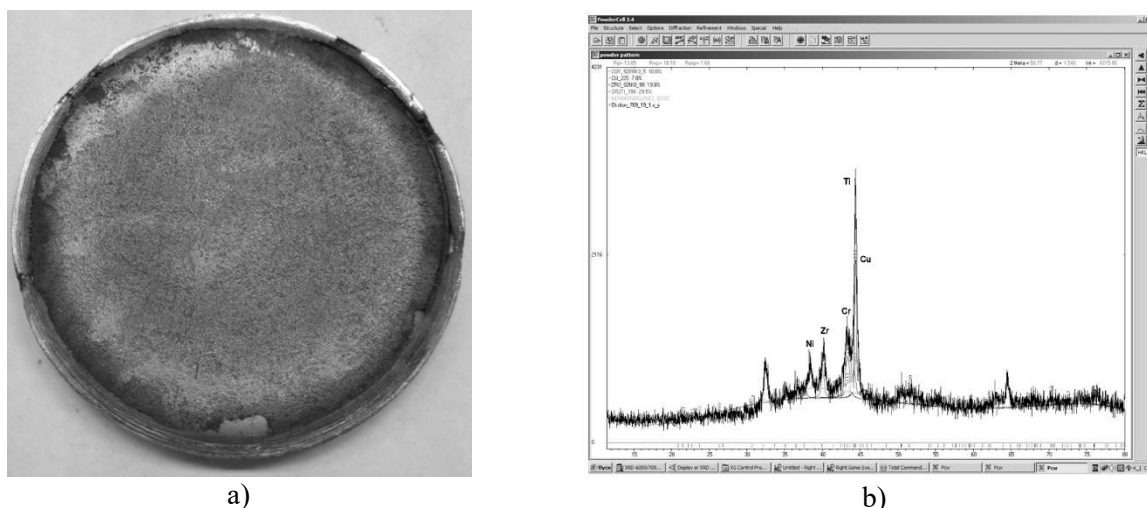


Fig. 1 Target CuCrNiZrTi for magnetron (a), phase composition of CuCrNiZrTi coating (b)

Table 1. The phase composition of the coating

Sample	Detected phases	The content of phases, at. %	Lattice parameters, Å
CuCrNiZrTi	Cu <sub>1,5</sub> ZrNi <sub>3,5</sub>	10	a = 6,7671
	Cu	7.8	a = 3,6178
	Zr <sub>0,02</sub> Ni <sub>0,98</sub>	19.8	a = 3,5406
	TiCr <sub>2</sub>	29.5	a = 4,9076 c = 15,9700
	NiTi	33	a = 2.8007 b=4.6192 c = 4.1824 β=97.5793
	Possible phase presence ZrNi, Cu <sub>3</sub> Ti <sub>2</sub>		

Its crystal lattice parameter B2 (a) and the degree of long-range atomic order ( $\eta$ ) turned out to be equal to  $a = 0.30125$  nm;  $\eta = 1.00 \pm 0.05$ . On the contrary, the Ti<sub>50,5</sub>Ni<sub>49,5</sub> alloy at room temperature is in the martensitic state B19', which unambiguously follows from the interpretation of the neutron diffraction pattern and makes it possible to determine its parameters:  $a = 0.2903$  nm,  $b = 0.4112$  nm,  $c = 0.4636$  nm,  $\beta = 97.25$ . The NiTi we observed turned out to be martensite with the B19' structure. Thus, of the five phases of the CuCrNiZrTi coating, three have an fcc structure, TiCr<sub>2</sub> gives the Laves phase, and NiTi gives martensite with the B19' structure.

Electron microscopy was performed on a TESCAN MIRA 3 scanning electron microscope. Figure 2 shows the XPS of the coatings and Table 2 shows the chemical composition.

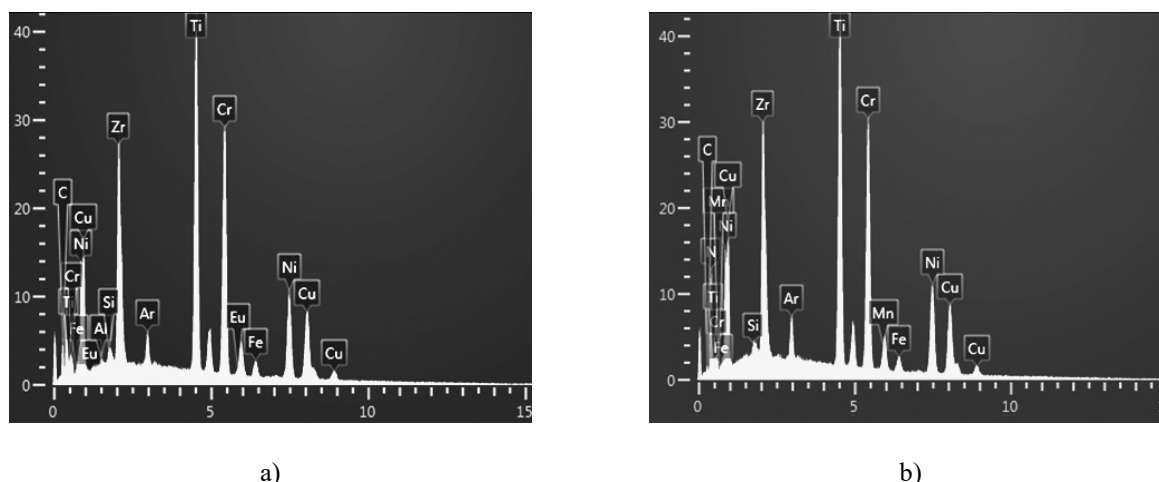
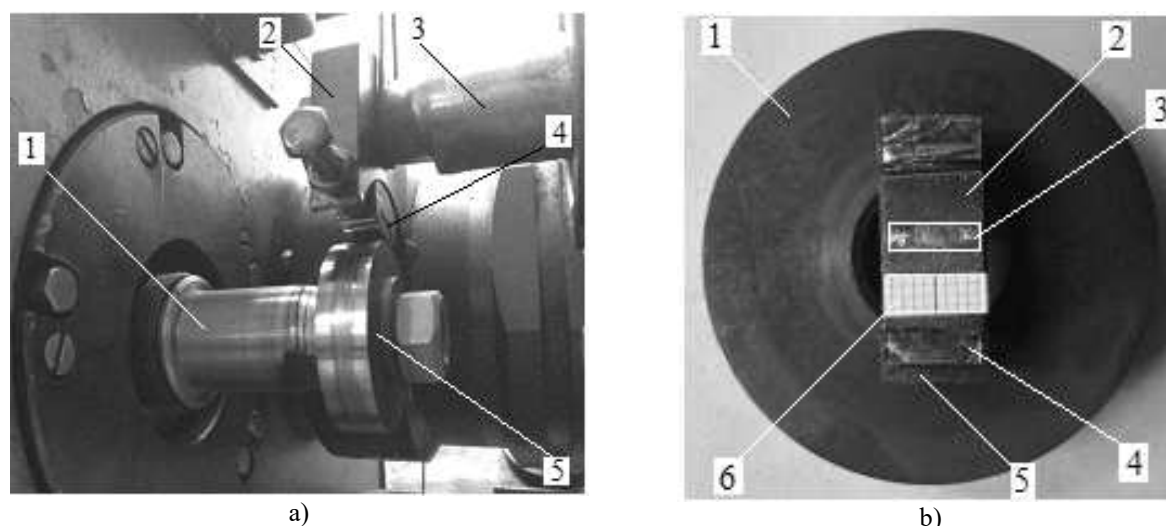


Fig. 2. XPS of CuCrNiZrTi in argon at 2 points (no difference)

**Table 2.** Quantitative chemical composition of CuCrNiZrTi, %

Element	Zr	Ti	Cr	Ni	Cu
Nominal	20	20	20	20	20
in argon	23.2	21.2	19.9	17.1	6.8
in nitrogen	22.8	20.8	19.7	16.9	7.0

Tribotechnical tests were carried out on a friction machine SMTs-2 in two stages on small-sized samples according to the friction pattern "movable disk - fixed block", Figure 3. At the first stage, the surfaces were run-in at a rotational speed of the movable disk  $n = 300 \text{ min}^{-1}$ , a stepwise loading of the contact with a normal force of 22 N, 45 N, 90 N, 140 N, 180 N, 230 N and holding at each of the loads for 3 min. The oil was fed into the friction zone by a drop method. In this case, both the micro-profile of the contact zones of the surfaces of the materials and the lubricating formations screening them were formed. At the second stage, the assessment of the manifestation of the properties of lubricating formations was carried out without oil supply. The rotational speed of the movable disk was  $n = 300 \text{ min}^{-1}$ . The stepwise loading of the contact was carried out with a normal force of 22 N, 45 N, 90 N, 140 N, 180 N, 230 N, 275 N, 320 N and holding at each of the loads for 2 min. At the same time, abundant grease was preliminarily removed from the surfaces of both samples. Thus, conditions were created for modeling the operation of the contact zones of the surfaces of materials through the formed lubricating formations. With a clear increase in resistance to movement, recorded by the recorder, the test was suspended. In case of manifestation of pathological wear accompanied by noise effects, oil was supplied to the friction zone, and the surfaces were again run-in to steady friction.

**Fig. 3.** Methodological support of tribotechnical tests: a - model interface "movable disk - fixed block":

1 - lower shaft; 2 - upper shaft holder; 3 - upper shaft; 4 - sample - block; 5 - sample - disk;  
 b - samples: 1 - disk; 2 - block; 3 - wear mark; 4 - sealant; 5 - shoe holder; 6 - measuring ruler

Transmission oil TAD-17I 85W90 with dynamic viscosity  $\mu = 0.106 \text{ Pa}\cdot\text{s}$  at  $50 \text{ }^\circ\text{C}$  was used as a lubricant. Samples - disks  $d = 50 \text{ mm}$ ,  $b = 12 \text{ mm}$  were made of the following materials:

- steel 5140H, 229 HV;
- steel 3310H, 116 HV;
- cast iron M500, 200 HV.

Samples - pads  $9 \times 15 \times 3$  were made of high-entropy alloy CuCrNiZrTi (890 HV). The assessment of the wear of the pads was carried out according to the energy intensity of wear  $I_m(\text{mg}\cdot\text{J}^{-1})$ , taking into account the determination of the work of friction forces at each stage of tribotechnical tests in accordance with the procedure described in [17]. In this case, the values of the wear of the pads by weight and the values of the coefficient of friction at each of the test stages were used. Taking into account the fact that the weight loss of the block samples was determined at the end of the second stage, the energy intensity of wear was presented as a generalized average.

The parameters of the adhesive bond were evaluated on a friction machine SMTs-2 with additional equipment in accordance with the procedure described in [1]. To estimate the pressure in the contact zone and the tangential shear strength, we used the average values of the contour areas, which were determined from the indentations. The values of the areas for tribosystems of materials at the end of the second stage of testing were: "CuCrNiZrTi - 5140H"  $S_1 = 9.5 \pm 0.5 \text{ mm}^2$ ; "CuCrNiZrTi - 3310H"  $S_2 = 7.5 \pm 0.5 \text{ mm}^2$ ; "CuCrNiZrTi - M500"  $S_3 = 12.5 \pm 0.5 \text{ mm}^2$ . To assess the parameters of adhesion without lubricant, the surfaces were thoroughly degreased with gasoline "Kalosha".

### 3. Research results and their discussion

The results of tribotechnical tests of the investigated high-entropy alloy and the manifestation of the properties of lubricating formations are presented in the form of the constructed regularities of the change in the friction coefficient from the normal force in the contact zone, Fig. 4. During the tests, the system of materials "5140H - CuCrNiZrTi" worked stably at both stages. The system of materials "3310H - CuCrNiZrTi" did not work at the second stage, for 15 seconds there was a breakdown of the frictional contact with a jump in the friction coefficient from 0.8 to 2.13. After that, the system was run-in again with a load of 22 N and 45 N. At the same time, for 2 minutes at each of the loads, the system showed a stable coefficient of friction of 0.35. At the second stage, the system of materials, the M500 - CuCrNiZrTi system, worked for 8.5 minutes. During this time, a decrease in the friction coefficient from 0.48 to 0.14 was observed. However, at a load of 180 N for 45 seconds, a jump in the friction coefficient to 0.24 appeared, followed by an increase within 3 seconds to 0.64. After that, the system was run-in again with a load of 45 N and 90 N. At the same time, for 2 minutes at each of the loads, the system showed a stable coefficient of friction of 0.16 and 0.12, i.e. there was a decline.

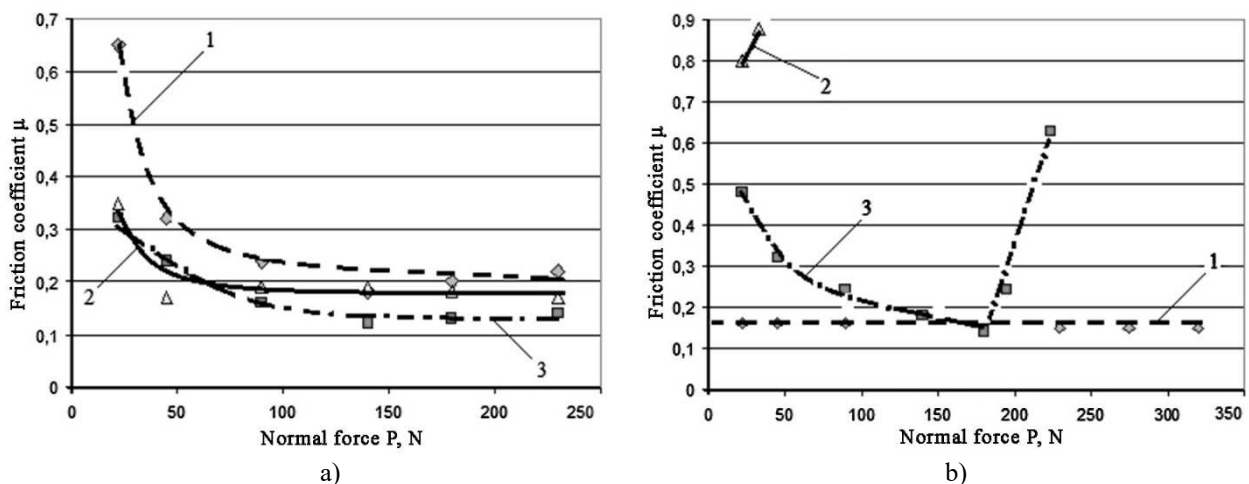


**Fig. 4.** Dependence of the dynamic coefficient of friction on the normal force:

a - 1st stage, running-in; b - 2nd stage, friction on residual lubricating formations;

1 - "CuCrNiZrTi - 5140H" system; 2 - system "CuCrNiZrTi - 3310H"; 3 - "CuCrNiZrTi - M500" system

The analysis of the obtained graphical dependencies in general indicates the following. Under conditions of drop lubrication, the surfaces of the samples of the studied materials appear to be compatible and are satisfactorily running in. In this case, the parameters of high-speed and force loading determine the manifestation of boundary lubrication. The time reaching the steady-state friction mode is practically the same for all systems, and is observed after 7.5 minutes. In this case, the systems of materials were equally stable in the range of normal loading forces from 140 to 230 N:

- the smallest coefficient of friction  $\mu = 0.13$  was observed in the system of materials "CuCrNiZrTi - M500";
- the highest coefficient of friction  $\mu = 0.22$  - in the system of materials "CuCrNiZrTi - 5140H";
- an intermediate place was taken by the system of materials "CuCrNiZrTi - 3310H" with a coefficient of friction  $\mu = 0.17$ .

It is possible to explain such a tribological state based on the stiffness of the contact between the surfaces, due to the correlation of the hardness of the interacting materials and the presence of free carbon in cast iron.

Free carbon causes a decrease in the shear resistance between the tops of the micro-profile irregularities, thereby intensifying the effect of increasing the lubricating effect of the transmission oil molecules. Carbon in carbides of steels 5140H and 3310H does not exhibit such an effect. However, with a relative equality of the hardness of steels 5140H and M500, the hardness of steel 12X2H4 is two times less. In this regard, the possibility of the formation of stable bonds of oil molecules on a less hard surface is greater, which was indirectly manifested in the system of materials "5140H - CuCrNiZrTi". However, this system turned out to be more susceptible to deformation of the surface layer of steel 3310H when it was loaded with a harder surface of the CuCrNiZrTi alloy in the absence of abundant lubrication, which manifested itself at the second stage of testing. As a result of processing tribograms and evaluating the weight loss of the samples-pads, the values of the energy intensity of wear  $I_m$  were calculated, the data are given in Table 3.

**Table 3.** Parameters for assessing the energy intensity of wear

Roller material	Friction force work $A_{tr}$ , J	Mass pad wear $\Delta m$ , mg	Wear rate $I_m \cdot 10^{-8}$ , $mg \cdot J^{-1}$
5140H	41184.4	0.0016	7.7
M500	23380.4	0.0025	21.3
3310H	21343.2	0.0033	30.9

Analysis of the data in Table 3 indicates the following. First, the smallest wear value per unit of friction force work is characteristic of the frictional interaction with steel 40X. Moreover, in accordance with the data in Figure 2, wear accumulated mostly evenly throughout both stages of testing, for which steady-state friction was characterized by dynamic coefficients of friction of 0.22 and 0.16. Secondly, significantly higher values of the wear rate were observed when interacting with M500 cast iron - by a factor of 2.8, and with steel 3310H - by a factor of 4, respectively. Moreover, as can be seen from Figure 4, a large proportion of the total wear was formed for M500 at the second stage of testing, since at the first stage the friction coefficient was the smallest and amounted to 0.13. Almost all of the wear at the first stage was formed by interaction with steel 3310H, the steady-state dynamic coefficient of friction was 0.17. From it follows that the mechanical wear of the CuCrNiZrTi material under boundary friction conditions was influenced by:

- microrelief of surfaces on the actual area of frictional contact, formed by both phase components 3310H, M500 and 3310H and CuCrNiZrTi with a characteristic distribution of their microhardness, which was formed by the process of destruction of cohesive and adhesive bonds between them under the action of normal and tangential loading forces of microvolumes of materials;

- layer thickness and properties of lubricants formed under the action of the forces of adhesive interaction of TAD-17I oil molecules with active metal centers. Moreover, the ratio of such centers based on the chemical composition of the materials of the tested systems is ambiguous. Large heterogeneity is characteristic of the "3310H - CuCrNiZrTi" system. For this system, such an inhomogeneity, together with a lower surface hardness, did not at all ensure the stability of the bonds without supplying components to the friction zone, and predetermined their greater destruction than restoration with abundant lubrication of the contact zone. Based on the results of modeling the shear of surfaces, a graphical approximation of the averaged data of changes in the tangential strength of their frictional bond in a limited area with multiple distributed contact of microroughnesses in the form of linear dependencies was performed, fig. 5-7. The surface microrelief was previously formed by contact interaction during friction at the second stage of tribotechnical tests. At the same time, according to the parameters of the trend lines in the Excel program, their equations and the reliability of the approximation  $R^2$  were determined, the results are shown in table 4, 5.

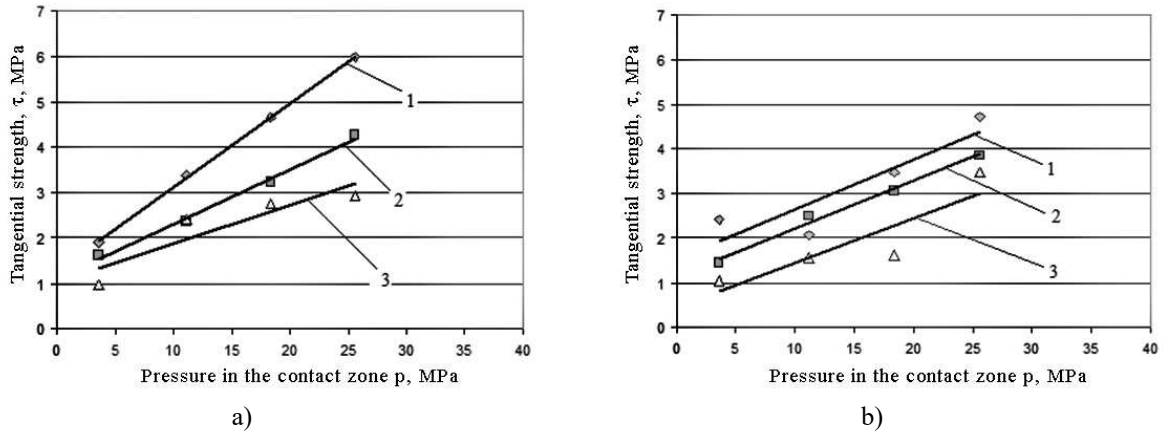


**Fig. 5.** Tangential strength of adhesive bond in contact of materials "CuCrNiZrTi - M500":  
 a - in the environment of TAD-17I transmission oil; b - without lubricant; 1 - mm/s; 2 - mm/s; 3 - shear rate mm/s.

Analysis of the results obtained indicates the following. The high values of the reliability of the approximation of the experimental data results confirm the correctness of the graphic expression of the described processes and indicate once again the binomial nature of the law of molecular friction in the studied systems of materials. In all systems of materials under study, the parameter  $\tau_0$  occurs at  $p = 0$  MPa, both during lubrication and during dry contact. From which it follows that in the absence of a load in the distributed contact zone, the molecular component of the forces of contact interaction between the elements "surface No. 1 - lubricating formations - surface No. 2" appears.

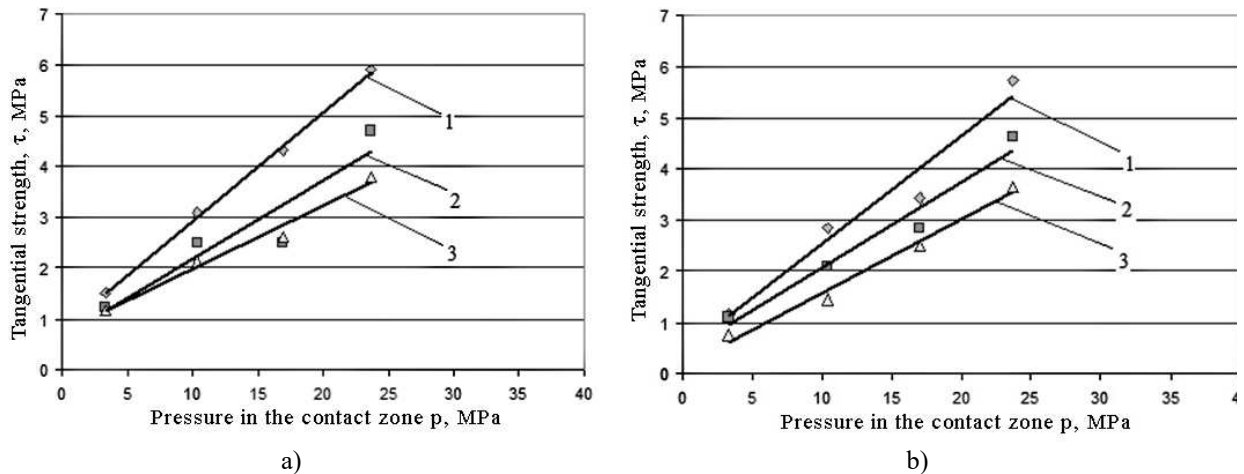


**Fig. 6.** Tangential strength of adhesive bond in contact of materials "CuCrNiZrTi - 3310H":  
 a - in the environment of TAD-17I transmission oil; b - without lubricant; 1 - mm/s; 2 - mm/s; 3 - shear rate mm/s

The largest values of the parameter  $\tau_0$  during lubrication are characteristic for the system of materials "CuCrNiZrTi - 5140H", the smallest values are characteristic for the system "3310H - CuCrNiZrTi", and the system "M500 - CuCrNiZrTi" occupies an intermediate position. At the same time, the  $\beta$  parameter for the system of materials "CuCrNiZrTi - 5140H" when lubricated is the smallest, while for the system "3310H - CuCrNiZrTi" it is the largest.

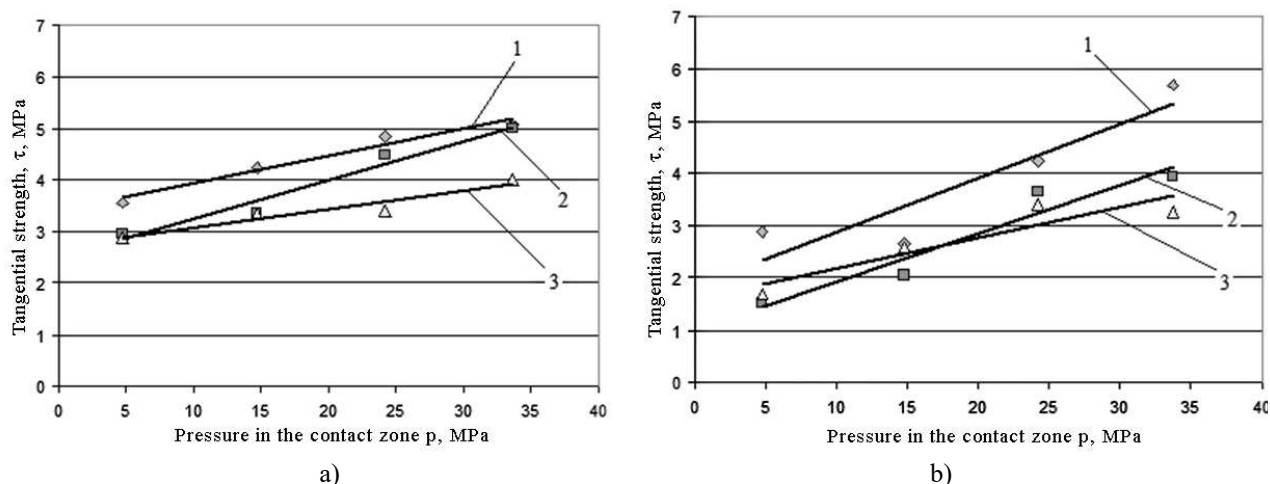


**Fig. 7.** Tangential strength of adhesive bond in contact of materials "CuCrNiZrTi - 5140H":  
a - in the environment of TAD-171 transmission oil; b - without lubricant; 1 - mm/s; 2 - mm/s; 3 - shear rate mm/s

A graphic illustration of the nature of the change in the parameters of the adhesive bond according to the Table. 4, 5 for a more informative presentation is shown in Fig. 6-8. Interpreted in this way, graphical dependencies clearly display the following.

First, there is practical independence:

- parameter  $\beta$  on the shear rate at dry contact, which was observed for the system "CuCrNiZrTi - M500, Fig. 6 a, pos. 2, the value was  $\beta = 0.1 \pm 0.006$ , and when lubricated for the "CuCrNiZrTi - 5140H" system, Fig. 8 a, pos. 1, the value was  $\beta = 0.05 \pm 0.014$ ;

- parameter  $\tau_0$  on the shear rate during lubrication for the "CuCrNiZrTi - 3310H" system, Fig. 7 b item 1, the value of which was  $\tau_0 = 0.72 \pm 0.06$  MPa.

**Table 4.** Parameters of approximation of experimental data for tribological systems of materials in the environment of TAD-171 transmission oil

Parameter	5140H – CuCrNiZrTi			M500 – CuCrNiZrTi			3310H – CuCrNiZrTi		
	$v_1$	$v_2$	$v_3$	$v_1$	$v_2$	$v_3$	$v_1$	$v_2$	$v_3$
Equation type	$\tau = \beta \cdot p + \tau_0$			$\tau = \beta \cdot p + \tau_0$			$\tau = \beta \cdot p + \tau_0$		
Approximation reliability $R^2$	0.96	0.95	0.93	0.99	0.99	0.82	0.99	0.87	0.97
Piezo coefficient $\beta$	0.053	0.075	0.036	0.185	0.12	0.085	0.21	0.15	0.12
Tangential strength $\tau_0$ , MPa	3.39	2.48	2.71	1.26	1.09	1.02	0.79	0.63	0.74

**Table 5.** Parameters of approximation of experimental data for tribological systems of materials in dry contact

Parameter	5140H – CuCrNiZrTi			M500 – CuCrNiZrTi			3310H – CuCrNiZrTi		
	$v_1$	$v_2$	$v_3$	$v_1$	$v_2$	$v_3$	$v_1$	$v_2$	$v_3$
Equation type	$\tau = \beta \cdot p + \tau_0$			$\tau = \beta \cdot p + \tau_0$			$\tau = \beta \cdot p + \tau_0$		
Approximation reliability $R^2$	0.84	0.93	0.84	0.79	0.98	0.78	0.95	0.96	0.98
Piezo coefficient $\beta$	0.1	0.09	0.06	0.11	0.107	0.09	0.21	0.17	0.14
Tangential strength $\tau_0$ , MPa	1.87	1.0	1.6	1.51	1.14	0.45	0.41	0.38	0.13

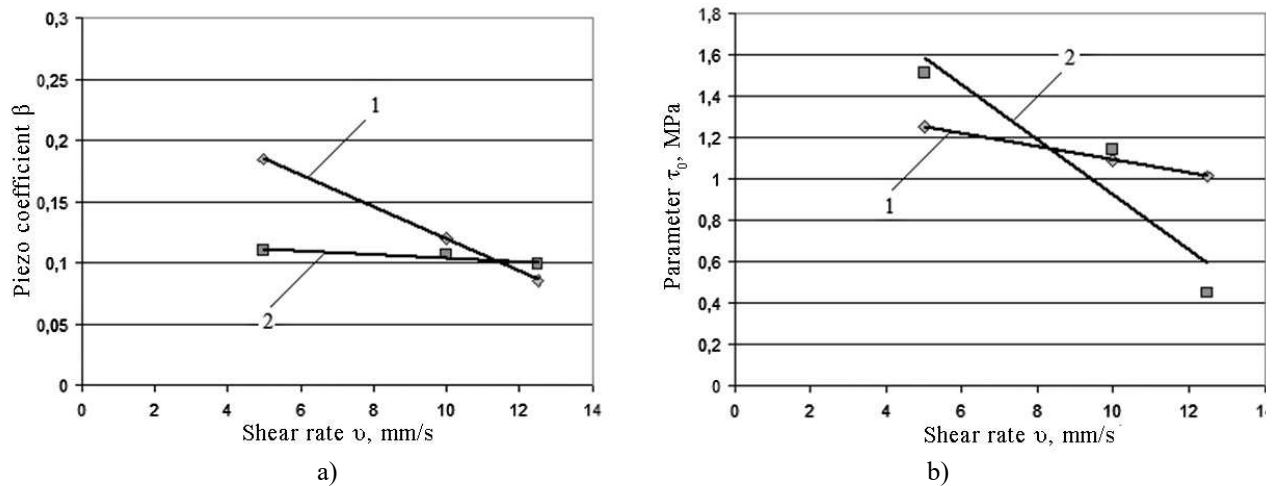


**Fig. 8.** Changing the parameters of the adhesive bond in the contact of materials "CuCrNiZrTi - M500" depending on the shear rate: a - piezoelectric coefficient; b - parameter  $\tau_0$ ; 1 - in the environment of TAD-17I transmission oil; 2 - without lubricant.

Second, there is an explicit dependence of the parameter  $\tau_0$  on the shear rate for the systems of materials "CuCrNiZrTi - 3310H" and "CuCrNiZrTi - 5140H". Moreover, for these systems, lubricant formations formed in the friction zone increase the values of the parameter  $\tau_0$  through lubricant formations by an average of 2 times.

Thirdly, for the system of materials "CuCrNiZrTi - M500" there is a change in the mechanism of manifestation of the adhesive bond, caused by the presence of lubricant formations at a shear rate of 8 mm/s, Fig. 6 b. At  $v \approx 8$  mm/s, the value of the parameter  $\tau_0$  is the same for both dry contact and contact through lubricating formations and is  $\tau_0 = 1.1 \pm 0.05$  MPa. This can be explained by the fact that at  $v \approx 8$  mm/s, the parameter  $\tau_0$  through the lubricating formations is less than at dry contact, due to the action of free carbon additionally released into the thinnest layers of lubricant from the disk surface. Without lubrication, the parameter  $\tau_0$  is larger due to the metal bond and a smaller amount of carbon, which is insufficient to reduce the shear resistance. In this case, the time spent on overcoming the adhesion forces is less than the time for the manifestation of the action of these forces. And lubrication reduces the effect of these forces. At  $v > 8$  mm/s, the lubricating formation saturated with additional carbon continues to maintain adhesion forces due to its molar mass increased by the additional carbon.

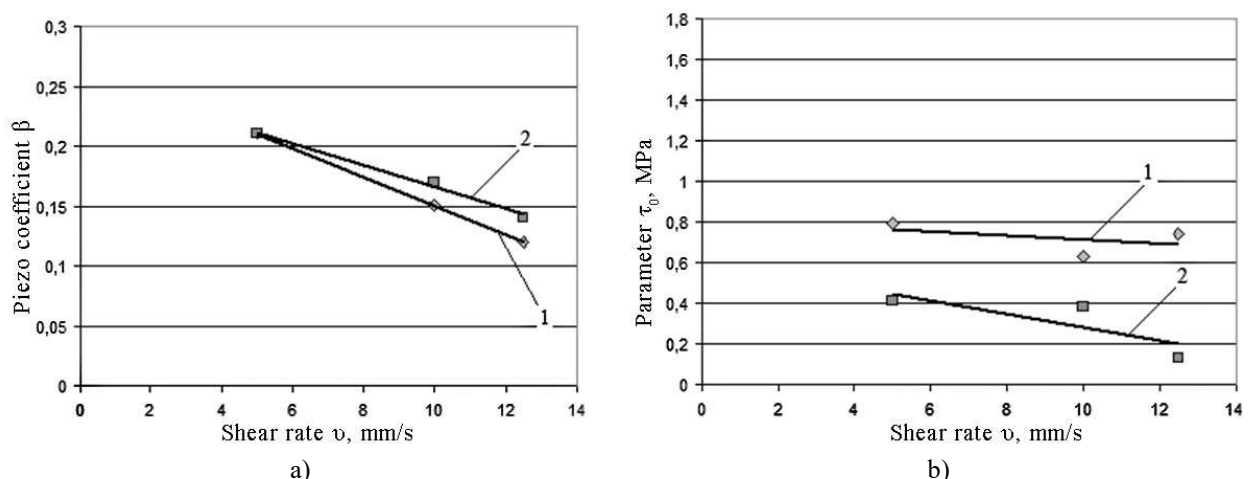


**Fig. 9.** Changing the parameters of the adhesive bond in the contact of materials "CuCrNiZrTi - 3310H" depending on the shear rate: a - piezoelectric coefficient; b - parameter  $\tau_0$ ; 1 - in the environment of TAD-17I transmission oil; 2 - without lubricant.

In this case, the time spent on overcoming the adhesion forces through the lubricant continues to be conditionally insufficient for their destruction, which cannot be said for the time spent for the destruction of the metal bond forces.

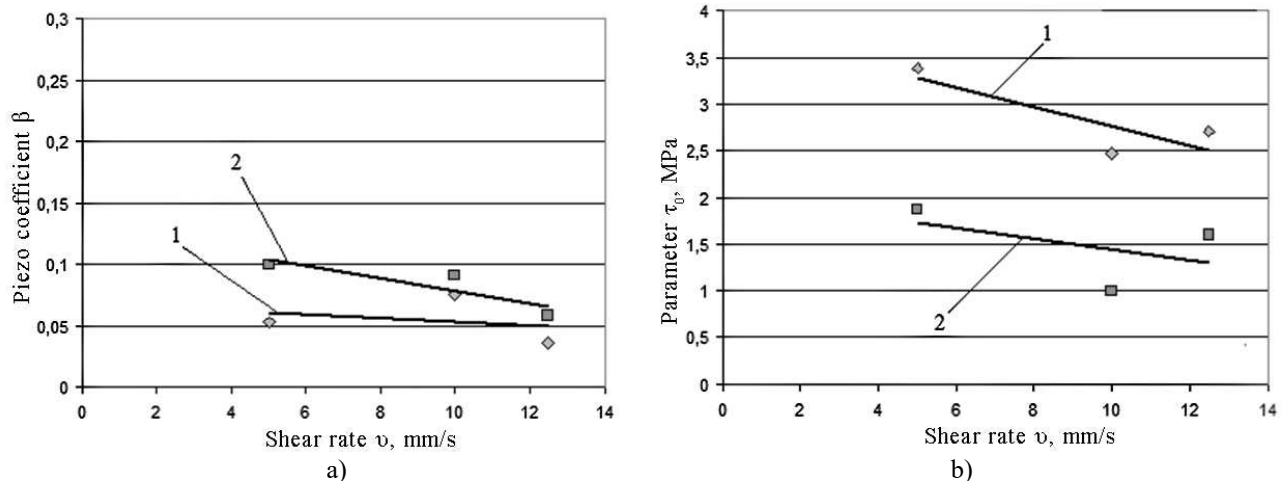


**Fig. 10.** Changing the parameters of the adhesive bond in the contact of materials "CuCrNiZrTi - 5140H" depending on the shear rate: a - piezoelectric coefficient; b - parameter  $\tau_0$ ; 1 - in the environment of TAD-17I transmission oil; 2 - without lubricant.

We have shown above that during lubrication the dynamic coefficient of friction was 0.13; 0.17; 0.22. From which it follows that the displayed antifriction properties of the HEA of the CuCrNiZrTi system are not inferior to the antifriction properties of bronzes, brass, aluminum alloys and antifriction gray cast irons (Table 6).

**Table 6.** Characteristics of antifriction materials

Material	Coefficient of friction on steel
Babbitts	
B83, B16, BK2	0.07-0.12
Bronze	
Br010F1, Br05TS5S5, BrS30	0.1-0.2
Brass	
LTs16K4, LTs38bts2S2	0.15-0.24
Aluminium alloy	0.1-0.15
Anti-friction gray cast irons	
AChS-1, AChS-3	0.12-0.23

Lead bronze BrS30, containing 30 % lead, and aluminum alloys with a soft structure of lead or tin are the most widely used antifriction materials. The antifriction properties of these alloys, especially aluminum alloys, are quite high, since under boundary friction, soft metals are capable of forming a thin anti-seize film that prevents direct contact between the matrix and the steel counter body. Due to the good thermal conductivity, the lubricant layer on these alloys is maintained at high sliding speeds and high pressures. Lead bronzes (like tin ones) are distinguished by high thermal conductivity (four times higher than that of other bronzes), good fatigue resistance, withstand very high specific loads, and are widely used as an antifriction layer for heavily loaded bearings with high specific pressures. As follows from the table 6, antifriction alloys of the Al-Sn system are capable of operating at the highest specific friction power.

The specific resistance of the CuCrNiZrTi alloy is  $\rho = 3.1 \cdot 10^{-8}$  (Ohm•m), and for aluminum Al it is  $\rho = 2.7 \cdot 10^{-8}$  (Ohm•m), that is, our alloy has high thermal conductivity. The microhardness of the CuCrNiZrTi coating (890 HV) is not inferior to high-entropy equiatomic alloys. Tests have shown that the wear resistance of the CuCrNiZrTi coating is  $\sim 3 \cdot 10^{-4}$  g/min, which corresponds to the wear-resistant coatings. At the same time, the calculated energy intensity of wear obtained in this work with an order of  $10^{-8}$  also confirms the high class of wear resistance of the coating under study. Based on the above, high-entropy coatings of the CuCrNiZrTi system turn out to be



antifrictional, which leads to energy savings and, along with a low coefficient of friction (0.13-0.22), can compete with bronzes and aluminum alloys, which are more expensive than our coatings.

## Conclusion

The results obtained in this work revealed the features of the manifestation of friction and wear of the HEA of the CuCrNiZrTi system during contact interaction with structural materials - alloyed steels 5140H, 3310H and cast iron M500, as well as the parameters of adhesion properties when modeling shear on small samples. It was found that under conditions of drop lubrication, the surfaces of the samples of the studied materials appear to be compatible and are satisfactorily run-in. In this case, the parameters of high-speed and force loading determine the manifestation of boundary lubrication. The CuCrNiZrTi system demonstrated the best antifriction properties during lubrication when interacting with steel 3310H, and without lubrication with steel 5140H. At the same time, the lowest wear resistance was observed when working with 5140H steel. The CuCrNiZrTi system showed average properties when working with cast iron M500.

The obtained graphic patterns and the parameters of their mathematical approximation made it possible to determine the nature of the change in the adhesive properties of the CuCrNiZrTi system with a change in shear rates. It was found that the highest values of the parameter  $\tau_0$  during lubrication are characteristic for the system of materials "CuCrNiZrTi - 5140H" and depend on the shear rate, the smallest values of  $\tau_0$  are characteristic for the system "3310H - CuCrNiZrTi", the system "M500 - CuCrNiZrTi" occupies an intermediate position. At the same time, the  $\beta$  parameter for the system of materials "CuCrNiZrTi - 5140H" when lubricated is the smallest, while for the system "3310H - CuCrNiZrTi" it is the largest and depends on the shear rate. It was also found that the  $\beta$  parameter does not depend on the shear rate at dry contact for the "CuCrNiZrTi - M500" system and during lubrication for the "CuCrNiZrTi - 5140H" system.

The character of manifestation of the adhesive properties of the CuCrNiZrTi system in contact with alloyed steels 5140H, 3310H and M500 cast iron with a change in shear rates has been established. At the same time, it was determined that the parameter  $\tau_0$  manifests itself in the entire simulated pressure range regardless of the lubrication conditions and depends on the shear rate, while the  $\beta$  parameter turned out to be independent of the shear rate during dry contact for the system of materials "CuCrNiZrTi - M500" and during lubrication for systems "CuCrNiZrTi - 5140H". New information on the numerical values of the dynamic coefficient of friction and the parameters of the adhesion properties of the HEA of the CuCrNiZrTi system expands the information on alloys of this kind. At the same time, it is recommended to use it in the selection of materials for joint work with it in friction pairs of mechanical engineering objects, as well as in the performance of analytical calculations for the predictive assessment of the effect of the adhesion component of friction on the state of the tribological contact of the surfaces of parts, taking into account their loading conditions and operating conditions.

## REFERENCES

- 1 Kubich V.I., Cherneta O.G., Yurov V.M. Potential difference of metal machine parts methodology for determining the parameters of adhesion properties of materials on the SMC-2 friction machine. *Eurasian Physical Technical Journal*, 2019, Vol.16, No. 2(32), pp. 78-82.
- 2 Yeh J.W., Chen Y.L., Lin S.J. High-entropy alloys – a new era of exploitation. *Materials Science Forum*, 2007, Vol. 560, pp. 1-9.
- 3 Azarenkov N.A., Sobol O.V., Beresnev V.M., et al. Vacuum-plasma coatings based on multi-element nitrides. *Metallofiz. Noveishie Tekhnol.* 2013, Vol. 35, No. 8, pp. 1061-1084.
- 4 Firstov S.A., Gorban V.F., Krapivka N.A., Pechkovsky E.P. A new class of materials - highly entropic alloys and coatings. *Vestnik TSU*, 2013, Vol.18, No. 4, pp. 1938-1940.
- 5 Firstov S.A., Gorban V.F., Andreev A.O., Krapivka N.A. Superhard coatings of highly entropic alloys. *Science and Innovation*, 2013, Vol. 9, No. 5, pp. 32 – 39.
- 6 Pogrebnyak A.D., Bagdasaryan A.A., Yakushchenko I.I., et al. The structure and properties of highly entropic alloys and nitride coatings based on them. *Uspekhi Khimii*, 2014, Vol. 83, No. 11, pp. 1027-1061. [in Russian]
- 7 Maksimchuk I.N., Tkachenko V.G., Vovchok A.S., et al. The decay kinetics and thermal stabilization of the cast alloy system Mg-Al-Ca-Mn-Ti. *Metallofiz. Noveishie Tekhnol.* 2014, Vol. 36, No. 1, pp. 1-15.
- 8 Firstov S.A., Gorban V.F., Krapivka N.A., et al. The relationship between the ratio of the  $\sigma$  phase and the fcc phase with the electron concentration of cast two-phase high-entropy alloys. *Composites and Nanostructures*, 2015, Vol. 7, No. 2, pp. 72-84.

- 
- 9 Shaginyan L.R., Gorban V.F., Krapivka N.A., Firstov S.A., Kopylov I.F. Properties of coatings of the high-entropy Al–Cr–Fe–Co–Ni–Cu–V alloy obtained by magnetron sputtering. *Superhard Materials*, 2016, No.1, pp. 33-44.
- 10 Firstov S.A., Gorban V.F., Krapivka N.A., Danilenko N.I., Kopylov V.I. The effect of plastic deformation on the phase composition and properties of high-entropy alloys. *Міжвузівський збірник "Наукові Notes"*, Lutsk, 2016, No. 54, pp. 326-338. [in Ukrainian]
- 11 Gorban V.F., Krapivka N.A., Firstov S.A. High entropy alloys - electron concentration - phase composition - lattice parameter – properties. *Physics of Metals and Metallurgy*, 2017, Vol. 118, No. 10, pp.1017-1029.
- 12 Firstov G., Koval Y., Timoshevskii A., Yablonovskii S., Van Humbeeck J. Chemical bonding and crystal structure of Zr-based intermetallic high-temperature shape memory alloys. *Chem. Met. Alloys*, 2013, Vol. 6, pp. 205-208.
- 13 Kosorukova T., Firstov G., Koval Y., et al. Structural phase transformations and shape memory effect in ZrCu along with Ni and Hf additions. *MATEC Web of Conferences*, 2015, Vol. 33, pp. 06005.
- 14 Lyakisheva N.P. (editor). *State diagrams of binary metal systems*. Engineering, 1996 – 2000, 832 p.
- 15 Pushin V.G., et al. Baroelastic effects of shape memory in titanium nickelide alloys subjected to plastic deformation under high pressure. *Journal of Technical Physics*, 2012, Vol. 82, No. 8, pp. 67-75.
- 16 Petrov A.A. *Functional properties of titanium nickelide under thermomechanical effects characteristic of active devices*. The dissertation of the candidate of physical and mathematical sciences, St. Petersburg, 2004, 114 p.
- 17 Boguslaev V.O., Greshta V.L., Kubich V.I., et al. The inflow of heat-resistant gorges on the third tribotechnical and physical and mechanical authorities. *Science visitor of the National Guard University*. NTU "DP", 2020, pp. 41 – 47.

## ASSEMBLING A MULTISENSORY DEVICE FOR MONITORING AND ASSESSING CONCRETE CURING CONDITIONS

Utepov Ye.B.<sup>1,2</sup>, Tolkynbayev T.A.<sup>1</sup>, Aniskin A.<sup>3</sup>, Akhazhanov S.B.<sup>4</sup>, Zharassov Sh.Zh.<sup>1,2\*</sup>, Tulebekova A.S.<sup>1,2</sup>, Akishev M.S.<sup>2,5</sup>

<sup>1</sup> L.N. Gumilyov Eurasian National University, Nur-Sultan, Kazakhstan, [\\*zhshzh95@gmail.com](mailto:zhshzh95@gmail.com)

<sup>2</sup> CSI Research & Lab (LLP), Nur-Sultan, Kazakhstan

<sup>3</sup> University North, Varaždin, Croatia

<sup>4</sup> E.A. Buketov Karaganda University, Karaganda, Kazakhstan

<sup>5</sup> BI Group (JSC), Nur-Sultan, Kazakhstan

*The conventional direct and indirect methods to study the mechanical characteristics of concrete are mainly performing discrete measurements, omitting the continuous internal and external phenomena occurring in the concrete body that may significantly affect its strength and quality. This study presents a multisensory device and a method that simultaneously measures and assesses the impact of curing temperature, ambient temperature and relative humidity on the concrete strength. The device was assembled on the basis of Arduino Pro Mini microcontroller connected with various sensors, as well as clock reading and memory modules. The method proposed to assess the impact of different factors on concrete strength is based on strength tests and their confidence curve, monitoring of concrete curing conditions, correlation and weighting techniques. The performance of proposed device and its method was justified experimentally using the concrete cubic specimens of different size. To visualize the specimens monitoring results the color gradations, petal and bar chart representations were used, and taken into account for the future implementation of a software interface for the multisensory device.*

**Keywords:** concrete strength, sensors, continuous phenomena, Arduino, monitoring.

### Introduction

There exist many methods to control the concrete strength both in the laboratory and construction site, depending on the structure and the applied load. A distinction is made between direct and indirect methods. Often construction crews use indirect methods in the initial stages of concrete curing to save on laboratory costs. Direct methods are mostly used during the scheduled curing periods (i.e., 3, 7, and 28 days) of concrete to obtain test reports allowing further loading of the structure [1]. The strength control methods by which structural loading decisions made are based on standards or regulatory documentation on a national, regional or organizational scale. The importance of this documentation is justified by international design standards, because through these documents, one community is in contact with another under predetermined regulations. There are different categories of this documentation: standards, codes, specifications, and other national regulations. Abroad, in such countries as the United States, Great Britain, Germany, Australia, and Japan, there are entire communities to control and improvement of regulations in this direction [2]. It is worth noting that independent institutions also make adjustments in the application of standards; their number is not great, but cooperation is at a high level.

All standards take into account the influence of various external and internal factors on the concrete strength gain. [3] identified about 20 influencing factors. It is not easy to judge the degree of influence of one or another factor at the time of concrete strength gain as it is a complex process, but summarizing it is possible to classify them into 3 groups: 1) Factors affecting the strength before concrete batching; 2) Factors affecting the strength at the time of batching the concrete; 3) Factors affecting the strength after concrete batching. The predominance of one of the groups in case of non-

compliance with the technology of production of concrete is revealed only at the stage of its strength gain, which is fraught with financial and time losses [2].

Most of the errors that reduce the design strength of the structure is associated with the 3<sup>rd</sup> group of factors, in the period of care of the concrete. This is justified by the fact that factors 1 and 2 are formed in the laboratory or factory conditions, where the probability of making an error in the technology of concrete batching is negligible, which is not possible to state about the field temperature and humidity conditions. As much depends on the process of paving and care of the concrete. It should be noted that the paving process, depending on the volume can take several hours or even a whole day. While care, regardless of the volume lasts all 28 days without exception. During this time, the concrete is exposed to many internal and external factors and their study provides an opportunity to properly examine their impact on the structure to avoid risks that can lead to dire consequences. Conventional methods [4,5] do not provide a detailed picture on the processes taking place in the concrete body, since they are based on mechanical reactions when being applied. Also, they examine characteristics on certain points or parts of structure, but not a whole, and reveal discrete values. As is known, the most influencing factors for concrete strength are curing temperature, ambient temperature and relative humidity. All three are continuous phenomena [6]. Therefore, to monitor their impact and make timely and preventive decisions, corresponding techniques and equipment should be used. One of promising techniques is application of maturity sensors [7–9] that enable estimation of concrete strength using a predefined maturity-strength relationship. However, these sensors may register mostly only curing temperature; but those for several parameters – disable simultaneous measurements. Therefore, to take into account external factors, these sensors need to be substantially redesigned. Moreover, the Maturity methods [10] that they apply do not consider joint effect of internal and external factors on concrete strength. The literature lacks sensor-based solutions on real-time monitoring of concrete curing conditions taking into account several factors at a time. In addition, the proper method to examine the patterns between the concrete strength and influencing factors are poorly addressed in previous studies [11–15]. These patterns appear to be important to assess the degrees of impact of the factors on concrete strength.

In view of the above, this work is aimed at the development of a multisensory device for monitoring and a method for assessing concrete curing conditions. The device is assembled from sensors for concrete curing temperature, ambient temperature and relative humidity on the basis of Arduino microcontroller. The assessing method is based on strength tests, monitoring of parameters, correlation analysis to recognize patterns of interdependency of parameters with concrete strength [16], calculation of parameter weights, as well as visual representation of the patterns. The calculation of weights is assumed to be a proper technique to demonstrate the degree of influence of the parameters.

## 1. Development of multisensory device

The multisensory device (MSD) development was carried out in steps. The first step was to design the IT-architecture that consisted of microcontroller Arduino Pro Mini (1), four waterproof temperature sensors DS18B20 (2), ambient temperature and relative humidity module DHT11 (3), real time clock module DS3231 (4), micro-SD card module (5) with the card (6), and two Li-ion batteries INR18650-20S 3.7V connected in parallel (7) as shown in Fig. 1.

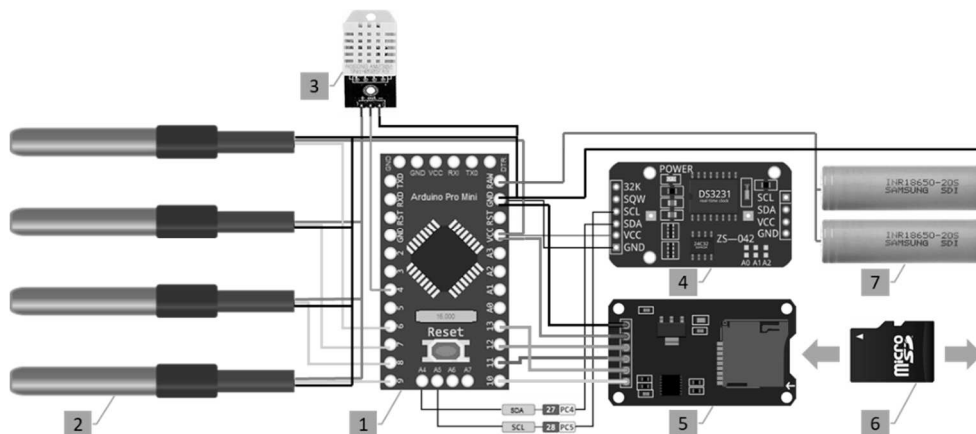


Fig. 1. MSD IT-architecture

The next step was to solder the components together according to the connections indicated in the IT-architecture, for which an electric soldering iron was used. Further steps were to program the microcontroller in “C” language using an open-source Arduino integrated development environment (or Arduino IDE), to conduct test measurements and validate the measurement interval, saving to the SD card, as well as structure and content of the measurement data. Final step was to envelop the electronic components into a safe housing, for which a standard plastic case with dimensions of 15×10×5 cm was chosen (Fig. 2).



Fig. 2. Programming the microcontroller of MSD

It should be noted that the developed MSD has not the same design and functionality as its analogues [7–9,14,15]; it has certain differences that makes it more convenient to use: 1) Reusability (only wired temperature sensors are replaced), since the analogues are mostly embedded fully in the concrete body forever and each time new device should be purchased; 2) Storage of monitoring data in a single SD card that is easy to extract and use in PCs; 3) Central control of sensors via a single microcontroller, which makes synchronic and accurate measurements without the risk of data loss; 4) Longer service life due to energy-efficient components, powerful battery and efficient electronic circuit (analogues are mostly based on energy-intensive IoT concepts). Therefore, this makes MSD a fairly affordable alternative for construction companies of all sizes.

## 2. Materials and methods

The experimental studies were carried out using a commercial concrete with grade of B25 M350 produced by LLP "Temirbeton-1" (Almaty, Kazakhstan). Freshly mixed concrete was used to prepare 15 small cubic specimens with rib size of 10 cm and 2 large cubic specimens with rib size of 50 cm

for the testing procedures. Testing equipment composed of a newly developed MSD with measurement accuracy of  $\pm 0.1^\circ\text{C}$  for temperature and 1% for relative humidity, hydraulic press from NIISTROMPROJECT, LLP (Almaty, Kazakhstan) with accuracy of  $\pm 1\%$  and sclerometer IPS-MG4.03 from CSI Research&Lab, LLP (Nur-Sultan, Kazakhstan) with accuracy of  $\pm 8\%$ .

Compression testing of small cubic specimens was carried out using the hydraulic press in series of 3 cubes on 1, 3, 7, 14 and 28 days of curing according to [4] (Fig. 3a). On the same curing ages, the large specimens were tested for strength on the side surfaces using the sclerometer according to shock pulse method [5], for which the average values from the two specimens were deduced (Fig. 3b). It was the average strength values that were used for further analysis. The curing temperature of large specimens, as well as ambient temperature and relative humidity on their curing conditions were measured each 0.5 hours [17] (Fig. 3c). The strength values at 1, 3, 7, 14, 28 days of curing were obtained in the course of testing of small and large specimens (Table 1) and strength curves were plotted according to them later.

Further the received curves have been superimposed on the single diagram and on their crossings the *confidence curve* (i.e., containing the least of values received by methods of compression and a shock pulse) was detected. In order to accurately determine the values of the confidence curve for both strength gain curves (for compression and for shock pulse), the trend lines were constructed, their equations and approximation reliabilities (coefficients of determination) were extracted. The equations made it possible to calculate the strength values for every 0.5 hours.

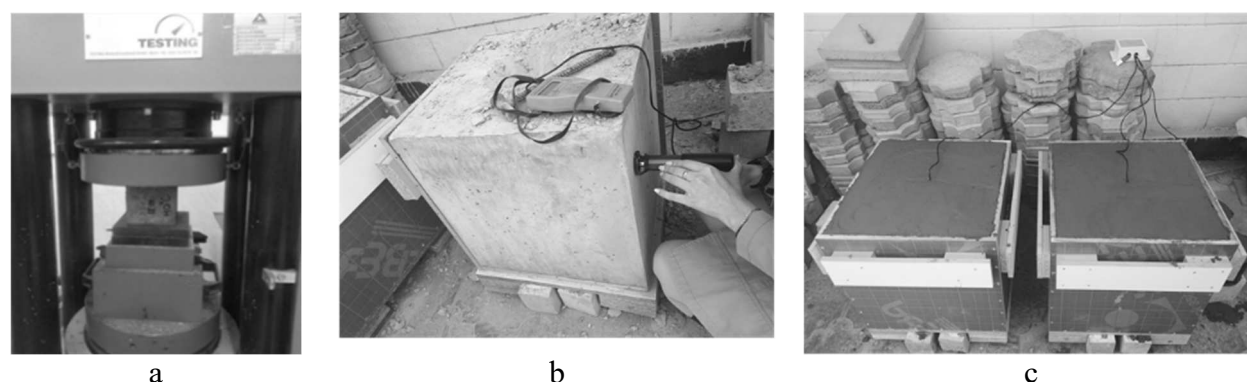


**Fig. 3.** Testing setup: a) compression test; b) shock pulse test; c) temperature and humidity monitoring.

**Table 1** – Strength test results

Age, day	Compressive strength of small cubes (average of 3 per day)	Surface strength of large cubes, MPa		
		No. 1	No. 2	Average in cubes
1	14.2	10.15	10.35	10.25
3	20.45	24.25	21.65	22.95
7	25.25	27.75	28.45	28.1
14	28.75	30.3	29.95	30.13
28	33.2	31.3	31.35	31.33

Confidence curve values were determined for each 0.5 hour by selecting the lowest of the curve values (i.e., from compression and shock pulse tests) with an accuracy of 99.9%. Table 2 below was prepared to better structure the estimated values and monitoring readings for further analysis and assessment of curing conditions of considered B25 M350 concrete.

**Table 2** – Hourly estimates and readings

Age, hour	Curing temperature of large cubes, °C			Relative humidity, %	Ambient temperature, °C	Compressive strength, MPa	Surface strength (average), MPa	Strength values of confidence curve, MPa
	No. 1	No. 2	Average					
0.5	21.44	20.5	20.97	29.7	23.9	0.29583333	0.21354167	0.21354167
1	21.63	20.75	21.19	30.6	23.4	0.59166666	0.42708333	0.42708333
1.5	22	21.19	21.595	33.8	23.3	0.8875	0.640625	0.640625
2	22.5	21.69	22.095	31.3	23.2	1.18333333	0.85416667	0.85416667
2.5	23.13	22.31	22.72	30.9	23.5	1.47916667	1.06770833	1.06770833
etc.*								
24	32.5	32.88	32.69	33.1	22.6	14.198	10.25	10.25
etc.*								
671	8.13	7.44	7.785	43.7	12.9	32.9875642	31.3221343	31.3221343
671.5	8.31	7.69	8	43.1	13.2	32.9917663	31.3234239	31.3234239
672	8.63	7.88	8.255	40.9	13.8	32.9959653	31.3247124	31.3247124

\* Since the table contains 1344 lines of data, majority of them were omitted.

Subsequently, these values were used to determine the daily correlation coefficients [16] (Eq. 1) with the values of the parameters of curing temperature, ambient temperature and relative humidity, as well as to determine the degree of influence (Eq. 2) of these parameters on the concrete strength gain.

$$r_{i,t} = \frac{\sum_{t=\frac{1}{48}}^1 (P_i - \bar{P}_i) \cdot (S - \bar{S})}{\sqrt{\sum_{t=\frac{1}{48}}^1 (P_i - \bar{P}_i)^2 \cdot \sum_{t=\frac{1}{48}}^1 (S - \bar{S})^2}} \tag{1}$$

where:  $i$  – parameter that affects the strength gain of concrete (there are three considered parameters in this study: curing temperature, ambient temperature, and relative humidity);  $t$  – curing time of concrete, which can range from 1/48 to 28 within this study, days;  $P_i$  and  $\bar{P}_i$  –  $i$  parameter and its average value for time  $t$  (day), respectively, in units of one or another parameter;  $S$  and  $\bar{S}$  – strength and its average value for time  $t$  (day) respectively, MPa.

$$\gamma_{i,t} = \frac{|r_{i,t}|}{\sum_{i=1}^3 |r_{i,t}|} \tag{2}$$

Here it should be noted that the sum of the degrees of influence must be equal to one (Eq. 3).

$$\sum_{i=1}^3 \gamma_{i,t} = 1 \tag{3}$$

The obtained values of correlation coefficients and degrees of influence were visualized using color gradations, petal diagram and bar chart, as potential representation of monitoring results that may be further integrated into a software interface of multisensory device. The accuracy of proposed assessment method mainly depends on the equipment used for compressive and shock pulse tests, which were  $\pm 1\%$  and  $\pm 8\%$  respectively in current study, since the uncertainty of MSD and its sensors is negligible. Therefore, the confidence curve is assumed a suitable and less risky approach to reduce potential losses of assessment accuracy.

### 3. Results and Discussion

The strength gain results of the two large specimens obtained with the shock pulse method are shown below in Fig. 4a. It can be seen from the strength gain curves that their difference is insignificant. Nevertheless, the curve of their average values at 1, 3, 7, 14, 28 days was used for further analysis. In Fig. 4b, the cubic marker shows the strength gain curve obtained by the compression testing of small specimens, which was compared with the average curve obtained by the shock pulse method, denoted by the triangular marker. The bold line indicates the confidence curve of the strength values. This curve is made up of the lowest strength values between the compression test and the shock pulse method for each curing age of concrete, to provide some redundancy. It

shows that for the first 2 days and the last 10 days, it coincides with the curve of average values of strength obtained by the shock-pulse method, and from day 2 to day 18 with the curve of strength values obtained by the compression testing of small specimens.

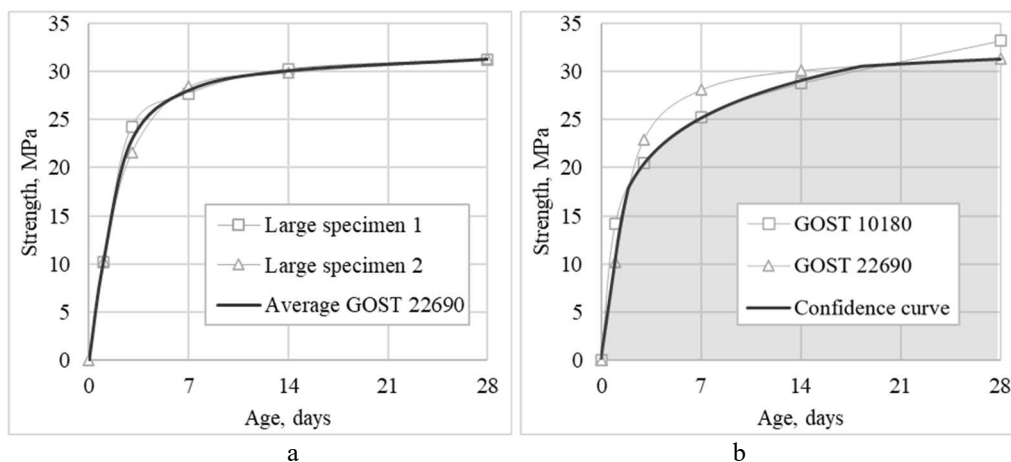


Fig. 4. Strength gain charts: a) shock pulse method; b) comparison and derivation of the confidence curve.

Figs. 5a and 5b show the trend lines, their equations and the coefficients of determination of the strength gain curves of the compression and shock impulse methods, respectively. According to the figures above, the trend lines were constructed in such a way that they converged to their strength gain curves as much as possible. For this purpose, sections were created with intervals of 0-1 and 1-28 days for the compression method curve, and 0-1, 1-3, 3-7, 7-14, and 14-28 days for the shock pulse method curve, respectively. For each of the sections, different equations and coefficients of determination ( $R^2$ ) were derived. According to the values of these coefficients one can assert a high degree of approximation reliability. Thus, almost all  $R^2$  of the obtained linear and logarithmic equations are equal to 1, with the exception of the one in the segment 1-28 days of the compression method curve. Given these coefficients as a percentage, their average value is 99.9%. Using the equations by section, the accurate strength values for every 0.5 hours up to and including 28 days were estimated for both methods.

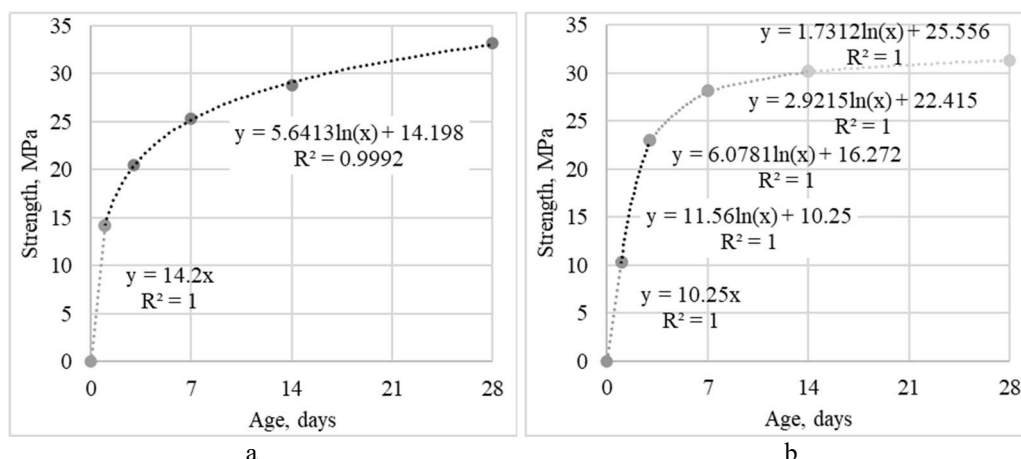
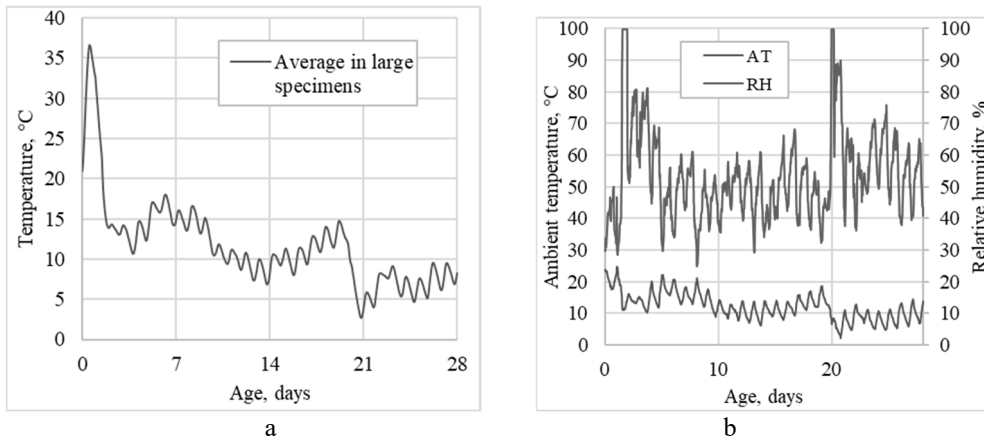


Fig. 5. Trend lines: a) compression method; b) shock pulse method.

Figs. 6a and 6b show the results of monitoring the curing temperature of the large specimens (average of two) and the air temperature and relative humidity in the specimens' storage area with intervals of 0.5 hours over a period of 28 days. Fig. 6a demonstrates a sharp jump in temperature to 36.7 °C on the first and second day of curing due to the beginning of concrete setting, after which a gradual decline with fluctuations during the day and night. Over 28 days, the minimum curing



temperature decreased to 2.65 °C. A similar trend can be observed in the ambient temperature curve (Fig. 6b), indicating its certain influence on the concrete strength gain process, as well as on the exothermic process itself occurring in its body. The air temperature varied between 2.2 and 24.8 °C. As can be seen in Fig. 6b, there is an inverse relationship between relative humidity and ambient temperature: as the temperature increases, the humidity decreases, and vice versa. The humidity varied between 24.9 and 100%, with an average value of 53.2%.



**Fig. 6.** Results of monitoring: a) curing temperature (T); b) ambient temperature (AT) and relative humidity (RH).

The next step, using Eq. 1, the correlation coefficients between the values of the 3 parameters considered and the strength of the confidence curve for each of the 28 days of concrete curing were estimated. The results of these estimates are shown in Fig. 7 as two-color gradations (white-green), with each cell assigned a shade depending on the modulus value of the correlation coefficients for all 3 parameters. In other words, the cells with the lowest values among all 84 (28×3) were tinted close to white, and the cells with the highest values were tinted green.

$ r_T $	0.8	1	0.8	0.9	0.4	0.1	0.9	0.8	0.8	0.9	0.9	0.9	0.9	0.8	0.1	0.9	0.5	0.6	0.6	0.9	1	0.2	0.1	0.9	0.8	0.5	0.9	0.7
$ r_{RH} $	0.2	0.8	0.5	0	0.2	0.3	0.7	0.2	0.9	0.3	0.8	0.4	0.4	0.3	0.6	0.4	0	0.1	0.2	0.7	0.6	0.1	0.4	0.5	0.2	0.1	0.4	0.3
$ r_{AT} $	0.5	0.9	0.5	0.2	0.2	0.5	0.8	0.3	0.7	0.8	0.8	0.6	0.6	0.5	0.6	0.5	0	0.2	0.3	1	0.4	0.2	0.8	0.6	0.4	0.1	0.4	0.4
AVG	0.5	0.9	0.6	0.4	0.2	0.3	0.8	0.4	0.8	0.7	0.8	0.6	0.6	0.5	0.4	0.6	0.2	0.3	0.4	0.9	0.7	0.2	0.4	0.7	0.5	0.2	0.6	0.5
Age, days	1	2	3	4	5	6	7	8	9	10	11	12	13	14	15	16	17	18	19	20	21	22	23	24	25	26	27	28

**Fig. 7.** Color gradation of correlation coefficients.

From the figure above, one can observe a markedly high correlation between curing temperature and concrete strength gain, especially on days 2, 4, 10, and 21, since the correlation coefficients at those days were within the range of  $0.9 \div 1$ . Relative humidity and ambient temperature correlate well with strength on days 2, 9, 11, 20 and 23, with the correlation coefficients laying in the range of  $0.4 \div 0.9$ . The cumulative correlation of the considered parameters with the strength, plotted red as an average between the three parameters for each day, vividly expressed cells on days 2, 7, 9, 11, and 20. This pattern can be further used in expressing the dependence (function) of the strength from the considered parameters, for which it would be logical to make a selection of parameter values exactly on 2, 7, 9, 11 and 20 days as the initial data. The degrees of influence of the considered parameters on the concrete strength gain, calculated according to Eqs. 2 and 3, are represented by a similar color gradation (Fig. 8) on the basis of white and blue.

$\gamma_T$	0.5	0.4	0.4	0.8	0.5	0.1	0.4	0.6	0.3	0.5	0.4	0.5	0.5	0.5	0.1	0.5	0.9	0.6	0.5	0.3	0.5	0.4	0.1	0.5	0.6	0.8	0.5	0.5
$\gamma_{RH}$	0.1	0.3	0.3	0	0.2	0.4	0.3	0.1	0.4	0.2	0.3	0.2	0.2	0.2	0.4	0.2	0	0.2	0.2	0.3	0.3	0.2	0.3	0.2	0.2	0.1	0.2	0.2
$\gamma_{AT}$	0.3	0.3	0.3	0.2	0.3	0.6	0.3	0.3	0.3	0.4	0.3	0.3	0.3	0.3	0.5	0.3	0.1	0.2	0.3	0.4	0.2	0.4	0.6	0.3	0.3	0.1	0.3	0.3
Age, days	1	2	3	4	5	6	7	8	9	10	11	12	13	14	15	16	17	18	19	20	21	22	23	24	25	26	27	28

Fig. 8. Color gradation of the influence degrees of parameters.

The results of the calculation of the degrees of influence for each of the 28 days show a fairly logical pattern. Thus, the figure above shows that the effect of curing temperature on the strength of the concrete noticeably prevails ( $\gamma_{Tmax} = 0.9$ ) in comparison with those of the other two parameters ( $\gamma_{RHmax} = 0.4$ , and  $\gamma_{ATmax} = 0.6$ ). However, at 6, 9, 15, 20, 22 and 23 days, the external temperature and relative humidity influenced more. Referring to Fig. 6a and 6b, it can be understood that it was on these days that the temperature and humidity conditions were quite critical for the concrete in the large specimens.

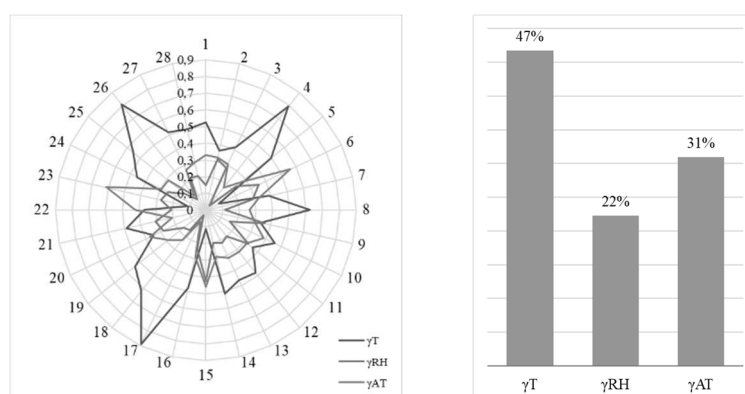


Fig. 9. Spatiotemporal representation of monitoring results as petal diagram (left) and bar chart (right).

An alternative representation of the results of calculating the degrees of influence is presented in Fig. 9a as a three-color petal diagram, where blue, orange, and gray colors correspond to the degrees of influence of curing temperature, relative humidity, and ambient temperature. The percentage ratio of the area of these petals is shown in Fig. 9b. The pattern can be seen that this ratio is equivalent to the ratio obtained by averaging the degrees of influence for all 28 days for each parameter separately. And their sum is always equal to 100%.

## Conclusion

As a result of this work, a reusable multisensory device was developed that allows monitoring of concrete curing temperature, ambient temperature and relative humidity simultaneously, which indicates the advantage of the solution compared to previous works. Moreover, its electronic circuit administered by Arduino Pro Mini microcontroller ensure its longer service life due to energy-efficient components and powerful battery used, as well as a long-term economic benefit.

A method of assessing the influence of the main internal and external factors on the concrete strength gain, based on correlation analysis and weighting of parameters, has been proposed.

The proposed method for determining the concrete strength confidence curve, or in other words, the Least Risk values, may allow engineers and contractors to optimize construction phases, contribute to a reasonable reduction in project delivery time and reduce risks in the loading of concrete structures.

The color gradation and petal diagram offered to demonstrate the correlation and the degree of influence of one or another parameter by means of spatial-temporal visualization have potential to present the current picture of processes taking place in the concrete body quite qualitatively and

promptly and to communicate its nature to concrete engineers. These representation techniques will form the basis of the interface of the software, which is in the plans for future work.

### Acknowledgments

This research was funded by the Science Committee of the Ministry of Education and Science of the Republic of Kazakhstan (Grant № AP08052033).

### REFERENCES

- 1 Gerald B., Neville, P.E. The Strength of Concrete, in *Concrete Manual*. International Code Council. 2015, pp. 24–31. Available at: <https://shop.iccsafe.org/media/wysiwyg/material/9090S15-Sample.pdf>.
- 2 IAE. *Guidebook on non-destructive testing of concrete structures*. Vienna: IAEA. 2002. Available at: <https://www.osti.gov/etdeweb/servlets/purl/20305546>.
- 3 Prasad C. (no date) *20 Factors Affecting Durability of Concrete, Structural Guide*. Available at: <https://www.structuralguide.com/20-factors-affecting-durability-of-concrete/>.
- 4 GOST 10180. *Concretes. Methods for strength determination using reference specimens*. 2012. [in Russian]
- 5 GOST 22690. *Concretes. Determination of strength by mechanical methods of nondestructive testing*. 2015. [in Russian]
- 6 Lorkowski P. *Monitoring Continuous Phenomena*. CRC Press. 2021. doi: 10.1201/9780429440960.
- 7 Lukpanov R., et al. Performance of maturity method for estimation of concrete strength based on cubic specimens. *Technobius*. 2021, 1(4), p. 0008. doi: 10.54355/tbus/1.4.2021.0008.
- 8 Uteпов Y.B. et al. Prototyping an embedded wireless sensor for monitoring reinforced concrete structures. *Computers and Concrete*. 2019, 24(2), pp. 95–102. doi: 10.12989/cac.2019.24.2.095.
- 9 Taheri S. A review on five key sensors for monitoring of concrete structures. *Construction and Building Materials*. 2019, 204, pp. 492–509. doi: 10.1016/j.conbuildmat.2019.01.172.
- 10 ASTM C1074. *Standard Practice for Estimating Concrete Strength by the Maturity Method*. USA, West Conshohocken, PA: American Society for Testing and Materials. 2019.
- 11 Sun B., et al. Prediction of early compressive strength of mortars at different curing temperature and relative humidity by a modified maturity method. *Structural Concrete*. 2021, 22(S1). doi: 10.1002/suco.202000041.
- 12 Soutsos M., et al. Effect of in situ temperature on the early age strength development of concretes with supplementary cementitious materials. *Construction and Building Materials*. 2016, 103, pp. 105–116.
- 13 Barroca N., et al. Wireless sensor networks for temperature and humidity monitoring within concrete structures. *Construction and Building Materials*. 2013, 40, pp. 1156–1166. doi: 10.1016/j.conbuildmat.2012.11.087.
- 14 Giatec S. *The World's Leading Wireless Concrete Sensor for Temperature and Strength Monitoring, Giatec Scientific Inc*. Available at: <https://www.giatecscientific.com/products/concrete-sensors/smartrock-maturity-meter/> (Accessed: 23 March 2022).
- 15 Hilti. *HCS THI Concrete Sensors, Concrete Monitoring Systems*. 2022. Available at: [https://www.hilti.com/c/CLS\\_MEA\\_TOOL\\_INSERT\\_7127/CLS\\_CONCRETE\\_MONITORING\\_SYSTEMS/r13232456](https://www.hilti.com/c/CLS_MEA_TOOL_INSERT_7127/CLS_CONCRETE_MONITORING_SYSTEMS/r13232456) (Accessed: 23 March 2022).
- 16 Novak L., et al. Estimation of coefficient of variation for structural analysis: The correlation interval approach. *Structural Safety*. 2021, 92. doi: 10.1016/j.strusafe.2021.102101.
- 17 Uteпов Y.B., et al. Complex Maturity Method for Estimating the Concrete Strength Based on Curing Temperature, Ambient Temperature and Relative Humidity. *Applied Sciences*. 2021, 11(16), p. 7712. doi: 10.3390/app11167712.

## ELECTROHYDRAULIC METHOD FOR PROCESSING OF THE PHOSPHORUS CONTAINING SLUDGES

Nussupbekov B.R., Sakipova S.E., Edris A., Khassenov A.K., Nussupbekov U.B., Bolatbekova M.

E.A. Buketov Karaganda University, Karaganda, Kazakhstan, bek\_nr1963@mail.ru

*The creation of an effective method for processing toxic waste from phosphorus production, as well as the suppression of the sludge formation process itself, are still relevant. This article discusses a method for processing toxic phosphorus sludge using electro hydraulic impulses. The phosphorus sludge structures before and after treatment with electric discharges are shown. The histograms of the distribution of phosphorus sludge particles by size after processing with electrohydraulic pulses are considered. It's established the content of large droplets is low and on the contrary the high content of droplets of small size in the phosphorus sludge at the electro hydraulic treatment result.*

**Keywords:** phosphorus, sludges, electro-hydraulic processing, structure, pulses number, dispersed composition, toxic waste

### Introduction

The development of an effective method for extracting phosphorus from phosphorus sludges and processing the residues into safe waste is still one of the urgent problems due to their high toxicity. At large phosphorus plants, up to a thousand tons of phosphorus sludge is produced, and large mechanized installations are being built to process it [1-7]. The toxic and flammable properties of phosphorus, the storage of sludge in storage tanks worsen the ecological situation in the surrounding area, and also require free space and large investments. The increasing needs for phosphoric salts and feed phosphates are one of the reasons for the intensive development of the electrothermal method of phosphorus production [1].

The main raw materials for the electrothermal phosphorus production are the phosphorites mined from the deposits of Karatau. Currently, in the city of Zhanatas, the chemical complex of «EuroChem» is operating, where mining complexes have been built including units of medium crushing and dry grinding [2]. The phosphorites of the Karatau basin contain low useful components, approximately 25%, but a high content of impurities. At the same time, the specific weight of the necessary products is about 24.7% [3], and up to 30% of phosphorus was produced in the form of phosphoric sludge [4]. Therefore, the use of a pulsed high-voltage discharge to extract marketable products from sludge is an urgent task for the industry, and the introduction of energy-saving technologies makes it possible to increase production efficiency [6].

Phosphorus plants in Kazakhstan mainly use two methods of sludge processing: stripping of phosphorus with water vapor (distillation method) and direct combustion of sludge in special furnaces to obtain sludge phosphoric acid [7]. The first method is characterized by a low intensity of sludge processing when obtaining low-quality phosphorus, the second - by the low quality of the resulting product. There are also several chemical methods for extracting phosphorus from water sludge. The phosphorus sludge is separated into an aqueous suspension containing suspended particles of phosphorus and contaminants, and coarse solid particles. The reagent is added. The coarse solids are mixed with hot water to melt the phosphorus sludge in them, which is then separated from the inert solids. The solids are heated to burn off any residual elemental phosphorus. Molten phosphorus sludge is mixed with a solution of chromic acid to extract phosphorus as a separate phase. Then they again act with other reducing agents. The reaction mass is filtered and then in the form of a cake can be buried as safe waste.

Without listing all the features and details, we can conclude that almost all methods use exposure to the aquatic environment at high temperature and pressure. These effects can be provided by using the electrohydraulic (EH) method of processing phosphorus sludge. Let us consider some aspects of the application of an EH processing of the phosphorus sludge.

## 1. Method for processing phosphorus sludge using electro-discharge action

When using an electric discharge effect for the treatment of phosphorus sludge in an aqueous medium, the structure of its dispersed particles is destroyed, the shells of phosphorus droplets are destroyed, preventing the process of coalescence [8-11]. To implement this process, a high-voltage pulse is applied to the electrodes placed directly in the phosphorus sludge medium, which causes the development and implementation of an electric discharge in a liquid medium. In this case, all the energy stored in the capacitor bank almost instantly enters the working gap in the liquid and is released in the form of a short electric pulse of high power. Further, a high-pressure zone appears around the discharge channel. The liquid, having received acceleration from the expanding discharge channel, moves in all directions at high speed. At the site of the discharge formation, a cavitations are formed, which generates shock waves. Shock waves or compression waves act on phosphorus droplets surrounded by a shell of the mineral part of the sludge and organic impurities and destroy these shells. Drops of phosphorus free from the shielding shell settle, then in the process of coalescence (fusion) of phosphorus particles, the phosphorus sludge is separated into pure phosphorus and impurities.

It is possible to intensify the process of obtaining phosphoric acid from phosphorus sludge because the mineral shell of phosphorus particles is destroyed. Then phosphorus sludge with a strong stabilized structure is processed into an emulsion-suspension of phosphorus particles and solid mineral impurities cleaned from the shell. It should also be noted that in the EH processing method it is possible to adjust the parameters of the electric discharge (energy, power, number of pulses, pressure at the front of the shock wave, ect.) depending on the type of phosphorus sludge [10].

## 2. Experimental part

The experiments were carried out on a bench consisting of a thermostat, a measuring cell with a plane-parallel capacitor (Fig.1.), an impedance meter that measures the total resistance modulus and phase angle within the resistance range of  $1 \div 10^7$  Ohm in the frequency range of  $5 \div 10^8$  Hz. This instrument can be used to directly measure the inductance and capacitance of dispersed particles by measuring the reactance at various frequencies. To eliminate the effect of electrode polarization in the case of high conductivity of the test substance, measurements can be carried out by varying the distance between the electrodes [11].

On fig. 1 is the scheme of the measuring block into which the phosphorus sludge samples are placed. The bottom electrode 1 is grounded, and the top electrode 2 moves in the vertical-axial direction. To maintain the temperature regime, the sensors are placed in a thermostatically controlled metal cup 4, the body 3 is made of fluoroplast-4. Electrode 2 is insulated with a sleeve 5. There are branch pipes 6 on the glass for connection to a thermostat.

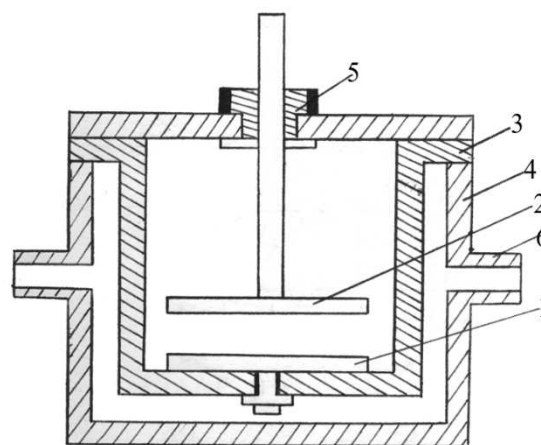


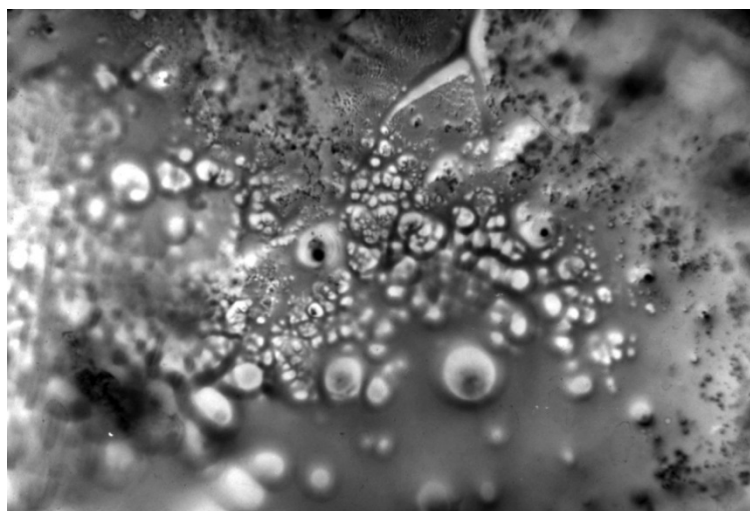
**Fig.1.** Measuring block of a laboratory electro-hydraulic installation.

In the experiments, the values of the particles electric capacitance were obtained for various EH processing parameters. These results obtained can be used to calculate the energy losses at the stage of formation of a high-voltage discharge in the aqueous medium of phosphorus sludge. It is also possible to determine the optimal values of the parameters of the electric discharge pulse for sludges of various compositions. Practice shows that in the process of phosphorus production slimes of various composition are

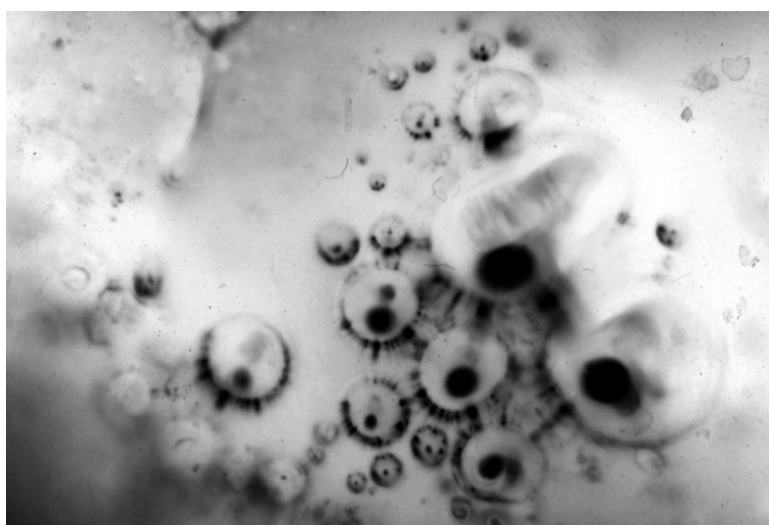
formed and the choice of a reliable method for their processing is impossible without a detailed analysis of the properties, structure and dispersed composition of slimes.

### 3. Results and discussion

The structure was analyzed using a scanning microscope. Data on changes in the microstructure as a result of electropulse processing have been obtained. Using EH processing, you can change the number of discharges. Now consider microscopic analysis and histograms of the distribution of phosphorus sludge particles by size after processing with electrohydraulic pulses. For microscopic studies, a hermetically sealed preparation with a thin section of solidified «monolithic» phosphoric slime or a layer of granular slime was placed in an «Epiquant» structural analyzer, examined visually and selectively photographed in transmitted light using a photo attachment. To complete the picture, microscopic studies of samples of phosphorus sludge with phosphorus content of 70%, 50%, 30% and the mineral part of the sludge were carried out. Microphotography of initial samples of sludge with a  $P_4$  – 30% content before treatment with electric discharges was also performed (Fig.2). On the Fig. 3 shows microphotography of the sludge during settling after electric discharge treatment, and it can be seen from the predominance of large droplets that there is a process of micelle formation and phosphorus coalescence with its subsequent separated.

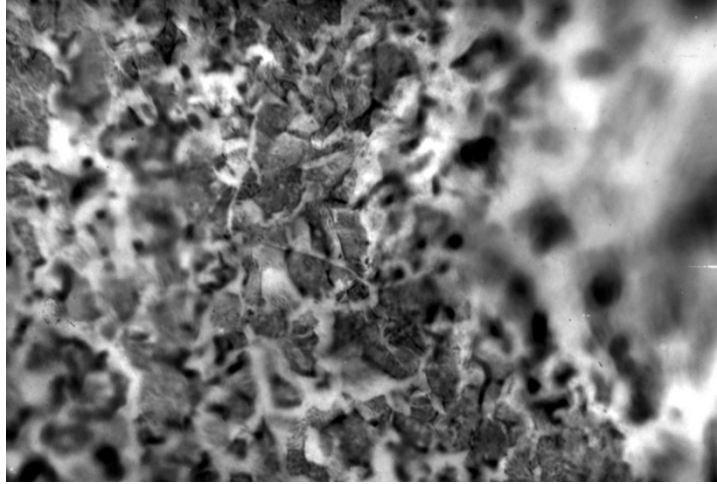


**Fig.2.** Microphotography of the initial sludge before treatment with electric discharges



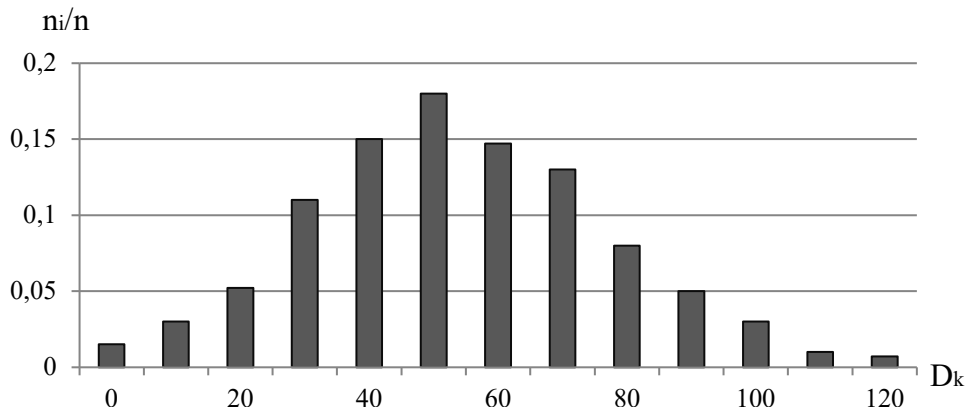
**Fig.3.** Microphotography of phosphorus droplets after treatment with electric discharges during micelle formation and coalescence

Figure 4 shows a microphotograph of the mineral part of the sludge after settling. Photoprints were used to determine the size distribution of phosphorus droplets by the method of A.G. Spector chords method, the volume fraction of phosphorus droplets in the sludge was determined by A. Rozival's linear method, and the specific surface area was determined by the random secant method for the space of S.A. Saltykov [1, 6].



**Fig.4.** Microphotographs of the mineral part of the sludge after electric discharge treatment and sedimentation

A typical histogram obtained by microscopic analysis of the sludge is shown in figure 5. Dimensionless values of the number of dispersed sludge particles are plotted on the vertical axis  $n_i/n$ . Statistical processing of the analysis results showed that the most accurate description of the histogram is the differential distribution function that obeys the logarithmically normal distribution law.



**Fig.5.** Typical histogram obtained by microscopic analysis of sludge.

In fact, larger droplets are aggregatively and sedimentally unstable, since the force of gravity becomes greater than the forces of flocculation interaction between the particles and the phosphorus drop, overcoming the structural and mechanical barrier, settles to the bottom of the vessel. Apparently, this is why the content of large droplets is low. On the contrary, the smaller the droplet diameter  $D_k$ , so they are stable and sedimentation stable, this explains the high content of droplets of small size.

All these factors determine the skewness of the histogram to the left of the maximum, which is characteristic for the logarithmically normal distribution law. Figure 6 shows a histogram of the size distribution of sludge particles after treatment with an electric discharge pulse of average power ( $U_0=20$  kV,  $C=0.15$   $\mu$ F). Figure 7 shows a histogram of the distribution of sludge particles after exposure to a more powerful high-voltage pulse ( $U_0=30$  kV,  $S=0.35$   $\mu$ F). A significant increase in the content of smaller droplets (0 – 40 microns) after exposure to a powerful discharge pulse, which indicates an intensive process of dispersion of phosphorus particles and the dependence of this process on the pulse parameters. During the shockwave effect on the phosphorus emulsion in water, the stabilizing shell of the phosphorus droplets is destroyed, after which, during the subsequent settling, the phosphorus droplets coalesce (merge), they settle,

and now the phosphorous sludge has an oil/water emulsion structure, that is, water droplets (the dispersed phase), the so-called reverse-type emulsion, are distributed in the dispersion medium of phosphorus. The phosphorus content in this type of sludge is more than 70%. Here the water droplets are already stabilized by a shell of organic and mineral impurities.

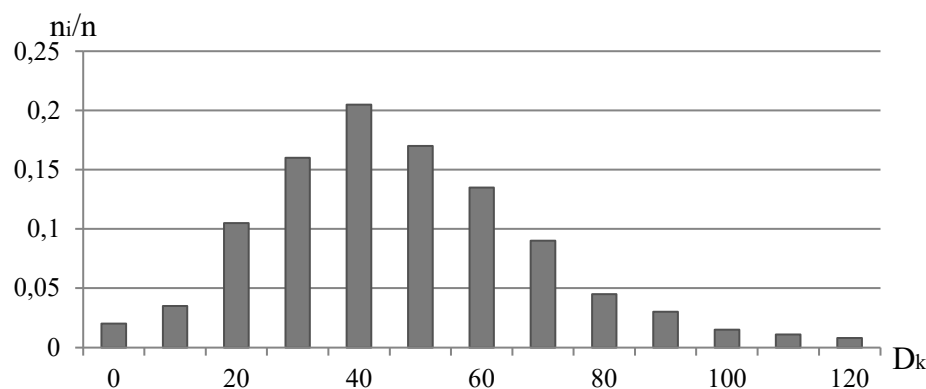


Fig. 6. The size distribution of sludge particles after treatment with an electric discharge pulse of average power.

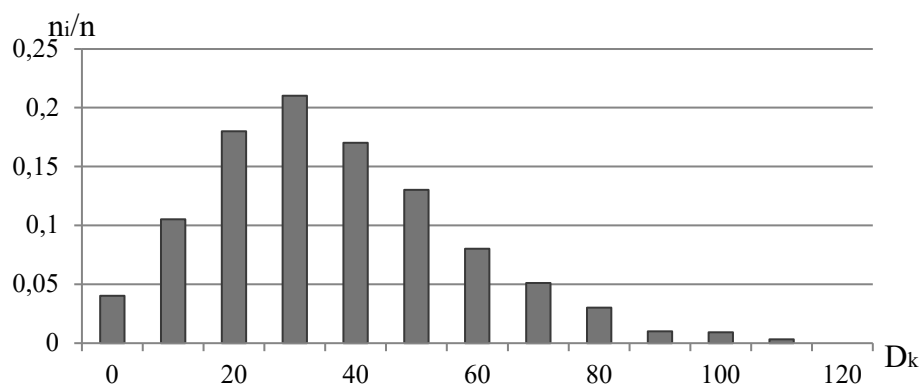


Fig. 7. The distribution of sludge particles after exposure to a powerful high-voltage pulse

Of particular interest are the dependences of the dispersed characteristics of phosphoric sludge on the parameters of processing pulses. In subsequent experiments, the value of the initial voltage varied in the range of 15÷40 kV, with the value of the interelectrode gap, mm-11. As can be seen, that the main factor determining the process of dispersion of phosphorus drops is the energy released in the discharge channel during the first half-period of the discharge current oscillation. This value, in turn, determines the value of the pressure amplitude at the front of the compression wave, which is the main tool for crushing phosphorus droplets. The dependence of the dispersed characteristics of phosphoric sludge on the number of processing pulses is studied. Figure 8 shows the dependence of the average diameter of the phosphorus sludge particles  $D$  on the number of processing pulses  $N$ .

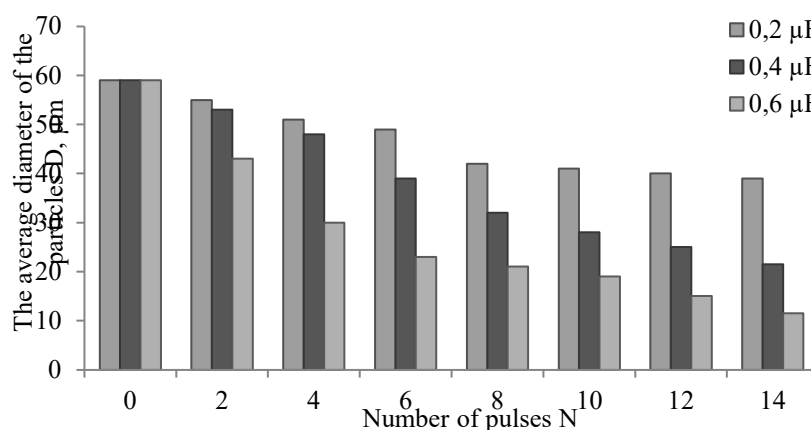


Fig. 8. The average diameter of phosphorus sludge particles distribution at different capacitors.



The figures show that as the number of discharges increases, not only the average diameter decreases, but also the dispersion decreases. This shows that the sludge is becoming more uniform in its dispersed composition. Attention is also drawn to the fact that with an increase in the number of pulses, the average diameter and dispersion change less significantly, the crushing process slows down.

## Conclusions

The effect of electro-pulse processing with different parameters is analyzed on the basis of a comparison of the properties and structure after processing. In conclusion, it should be noted, based on the analysis of the above results, the possibility of using high-voltage electrical discharges in the processing of emulsions. By adjusting the parameters and number of processing electric discharge pulses, you can adjust the particle size of the dispersed phase and prepare emulsions with the desired dispersion characteristics. Statistical analysis of the obtained curves shows that particles of a certain size obey the logarithmically normal distribution law. Moreover, during electrohydraulic treatment, some dispersion of phosphorus droplets is first observed, but after settling and coagulation and coalescence processes, the droplet diameter increases, after which the emulsifier separates with released phosphorus. The results of the experiments showed that the use of a pulsed high-voltage discharge makes it possible to extract environmentally friendly products from phosphorus sludge with specified sizes of dispersed particles. This means that the electrochemical processing of phosphorus sludge into high-quality products can improve technical and economic performance and improve environmental performance, in which the environment is less polluted by toxic waste.

## REFERENCES

- 1 Cherepanova G.P. Extraction of phosphorus from sludge in a dynamic coagulation apparatus. Abstract dis. ... candidate of chemical sciences. St. Petersburg, 1992, 16 p. [in Russian]
- 2 Saran M.S., Laxbacker D.W. Method for extracting phosphorus from water sludge. Patent RU 2351665. Glenn spring holding, INC. (US). Publ. 03.21.2013, 6 p.
- 3 Mukashev B.N., Beketov B.A., Chokin K.Sh., Tamendarov M.F. *Method for processing phosphorus sludge*. Patent of the Republic of Kazakhstan No. 8628. Published: 03/15/2000, 4 p.
- 4 Tuyakbaev A.A., Tulebaev A.K., Beketov B.A. Method for processing phosphorus sludge. Patent RU 1816735C. Publ. 05/23/1993, 7 p.
- 5 Dormeshkin O.B., et al. Study of the process of hydraulic classification of phosphorus sludge in order to extract phosphorus for the production of glyphosate. *Proceedings of the National Academy of Sciences of the Republic of Kazakhstan. Chemistry and Technology Series*. 2017, No. 6 (426), pp. 97–102.
- 6 Zakolodina T.V. System analysis of phosphorus industry waste disposal based on the CALS concept. Abstract diss. candidate of technical sciences. 2008, 22p.
- 7 Aldashov B.A., Lisitsa V.I. *Utilization of Karatau phosphorite waste - the path to a competitive economy and environmental improvement*. Almaty: Gylym, 2007, 428 p.
- 8 Bekaev A.A., et al. Using the L.A. effect Yutkin in electrohydraulic devices. *Proceedings of the Intern. scientific and technical Conf. dedicated to the 145th anniversary of MSTU, "MAMI"*, 2010, pp. 22 - 32. [in Russian]
- 9 Yutkin effect. Spheres of application of electrohydraulic effect. ElectroHydroDynamics. Available at: <https://electro-hydrodynamics.rf/effect-yutkin/> [in Russian]
- 10 Sakipova S.E., Nussupbekov B.R., Ospanova D.A., et al. Effect of electric pulse processing on physical and chemical properties of inorganic materials. *IOP Conf. Series: Materials Science and Engineering*. 2015, Vol. 81, pp. 012051. doi:10.1088/1757-899X/81/1/012051
- 11 Satybaldin A.Zh., et al. The influence of a high-voltage discharge on the oil bottom sediments formed at the oil storage facilities of the Atasu-Alashankou station. *Eurasian phys. tech. j.* 2021, Vol.18, No.3(37), pp. 71 - 75.

## INVESTIGATION OF INTERMETALLIC GdFeAl TERNARY COMPOUND BY ELASTIC, THERMOPHYSICAL AND ULTRASONIC ANALYSIS

Yadawa P.K.\*, Rai S., Chaurasiya N., Prajapati A.K.

Department of Physics, Prof. Rajendra Singh (Rajju Bhaiya) Institute of Physical Sciences for Study and Research, V. B. S. Purvanchal University, Jaunpur, India, \* [pk Yadawa@gmail.com](mailto:pk Yadawa@gmail.com)

*Higher order elastic constants were calculated of the intermetallic GdFeAl ternary compound using Lennard Jones potential approach. With the using of second order elastic constants (SOECs), other elastic moduli; shear modulus, bulk modulus, Young's modulus, Pugh's ratio, constants of elastic stiffness and Poisson's ratio are estimated for mechanical and elastic characterization at room temperature. Born stability and Pugh's criteria are used to examine the nature and strength of the intermetallic ternary compound and found that it is mechanically stable compound. For the investigation of anisotropic behaviour and thermophysical properties, ultrasonic velocities and thermal relaxation time have been also calculated along with different orientations from the unique axis of the crystal. The temperature variation of ultrasonic velocities, Debye average velocity and thermal relaxation time along the z axis is evaluated using SOECs. The ultrasonic properties correlated with elastic, thermal and mechanical properties which is temperature dependent is also discussed. Ultrasonic attenuation was calculated at different temperatures due to phonon – phonon (p – p) interactions. The responsible reason of attenuation is p-p interactions; it was got that the thermal conductivity is a core contributor to the characteristic of ultrasonic attenuation as a role of temperature. GdFeAl ternary compound behave as its purest form at lower temperature and are more ductile demonstrated by the minimum attenuation.*

**Keywords:** intermetallic ternary compound, elastic properties, mechanical properties, thermal conductivity, ultrasonic properties

### Introduction

Use Times New Roman font and A4 format (210×297 mm) in portrait orientation with margins 2.7 cm  
RTX types of intermetallic ternary compounds, including rare earth R, transition metal T and p element X, have performed an extremely classy variation of the crystallographic structures for magnetic characterization. These ternary compounds have different crystallographic structures [1]. The GdFeAl ternary compound was seen crystallize into MgZn<sub>2</sub>- type hexagonal crystal structure, wherever rare-earth atoms involve the 4f site while Fe and Al are positioned at sites 2a and 6h [2, 3]. The GdFeAl had been observed an MgCu<sub>2</sub>-type structure, when cooling gradually after annealing [4]. TbFeAl and GdFeAl ternary compounds had been observed as a ferrimagnet's nature with transition temperatures 195 K and 260 K respectively, with decreased the magnetic moment of rare-earth atoms due to disordered contribution detected by the neutron experiments. A second order magnetic phase transition has confirmed at 265K [5, 6]. Magnetocaloric effect (MCE) was attracted considerable attention predominantly because of likely application in magnetic cooling or the gas liquefaction. These ternary compounds have excellent magnetocaloric properties, namely high entropy change and large temperature change [7,8]. In the last few years compounds with magnetic transition had been commonly connected with structural transition due to his huge entropy change [9, 10]. In last decay, it may be used in magnetic refrigeration cycle.

It is probable that magnetic cooling would be obtainable to buyer in several years as a more effective environmentally safe for the traditional type of refrigerator [11, 12]. The properties of GdPdX (X = Al, Si, Ga, Ge, In, Si) compounds were expansively examined their characterization [13]. Ultrasonic attenuation (UA) is the exact main physical parameter to describe a material, whichever appreciates the specific relationship between the anisotropic behaviour of the proximal hematitic planes and affinity of structural motion, some physical measures like thermal energy density, specific heat and thermal conductivity, is well associated with higher-order elastic constants [14].

In this work, we were worked diligently to make the relationship between thermo physical and microstructural properties for intermetallic ternary compound. Intermetallic GdFeAl ternary compound will help in understanding the mechanical behaviour of intermetallic ternary compounds and it will performance

and significant role in the illustration of manufacturing apparatus with useful physical properties under moderate working conditions. For that, we have considered temperature dependent ultrasonic attenuation coefficient, elastic stiffness constant, acoustic coupling constants, thermal relaxation time and the ultrasonic velocity for ternary compounds. Bulk modulus (B), Young's modulus (Y), shear modulus (G), Pugh's ratio (B / G) and Poisson's ratio were also calculated and then discussed for this ternary compounds. The findings should serve as a theoretical foundation for future research of intermetallic ternary compound. The theoretical technique and calculation methods of this analysis will be presented in this paper, which will be accompanied by theoretical results, discussion and conclusions.

### 1. Computational theory

There exists numerous approaches to analyses high-order (SOECs, TOECs) elastic factors of hexagonal materials. According present our effort, the Lenard Jones interaction potential approaches was using for the evaluation for SOECs and TOECs. Higher order elastic constants of hexagonally based materials are a consequence to lattice parameters, according to the potential methodology to evaluation. A general description of elastic coefficient of  $n^{th}$  order is the fractional derivatives of the medium constrained to determinate deformation as well as mathematically conveyed by subsequent expression as [14, 15]:

$$C_{ijklmn\dots} = \frac{\partial^n F}{\partial \eta_{ij} \partial \eta_{kl} \partial \eta_{mn} \dots} \tag{1}$$

Whenever,  $F$  (free energy density) may be extended in relations of strain  $\eta_{ij}$  (Lagrangian strain component tensor) Taylor series expansion as:

$$F = \sum_{n=0}^{\infty} F_n = \sum_{n=0}^{\infty} \frac{1}{n!} \left( \frac{\partial^n F}{\partial \eta_{ij} \partial \eta_{kl} \partial \eta_{mn} \dots} \right) \eta_{ij} \eta_{kl} \eta_{mn} \dots \tag{2}$$

Thereby, the free energy density is written such as:

$$F_2 + F_3 = \frac{1}{2!} C_{ijkl} \eta_{ij} \eta_{kl} + \frac{1}{3!} C_{ijklmn} \eta_{ij} \eta_{kl} \eta_{mn} \tag{3}$$

In order that HCP compounds the basis vectors are  $a_1 = a \left( \frac{\sqrt{3}}{2}, \frac{1}{2}, 0 \right)$ ,  $a_2 = a(0,1,0)$  and  $a_3 = a(0,0,c)$ . Where  $a$  and  $c$  are the lattice parameters. For hexagonal compound, unit cell contains 6- atoms in basal plane and 3-3 atoms upper and lower the basal plane. The consequently, both first and second neighborhood contains of 6 atoms. Here  $r_1 = a(0,0,0)$  and  $r_2 = \left( \frac{a}{2\sqrt{3}}, \frac{a}{2}, \frac{c}{2} \right)$  represent position vectors.

The form of potential energy is written as following:

$$U_2 + U_3 = \sum_{I=1}^6 U(r_I) + \sum_{J=1}^6 U(r_J) \tag{4}$$

Wherever, I represent the above basal plane and J denote below the basal plane. Interatomic vectors in non-deformed state ( $r$ ) and deformable state ( $r'$ ) are associated as:

$$(r')^2 - (r)^2 = 2\varepsilon_i \varepsilon_j \eta_{ij} = 2\theta \tag{5}$$

Whenever,  $\varepsilon_i$  and  $\varepsilon_j$  are the component of cartesian vector  $r$ .  $U$  (energy density) may be describing based on  $\theta$  as [17-18]:

$$U_n = (2V_c)^{-1} \sum \frac{1}{n!} \theta^n D^n \varphi(r) \tag{6}$$

Equations (4) and (6) give the  $U$  including cubic terms as:

$$U_2 + U_3 = (2V_c)^{-1} \left[ \sum_{I=1}^6 \frac{1}{2!} \theta_I^2 D^2 \varphi(r_I) + \sum_{J=1}^6 \frac{1}{2!} \theta_J^2 D^2 \varphi(r_J) \right] + (2V_c)^{-1} \left[ \sum_{I=1}^6 \frac{1}{3!} \theta_I^3 D^3 \varphi(r_I) + \sum_{J=1}^6 \frac{1}{3!} \theta_J^3 D^3 \varphi(r_J) \right] \tag{7}$$

Wherever,  $D=R^{-1}d/dR$  and  $\varphi(r)$  represents the interaction potential, The value of  $V_c = [3^{1/2}/2] a^2 c$  signifying the per unit volume. The energy density is examined in terms of Lennard Jones potential and specified as:

$$\varphi(r) = -\frac{a_0}{r^m} + \frac{b_0}{r^n} \tag{8}$$

Wherever,  $a_0$  and  $b_0$  are constants. Establish the Lenard Jones potential approach leads to computed 6 SOECs and 10 TOECs of the hexagonal compound and formulations of elastic constants were taken by our previous papers [14, 15].

Bulk modulus and shear modulus were calculated using Voigt and Reuss' methodologies [16, 17]. The calculations of unvarying stress and unvarying strain were used in the Voigt and Reuss' methodologies, correspondingly. Furthermore, the average values of the both methodologies were used toward compute ensuing values of B and G using Hill's methods, [17, 18]. Using the values of Bulk modulus (B), Shear modulus (G), Poisson's ratio ( $\sigma$ ) and Young's modulus (Y) are evaluated [19, 20]. The following expressions were used for the evaluation of Y, B, G and  $\sigma$ .

$$\left. \begin{aligned} M &= C_{11} + C_{12} + 2C_{33} - 4C_{13}, C^2 = (C_{11} + C_{12})C_{33} - 4C_{13} + C_{13}^2; \\ B_R &= \frac{C^2}{M}; B_V = \frac{2(C_{11}+C_{12})+4C_{13}+C_{33}}{9}; \\ G_V &= \frac{M+12(C_{44}+C_{66})}{30}; G_R = \frac{5C^2 C_{44} C_{66}}{2[3B_V C_{44} C_{66} + C^2(C_{44} + C_{66})]}; \\ Y &= \frac{9GB}{G+3B}; \quad B = \frac{B_V+B_R}{2}; \quad G = \frac{G_V+G_R}{2}; \quad \sigma = \frac{3B-2G}{2(3B+G)} \end{aligned} \right\} \quad (9)$$

Ultrasonic velocities in hexagonal compound are one longitudinal  $V_L$  and two shear ( $V_{S1}$ ,  $V_{S2}$ ) waves velocities, where,  $V_L$  is the longitudinal and  $V_{S1}$  and  $V_{S2}$  are shear and quasi-shear and shear wave velocities [21]. The Debye average velocity is specified by the equation as [22]:

$$V_D = \left[ \frac{1}{3} \left( \frac{1}{V_L^3} + \frac{1}{V_{S1}^3} + \frac{1}{V_{S2}^3} \right) \right]^{-1/3} \quad (10)$$

At the low temperature regime, the mean free path of electron is alike as the mean free path of acoustical phonons. Accordingly, a high probability coupling arises between acoustic phonons and free electrons [14]. The mathematical formulation of UA for longitudinal ( $\alpha$ )<sub>Long</sub> and shear waves ( $\alpha$ )<sub>Shear</sub> is given by:

$$\alpha_{long} = \frac{2\pi^2 f^2}{\rho V_L^3} \left( \frac{4}{3} \eta_e + \chi \right) \quad (11)$$

$$\alpha_{shear} = \frac{2\pi^2 f^2}{\rho V_S^3} \eta_e, \quad (12)$$

where ' $\rho$ ' is the density and ' $f$ ' is the frequency of the ultrasonic wave of hexagonal compound, ' $\eta_e$ ' represent the electron viscosity and ' $\chi$ ' is the compressional viscosity,  $V_L$  and  $V_S$  are given as:

$$V_L = \sqrt{\frac{C_{33}}{\rho}} \text{ and } V_S = \sqrt{\frac{C_{44}}{\rho}} \quad (13)$$

The viscosity of the electron gas ( $\eta_e$ ) [21, 22] is given by

$$\eta_e = \frac{9 \times 10^{11} \hbar^2 (3\pi^2 N)^{2/3}}{5e^2 R}, \quad (14)$$

where ' $R$ ' is the resistivity and ' $N$ ' represents the number of molecules per unit volume.

At high temperature, p-p interaction (Akhieser's type of losses) and thermoelastic losses are the two prevailing methods, whichever are considerable for ultrasonic attenuation. The Akhieser's type of loss is specified by the subsequent equation:

$$(\alpha/f^2)_{Akh} = \frac{4\pi^2 \tau E_0 (D/3)}{2\rho V^3}. \quad (15)$$

Here  $E_0$  represent thermal energy density. Also, the acoustical coupling constants (D) is given by:

$$D = 3(3E_0 \langle (\gamma_i^j)^2 \rangle - \langle \gamma_i^j \rangle^2 C_V T) / E_0 \quad (16)$$

Here  $C_V$  is the specific heat per unit volume and  $\gamma_i^j$  is the Grüneisen number of the material. The thermal relaxation time, signified by ' $\tau$ ' is given by:

$$\tau = \tau_S = \tau_L / 2 = \frac{3k}{C_V V_D^2} \quad (17)$$

Here  $\tau_L$  and  $\tau_S$  are the thermal relaxation time for the longitudinal wave and shear wave respectively, the thermal conductivity represents as ' $k$ '. The thermoelastic loss  $(\alpha/f^2)_{Th}$  is evaluated by the subsequent equation [21, 22]:

$$(\alpha/f^2)_{Th} = 4\pi^2 \langle \gamma_i^j \rangle^2 \frac{kT}{2\rho V_L^5}. \quad (18)$$

The total ultrasonic attenuation is specified by the subsequent equation as:

$$(\alpha/f^2)_{Total} = (\alpha/f^2)_{Th} + (\alpha/f^2)_L + (\alpha/f^2)_S. \quad (19)$$

Wherever  $(\alpha/f^2)_{Th}$  is the thermoelastic loss,  $(\alpha/f^2)_L$  and  $(\alpha/f^2)_S$  are the ultrasonic attenuation coefficient for the longitudinal wave and shear wave correspondingly.

## 2. Results and discussion

### 2.1 Higher order elastic constants

We have used interaction potential approach to calculate the elastic constants (six of SOECs, ten of TOECs) in this investigation. The lattice parameters ‘a’ (basal plane parameter) and ‘p’ (axial ratio) for intermetallic GdFeAl ternary compound is 5.442 Å and 1.622 respectively [23]. The chosen values of m and n for intermetallic GdFeAl ternary compounds are 6 and 7. Values of  $b_0$  are  $1.13 \times 10^{-62}$  erg cm<sup>7</sup> for GdFeAl compound. SOECs and TOECs were calculated for the intermetallic GdFeAl ternary compound at room temperature is offered now Table 1.

**Table 1.** Second and third order elastic constants (SOEC and TOEC) in (GPa) at room temperature.

Ternary compound	C <sub>11</sub>	C <sub>12</sub>	C <sub>13</sub>	C <sub>33</sub>	C <sub>44</sub>	C <sub>66</sub>	B
GdFeAl	64.5	15.83	13.56	64.28	16.27	25.27	32.5

Ternary compound	C <sub>111</sub>	C <sub>112</sub>	C <sub>113</sub>	C <sub>123</sub>	C <sub>133</sub>	C <sub>344</sub>	C <sub>144</sub>	C <sub>155</sub>	C <sub>222</sub>	C <sub>333</sub>
GdFeAl	-1050	-1666	-347	-442	-2171	-2035	-515	-343	-8315	-8042

Intermetallic GdFeAl ternary compound had the highest elastic constant values, which are important for the material, as these are associated with the stiffness parameter. SOECs are used to determine the UA and associated parameters. Highest elastic constant values found for this intermetallic ternary compound are indicative of their better mechanical properties over another intermetallic ternary compound.

Evidently, for steady of the hexagonal compound, they would satisfy the renowned Born- Huang’s stability norms [19, 20], i.e.  $C_{11} - |C_{12}| > 0$ ,  $C_{11} > 0$ ,  $C_{44} > 0$  and  $(C_{11} + C_{12}) C_{33} - 2C_{213} > 0$  (Table-1). It is evident that the values of above elastic constant are positive too satisfies Born-Huang's mechanical stability criteria and therefore totally this intermetallic GdFeAl ternary compound are mechanically stable. The bulk modulus for intermetallic GdFeAl ternary compound can be calculated and presented in Table 1. Comparing our results with the Debye temperature of GdFeAl ternary compound. The current value of Debye temperature is 170.6 K, evaluated using SOECs, while the Debye temperature experimentally determined by Kastil et al. [24] is 170 K. Thus, there is good agreement between the present value and reported value by Kastil et al.

Thus, there is respectable agreement between the presented and the informed values, which is correlated with second order elastic constants. Therefore, our theoretical methodology is well justified for the evaluation of SOECs of hexagonal ternary compound. We present the calculated values of TOECs in table 1. The negative sign of TOECs designate a negative strain in the solid. Negative TOECs appear in the previous paper on hexagonal structure ternary compound. Therefore, this applied theory for valuation of higher order elastic constants is justified [25, 26]. Also, this theory is applicable for other hexagonally binary and quaternary compounds [27, 28].

The values of B, G, Y, B/G and ‘σ’ for intermetallic GdFeAl ternary compound at room temperature are calculated using Equation (9) and existing in Table 2.

**Table 2.** Voigt–Reus’ constants (M and C<sup>2</sup>), B (x 10<sup>10</sup>Nm<sup>-2</sup>), G (x 10<sup>10</sup>Nm<sup>-2</sup>), Y (x 10<sup>10</sup>Nm<sup>-2</sup>), σ, B/G for intermetallic GdFeAl ternary compound.

Ternary compound	M	C <sup>2</sup>	B <sub>r</sub>	B <sub>v</sub>	G <sub>r</sub>	G <sub>v</sub>	Y	B/G	G/B	σ
GdFeAl	155	5290	34	31	21	22	53	1.51	0.66	0.228

The intermetallic GdFeAl ternary compound has little Stiffness and bonding. B/G and ‘σ’ are the measure of brittleness and ductility of solid. If  $\sigma = 0.228 \leq 0.26$  and  $B/G = 1.51 \leq 1.75$ , the solid is generally brittle, otherwise it is ductile in nature [28, 29]. Our finding of lower values of B/G and σ compared to their critical values indicates that chosen ternary compound are brittle in nature at room temperature. It is well

known that for stable and elastic material the value of  $\sigma$  should be less than 0.5. The value of ' $\sigma$ ' evaluated for GdFeAl is smaller than its critical value. The compressibility, hardness, ductility, toughness, brittleness and bonding nature of the material are also well connected with the SOECs.

## 2.2 Ultrasonic Velocity and allied parameters

In present analysis, we have correlated the mechanical and isotropic behavior of the hexagonal compound with ultrasonic velocity. We have calculated all three velocities  $V_L$ ,  $V_S$ ,  $V_D$  and thermal relaxation time ( $\tau$ ) for intermetallic GdFeAl ternary compound. The thermal conductivity of intermetallic GdFeAl ternary compound has been evaluated from electrical resistivity using Wiedemann- Franz law [23] and presented in Table. 3 The values of temperature dependent thermal energy density ( $E_0$ ) and specific heat per unit volume ( $C_V$ ) are calculated using the tables of physical constant are presented in Table. 3. The values of temperature dependent acoustic coupling constant ( $D_L$  and  $D_S$ ) are shown in Table. 3

**Table. 3.** Density ( $\rho$ : x  $10^3$  kg m $^{-3}$ ), specific heat per unit volume ( $C_V$ : x  $10^5$  Jm $^{-3}$ K $^{-1}$ ), thermal energy density ( $E_0$ : x  $10^8$  Jm $^{-3}$ ), thermal conductivity ( $k$ : x  $10^4$  Wm $^{-1}$ K $^{-1}$ ) and acoustic coupling constant ( $D_L$ ,  $D_S$ ) of GdFeAl ternary compound.

Temp	$\rho$	$C_V$	$E_0$	$k$	$D_L$	$D_S$
50	6.18	3.84	7.57	0.76	53.65	1.12
100	6.16	5.58	3.22	1.45	54.81	1.12
150	6.14	6.01	6.11	2.19	55.18	1.12
200	6.12	6.15	9.15	2.84	55.37	1.12
250	6.10	6.21	12.19	3.42	55.47	1.12
300	6.08	6.23	15.22	4.04	57.14	1.12

It is clear from Table 3 that for all temperature, the values of  $D_L$  are larger than those of  $D_S$  for GdFeAl ternary compound. It indicates that for the shear ultrasonic wave the transformation of ultrasonic energy into thermal energy is less than for longitudinal ultrasonic wave.

The angular dependence ultrasonic velocities are shown in Figs. 1-4. The angles are measured from the z-axis of the crystal. From figs. 1 and 2, velocities  $V_L$  and  $V_{S1}$  of GdFeAl ternary compound has minima and maxima at  $45^\circ$  at all temperatures. In Figure 3, we find that  $V_{S2}$  increases with temperatures along the z- axis. The irregular behavior of orientation dependent velocity is due to combined effect of second order elastic constants and density of the material. The nature of the orientation dependent velocity curves in this work is similar to nature of orientation dependent velocity curve found for other hexagonal type's material [25, 26]. Thus, the angle dependence of the velocities in intermetallic GdFeAl ternary compound is justified.

Figure 4 shows the variation of Debye average velocity ( $V_D$ ) with the angle made with the z- axis of the crystal. It is clear that  $V_D$  increases with the angle and reaches maximum at  $55^\circ$  for intermetallic GdFeAl ternary compound. As the calculation of  $V_D$  involves the velocities  $V_L$ ,  $V_{S1}$  and  $V_{S2}$  [26, 28]. It is understandable that the variation of debye average velocity is affected by the fundamental acoustics velocities. The maximum value of  $V_D$  at  $55^\circ$  is due to a significant increase in pure shear and longitudinal wave velocities and a decrease in quasi-shear wave velocity. It may be determined that average sound wave velocity is a maximum when a sound wave travels at  $55^\circ$  angles with the z- axis of this crystal.

Figures 5 shows a plot of the calculated thermal relaxation time ' $\tau$ ' with the orientation dependent. Angle dependent ' $\tau$ ' curves track the reciprocal nature of  $V_D$  as  $\tau \propto 3K/C_V V_D^2$ .

It is clear that thermal relaxation time for intermetallic GdFeAl ternary material is mostly affected by ' $k$ '. Thermal relaxation time ' $\tau$ ' for hexagonally type structured compounds is of order at picoseconds [29, 30, 31]. Therefore, the calculated ' $\tau$ ' explains the hexagonal structure of intermetallic GdFeAl ternary compound. Along  $\theta = 55^\circ$ , the lowest value of ' $\tau$ ' for wave propagation denotes that the re-establishment time for equilibrium distribution of thermal phonons will be minimum for propagation of wave along this direction. Ultrasonic attenuation due to p-p interaction and thermal relaxation occurrences.

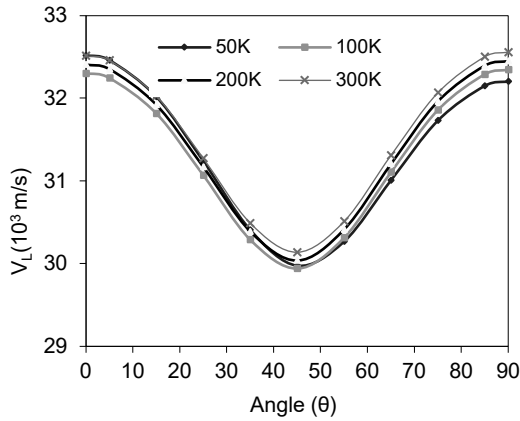


Fig.1.  $V_L$  vs angle with z- axis of crystal.

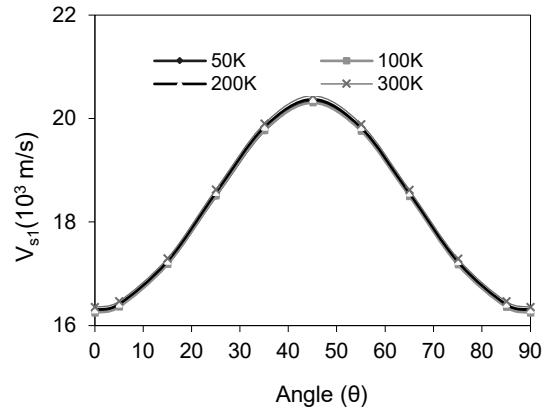


Fig. 2.  $V_{s1}$  vs angle with z- axis of crystal.

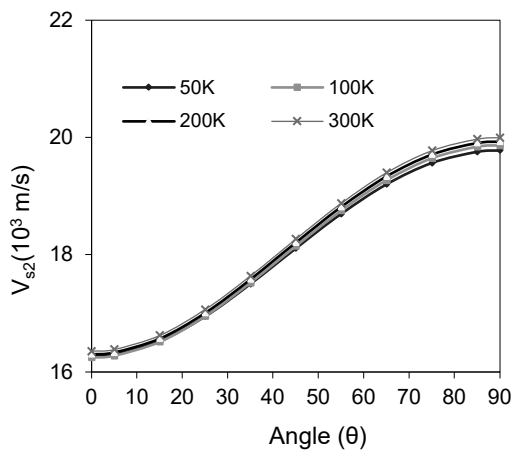


Fig.3.  $V_{s2}$  vs angle with z- axis of crystal.

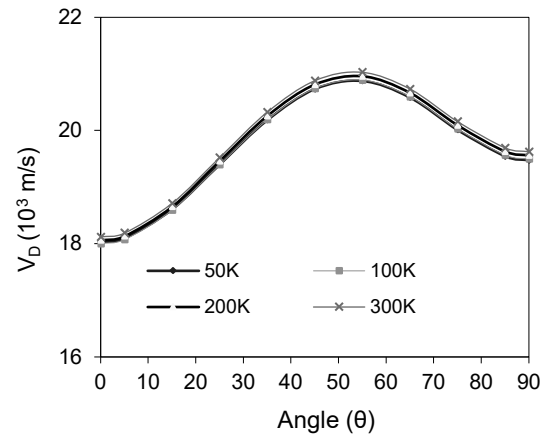


Fig.4.  $V_D$  vs angle with z- axis of crystal.

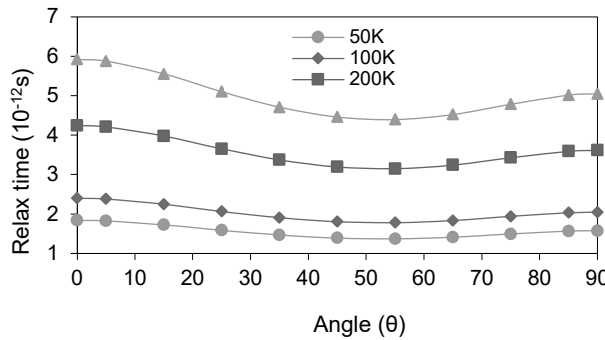


Fig.5. Relaxation time vs angle with z- axis of crystal

### 2.3 Ultrasonic attenuation due to phonon-phonon interaction and thermal relaxation phenomena

While evaluating the UA, the attenuation coefficient divided by frequency squared  $(\alpha/f^2)_{Akh}$  is calculated for the longitudinal wave  $(\alpha/f^2)_L$  and for the shear wave  $(\alpha/f^2)_s$  using Eqns. 11 and 12 under the condition  $\omega\tau \ll 1$  at different temperature along the z- axis of intermetallic GdFeAl ternary compound. Eqn. 18 has been used to calculate the thermo-elastic loss divided by frequency squared  $(\alpha/f^2)_{Th}$ . Figures 6-7 present values of the temperature dependent longitudinal, shear and total attenuation of intermetallic GdFeAl ternary compound.

In this work, the acoustic wave is assumed to propagate along the z- axis of the crystal from Fig. 6-7. It is evident that the Akh. type of energy losses  $(\alpha/f^2)_{Akh}$  proportional to  $D$ ,  $E_0$ ,  $\tau$  and  $V^{-3}$  (Eqns. 15 and 18). Table 3 shows that '  $E_0$ ' and '  $V$ ' are increasing with temperature. Hence Akhieser losses in GdFeAl ternary

compound are overwhelmingly affected by  $E_0$  and the 'k'. Consequently, the increase in UA is due to the increase in thermal conductivity. Therefore, it is the p-p interaction which predominantly governs the ultrasonic attenuation; outstanding to deficiency of theoretical/experimental facts in the literature a comparison of UA could not be made.

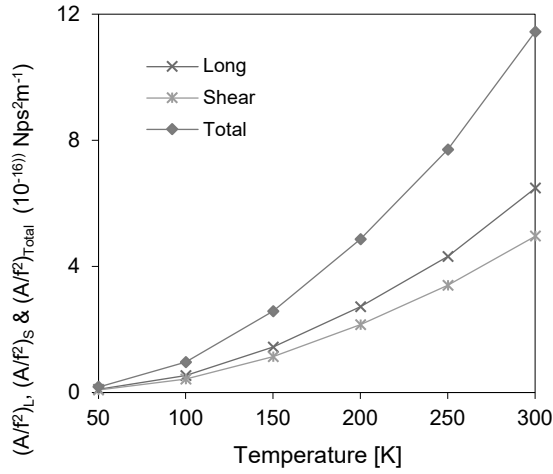


**Fig.6.** Long.& Shear and Total attenuation vs temperature of GdFeAl compound.

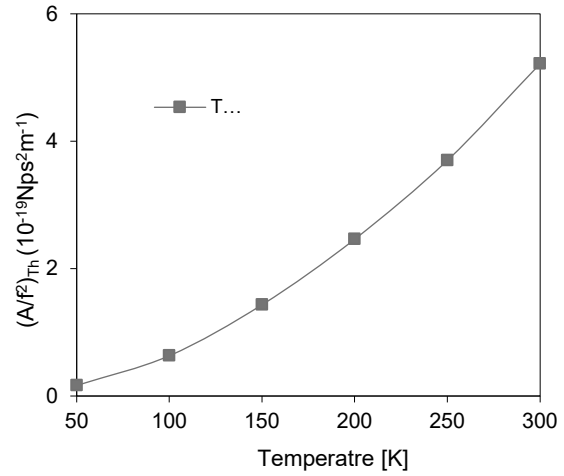


**Fig.7.** Th. attenuation vs temperature of GdFeAl compound.

In Figures 6-7, it is clear that the thermo-elastic loss is much lower in comparison to Akhieser loss for intermetallic GdFeAl ternary compound, and also the total attenuation using Eqn. 19. UA due to p-p interaction for longitudinal wave and shear wave is leading factor. The thermal conductivity and thermal energy density are main factor that affects the total attenuation. Thus, it may be predicted that the GdFeAl ternary compound behave as his purest form at low temperature (50K) and are further ductile demonstrated by the minimum attenuation although at high temperature (room temperature) of intermetallic GdFeAl ternary compound are least ductile.

Therefore, at lower temperature there will be least impurity in intermetallic GdFeAl ternary compound. Since the velocities is largest for intermetallic GdFeAl ternary compound at this temperature and the ternary compound would be most ductile. Minimum values of UA for intermetallic GdFeAl ternary compound at lower temperature defends its quite stable hexagonal type structure state.

## Conclusions

Based on the above conversation is valuable to state that:

- The principle established on simple interaction potential approach remains valid for calculating higher-order elastic coefficients for hexagonally structured intermetallic ternary compound.
- The elastic constants should satisfy the renowned Born's stability criteria for stable nature of intermetallic ternary compound. The Pugh's ratio confirms the ductile nature of ternary compound.
- Intermetallic GdFeAl ternary compound. ' $\tau$ ' is found to be of the picoseconds order, which defends their hexagonal structure. As ' $\tau$ ' has smallest value along  $\theta = 55^\circ$  at all temperatures, the time for re-establishment of symmetry spreading of phonons, will be minimum, for the wave propagation in this direction.
- Over total attenuation, UA caused by p-p interaction mechanism is dominant and is a leading factor of thermal conductivity and energy density.
- GdFeAl ternary compound behave as its purest form at lower temperature and are more ductile demonstrated by the minimum UA while at higher temperature this compound is least ductile.

The research could help with ternary intermetallic compounds processing and non-destructive characterization. These studies will form a basis for further research into the essential thermophysical features of various another ternary compounds.



## REFERENCES

- 1 Oboz M., Talik E. Properties of the GdTX (T=Mn, Fe, Ni, Pd, X= Al, In) and GdFe<sub>6</sub>Al intermetallics. *J. Alloys Compd.* 2011, Vol. 509, pp. 5441-5446.
- 2 Kastil J., Javorsky P., Kamarad J., et al. Magnetic and magnetocaloric properties of partially disordered RFeAl 9R= Gd, Tb) intermetallic. *Intermetallics*, 2014, Vol.54, pp.15-19.
- 3 Tishin A.M., Derkach A.V., Spichkin Y.I., et al. Magnetocaloric effect near a second order magnetic phase transition. *J. Magnetism and Magnetic Materials*. 2007, Vol. 310, pp.2800-2804.
- 4 Jarosz J., Talik E., Kusz J., et al. Crystallographic, electronic structure and magnetic properties of the GdTAl; T=Co, Ni and Cu ternary compounds. *Magn. Mater.* 2000, Vol.208, pp.169.
- 5 Dong Q.Y., Shen B.G., Chen, J., et al. Magnetic entropy change and refrigerant capacity in GdFeAl compound. *J. Applied Physics*. 2009, Vol.105, pp. 07A305.
- 6 Levin E.M., Pecharsky V.K., Gschneidner Jr K.A. Unusual magnetic behaviour in Gd<sub>5</sub>(Si<sub>1.5</sub>Ge<sub>2.5</sub>) and Gd<sub>5</sub>(Si<sub>2</sub>Ge<sub>2</sub>). *Physical Review B*. 2000, Vol.62, pp. R14625.
- 7 Talik E., Klimczak M. Giant magnetocaloric effect in Tb<sub>3</sub>Rh. *J. Alloys Compd.* 2009, Vol.486, pp. L30-L33.
- 8 Liu F.S., Wang Q.B., Ao W.Q., et al Magnetocaloric effect in high Ni content Ni<sub>52</sub>Mn<sub>48-x</sub>In<sub>x</sub> alloys under low field change. *J. Magn. Magn. Mater.* 2012, Vol.324, pp.514-518.
- 9 Dung N. H., Zhang L., Ou Z.Q., Brück E. From first-order magneto-elastic to magneto-structural transition in (Mn,Fe)<sub>1.95</sub>Po<sub>0.50</sub>Si<sub>0.50</sub> compounds. *Appl. Phys. Lett.* 2011, Vol.99, pp.092511.
- 10 Pecharsky A.O., Gschneidner Jr K.A., Pecharsky V.K., The giant magnetocaloric effect between 190 and 300 K in the Gd<sub>5</sub>Si<sub>x</sub>Ge<sub>4-x</sub> alloys for 1.4≤x≤2.2. *J. Magn Magn Mater*, 2003, Vol.267, pp.60-68.
- 11 Brück Ekkes. Developments in magnetocaloric refrigeration. *Journal of Physics D: Applied Physics*. 2005, Vol.38, No. 23, pp. R381.
- 12 Cam Thanh D.T., Brück E., Tegus O. Influence of Si and Ge on the magnetic phase transition and magnetocaloric properties of MnFe (P, Si, Ge). *J. Magn. Magn. Mater.* 2007, Vol.310, pp. e1012-e1014.
- 13 Talik E., Kusz J., Hofmeister W., Matlak M., Skutecka M., Klimczak M. Properties of the GdPdX (X = Al, Si, Ga, Ge, In, Sn) intermetallics. *J. Alloys Comp.* 2006, Vol.423, pp.47-51.
- 14 Pandey D.K., Yadawa P.K., Yadav R.R., Ultrasonic properties of hexagonal ZnS at nanoscale. *Mater. Lett.* 2007, Vol.61, pp.5194-5198.
- 15 Yadawa P.K. Ultrasonic characterization of ceramic material titanium diboride. *Ceramics-Silikaty*. 2011, Vol. 55, pp. 127-133.
- 16 Yadawa P.K. Non-destructive characterization of superionic conductor: lithium nitride. *Material Science – Poland*. 2014, Vol. 32 (4), pp. 626-632.
- 17 Hill R. The elastic behaviour of a crystalline aggregate. *Proc. Phys. Soc.* 1952, Vol.A. 65, pp.349-354.
- 18 Turkdal N., Deligoz E., Ozisik H., Ozisik H.B. First-principles studies of the structural, elastic, and lattice dynamical properties of ZrMo<sub>2</sub> and HfMo<sub>2</sub>. *Ph Transit.* 2017, Vol. 90, pp.598-609.
- 19 Weck P.F., Kim E., Tikare V., Mitchell J. A. Mechanical properties of zirconium alloys and zirconium hydrides predicted from density functional perturbation theory. *Dalton Trans.* 2015, Vol.44, pp.18769-18779.
- 20 Singh D., Pandey D.K., Yadawa P.K., Yadav A.K., Attenuation of ultrasonic waves in V, Nb and Ta at low temperatures. *Cryogen*. 2009, Vol.49, pp.12-16.
- 21 Singh S.P., Yadawa P.K., Dhawan P.K., et al. Effect of pressure and electrical resistivity on ultrasonic properties of MgB<sub>2</sub> single crystal at low temperatures. *Cryogenics*. 2019, Vol.100, pp.105-108.
- 22 Singh D., Yadawa P. K., Sahu S.K. Effect of electrical resistivity on ultrasonic attenuation in NpTe. *Cryogen*. 2010, Vol.50, pp.476-479
- 23 Klimczak M., Talik E., Jarosz J., Mydlarz T. Properties of GdFeAl ternary compound in two crystallographic structures. *Materials Science-Poland*. 2008, Vol. 26, pp.4.
- 24 Kaštil J., Javorský P., Kamarád J., et al. Magnetic and magnetocaloric properties of partially disordered RFeAl (R = Gd, Tb) intermetallic. *Intermetallic*. 2014, Vol. 54, pp. 15.
- 25 Jaiswal A.K., Yadawa P.K., Yadav R.R. Ultrasonic wave propagation in ternary intermetallic CeCuGe compound. *Ultrasonics*. 2018, Vol. 89, pp.22-25.
- 26 Yadawa P.K. Computational Study of Ultrasonic Parameters of Hexagonal Close-Packed Transition Metals Fe, Co, and Ni. *The Arabian Journal for Science and Engineerin*. 2012, Vol.37, pp.255.
- 27 Rai S., Chaurasiya N., Yadawa P.K. Elastic, Mechanical and Thermophysical properties of Single-Phase Quaternary ScTiZrHf High-Entropy Alloy. *Physics and Chemistry of Solid State*. 2021, Vol.22, pp.670-680.
- 28 Turkdal N., Deligoz E., Ozisik H., Ozisik H. B. First-principles studies of the structural, elastic, and lattice dynamical properties of ZrMo<sub>2</sub> and HfMo<sub>2</sub>. *Ph. Transit.* 2017, Vol. 90, pp. 598.
- 29 Yadav C. P., Pandey D. K., Singh D. Ultrasonic study of Laves phase compounds ScOs<sub>2</sub> and YO<sub>2</sub>. *Indian J Phys.* 2019, Vol.93, pp.1147-1153.
- 30 Yadav N., Singh S. P., Maddheshiya A. K., et al. Mechanical and thermophysical properties of high-temperature Ir<sub>x</sub>Re<sub>1-x</sub> alloys. *Phase Transitions*. 2020, Vol.93, pp.883-894.
- 31 Singh S. P., Singh G., Verma A.K., et al. Ultrasonic wave propagation in thermoelectric ZrX<sub>2</sub> (X= S, Se) compounds. *Pramana - J. Phys.* 2019, Vol.93, No. 5 pp.83-91.

## NUCLEAR STRUCTURE OF THE HEAVIEST BORON ISOTOPE

Waleed S. Hwash

Department of Physics, Faculty of Education for Pure Sciences,  
Anbar University, Anbar, Iraq, [waleed973@yahoo.com](mailto:waleed973@yahoo.com)

*The two-neutron Halo of 19-Boron has been investigated within this work. This investigation used the Microscopic Cluster Model (MCM). The main properties of Halo nuclei such as binding energy, radius, and deformation of the core have been calculated in this study. The  $^{19}\text{B}$  has been defined in the shape of core-n-n. The  $^{17}\text{B}$  is the core of the system. The feature of the three-body system depended on a structure and a deformation of the core. The core of  $^{17}\text{B}$  hasn't been considered as an inert core but has some degree of freedom. This degree has a high influence on the structure of a three-body system. So we used the Microscopic Cluster Model (MCM). The main aim of this study is to expand using cluster model in a new version which is Microscopic Cluster Model.*

**Keywords:** Halo-nuclei,  $^{19}\text{B}$ , Microscopic cluster model, neutron-halo structure, Wood-Saxon equation.

### Introduction

The facilities of radioactive nuclear-beam have made in considerations and brought to light a lot of exciting phenomena in nuclear structure physics, the study of atomic nuclei away from the line of the  $\beta$ -stability. The development of these facilities has proven to study the nuclear structure of neutron-rich atomic nuclei near to neutron-drip line (the threshold) for Fragmentation into core and neutrons in a very useful way.

In this study, of specific interest are the heaviest isotope of Boron, the two-neutron halo nucleus,  $^{19}\text{B}$  also the associated bound or unbound sub-system  $^{18}\text{B}$ , which are critical to determining the  $^{17}\text{B}$ -n interaction in the three-body model. Actually, the nuclear level structures of  $^{18}\text{B}$  can focus on the growth of the  $v2s_{1/2}$  level which can become degenerate in this area [1,2]. In terms of realizing the halo structure of a nucleus; calculations of total cross sections give the first indications [3]. The  $^{19}\text{B}$  measurements were started some time ago with very elevated energy (800 MeV per nucleon) and explained in a Glauber optical model analysis [4].

The matter radius of  $^{19}\text{B}$  was deduced  $3.11 \pm 0.13$  fm as compared to  $^{17}\text{B}$ , it is about  $2.99 \pm 0.09$  fm. This was slightly proposed that it may be defined as a  $^{15}\text{B}$  core and 4 neutrons. Enhanced electric-dipole (E1) is recognized just above the threshold of the two-neutron decay and E1 strength of  $(E1) = 1.64 \pm 0.06(\text{stat}) \pm 0.12(\text{sys}) e^2 \text{fm}^2$  for energies lower than 6 MeV. This feature, identified as E1 excitation, gives the first evidence that  $^{19}\text{B}$  has a structure of a two-neutron halo [5]. Actually, the boron  $^{19}\text{B}$  is a candidate for in detailed studies of a probable multi neutron halo. Experimentally, this nuclide has little information: its binding energy is very low (but inexact) separation energy of two valence neutrons ( $S_{2n} = 0.089^{+0.56}_{-0.089} \text{ MeV}$ ) [4] and it's an enhanced interaction cross-section [4]. Then  $^{18}\text{B}$  is unbound,  $^{19}\text{B}$  has a Borromean property, where the  $^{19}\text{B}$  is bound as a three-body system. These features are indicative of the structure of a two-neutron halo. Anyway, being also loosely bound to four-neutron separation ( $S_{4n} = 1.47 \pm 0.35 \text{ MeV}$ ) [6],  $^{19}\text{B}$  might slightly be described as "core-n-n-n" halo or as has a neutron skin [4,7].

The virtual state of even higher numbers of neutrons the n-A body starts closing the threshold. A spectacular value of this trend obvious with the  $^{17}\text{B}$  isotope, where the virtual state of n- $^{17}\text{B}$  is placed at the excessiveness of  $^{18}\text{B}$  threshold ground-state. This consequence is because the biggest value of the nucleus-neutron scattering length noticed until now, as  $\sim -100$  fm [8]. Though, acceptance of the experiment and the limited did not permit to fix the scattering length a lower bound, and was determined an upper bound as  $\sim -50$  fm only [8].

In spite of this experimental value uncertainty, the potentially massive n- $^{17}\text{B}$  scattering length gives interesting property to  $^{19}\text{B}$ , a two-neutron halo nuclide [4] showing a weakly binding energy of core-n-n

system [9]. Furthermore, because of its very weak binding energy ( $2n$  separation of  $S_{2n} = 0.14 \pm 0.39$  MeV [10]),  $^{19}\text{B}$  has no excited states.

Cluster models have a high range of applications in specific nuclear structure physics, from the light nuclei spectroscopy to low-energy reactions. When applying on exotic nuclei like halo nuclei or molecular states, the rest models unable to compete through cluster approaches up to now. For example, the shell-model has great problems to investigate cluster states. However, the difficulties related to this method make it appropriate basically to the light nuclei spectroscopy. Most microscopic cluster models or cluster models will likely be still commonly applied in the next works.

### 1. Theoretical Background

The  $^{19}\text{B}$  has been defined in the shape of core-n-n. The Hamiltonian of the  $^{17}\text{B}$  core defines a set of eigenstates  $\phi_{core}$  and eigenvalues  $\epsilon_{core}$

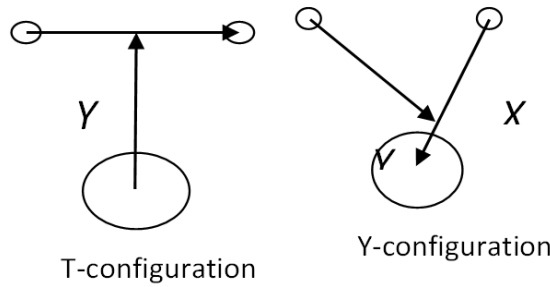


Fig.1. Jacobi coordinates for a three-body system.

$$\hat{h}_{core}(\xi_{core})\phi_{core}(\xi_{core}) = \epsilon_{core}\phi_{core}(\xi_{core}) \tag{1}$$

The total wavefunction is

$$\Psi^{JM}(x, y, \vec{\xi}) = \phi_{core}(\xi_{core})\psi(x, y) \tag{2}$$

The Jacobi coordinates  $(x, y)$  well-defined as [11,12,13]

$$\rho^2 = x^2 + y^2 \text{ and } \theta = \arctan\left(\frac{x}{y}\right)$$

$$\psi_k^{l_x l_y}(\theta) = N_k^{l_x l_y} (\sin \theta)^{l_x} (\cos \theta)^{l_y} P_n^{l_x + \frac{1}{2}, l_y + \frac{1}{2}}(\cos 2\theta) \tag{3}$$

The valence neutrons wave function is

$$\psi_{n,k}^{l_x l_y}(\rho, \theta) = R_n(\rho)\psi_k^{l_x l_y}(\theta) \tag{4}$$

So  $\psi(x, y)$  in eq(2) is  $\psi(x, y) = \psi_{n,k}^{l_x l_y}(\rho, \theta)$

The hyper spherical harmonics formalism as in Refs. [14,15]. The total Hamiltonian  $\hat{H}$ , is

$$\hat{H} = \hat{T} + \hat{h}_{core}(\vec{\xi}) + \hat{V}_{core-n1}(r_{core-n1}, \vec{\xi}) + \hat{V}_{core-n2}(r_{core-n2}, \vec{\xi}) + \hat{V}_{n-n}(r_{n-n}) \tag{5}$$

The potentials of deformed Wood-Saxon and a spin-orbit have been used [16, 17].

$$\hat{V}_{core-n}(r_{core-n}, \vec{\xi}) = \frac{-V_0}{\left[1 + \exp\left(\frac{r_{core-n} - R(\theta, \phi)}{a}\right)\right]} \tag{6}$$

$$+ \frac{-\hbar^2}{m^2 c^2} (2l.s) \frac{V_{s.o}}{4r_{core-n}} \frac{d}{dr_{core-n}} \left( \left[1 + \exp\left(\frac{r_{core-n} - R_{so}}{a_{so}}\right)\right]^{-1} \right)$$

$$V_{n-n}(r_{n-n}) = -\frac{\hbar^2}{m^2 c^2} (2l.s) \frac{V_{s.o}}{4r_{n-n}} \frac{d}{dr_{n-n}} \left( \left[1 + \exp\left(\frac{r_{n-n} - R_{so}}{a_{so}}\right)\right]^{-1} \right) \tag{7}$$

$$R = R_0 [1 + \beta_2 Y_{20}(\theta, \phi)] \tag{8}$$

For more details about theoretical background is in [17,18]

## 2. Calculation

A valence neutron wavefunction has been described in eq. (5) whereas a core wavefunction is in eq. (2) ( $\phi_{core}$ ). Equation (5) describes the Hamiltonian of  $^{19}\text{B}$ . The Wood-Saxon potential has been applied to describe the central potential formula among the constituents along with s-p interaction as in eq. (6). The binding energy and radius of  $^{19}\text{B}$  and deformation of  $^{17}\text{B}$  have been calculated within this work. The central W-S potential relies on Quadrupole moment of  $^{17}\text{B}$ . From the figs. (2,3,4) the variation of nuclear potential with core deformation parameter  $\beta_2$  is clear and that means the shape of the core has high role in affecting on the nuclear force. In fig. (2) the nuclear potential of the s-state has ranged from (-5 to -17)MeV and the prolate shape has increased the potential widely. The potential between core and valence neutron in s-state in fig. (2) refers to a strong interaction between them and also refers to if the valence neutron in the s-state that means the core and valence neutron within the structure of shell model and it far from Halo shape. The figs. (3) and (4) more suitable with a halo structure.

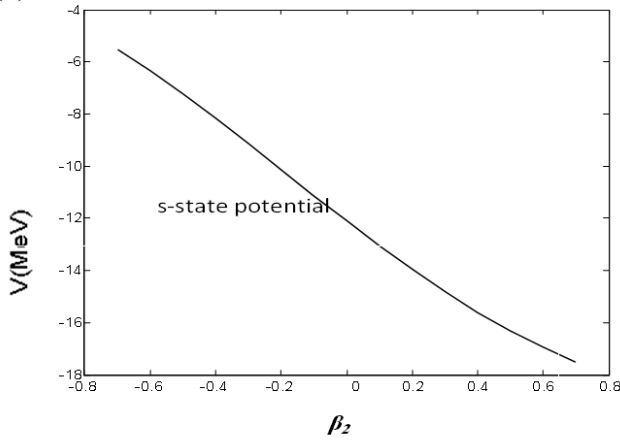


**Fig.2.** The s-state potential of  $^{17}\text{B}$ -n as function of deformation

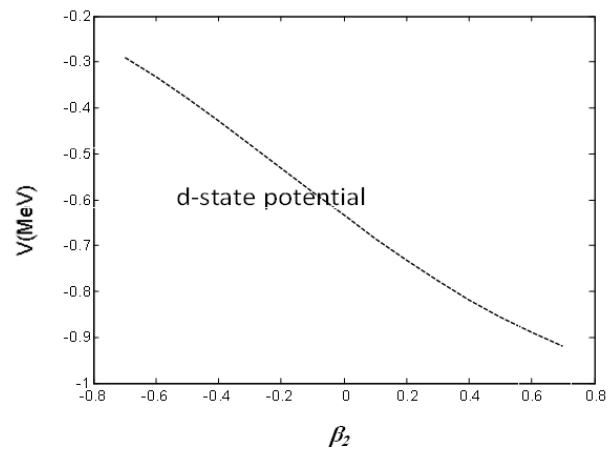


**Fig.3.** The d-state potential of  $^{17}\text{B}$ -n as function of deformation

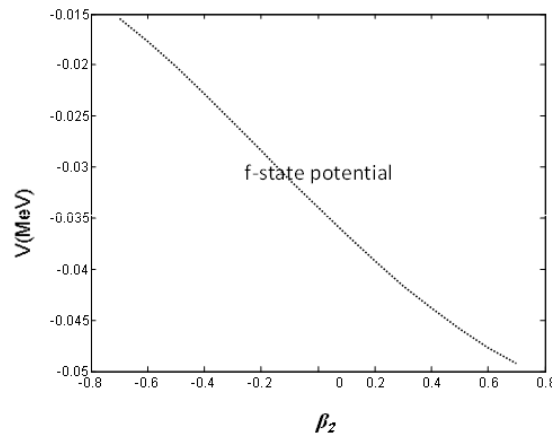


**Fig.4.** The f-state potential of  $^{17}\text{B}$ -n as function of deformation

The two-body energy state of  $^{18}\text{B}$  has been affected by the potential as seen in fig. (5). From the fig. (5), the two-body (the valence neutron and the core) has bounded energy. That means the  $^{19}\text{B}$  hasn't Borromean property. That isn't proved, because the bounded state of  $^{18}\text{B}$  is little, especially in the d-state as shown in fig.(5). So regarding s-state or f-state, we can say it has Borromean property. However, no experimental data indicate to the  $^{19}\text{B}$  has or hasn't Borromean property. But our calculation referred to no Borromean in  $^{19}\text{B}$ . The total angular momentum ( $J^\pi$ ) of  $^{17}\text{B}$  is  $J^\pi(^{17}\text{B})=3/2^-$ . The valence neutron bounded to the ground state ( $^{17}\text{B}$ ) to form  $J^\pi(^{18}\text{B})$  or to excited state of ( $^{17}\text{B}$ ). Also, the prolate shape of the core has a high influence in bound of two-body more than the oblate shape. So we can conclude from that, if the  $^{18}\text{B}$  bounded then the core has a prolate shape or if the  $^{18}\text{B}$  unbound then the core has an oblate shape.

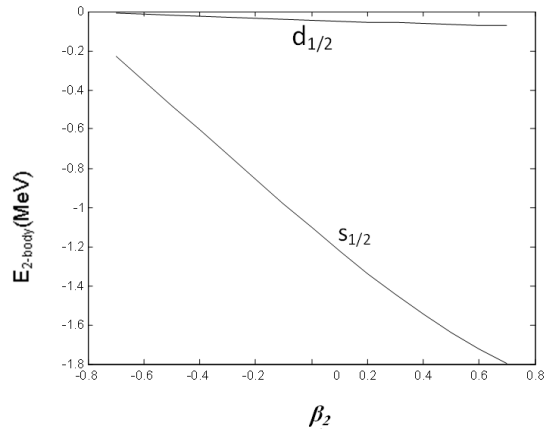


**Fig.5.** Two-body energy in  $^{18}\text{B}$  as function of deformation with ground state of the core ( $^{17}\text{B}$ )  $d_{5/2}, s_{1/2}$

The fig. (6) showed the three-body binding energy as a function of the deformed core ( $^{17}\text{B}$ ). The two configurations ( T-configuration and Y-configuration) have been applied in the present calculation as shown in fig. (6). There isn't a big difference between the two configurations, especially with the oblate shape. Also, that meant the interaction between two valence neutrons hasn't high influence on the binding of the Halo nucleus. The features of  $^{19}\text{B}$  have been investigated with normalization and using experimental values. The radius of  $^{19}\text{B}$  is also diverse with deformation of the core as shown in the fig(7).

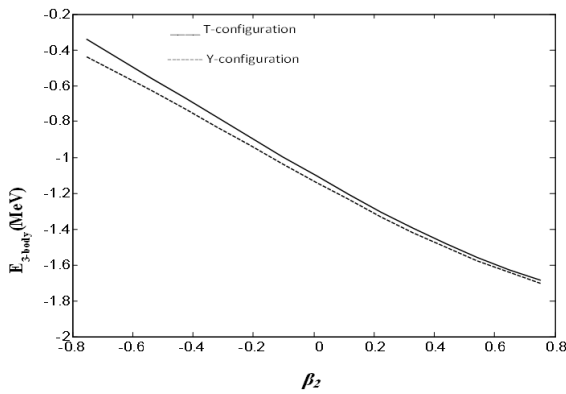


**Fig.5.** Energy of bound state of  $^{19}\text{B}$  Boron as function of deformation with ground state of the core  $p_{3/2}$

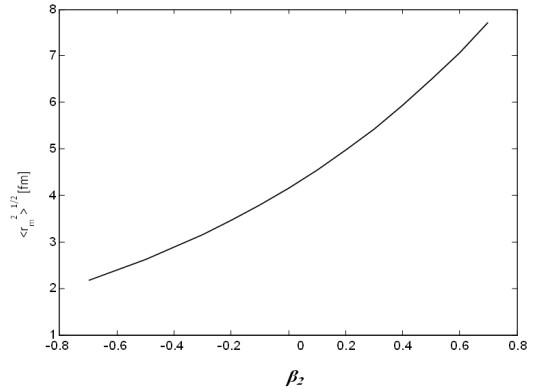


**Fig.7.** Radius of  $^{19}\text{B}$  Boron as function of deformation

As seen in the figures, the deformation has high effect on the properties of  $^{19}\text{B}$ . The  $^{17}\text{B}$  has 5 protons and 12 neutrons, therefore it is far from the closest closed shells (2,8,20) for both neutrons number and protons number. So it must have high deformation. Experimentally, there isn't evidence about the value of deformation. Regarding the experimental data, the core has the oblate shape with a high negative value as seen in the table (1).

**Table 1.** Experimental data of binding energy and matter radius of 19-Boron

Element	$E_{\text{exp}}(\text{MeV})$ [10]	$R_{\text{exp}}(\text{fm})$ [5]	quadrupole
19-Boron	$0.14 \pm 0.39$	$3.11 \pm 0.13$	
17-Boron			No evidence

By normalization, the experimental value of binding energy from table (2) has been used in figure (6) to determine the ( $^{17}\text{B}$ ) deformation which be ( $> -0.6$ ). And this deformation referred to in figure (7) to determine the radius of (19-Boron) is about 3fm as in table (2).

**Table 2.** Experimental value of binding energy of 19-Boron with theoretical value (calculated) of matter radius of  $^{19}\text{B}$  and deformation parameter of  $^{17}\text{B}$ 

element	$E_{\text{exp}}(\text{MeV})$	Deformation parameter	R(fm) Present work
$^{19}\text{B}$	$0.14 \pm 0.39$		3
$^{17}\text{B}$		$> -0.6$	

Also by normalization, the experimental value of root-mean-square is  $(3.11 \pm 0.13 \text{fm})$  and has been used in figure (7) to obtain the deformation parameter value  $(-0.6)$ , which used in figure (6) to get the binding energy of 19-Boron which was  $0.33 \text{MeV}$  regarding figure (6) as seen in the table (3)

**Table 3.** Experimental value of matter radius of 19B with theoretical value (calculated) of binding energy of 19B and deformation parameter of  $^{17}\text{B}$ .

element	$R_{\text{exp}}(\text{fm})$	Deformation parameter	E (MeV) Present work
$^{19}\text{B}$	$3.11 \pm 0.13$		0.33
$^{17}\text{B}$		$-0.6$	

In the 19-Boron study, the transparent physical input has been used with the quantum mechanically rigorous at the same time to produce the main properties of this nucleus. In the 19-Boron case, we can consider the study has met the goal. The Pauli principle has been handled within this work. Improvement of the model can be done, and ideas of model development will be debated in the new study. For 19-Boron the study was able to produce a halo structure of this nucleus, and a huge difference between its radius and charge. The results are slightly similar to the experimental data. The study confirmed that  $^{19}\text{B}$  is loosely restricted, with the structure of the core-dineutron in agreement with most other theories. The results with Microscopic Cluster Model were better than with the Cluster Model and also we think the Wood-Saxon potential will be better than other potentials. The quadrupole moment was fairly big within this study. The Microscopic Cluster Model and Wood-Saxon potential show a very dominant core-dineutron system.

## Conclusion

The heaviest Boron's Isotopes (19-Boron) has been studied in the current work. The approach of this study is the Microscopic Cluster Model (MCM), which has more degree of freedom when dealing with a core. The 19-Boron is considered as a two-neutron Halo nucleus or a three-body system. It is built on an  $n$ - $^{17}\text{B}$  real interaction which, supplemented through a realistic valence  $n$ - $n$  potential, provides an acceptable explanation of  $^{19}\text{B}$  ground and states of resonant in terms of a three-body system  $^{17}\text{B}$ - $n$ - $n$ . The excitation and deformation of the core has a great effect on the structure of the three-body nucleus. So we can't deal with a core as an inert body as in Cluster Model. The calculations have confirmed the 19-Boron has the Halo structure. The calculations have confirmed the success of the microscopic cluster model and can use this model in other systems such as the molecules. The calculations referred to the two-body energy of  $^{18}\text{B}$  is bounded which means the  $^{19}\text{B}$  hasn't Borromean property, which made the  $^{19}\text{B}$  contrasted with all known Two-neutron Halo nuclei. From the results, we should in general use a better handling of the spin-orbit interaction to improve the results of the Halo structure.

## REFERENCES

- 1 Jansen G. et al. Ab Initio Coupled-Cluster Effective Interactions for the Shell Model: Application to Neutron-Rich Oxygen and Carbon Isotopes. *Phys. Rev. Lett.* 2014, Vol. 113, No. (14), pp. 142502-142507.
- 2 Orr N. A. Exploring the Structure of the Most Neutron-rich Boron and Carbon Isotopes. *EPJ Web Conf.* 2016, Vol. 113, No. (06011), pp. 06011-p.1-06011-p.6.
- 3 Tanihata I. et al. Measurements of Interaction Cross Sections and Nuclear Radii in the Light p-Shell Region. *Phys. Rev. Lett.* 1985, Vol. 55, No. (24), pp. 2676-2679.
- 4 Suzuki T., Kanungo R., Bochkarev O., et al. Nuclear radii of  $^{17}\text{B}$ ,  $^{19}\text{B}$  and  $^{14}\text{Be}$ . *Nuclear Physics A.* 1999, Vol. 658, No. (4), pp. 313-326.
- 5 Cook K.J., et al. Halo Structure of the Neutron-Dripline Nucleus  $^{19}\text{B}$ . *Physical review letters.* 2020, Vol. 124, No. (21), pp. 212503-1 - 212503-7.

- 6 Meng W., Audi G., Kondev F.G., et al. The AME2016 atomic mass evaluation (II). Tables, graphs and references. *Chinese Physics C*. 2017, Vo. 41, No. (3), pp. 030003-1 - 030003-442.
- 7 Kanada Y., Horiuchi H. Structure of Light Unstable Nuclei Studied with Antisymmetrized Molecular Dynamics. *Prog. Theor. Phys. Suppl.* 2001, Vol.142, pp.205-263.
- 8 Spyrou A., Baumann T., Bazin D. First evidence for a virtual  $^{18}\text{B}$  ground state. *Physics Letters B*. 2010, Vol. 683, No. 2-3, pp. 129-133.
- 9 Zhukov M.V., Danilin B.V., Egorov D. V. Bound state properties of Borromean halo nuclei:  $^6\text{He}$  and  $^{11}\text{Li}$ . *Physics Reports*. 1993, Vol. 231, No. (4), pp. 151-199.
- 10 Gaudefroy L., Mittag W.W., Orr N. . Direct Mass Measurements of  $^{19}\text{B}$ ,  $^{22}\text{C}$ ,  $^{29}\text{F}$ ,  $^{31}\text{Ne}$ ,  $^{34}\text{Na}$  and Other Light Exotic Nuclei. *Phys. Rev. Lett.* 2012, Vol. 109, No. (20), pp. 202503-1 – 202503-5.
- 11 Hwash W.S. Yahaya R., Radiman S. Nuclear structure of  $^{14}\text{Be}$  nucleus. *J. of the Korean Phys. Soc.* 2012, Vol. 61, No.1, pp. 27-32.
- 12 Hwash W.S. Yahaya R., Radiman S. Structure of two-neutron Halo nuclei,  $^{11}\text{Li}$ . *International Journal of Modern Physics E*. 2012, Vol. 21, No. (7), pp. 1250066\_1- 1250066\_13.
- 13 Hwash W.S., Yahaya R., Radiman S. Effect of core deformation on  $^{17}\text{B}$  halo nucleus. *Physics of Atomic Nuclei*. 2014, Vol. 77, No.(3), pp. 275–281.
- 14 Nunes F. M. Christley J.A., Thompson I. J., et al. Core excitation in three-body systems: Application to  $^{12}\text{Be}$ . *Nuclear Physics A*. 1996, Vol. 609, No. (1), pp.43-73.
- 15 Tarutina T., Thompson I. J., Tostevin J.A. Study of  $^{14}\text{Be}$  with core excitation. *Nuclear Physics A*. 2004, Vol. 733, No. 1-2, pp. 53-66.
- 16 Hwash W.S. Study of the two-proton halo nucleus  $^{17}\text{Ne}$ . *International Journal of Modern Physics E*. 2016, Vol. 25, No.12, pp. 1650105-1- 1650105-11.
- 17 Hwash W.S. Lightest and heaviest two-neutron halo nuclei,  $^6\text{He}$  and  $^{22}\text{C}$ . *Turkish Journal of Physics*. 2017, Vol. 41, pp. 151 – 159.
- 18 Hornyak W.E. *Nuclear Structure Book*. Maryland: Academic Press. 1975, 355 p.

## PARAMETRIZED EIGHT-VERTEX MODEL AND KNOT INVARIANT $10_{136}$

Kassenova T.K.

L.N. Gumilyov Eurasian National University, Nur - Sultan, Kazakhstan,  
M.Kh.Dulaty Taraz Regional University, Taraz, Kazakhstan, tkkasenova@gmail.com

*The article discusses and expands the known elements of the eight-vertex model, paying special attention to the parameterization of the matrix. The matrix values are interconnected with the knot through the braids and this model is valid on finite square lattices in two-dimensional space. A new solution of the parametrized eight-vertex model of free fermions with a complex version of elliptic functions, which is valid on a finite lattice, will be constructed. The range of applicability of the eight-vertex model with elements of the Jacobi elliptic function and the construction of a knot invariant on its basis is discussed by comparing the results obtained analytically for the model. The construction of the knot invariant using the Clebsch-Gordan coefficients and the main tool of statistical mechanics of the Yang-Baxter equation will be studied in detail.*

**Keywords:**  $10_{136}$  knot, elliptic function, Clebsch-Gordan coefficients.

### Introduction

In recent years, scientists in the fields of mathematics and physics have been diligently pursuing related theories, especially the theory of knots, which has generated interest for a small number of scientists and has since become one of the most fashionable hobbies of mathematicians, physicists and even geneticists. This, in turn, gave rise to a number of methods linking two, at first glance, very distant from each other areas of mathematics and physics: knot theory and statistical mechanics.

In [1], the Boltzmann weights of the doubled Ising model, parametrized using elliptic functions, are considered, and an alternative way of checking the Yang-Baxter equation in the parameterization of matrix elements using the star-triangle equation is shown. Thus, in [2], a quantum decomposition of the eight-vertex model was introduced and a set of closure properties in various regions of the parameter space was proved. In [3], it was proved that the sixteen-vertex model gives an exact description of the thermodynamics of artificial spin ice models. The work [4] confirms the complexity dichotomy theorem for the eight-vertex model. For each setting of the model parameters, the calculation of the partition function is proved, which is either solvable in polynomial time or is  $\#P$ -complexity.

The paper investigates the solution of models of statistical mechanics and knot theory, which in turn, this connection is occupied by the Temperley-Lieb algebra [5] and the Birman-Murakami-Wenzl algebra (BMW) [6]. Also, in [7], the latest research on the connection of vertex models of statistical mechanics with the main problems of mathematics is studied. The origins of the connection with physics go back to the very close relationship between the state models of knot polynomials and the partition function in statistical mechanics. This connection in [8] led to the construction of a number of invariants that go beyond the original skein polynomials. Thus, in the source [9], the Jones polynomial in a closed braid is the partition function of the statistical mechanic's model on the braid. The work [10] summarizes procedure outputting braid generator representations from three-partite vertex model. This representation made it possible to study the invariant of a knot with multi-colored links, where the components of the knot have different spins. The formula for the invariant of knot with a multi-colored link is studied from the point of view of the braid generators obtained from the R-matrices of three-partite vertex models. The resulting knot invariant corresponds to the Jones polynomial and HOMFLY-PT. Description of Boltzmann weights and finding  $SO(N)$  for any  $N$  spin vertex model of algebra in [11] opened up new problems in the field of statistical physics. The representations of the braid group in [12], obtained from rational conformal field theories, can be used to obtain explicit representations of the Temperley-Lieb-Jones algebras. In the source [13], the Yang-Baxter equation provides both an algebraic and a graphical method in knot theory. The method of commuting



transfer matrices in [14] for this equation is a generalization possibility for solving the eight-vertex model. The solution to the quantum Yang-Baxter equation [15] is an  $R$ -matrix, which corresponds to the transfer  $R$ -matrix of the eight-vertex model of statistical mechanics.

The method for solving invariants is associated with multi-colored links [16], with the statistical sum of the Chern-Simons theory [17] and with obtaining the topological solution (2) of the Chern-Simons theory on  $S^3$  [18]. In similar sources, as in [19], the connection between the invariant of knot theory and a new ten-vertex model of statistical mechanics was studied using the transition of a commuting transfer matrix, including Boltzmann weights in the braid matrix. Subsequently, in the source [20], the solutions are described using the Clebsch-Gordan coefficients and the transformation matrix.

Thus, in [21], the exact solution of the classical two-dimensional eight-vertex model is the greatest achievement in the field of exactly solvable models and the contradiction with the hypothesis of universality and independence of critical indicators from interaction details was studied in the early 70s. All these studies have found a place in the connection of the eight-vertex model with elements of elliptic functions and knot theory.

In this paper, we consider obtaining braid generators from an eight-vertex model by parametrizing matrix elements with a suitable normalization factor using the quantum form of the Clebsch-Gordan coefficients, the so-called  $3j$ -symbol. The solution is based on the observation that the rows in the transfer matrices commute for a specific parametrization of the four Boltzmann weights. The presented solution will help to understand how to find the connection between the invariants of knots and lattice models of statistical mechanics through the mathematical apparatus of quantum physics.

The work plan is as follows. In Section 2, we consider the construction of braid matrices from the  $R(u)$ -matrix of eight-vertex models for the same spins and the derivation of an algebraic formula for the knot invariant. Section 3 generalizes the procedure for defining a new representation of the braid generators from a  $R(u)$ -matrix associated with a parametrized vertex model with elliptic functions, and proposes a solution to the invariant of a knot with links. Section 4 presents the results of the work.

### 1. Parameterized 8-vertex model

The parameterized eight-vertex model is a generalization of the six-vertex model, where spins  $j_1 = j_2 = \frac{1}{2}$  are placed on four edges that intersect each vertex Boltzmann weights of  $(R^{\frac{1}{2}, \frac{1}{2}})^{n_1, n_2}_{m_1, m_2}(u \rightarrow 0)$  matrices are associated with each nonzero vertex if only  $m_1 + m_2 = n_1 + n_2$ , where  $m_1, m_2, n_1, n_2 \in \frac{1}{2}, -\frac{1}{2}$ . This condition allows 8 nonzero Boltzmann weights, which are called the parameterized eight-vertex model

$$(R^{\frac{1}{2}, \frac{1}{2}})^{n_1, n_2}_{m_1, m_2}(u \rightarrow 0) = \begin{bmatrix} (R^{\frac{1}{2}, \frac{1}{2}})^{n_1, n_2}_{m_1, m_2} & \uparrow\uparrow & \downarrow\uparrow & \uparrow\downarrow & \downarrow\downarrow \\ \uparrow\uparrow & \text{snh}(\mu - u) & 0 & 0 & k\text{snh}\mu\text{snh}u\text{snh}(\mu - u) \\ \downarrow\uparrow & 0 & \text{snh}u & \text{snh}\mu & 0 \\ \uparrow\downarrow & 0 & \text{snh}\mu & \text{snh}u & 0 \\ \downarrow\downarrow & k\text{snh}\mu\text{snh}u\text{snh}(\mu - u) & 0 & 0 & \text{snh}(\mu - u) \end{bmatrix}. \quad (1)$$

To construct the braid generators  $b_i$ , we take the limit  $u \rightarrow 0$  and divide the elements of the previous matrix by the Boltzmann weight  $(R^{\frac{1}{2}, \frac{1}{2}})^{\uparrow, \uparrow}_{\uparrow, \uparrow}(u \rightarrow 0)$ . Subsequently, we will choose an appropriate normalization so that the matrix elements are finite, as shown below

$$\frac{(R^{\frac{1}{2}, \frac{1}{2}})^{n_1, n_2}_{m_1, m_2}(u \rightarrow 0)}{(R^{\frac{1}{2}, \frac{1}{2}})^{\uparrow, \uparrow}_{\uparrow, \uparrow}(u \rightarrow 0)} = \begin{bmatrix} (R^{\frac{1}{2}, \frac{1}{2}})^{n_1, n_2}_{m_1, m_2} & \uparrow\uparrow & \downarrow\uparrow & \uparrow\downarrow & \downarrow\downarrow \\ \uparrow\uparrow & 1 & 0 & 0 & k\text{snh}\mu\text{snh}u \\ \downarrow\uparrow & 0 & \frac{\text{snh}u}{\text{snh}(\mu - u)} & \frac{\text{snh}\mu}{\text{snh}(\mu - u)} & 0 \\ \uparrow\downarrow & 0 & \frac{\text{snh}\mu}{\text{snh}(\mu - u)} & \frac{\text{snh}u}{\text{snh}(\mu - u)} & 0 \\ \downarrow\downarrow & k\text{snh}\mu\text{snh}u & 0 & 0 & 1 \end{bmatrix}. \quad (2)$$

The Wess-Zumino conformal field theory implies a compact relation for the braid generators  $b_i$  obtained from  $(R^{\frac{1}{2}, \frac{1}{2}})_{m_1, m_2}^{n_1, n_2}$  - the matrix of vertex models, as well as from the eigenvalues ( $\lambda$ ) of the monodromy matrix in  $SU(2)_k$  [22], where the values of the permutation matrix

$$(R^{\frac{1}{2}, \frac{1}{2}})_{m_1, m_2}^{n_1, n_2} = \frac{1}{\mathfrak{K}} \hat{P}^{\frac{1}{2}, \frac{1}{2}} (R^{j_1, j_2})_{m_1, m_2}^{n_1, n_2} (u \rightarrow 0), \quad \mathfrak{K} = (R^{j_1, j_2})_{j_1, j_2}^{j_1, j_2} (u \rightarrow 0)$$

are the normalization factor

$$(R^{\frac{1}{2}, \frac{1}{2}})_{m_1, m_2}^{n_1, n_2} = \frac{1}{\mathfrak{K}} \hat{P}^{\frac{1}{2}, \frac{1}{2}} (R^{j_1, j_2})_{m_1, m_2}^{n_1, n_2} (u \rightarrow 0) = \frac{1}{\mathfrak{K}} \hat{P}^{\frac{1}{2}, \frac{1}{2}} \sum_{J \in j_1 \otimes j_2} \begin{pmatrix} j_1 & j_2 & J \\ m_2 & m_1 & M \end{pmatrix} \lambda_j(j_1, j_2) \begin{pmatrix} j_1 & j_2 & J \\ n_1 & n_2 & M \end{pmatrix}, \quad (3)$$

where  $M = m_1 + m_2 = n_1 + n_2$  and the elements in brackets  $\begin{pmatrix} j_1 & j_2 & J \\ m_2 & m_1 & M \end{pmatrix}$  denote the quantum form of the formula for the Clebsch-Gordan coefficient ( $q - CG$ ) [23]. Matrix elements can be expanded in this way

$$(R^{\frac{1}{2}, \frac{1}{2}})_{m_1, m_2}^{n_1, n_2} (u \rightarrow 0) = \begin{pmatrix} (R^{\frac{1}{2}, \frac{1}{2}})_{m_1, m_2}^{n_1, n_2} & \uparrow\uparrow & \downarrow\uparrow & \uparrow\downarrow & \downarrow\downarrow \\ \uparrow\uparrow & 1 & 0 & 0 & ksnh\mu snhu \\ \downarrow\uparrow & 0 & \frac{snh\mu}{snh(\mu-u)} & \frac{snhu}{snh(\mu-u)} & 0 \\ \uparrow\downarrow & 0 & \frac{snhu}{snh(\mu-u)} & \frac{snh\mu}{snh(\mu-u)} & 0 \\ \downarrow\downarrow & ksnh\mu snhu & 0 & 0 & 1 \end{pmatrix}. \quad (4)$$

Therefore, it is possible to define the  $b_i \left[ \frac{1}{2}, \frac{1}{2} \right]$  matrix form of the braid generators using the  $R$  matrix.

Thus, we calculate the knot invariant by the formula

$$\alpha_{\underbrace{j_1 j_2 \dots j_n}_n} (A) = (\tau_j \overline{\tau_j})^{\frac{n}{2}} \left( \frac{\tau_j}{\overline{\tau_j}} \right)^{\frac{l}{2}} Tr[HA], \quad (5)$$

where  $l$  - sum of exponents  $b_i$  appearing in the word of braid  $A$ .  $H = \underbrace{h_j \otimes h_j \dots h_j}_r$ , where  $r$

$$h_j = \frac{1}{1+q+\dots+q^{2j}} \text{Diag}[1, q, \dots, q^{2j}], \quad (6)$$

and  $\tau_j, \overline{\tau_j}$  are

$$\tau_j = \frac{1}{1+q+\dots+q^{2j}}, \quad \overline{\tau_j} = \frac{1}{1+q+\dots+q^{2j}}. \quad (7)$$

Initially, there is only one braid generator  $b_i$ , for all braids  $A \in B_2$ , the matrix form of which will have the form  $4 \times 4$ , where the matrix elements are expressed by elliptic functions with a complex version

$$b_i = (R^{\frac{1}{2}, \frac{1}{2}})_{m_1, m_2}^{n_1, n_2}. \quad (8)$$

An invariant in the equation (5) for knot 1 will be developed according to the Rolfsen table. For knots and links obtained by closing the words of braid  $A = b_{136}^{10}$ , which are matrix  $4 \times 4$

$$b_1 = (R^{\frac{1}{2}, \frac{1}{2}})_{m_1, m_2}^{n_1, n_2} \times \mathfrak{S}, \quad (9)$$

$$b_2 = \mathfrak{S} \times (R^{\frac{1}{2}, \frac{1}{2}})_{m_1, m_2}^{n_1, n_2}. \quad (10)$$

For example, knot  $10_{136}$  is word braid  $A = b_{136}^{10}$ . It is important that such an action of the word braid on a braid of five strands implies the following order of the matrix operation on the initial state  $|j, m_1; j_2, m_2\rangle$

$$A|4\text{-strand}\rangle \equiv b_{136}^{10} |j, m_1; j_2, m_2\rangle. \quad (11)$$

From the above it follows that to derive the eigenvalue, depending on the spectral parameters  $\lambda_j(j_1, j_2; u)$  for spin  $j_1 = j_2 = 1/2$  such, belong to the parametrized eight-vertex model on a square lattice. This assumption  $\lambda_j(j_1, j_2; u)$  was formulated in [22]

$$\lambda_j(j_1, j_2; u) = \prod_{k_1=1}^J (\operatorname{sn}h(k_1\mu - u)) \prod_{k_2=J+1}^{2J} (\operatorname{sn}h(k_2\mu + u)), \quad (12)$$

accordingly, the eigenvalues of the matrix elements are elliptic functions with a complex version

$$\lambda_0(u) = \operatorname{sn}h(\mu + u), \quad \lambda_1(u) = \operatorname{sn}h(\mu - u). \quad (13)$$

Thus,

$$\begin{aligned} \lambda_0(0) &= \lambda_1(0) = \operatorname{sn}h\mu \equiv B(\mu), \\ \lambda_0(u)\lambda_0(-u) &= \lambda_1(u)\lambda_1(-u) = \chi_1(u)\chi_1(-u) + \chi_4(u)\chi_4(-u) = \chi_3(u)\chi_3(-u) + \chi_2(u)\chi_2(-u) = \\ &= \chi_2(u)\chi_2(-u) + \chi'_3(u)\chi'_3(-u) = \operatorname{sn}h(\mu + u)\operatorname{sn}h(\mu - u) \equiv A(\mu; u) \end{aligned}$$

as a result, matrices are obtained depending on the spectral parameter, where  $(R^{j_1, j_2})_{m_1, m_2}^{n_1, n_2}(u \rightarrow 0)$  are matrices associated with new vertex models

$$(R^{j_1, j_2})_{m_1, m_2}^{n_1, n_2}(u) = \sum_{J \in j \otimes j} \begin{pmatrix} J_1 & J_2 & J \\ m_2 & m_1 & M \end{pmatrix} \lambda_j(j_1, j_2) \begin{pmatrix} J_1 & J_2 & J \\ n_1 & n_2 & M \end{pmatrix}, \quad (14)$$

and the general view of the  $R$ -matrix will be

$$(R^{\frac{1}{2}, \frac{1}{2}})_{m_1, m_2}^{n_1, n_2}(u) = \begin{bmatrix} m_1, m_2 / n_1, n_2 & \frac{1}{2}, \frac{1}{2} & \frac{1}{2}, -\frac{1}{2} & -\frac{1}{2}, \frac{1}{2} & -\frac{1}{2}, -\frac{1}{2} \\ \frac{1}{2}, \frac{1}{2} & \chi_1(u) & 0 & 0 & \chi_4(u) \\ \frac{1}{2}, -\frac{1}{2} & 0 & \chi_2(u) & \chi_3(u) & 0 \\ -\frac{1}{2}, \frac{1}{2} & 0 & \chi_3(u) & \chi_2(u) & 0 \\ -\frac{1}{2}, -\frac{1}{2} & \chi_4(u) & 0 & 0 & \chi_1(u) \end{bmatrix}, \quad (15)$$

where

$$\begin{aligned} \chi_1 &= \frac{-i}{[2]} \left( \frac{\operatorname{sn}(i\mu)\operatorname{cn}(iu)\operatorname{dn}(iu) + \operatorname{sn}(iu)\operatorname{cn}(i\mu)\operatorname{dn}(i\mu)}{1 - m\operatorname{sn}^2(i\mu)\operatorname{sn}^2(iu)} \right), \\ \chi_2 &= \frac{-i}{[2]} \left( \frac{\operatorname{sn}^2(i\mu)\operatorname{cn}^2(iu)\operatorname{dn}^2(iu) + \operatorname{sn}(iu)\operatorname{cn}^2(i\mu)\operatorname{dn}^2(i\mu)}{1 - m\operatorname{sn}^2(i\mu)\operatorname{sn}^2(iu)} \right), \\ \chi_3 &= -i\operatorname{sn}(i\mu)e^{-u}, \quad \chi_4 = 0, \quad \chi'_3 = -i\operatorname{sn}(i\mu)e^u. \end{aligned}$$

Replacing  $u = 0$  и  $q = e^{2u}$  для  $j_1 = j_2 = \frac{1}{2}$ , there is

$$\frac{(R^{\frac{1}{2}, \frac{1}{2}})_{m_1, m_2}^{n_1, n_2}(u \rightarrow 0)}{(R^{\frac{1}{2}, \frac{1}{2}})_{\uparrow, \uparrow}^{\uparrow, \uparrow}(u \rightarrow 0)} = \begin{bmatrix} m_1, m_2 / n_1, n_2 & \frac{1}{2}, \frac{1}{2} & \frac{1}{2}, -\frac{1}{2} & -\frac{1}{2}, \frac{1}{2} & -\frac{1}{2}, -\frac{1}{2} \\ \frac{1}{2}, \frac{1}{2} & 1 & 0 & 0 & 0 \\ \frac{1}{2}, -\frac{1}{2} & 0 & \frac{(q^{\frac{1}{2}} - q^{-\frac{1}{2}}) + 1}{q^{\frac{1}{2}} - q^{-\frac{1}{2}}} & 1 & 0 \\ -\frac{1}{2}, \frac{1}{2} & 0 & -1 & \frac{(q^{\frac{1}{2}} - q^{-\frac{1}{2}}) + 1}{q^{\frac{1}{2}} - q^{-\frac{1}{2}}} & 0 \\ -\frac{1}{2}, -\frac{1}{2} & 0 & 0 & 0 & 1 \end{bmatrix}. \quad (16)$$

To obtain braid generators  $b\left(j_1 = \frac{1}{2}, j_2 = \frac{1}{2}\right)$ , choose the appropriate permutation matrix. For  $\hat{P}^{\hat{j}_1 = \frac{1}{2}, \hat{j}_2 = \frac{1}{2}}$ , maybe

$$\hat{P}^{\hat{j}_1 = \frac{1}{2}, \hat{j}_2 = \frac{1}{2}} = \begin{bmatrix} 1 & 0 & 0 & 1 \\ 0 & 0 & 1 & 0 \\ 0 & 1 & 0 & 0 \\ 1 & 0 & 0 & 1 \end{bmatrix}. \quad (17)$$

We apply this permutation matrix in the construction of the braid generator

$$\left(\hat{R}^{\hat{j}_1, \hat{j}_2}\right)_{m_1, m_2}^{n_1, n_2} = \left(\hat{P}^{\hat{j}_1, \hat{j}_2}\right)_{m_1, m_2}^{m_1, m_2} \lim_{u \rightarrow 0} = \frac{(R^{\frac{1}{2}, \frac{1}{2}})_{m_1, m_2}^{n_1, n_2}(u \rightarrow 0)}{(R^{\frac{1}{2}, \frac{1}{2}})_{\uparrow, \uparrow}^{n_1, n_2}(u \rightarrow 0)}, \quad (18)$$

as a result of which we obtain an explicit form of the  $\hat{R}^{\hat{j}_1 = \frac{1}{2}, \hat{j}_2 = \frac{1}{2}}$  - matrix for the parametrized eight-vertex model

$$\frac{(R^{\frac{1}{2}, \frac{1}{2}})_{m_1, m_2}^{n_1, n_2}(u \rightarrow 0)}{(R^{\frac{1}{2}, \frac{1}{2}})_{\uparrow, \uparrow}^{n_1, n_2}(u \rightarrow 0)} = \begin{bmatrix} m_1, m_2 / n_1, n_2 & \frac{1}{2}, \frac{1}{2} & \frac{1}{2}, -\frac{1}{2} & -\frac{1}{2}, \frac{1}{2} & -\frac{1}{2}, -\frac{1}{2} \\ \frac{1}{2}, \frac{1}{2} & 1 & 0 & 0 & 1 \\ \frac{1}{2}, -\frac{1}{2} & 0 & 1 & \frac{(q^{\frac{1}{2}} - q^{-\frac{1}{2}}) + 1}{q^{\frac{1}{2}} - q^{-\frac{1}{2}}} & 0 \\ -\frac{1}{2}, \frac{1}{2} & 0 & \frac{(q^{\frac{1}{2}} - q^{-\frac{1}{2}}) + 1}{q^{\frac{1}{2}} - q^{-\frac{1}{2}}} & 0 & 0 \\ -\frac{1}{2}, -\frac{1}{2} & 1 & 0 & 0 & 1 \end{bmatrix}. \quad (19)$$

A similar construction  $\hat{R}^{\frac{1}{2}, \frac{1}{2}}$  for  $\frac{1}{2}, \frac{1}{2}$  is the transposed matrix  $\hat{R}^{\frac{1}{2}, \frac{1}{2}}$ . The explicit form of the identity matrix can be written as

$$\hat{R}^{\hat{j}_1, \hat{j}_2} \left[ \hat{R}^{\hat{j}_1, \hat{j}_2} \right]^{-1} = \hat{R}^{\hat{j}_1, \hat{j}_2} \left[ \left[ \hat{R}^{\hat{j}_2, \hat{j}_1} \right]^T \right]^{-1} = \mathfrak{S}, \quad (20)$$

$$\hat{R}^{\hat{j}_1, \hat{j}_3} \left[ \hat{R}^{\hat{j}_1, \hat{j}_3} \right]^{-1} = \hat{R}^{\hat{j}_1, \hat{j}_3} \left[ \left[ \hat{R}^{\hat{j}_3, \hat{j}_1} \right]^T \right]^{-1} = \mathfrak{S}, \quad (21)$$

$$\hat{R}^{\hat{j}_2, \hat{j}_3} \left[ \hat{R}^{\hat{j}_2, \hat{j}_3} \right]^{-1} = \hat{R}^{\hat{j}_2, \hat{j}_3} \left[ \left[ \hat{R}^{\hat{j}_3, \hat{j}_2} \right]^T \right]^{-1} = \mathfrak{S}. \quad (22)$$

Thus, we have the opportunity to represent matrix forms  $b_i[j_1, j_2]$  of groupoids that satisfy the constructions of the braid generators

$$b_i[j_1, j_2] [b_i^{\hat{j}_1, \hat{j}_2}]^{-1} \mathfrak{S}, \quad (23)$$

$$b_i[j_2, j_1] [b_i^{\hat{j}_2, \hat{j}_1}]^{-1} \mathfrak{S}, \quad (24)$$

in this form

$$b_i[j_1, j_2] \underbrace{\mathfrak{S} \times \mathfrak{S} \times \dots \times \mathfrak{S}}_{i-1} \times \left( \hat{R}^{\hat{j}_1, \hat{j}_2} \right)^{-1} \times \mathfrak{S}_{i+2}, \quad (25)$$

$$b_i[j_2, j_1] \underbrace{\mathfrak{S} \times \mathfrak{S} \times \dots \times \mathfrak{S}}_{i-1} \times \left( \hat{R}^{\hat{j}_2, \hat{j}_1} \right)^{-1} \times \mathfrak{S}_{i+2}. \quad (26)$$

As a result, using the matrix representation, for any word of the braid  $A$ , the closure of which will give multicomponent links at the knot. Similarly to the link invariant formula (5), we present the following formula for the fermionic link invariant, in which the components of site  $\hat{\alpha}_{j_1, j_2}^{\approx}(A)$  have the same spins. The

invariant of a multi-colored knot (up to a general deformation coefficient of  $q^{\frac{1}{2}}$ ) for a four-component link, where the components of the knot have the same spins, obtained by closing any  $r$ -strand word of braid  $10_{136}$  is given by the formula  $A$

$$\alpha_{j_1, j_2} [A(10_{136})] = q^{\frac{1}{2}C} \alpha_{j_1, j_2} (A) = q^{\frac{1}{2}C} \prod (\tau_j \bar{\tau}_j)^{\frac{l_j}{2}} Tr\{HA\}, \tag{27}$$

where the first factor derives the conditioning factor from  $q$  with an integer of  $C$ , which depends on the spins, bending and the number between the constituent knots of the engagement.  $l_i$ 's is the number of strands in the braid generator, that is, when spin  $j_i$  is in a 5-strand braid  $A$ , where  $\sum_{i=1}^n l_i = r$ . In addition, the matrix representation of  $H$  depends on the order of such repeating spins occurring in the  $r$ -strand braid. This article describes a 5-strand braid obtained from a  $10_{136}$  knot, with a  $j$  weave on all strands, which implies

$$H = h_{j_1} \otimes h_{j_2}. \tag{28}$$

Coming back to the matrix operations for the word of braid  $A$ , we use formula (11), following the sequence of closure of each link in the braid, where each strand has the same spins mentioned above. From the above definition,  $h_{j_i}$ 's (6),  $\tau_{j_i}$  and  $\bar{\tau}_{j_i}$ 's (7). In the next section, we will calculate in detail the invariant of knot  $10_{136}$  with the same link.

### 2. Knot invariant with fermionic junction

At this point of the work, we will find the invariant of a knot with links with spins  $j_1 = j_2 = \frac{1}{2}$ , for this we first need to write the word for a braid of  $n$  strands that tracks the spins. For knot  $10_{136}$ , consisting of the links obtained by closing the five-strand braid and the matrix representation looks like this

$$A(10_{136}) = b_5 b_3^{-1} b_4 b_5^{-1} b_2^{-1} b_5 b_2 b_4 b_1 b_2, \tag{29}$$

and  $H = h_{\frac{1}{2}} \otimes h_{\frac{1}{2}}$  will give

$$\alpha_{\frac{1}{2}, \frac{1}{2}} [A(10_{136})] = \frac{k\delta\eta^{\frac{5}{2}}}{\psi}, \tag{30}$$

where

$$\begin{aligned} k &= q^2, \\ \eta &= ((1 + q + q^2 + q^3)(1 + q + q^2 + q^3)), \\ \psi &= ((-1 + q)^8 (1 + q)^2 (1 + q^2)^2), \\ \delta &= 256 - 2048q + 6928q^2 - 96q^{\frac{5}{2}} - 12176q^3 + 320q^{\frac{7}{2}} + 10352q^4 - 472q^{\frac{9}{2}} + 596q^5 + \\ &+ 464q^{\frac{11}{2}} - 5429q^6 - 464q^{\frac{13}{2}} - 596q^7 + 472q^{\frac{15}{2}} + 10352q^8 - 320q^{\frac{17}{2}} - 12176q^9 + \\ &+ 96q^{\frac{19}{2}} + 6928q^{10} - 2048q^{11} + 256q^{12} \end{aligned}$$

which is consistent with the Jones polynomial calculated on the basis of  $SU(2)$  Chern-Simons theory, braid generators, and a fermionic parametrized eight-vertex model.

### 3. Results and discussion

The paper discusses the construction of a braid group representation using the weighted Boltzmann coefficients of the eight-vertex model, where adjacent edges have different spins. In particular, a matrix representation of braid generators from eight vertex models has been developed. Using the Yang-Baxter

formula for the knot invariants, the Jones polynomial for the knot  $10_{136}$  is explicitly evaluated. Finally, the procedure for determining a new representation of braid generators from a  $R$ -matrix associated with a parametrized vertex model with elliptic functions is generalized, and a new knot invariant  $10_{136}$  is obtained when studying knots and connections using the Chern-Simons theory. Based on these results, the author comes to the conclusion that the knot invariant is proportional to the two-particle Jones polynomial, where the group representation  $SU(2)$  is used, which has state spins on the edges crossing the vertex. In conclusion, the process of finding the knot invariant is described, which is used to find the partition function of the previously known eight-vertex model.

## Conclusion

In the course of work on the article, a completely new  $R$ -matrix of a two-particle parameterized eight-vertex model with the identical links was obtained from the representations of the braid group for the only knot  $10_{136}$  in the Rolfsen knot table, which has a strand index less than the width of its minimum braid. In addition, the  $R$ -matrices defined on braids and constructed by the Markov theorem and the Reidmeister motions are obtained with exact results for the new parametrized eight-vertex model.

Further, we saw that the eight-vertex model is constructed as a modified extension of the integrable six-vertex model and in the three-dimensional positional space elementary particles with half-integer spin are one-dimensional representations of the permutation group acting on the space of wave functions. As a result, it was found that the knot invariant of site  $10_{136}$  is proportional to the two-particle Jones polynomial, where the group representation  $SU(2)$  is used, which has state spins  $j_1, j_2$  on the edges intersecting the vertex. In conclusion, the process of finding the knot invariant, which is used to find the partition function of the previously known eight-vertex model, is described.

Further research could fruitfully solve problems in knot theory and statistical mechanics, including the Jones polynomial. Therefore, the problem of graph isomorphism in knot theory and the statistical system may turn out to be an important area for future research.

## Acknowledgments

This study was funded by the Science Committee of the Ministry of Education and Science of the Republic of Kazakhstan AP0926114

## REFERENCES

- 1 Chicherina D., Derkachov S.E., Spiridonov V.P. New elliptic solutions of the Yang-Baxter equation. *Communications in Mathematical Physics*. 2014, Vol.345, pp. 507-543.
- 2 Jin-Yi Cai, Tianyu Liu, Pinyan Lu, Jing Yu. Approximability of the Eight-vertex Model. 2018, *arXiv:1811.03126v1* [cs.CC].
- 3 Levis D. Two-dimensional spin ice and the sixteen-vertex model. *UPMC Parisuniversitas*. 2012, version 1.
- 4 Jin-Yi Cai Zhiguo Fu. Complexity Classification of the Eight-Vertex Model. 2017, *arxiv.org/abs/1702.07938v2*.
- 5 Xian'an Jin, Fuji Zhang. Jones polynomials and their zeros for a family of links. *Physica A*. 2004, Vol. 333, pp. 183 – 196.
- 6 Gepner D.  $B_k$  spin vertex models and quantum algebras. *Nuclear Physics B*. 2020, Vol. 958, p. 115116.
- 7 J.-M. Maillard. Fa-Yueh Wu's contributions in physics. *Physica A*. 2003, Vol. 321, pp. 28 – 44.
- 8 Yang C.N., Ge M.L. Braid group, knot theory and statistical mechanics. *World Scientific Publishing*. 1989, Vol. 17, p. 452.
- 9 Jones V.F.R. Polynomial invariants of knots via von Neumann algebras. *Bull. Amer. Math.* 1985, pp. 448-458.
- 10 Kassenova T.K., Tsyba P.Yu., Razina O.V., Myrzakulov R. Three-partite vertex model and knot invariants. *Physica A: Statistical Mechanics and its Applications*. 2022, <https://doi.org/10.1016/j.physa.2022.127283>
- 11 Belavin V., Gepner D., Wenzl H. On  $(N)$  spin vertex models. *Nuclear Physics B*. 2020, Vol. 959, p. 115160.
- 12 Kaul R.K. The representations of Temperley-Lieb-Jones algebras. *Nuclear Physics B*. 1994, Vol. 417, pp. 267—285.

- 13 Deguchi T., Wadati M., Akutsu Y. Knot Theory based on Solvable Models at Criticality. Integrable Systems in Quantum Field Theory and Statistical Mechanics. *Advanced Studies in Pure Mathematics*. 1989, Vol. 19, pp. 193-285.
- 14 Baxter. R.J. Exactly Solved Models in Statistical Mechanics. *Academic Press*. 1982, p. 3.
- 15 Kassenova T.K., Tsyba P.Yu., Razina O.V. Eight-vertex model over Grassmann algebra. Proceeding of the 8th International Conf. on Mathematical Modeling in Physical Science. *Journal of Physics: Conference Series. IOP Publishing*. 2019, Vol. 1391, No. 012035. <https://doi.org/10.1088/1742-6596/1391/1/012035>.
- 16 Kaul. R.K., Govindarajan T.R. Three-dimensional Chern-Simons theory as a theory of knots and links (II). Multicoloured links. *Nuclear Physics B*. 1993, Vol. 393, pp. 392-412.
- 17 Kaul R.K., Ramadevi P. Three-Manifold Invariants from Chern–Simons Field Theory with Arbitrary Semi-Simple Gauge Groups. *Commun. Math. Phys.* 2001, Vol. 217, pp. 295 – 314.
- 18 Kaul R.K. Chern-Simons Theory, Coloured-Oriented Braids and Link Invariants. *Commun. Math. Phys.* 1994, Vol. 162, pp. 289-319.
- 19 Kassenova T.K., Tsyba P.Yu., Razina O.V. Investigation of the coupling of the ten–vertex model with Jones polynomials. *Vestnik KazNRTU*. 2020, Vol. 139, No. 3, p. 694.
- 20 Jucys A., Bandzaitis A. The theory of angular momentum in quantum mechanics. *Academy of Sciences of the Lithuanian SSR Institute of Physics and Mathematics publication*. 1965, Vol. 6, p. 531.
- 21 Baxter R.J. *Exactly Solved Models in Statistical Mechanics*. 1985, p.3.
- 22 Chen-Ning Y. Some Exact Results for the Many-Body Problem in one Dimension with Repulsive Delta-Function Interaction. *Physical Review Letters*. 1967, Vol. 19, No. 23, pp.1312-1314.
- 23 Kirillov A., Reshetikhin N.Yu. Representations of algebra  $(\mathfrak{sl}_2)$ ,  $q$ -orthogonal polynomials and invariants of links. Infinite dimensional Lie algebras and groups. *Adv.Ser. in Math.Phys.* 1989, Vol. 7, p. 285.

SUMMARIES	ТҮСІНІКТЕМЕЛЕР	АННОТАЦИИ
<p><i>Суржиков А.П., Малышев А.В., Лысенко Е.Н., Стary О.</i>  <b>Термиялық және радиациялық-термиялық режимдерде қатты фазалық күйдіру кезінде алынған литий ферриттерінің бастапқы магниттік өткізгіштігінің температуралық тәуелділіктері</b>  Жұмыста бастапқы магниттік өткізгіштігінің температуралық тәуелділігін қолдана отырып, термиялық және радиациялық-термиялық режимдердегі қатты фазалық күйдірудің уақыты мен температурасына байланысты литий-титан ферриттердегі фазалық және құрылымдық өзгерістердің ерекшеліктері зерттелген. Қатты фазалық күйдіру кезінде электрондық шоктың әсері қоспалық осылыстарының балқуын күрт жылдамдатады және литий-титан ферриттерінен жасалған өнімдердің фазалық гомогенділігін арттырады. Алынған нәтижелерді өндірістегі феррит өнімдерінің фазалық гомогенділігін жақсарту үшін пайдалануға болады.  <b>Кілт сөздері:</b> литий ферриттері, қатты фазалық күйдіру, электрондық шоктар, жоғары температуралар, бастапқы магниттік өткізгіштік.</p> <p><i>Суржиков А.П., Малышев А.В., Лысенко Е.Н., Стary О.</i>  <b>Температурные зависимости начальной магнитной проницаемости литиевых ферритов полученных при твердофазном спекании в термическом и радиационно-термическом режимах</b>  В работе изучены особенности фазовых и структурных превращений в литий-титановых ферритах в зависимости от времени и температуры твердофазного спекания в термических и радиационно-термических режимах с использованием температурной зависимости начальной магнитной проницаемости. Показано, что воздействие электронного пучка при твердофазном спекании резко ускоряет растворение примесных включений и повышает фазовую гомогенность изделий из литий-титановых ферритов. Полученные результаты могут быть использованы для улучшения фазовой гомогенности ферритовых изделий на производстве.  <b>Ключевые слова:</b> литиевые ферриты, твердофазное спекание, электронные пучки, высокие температуры, начальная магнитная проницаемость.</p>		
<p><i>Козловский А.Л.</i>  <b>Ауыр иондармен сәулелендіру кезінде нитридті керамиканың тозуға төзімділігінің деградация кинетикасын зерттеу</b>  Бұл жұмыс AlN керамикасының беріктік қасиеттерінің өзгерістерін, атап айтқанда құрғақ үйкеліс коэффициентін және 200 МэВ энергиясына ие Хе<sup>22+</sup> ауыр иондарымен сәулелену дозасына байланысты тозуға төзімділік пен беткі ақаулық параметрлерін зерттеуге арналған. Бұл керамикаларға деген қызығушылық олардың жоғары жылу өткізгіштік, қаттылық және тозуға төзімділік, сондай-ақ тамаша оқшаулау қасиеттерімен байланысты, бұл оларды ядролық энергетика, зымыран жасау және микроэлектроника саласындағы үміткер материалдар етеді. Сонымен қатар, бұл керамиканы механикалық үйкеліс, беткі қысым, сондай-ақ иондаушы сәулеленудің әсері сияқты сыртқы әсер ету жағдайында пайдалану қосымша зерттеулерді және қасиеттердің тұрақтылығы мен сақталуы туралы жаңа мәліметтерді талап етеді. Жүргізілген зерттеулер барысында 10<sup>10</sup>-10<sup>11</sup> ион/см<sup>2</sup> сәулеленудің төмен дозалары кезінде бір нүктелі ақаулардың пайда болуымен және газдың ісіну процестерінің инициализациясы нәтижесінде бетінің тозу ықтималдығының төмендігімен сипатталатын құрғақ үйкеліс коэффициенті іс жүзінде өзгермейтіндігі анықталды, бұл керамиканың механикалық үйкеліске жоғары төзімділігін көрсетеді. Алайда радиациялы-индукцияланған зақымданған аймақтардың қабаптасу үрдістерімен сипатталатын сәулелену 10<sup>12</sup> ион/см<sup>2</sup>-қа дейін ұлғаюы кезінде 15000 сынақ циклынан кейін құрғақ үйкеліс коэффициентінің нашарлауы байқалады, бұл керамикалық беттің тозуын және сыртқы әсерлер нәтижесінде деградациясын дәлелдейді.  <b>Кілт сөздері:</b> радиациялық ақаулар, нитридті керамика, тозуға төзімділік, құрғақ үйкеліс коэффициенті, ауыр иондар</p> <p><i>Козловский А.Л.</i>  <b>Изучение кинетики деградации износостойкости нитридных керамик при облучении тяжелыми ионами</b>  Работа посвящена изучению изменений прочностных свойств AlN керамики, в частности, коэффициента сухого трения и параметров износостойкости и дефектности поверхности, в зависимости от дозы облучения тяжелыми ионами Хе<sup>22+</sup> с энергией 200 МэВ. Интерес к данным керамкам обусловлен их высокими показателями теплопроводности, твердости и износостойкости, а также отличными изоляционными свойствами, что делает их перспективными материалами кандидатами в ядерной энергетике, ракетостроении и микроэлектронике. При этом эксплуатация данных керамик в условиях внешних воздействий, таких как механическое трение, давление на поверхность, а также воздействие ионизирующего излучения требует дополнительных исследований и получения новых данных об устойчивости и</p>		



сохранению свойств в течение всего срока эксплуатации. В ходе проведенных исследований было установлено, что при малых дозах облучения  $10^{10}$ - $10^{11}$  ион/см<sup>2</sup>, для которых характерно формирование одиночных точечных дефектов и малая вероятность деградации поверхности в результате инициализации процессов газового распухания, коэффициент сухого трения практически не изменяется, что свидетельствует о высоких показателях устойчивости керамики к механическому трению. Однако увеличение флюенса облучения до  $10^{12}$  ион/см<sup>2</sup>, для которого характерны процессы перекрытия радиационно-индуцированных поврежденных областей, наблюдается ухудшение коэффициента сухого трения после 15000 циклов испытаний, что свидетельствует об усталостном износе поверхности керамики и деградации в результате внешних воздействий.

**Ключевые слова:** радиационные дефекты, нитридные керамики, износостойкость, коэффициент сухого трения, тяжелые ионы

*Джуманов С., Курбанов У.Т., Худайбердиев З.С.*

#### **Кіші радиусты допантарға ие қосындалған лантанды асқын өткізгіштердегі металды-диэлектрик ауысулар**

Берілген жұмыста кіші радиусты қоспалар маңындағы және деформацияланатын торда (яғни қоспалар болмаған кезде) заряд тасымалдаушылардың локализациясы салдарынан кемтіктік қосындалған купраттарда металл-диэлектрик ауысуларының әр түрлі механизмдерін зерттелген. Купраттарда кемтіктік тасымалдаушылардың локализацияланған күйлерінің болу жағдайы зерттелген. Купраттардың заряд тасымалдау саңылауларында өте әлсіз қосындылау кезінде қоспалар маңында және деформацияланатын торда локализацияланған кемтіктік тасымалдаушыларының жеке деңгейлері түзілетіндігі көрсетілген. Қосындылау деңгейін жеткіліксіз қосындалған аймаққа қарай арттырған сайын, мұндай заряд тасымалдаушылардың энергия деңгейлері қосындалаудың жоғарылауымен бірте-бірте кеңейетін энергиялық аймақтар құрыла бастайды. La негізіндегі кемтіктік қосындыланған купраттағы асқын өткізгіште металл-диэлектриктің ауысуын зерттеу үшін екі тасымалдаушыға ие купратты асқын өткізгіштің жаңа үлгісі ұсынылды. Кемтіктік тасымалдаушылар қоспалы мен поляронды аймақтарда болғанда, кіші радиусты қоспаларға ие La негізіндегі асқын өткізгіштердегі металл-диэлектрик ауысулары сәйкесінше жоғары және төмен қосындылау деңгейлерінде жүретіні көрсетілген.

**Кілт сөздері:** Кемтіктік-қосындыланған купраттар, тасымалдаушылардың локализациясы, «металл-диэлектрик» ауысулары.

*Джуманов С., Курбанов У.Т., Худайбердиев З.С.*

#### **Металл-диэлектрик переходы в легированных лантановых сверхпроводниках с допантами малого радиуса**

В настоящей работе исследуются различные механизмы металл-диэлектрик переходов в дырочно легированных купратах, вызванных локализацией носителей заряда вблизи примесей малого радиуса и в деформируемой решетке (т.е. в отсутствие примесей). Исследовано условие существования локализованных состояний дырочных носителей в купратах. Показано, что при очень слабом легировании в щели переноса заряда купратов формируются отдельные уровни дырочных носителей, локализованные вблизи примесей и в деформируемой решетке. По мере увеличения уровня легирования в сторону недолегированной области энергетические уровни таких носителей заряда начинают формировать энергетические зоны, которые постепенно расширяются с ростом легирования. Предложена новая модель купратного сверхпроводника с двумя носителями для изучения металл-диэлектрик перехода в дырочно-легированном купратном сверхпроводнике на основе лантана. Показано, что, когда дырочные носители находятся в примесной и поляронной зонах, металл-диэлектрик переходы в сверхпроводниках на основе La с примесями малого радиуса происходят соответственно при высоком и низком уровнях легирования.

**Ключевые слова:** Дырочно-легированные купраты; локализация носителей; переходы «металл-диэлектрик».

*Рахадиллов Б.К., Сатбаева З.А., Кожанова Р.С., Kowalewski P., Байтанова Л.Б., Калитова А.А.*

#### **20Cr2Ni4A болаттың қаттылығы мен тозуға төзімділігіне көлемдік және беттік шынықтырудан кейін қалыптасқан құрылымның әсері**

Жұмыста 20Cr2Ni4A болаттың құрылымы мен қасиеттеріне көлемдік және беттік шынықтырудың әсерін салыстырмалы түрде жүргізілген зерттеу нәтижелері келтірілген. Беттік шынықтыру электролитті-плазмалық әдіспен жүзеге асырылды. Көлемдік шынықтыру 870°C температураға дейін қыздырып, кейін суда және майда салқындату жолымен жүзеге асырылды. 20Cr2Ni4A болат үлгілерінің құрылымдық-фазалық күйлері металлографиялық және рентгендік құрылымдық талдау әдістерімен зерттелген. Шар-диск сұлбасы бойынша үлгілердің трибологиялық сынақтары жүргізілді, сондай-ақ үлгілердің микроқаттылығы анықталды. Көлемдік және беттік шынықтырудан кейін 20Cr2Ni4A болаттың қаттылығы мен тозуға төзімділігі жоғарылайтыны анықталды. Бұл жағдайда электролитті-плазмалық шынықтырудан өткен

үлгілерде айтарлықтай өзгеріс байқалады. Электролитті-плазмалық шынықтырудан кейін 20Cr2Ni4A болатының қаттылығы мен тозуға төзімділігінің жоғары мәндері ұсақ инелі мартенситтің пайда болуымен байланысты екендігі анықталды.

**Кілт сөздері:** құрылым, фазалық құрам, электролитті-плазмалық шынықтыру, микроқаттылық, тозуға төзімділік.

*Рахадиллов Б.К., Сатбаева З.А., Кожанова Р.С., Kowalewski P., Баятанова Л.Б., Калитова А.А.*

**Влияние структуры, сформированной после объемной и поверхностной закалки, на твердость и износостойкость стали 20Cr2Ni4A**

В работе представлены результаты сравнительного изучения влияния объемной и поверхностной закалки на структуру и свойства стали 20Cr2Ni4A. Поверхностная закалка осуществлялась электролитно-плазменным методом. Объемная закалка проведена нагревом до температуры 870°C с последующим охлаждением в воде и в масле. Были изучены структурно-фазовые состояния образцов стали 20Cr2Ni4A методами металлографического и рентгеноструктурного анализа. Были проведены трибологические испытания образцов по схеме шар-диск, а также была определена микротвердость образцов. Определено, что после объемной и поверхностной закалки повышается твердость и износостойкость стали 20Cr2Ni4A. При этом самое значительное изменение наблюдается в образцах, прошедших электролитно-плазменную закалку. Установлено, что высокие значения твердости и износостойкости стали 20Cr2Ni4A после электролитно-плазменной закалки связаны с формированием мелкоигольчатого мартенсита.

**Ключевые слова:** структура, фазовый состав, электролитно-плазменная закалка, микротвердость, износостойкость.

*Аймуханов А.К., Зейниденов А.К., Рожкова К.С., Ахатова Ж.Ж.*

**Фталоцианиндер нанокұрылымдарының полимерлі күн элементінің оптикалық және фотовольтаикалық сипаттамаларына әсері**

Нанокөпозиттік полимерлі күн ұяшықтары алынды. Фталоцианиндердің нанокұрылымдары концентрациясы 0,5% фотоактивті қабаттың қоспасына қосылды. Фотоактивті қабат центрифугалау әдісімен айналу жылдамдығы 1500 айн/мин болған кезде жағылды. Атомдық күштік микроскоппен қабыршақтар беттерінің суреттері алынды. Көпозиттік қабыршақтардың жұтылу спектрлері өлшенді. Фотоактивті қабатқа фталоцианиндер нанокұрылымдарын енгізу жұтылу максимумда наноөзектер үшін 2,1 есе және нанобөлшектер үшін 1,9 есе артуына спектрдің кеңеюіне және оптикалық тығыздық мәнінің әкелетіні анықталды. Көпозиттік органикалық күн ұяшықтарының вольт-амперлік сипаттамалары өлшенді. Бұл үшін фотоактивті қабаттың бетіне  $10^{-5}$  Торр кезінде қалыңдығы 100 нм алюминий электрод бүркілді. Фотоактивті қабатқа фталоцианиндер және нанобөлшектер енгізген кезде, вольт-амперлік сипаттаманың қысқа тұйықталу тогының тығыздығы сәйкесінше 8% және 5% - ға артты, ал пайдалы әсер коэффициентінің мәні сәйкесінше 4,8% және 4,51% дейін өсті. Көпозиттік органикалық күн ұяшықтарының импеданс спектрлері өлшенді. Нанокөпозиттік қабыршақтардың годографтарын талдау фотоактивті қабатқа фталоцианиндердің наноөзектері мен нанобөлшектерін енгізу диффузия ұзындығының сәйкесінше 2,2 есе және 1,8 есе артуына және заряд тасымалдаушылардың қозғалғыштығының 1,4 есе және 1,2 есе өсуіне әкелетінін көрсетті.

**Кілт сөздері:** жартылайөткізгіш полимерлер, металофталоцианиндер, заряд тасымалдағыштардың генерациясы және транспорты, фотовольтаика.

*Аймуханов А.К., Зейниденов А.К., Рожкова К.С., Ахатова Ж.Ж.*

**Влияние наноструктур фталоцианинов на оптические и фотовольтаические характеристики полимерного солнечного элемента**

Получены нанокөпозиттные полимерные солнечные ячейки. Наноструктуры фталоцианинов добавляли в смесь фотоактивного слоя в концентрации 0,5%. Фотоактивный слой наносился методом центрифугирования при скорости вращения 1500 обр/мин. Атомно-силовым микроскопом были измерены изображения поверхности пленок. Измерены спектры поглощения композиционных пленок. Установлено, что внедрение наноструктур фталоцианинов в фотоактивный слой приводит к уширению спектра и возрастанию значения оптической плотности в максимуме поглощения в 2,1 раза для наностержней и 1,9 раз для наночастиц. Измерены вольт-амперные характеристики композиционных органических солнечных ячеек. Для этого на поверхность фотоактивного слоя при  $10^{-5}$  Торр напылялся алюминиевый электрод толщиной 100 нм. Показано, что при допировании фотоактивного слоя наностержнями и наночастицами фталоцианинов плотность тока короткого замыкания вольт – амперных характеристик увеличилась на 8% и 5% соответственно, а значение коэффициента полезного действия возросло до 4,58% и 4,51% соответственно. Измерены спектры импеданса композиционных органических солнечных ячеек. Анализ годографов нанокөпозиттных пленок показал, что допирование фотоактивного слоя наностержнями и наночастицами фталоцианинов приводит к увеличению длины диффузии в 2,2 раза и 1,8 раза соответственно и росту

значения подвижности носителей заряда в 1,4 раза и 1,2 раза.

**Ключевые слова:** полупроводниковые полимеры, металлофталоцианины, генерация и транспорт носителей заряда, фотовольтаика.

*Зейниденов А.К., Аймуханов А.К., Омарбекова Г.И., Ильясов Б.Р.*

**$\text{In}_2\text{O}_3$  қабыршақтарын күйдіру температурасының полимерлі күн элементінің фотоэлектрлік сипаттамаларына әсері**

$\text{In}_2\text{O}_3$  қабыршақтарының электронды тасымалының тиімділігін арттыру үшін, оны термиялық күйдірудің морфологиясына, жұтылуына, фотоэлектрлік қасиеттеріне әсерін анықтау қажет. Жұмыста спин-коатинг әдісімен алынған  $\text{In}_2\text{O}_3$  қабыршақтарын күйдіру температурасының полимерлі күн элементінің оптикалық және фотоэлектрофизикалық сипаттамаларына әсерін зерттеу нәтижелері келтірілген. Қабыршақтарды күйдіру температурасының жоғарылауы жұтылудың және қабыршақтың тыйым салынған аймағының оптикалық енінің жоғарылауына алып келетіні анықталды. Қабыршақтарды күйдірудің оңтайлы температурасы  $T=300^\circ\text{C}$  анықталды, бұл температурада фотобелсенді қабаттағы электрондар заряд тасымалдаушыларының максималды өмір сүру уақытына және төмен рекомбинация ықтималдығына ие. Осы температурада полимерлі күн элементінің ПӘК-нің максималды мәні байқалады.

**Кілт сөздері:**  $\text{In}_2\text{O}_3$ , полимерлі күн элементі, вольтамперлік сипаттамалары, импеданс спектрлері.

*Зейниденов А.К., Аймуханов А.К., Омарбекова Г.И., Ильясов Б.Р.*

**Влияние температуры отжига пленок  $\text{In}_2\text{O}_3$  на фотоэлектрические характеристики полимерного солнечного элемента**

Для повышение эффективности электронного транспорта пленок  $\text{In}_2\text{O}_3$  необходимо определить влияние термического отжига на морфологию, поглощение, фотоэлектрические свойства. В работе представлены результаты исследования влияния температуры отжига пленок  $\text{In}_2\text{O}_3$  полученных методом спин-коатинг на оптические и фотоэлектрофизические характеристики полимерного солнечного элемента. Установлено, что повышение температуры отжига пленок приводит к возрастанию поглощения и оптической ширины запрещенной зоны пленки. Определена оптимальная температура отжига пленок  $T=300^\circ\text{C}$ , при которой электроны в фотоактивном слое обладают максимальным временем жизни носителей заряда и низкой вероятностью к рекомбинации. При данной температуре наблюдается максимальное значение КПД полимерного солнечного элемента.

**Ключевые слова:**  $\text{In}_2\text{O}_3$ , полимерный солнечный элемент, вольтамперные характеристики, спектры импеданса.

*Калужский Д. Л., Мехтиев А. Д., Нешина Е. Г., Алькина А. Д., Сарсикеев Е. Ж.*

**Еркін поршеньді қозғалтқыш және кері генератор негізіндегі жылу энергетикалық қондырғы**

Мақалада Стирлинг қозғалтқышы мен поршеньді генераторы негізінде автономды электрмен қамсыздану жүйесі қарастырылған. Оның жұмыс істеу жағдайларға, сыртқы жану қозғалтқышын және сызықтық синхронды генераторды тандауға талдау жүргізілген. Автономды тұтынушыларды қалалық инфрақұрылымнан алыс орналасқан жылу және электр энергиясымен қамтамасыз ету мәселесін шешу барысында қуаттылығы 100 Вт дейінгі электр станциясы әзірленіп, дайындалды. Оның эксперименттік зерттеуі, сондай-ақ патенттік-аппараттық массивті талдау берілген техникалық объектіні пайдалану шекарасын анықтауға мүмкіндік берді. Кері-ілгерілмелі генератор сыртқы жылу берілісіне ие еркін поршеньді қозғалтқышпен жұмысқа қосылады. Табиғи эксперименттерді жүргізу үшін айнымалы тоқтың сызықтық генераторына ие сыртқы жылу бергіші бар еркін поршеньді қозғалтқыштың зертханалық үлгісінің прототипі әзірленді. Оның Стирлинг қозғалтқыштарының белгілі түрлерінен басты айырмашылығы - иінді білікпен және айналмалы механизміне ие массивті маховиктік болмауы, ал бұл өз кезекте жоғары герметизациялауға қол жеткізуге мүмкіндік береді және сыртқы өлшемдерді шектеу кезінде шығыс білігіндегі қуатты едәуір арттырады. Жұмыс денесі ретінде судың аз пайызы қосылған ауа қолданылады, бұл 10 МПа дейінгі қысымды дамытуға мүмкіндік береді. Генератор конструкциясының техникалық есебі келтірілген, жылжымалы элементтің кері-ілгерілмелі қозғалысы кезінде қажетті қуатты дамытуға қажетті күш анықталған. Тұтынушыларда жайсыздық тудыратын акустикалық шуды басу үшін шешімдер қабылданды. Атап айтқанда, мұны діріл сөндіргіштерді орналастыру және ПӘК-і жоғары генераторды жобалау арқылы жасауға болады. Жылжымалы элементтің конструкциясы орамалар немесе магниттерге салынатын механикалық жүктемені азайтуы тиіс. Ұсынылған генератор бәсекеге қабілетті болуы мүмкін және дизельді немесе бензин қозғалтқыштарымен дәстүрлі төмен қуатты электр көздерін сәтті алмастыра алады.

**Кілт сөздері:** микроэлектростанция, Стирлинг қозғалтқышы, поршеньді генераторы, балама көзі.

*Калужский Д. Л., Мехтиев А. Д., Нешина Е. Г., Алькина А. Д., Сарсикеев Е. Ж.*

**Тепловая энергетическая установка на основе свободного поршневого двигателя и обратного генератора**

В статье рассматривается автономная система электроснабжения на базе двигателя Стирлинга и поршневого генератора. Проанализированы условия его эксплуатации, выбор двигателя внешнего сгорания и линейного синхронного генератора. В ходе решения задачи по обеспечению автономных потребителей тепловой и электрической энергией, удаленных от городской инфраструктуры, была разработана и изготовлена электростанция мощностью до 100 Вт. Его экспериментальное изучение, а также анализ патентно-информационного массива позволили определить границы использования данного технического объекта. Возвратно-поступательный генератор приводится в действие свободнопоршневым двигателем с внешним подводом тепла. Для проведения натурных экспериментов разработан прототип лабораторного образца свободнопоршневого двигателя с внешним подводом тепла с линейным генератором переменного тока. Его главное отличие от известных типов двигателей Стирлинга - отсутствие массивного маховика с коленчатым валом и кривошипно-шатунным механизмом, что позволяет добиться большей герметичности и значительно увеличивает мощность на выходном валу при ограничении внешних габаритов. В качестве рабочего тела используется воздух с добавлением небольшого процента воды, что позволяет развивать давление до 10 МПа. Приведен технический расчет конструкции генератора, определена сила, необходимая для развития необходимой мощности при возвратно-поступательном движении подвижного элемента. Были приняты решения для подавления акустического шума, вызывающего дискомфорт у потребителей. В частности, это можно сделать, разместив гасители вибрации и спроектировав генератор с высоким КПД. Конструкция подвижного элемента должна сводить к минимуму механическую нагрузку на обмотки или магниты. Предлагаемый генератор может быть конкурентоспособным и может успешно заменить традиционные маломощные источники электроэнергии с дизельными или бензиновыми двигателями.

**Ключевые слова:** микроэлектростанция, двигатель Стирлинга, поршневой генератор, альтернативный источник.

*Новоселов И.Ю., Шрагер Э.Р., Тихонов А.Е.*

**Жоғары жиілікті алау разрядының төмен температуралы плазмасында уран-торий оксидті ұнтақтарын синтездеу**

Мақалада жаңа буынды отын – дисперсиялық ядролық отын үшін уран-торий оксидінің ұнтақтарын плазмохимиялық синтездеу процесі қарастырылған. Зерттеулер процесінде бастапқы прекурсорлардың жану көрсеткіштерін есептеуі жүргізілді. Прекурсорлар ретінде су-органикалық нитрат ерітінділері алынды, ал олардың негізі уранил және торий нитраттары (бөлінетін құраушылар), сондай-ақ магний нитраты (матрица материалы) болды. Ерітінділердің органикалық құраушысы ретінде ацетон алынды, себебі ол жылу шығару қабілеттілігінің жоғары мәніне және жақсы өзара ерігіштікке ие. Термодинамикалық есептеулер барысында төменгі температуралы ауа плазмасында бастапқы су-органикалық нитрат ерітінділерін қайта өңдеудің оңтайлы режимдері анықталды. Бұл режимдер қышқылданбаған көміртектің (күйенің) жанама қоспаларынсыз қажетті стехиометрияның отын композицияларының синтезін қамтамасыз етеді. Ұнтақтардың тәжірибелік партияларын алу бойынша эксперименттік зерттеулер модельдік қоспаларда жүргізілген, онда уранил мен торий нитраттары олармен периодтық кестенің бір тобында орналасқан неодим және церий нитраттарымен алмастырылды. Синтез процесі негізі жоғары жиілікті алау типті плазмотрон болатын плазмохимиялық стендті қолдану арқылы жүргізілген. Оксидті композициялардың синтезделген ұнтақтары электронды микроскопия, гранулометриялық талдау, рентгенді-фазалық талдау және БЭТ-талдауды қоса, бірқатар талдаулардан өтті. Талдау нәтижелері алынған ұнтақтарды наноөлшемдер класына жатқызуға болатындығын көрсетті.

**Кілт сөздері:** жоғары жиілікті алау разряды, плазма, ұнтақ, ядролық отын, уран, торий, талдау.

*Новоселов И.Ю., Шрагер Э.Р., Тихонов А.Е.*

**Синтез уран-ториевых оксидных порошков в низкотемпературной плазме высокочастотного факельного разряда.**

В статье рассмотрен процесс плазмохимического синтеза уран-ториевых оксидных порошков для топлива нового поколения – дисперсионного ядерного топлива. В процессе исследований проводился расчет показателей горения исходных прекурсоров. Прекурсорами выступали водно-органические нитратные растворы, основу которых составляли нитраты уранила и тория (делящиеся компоненты), а также нитрат магния (материал матрицы). Органическим компонентом растворов выступал ацетон ввиду достаточно высокого значения теплотворной способности и хорошей взаимной растворимости. В ходе термодинамических расчетов были определены оптимальные режимы переработки исходных водно-органических нитратных растворов в низкотемпературной воздушной плазме. Данные режимы обеспечивают синтез топливных композиций необходимой стехиометрии без побочных примесей неокисленного углерода (сажи). Экспериментальные исследования по получению опытных партий

порошков проведены на модельных смесях, в которых нитраты уранила и тория заменены на нитраты неодима и церия, которые находятся с ними в одной группе периодической таблицы. Процесс синтеза производился с использованием плазмохимического стенда, основу которого составлял высокочастотный плазмотрон факельного типа. Синтезированные порошки оксидных композиций подвергались ряду анализов, включая электронную микроскопию, гранулометрический анализ, рентгенофазовый анализ и БЭТ-анализ. Результаты анализов показали, что полученные порошки можно отнести к классу наноразмерных.

**Ключевые слова:** высокочастотный факельный разряд, плазма, порошок, ядерное топливо, уран, торий, анализ.

*Обухов С. Ж., Плотников, И. А., Климова Н.К.*

#### **Техникалық сипаттамаға сәйкес фотоэлектрлік модуль параметрлерін анықтаудың жаңа әдісі**

Берілген мақалада нақты жұмыс жағдайында фотоэлектрлік модульдің математикалық моделін құру әдістемесі берілген, бұл модель энергиялық сипаттамаларын қайта жаңғыртуға мүмкіндік береді. Сондай-ақ, фотоэлектрлік түрлендіргіштердің математикалық модельдерінің негізгі түрлері қарастырылып, олардың параметрлерін бағалаудың ең танымал әдістері талданды. Бағдарламалауды қолданбай және сандық бағалау алгоритмдерін құрмай-ақ, техникалық спецификация мәліметтері бойынша фотоэлектрлік модульдің параметрлерін анықтаудың түпнұсқа және қарапайым әдісі ұсынылған. Ұсынылған әдіс «шешімдерді іздеу» құралы орнатылған Excel кестелік бағдарламасында оңай жүзеге асырылады. Kuosera KC200GT фотоэлектрлік модульдің вольт-амперлік сипаттамасын модельдеудің нәтижелері температура мен жарықталуының кең диапазоны үшін ұсынылған. Сонымен қатар, модельдің сипаттамалары мен эксперименттік мәліметтерді салыстыру арқылы дәлдік бағаланды. Бірқатар фотоэлектрлік модульдер үшін модельге сынақ жүргізілді, модельдеу нәтижелерінің өндірушінің мәліметтерімен жақсы сәйкестілігін көрсетті. Модель MPP аймағында (максималды қуат нүктесі) модельдеудің жоғары дәлдігін қамтамасыз етеді. Бұл факт оны фотоэлектрлік станция контроллерлерінің тиімді алгоритмдерін жасау, түрлендіргіш құрылғылардың электр тізбегін жақсарту, электр энергиясын өндіруін болжау, жұмыс режимдерін талдау және фотоэлектрлік жүйелерді оңтайландыру үшін пайдалануға мүмкіндік береді.

**Кілт сөздері:** фотоэлектрлік модуль, күн элементі, бір диодтағы эквивалентті алмастыру сұлбасы, фотоэлектрлік модуль параметрлерін анықтау.

*Обухов С.Г., Плотников И.А., Климова Г.Н.*

#### **Новый метод определения параметров фотоэлектрического модуля по данным технической спецификации**

В данной статье представлена методика построения математической модели фотоэлектрического модуля, позволяющая воспроизвести его энергетические характеристики в реальных условиях эксплуатации. Также рассмотрены основные типы математических моделей фотоэлектрических преобразователей и проанализированы наиболее известные методы оценки их параметров. Предложен оригинальный и простой способ определения параметров фотоэлектрического модуля по данным технической спецификации без использования программирования и разработки алгоритмов численной оценки. Предлагаемый метод легко реализуется в табличной программе Excel с установленным инструментом «Поиск решений». Представлены результаты моделирования ВАХ (ВАХ) фотоэлектрического модуля Kuosera KC200GT в широком диапазоне изменения температуры и освещенности. Кроме того, производится оценка точности путем сравнения характеристик модели и экспериментальных данных. Модель была протестирована на ряде фотоэлектрических модулей и показала хорошее соответствие результатов моделирования данным производителя. Модель обеспечивает высокую точность моделирования в районе MPP (точка максимальной мощности). Этот факт позволяет использовать его для разработки эффективных алгоритмов контроллеров фотоэлектрических станций, усовершенствования схмотехники преобразовательных устройств, прогнозирования выработки электроэнергии, анализа режимов работы и оптимизации фотоэлектрических систем.

**Ключевые слова:** фотоэлектрический модуль, солнечный элемент, эквивалентная схема замещения на одном диоде, определение параметров фотоэлектрического модуля.

*Сенють В.*

#### **Жоғары қысым мен жоғары температура жағдайында алюминий қосылған, механикалық белсендірілген графит тәрізді бор нитридінен синтезделген нано- және микроөлшемді кубтық BN негізіндегі материалдың құрылымын зерттеу**

Мақалада hBN → cBN фазалық түрлендірудің бастамашысы рөлін атқаратын алюминийдің (Al) қатысуымен жоғары қысым мен жоғары температура жағдайында механикалық белсендірілген графит тәрізді бор нитридінен алынған нано- және микроөлшемді кубтық бор нитридіне (cBN) негізделген материалдың құрылымы мен фазалық құрамы зерттелген. Механикалық белсендіруді қолдану hBN-де cBN

дәндерінің пайда болуына ықпал ететіні көрсетілген, бұл соңғы өнімнің дисперсиясын арттыруға мүмкіндік береді. cBN синтезінің технологиялық параметрлері және Al мөлшері - материалдың құрылымына, сондай-ақ ондағы BN кубтық фазасының құрамына айтарлықтай әсер етеді. hBN(MA)-10%Al жүйесі үшін қысымның 2,5-тен 5,5 ГПа-ға дейін және температураның 1550°C-тан 1750°C-қа дейін жоғарылауы cBN фазасының құрамының 10-15% - дан 90% - ға дейін жоғарылауына ықпал етеді. Сонымен қатар, 2,5 және 5,5 ГПа қысымында синтезделген cBN дәндерінің өлшемі сәйкесінше 200-500 нм және 40-120 нм аралығында болады. Al мөлшерінің, температураның және cBN синтезінің ұзақтығының артуы шамамен 10-50 мкм үлкен cBN дәндерінің пайда болуына әкеледі.

**Кілт сөздері:** механикалық белсендіру, фазалық түрлену, бордың нанокұрылымдық кубтық нитриді, жоғары қысым және температура, синтез.

*Сенють В.Т.*

**Исследование структуры материала на основе нано- и микроразмерного кубического BN, синтезированного из механоактивированного графитоподобного нитрида бора с добавкой алюминия в условиях высокого давления и высокой температуры**

В статье исследована структура и фазовый состав материала на основе нано- и микроразмерного кубического нитрида бора (cBN), полученного в условиях высоких давлений и высоких температур из механоактивированного графитоподобного нитрида бора (hBN) в присутствии алюминия (Al), который играет роль инициатора фазового превращения hBN → cBN. Показано, что использование механоактивации способствует образованию зародышей cBN в hBN, что позволяет повысить дисперсность конечного продукта. Технологические параметры синтеза cBN и количество Al оказывают существенное влияние на структуру материала, а также на содержание в нем кубической фазы BN. Повышение давления для системы hBN(MA)-10%Al с 2.5 до 5.5 ГПа и температуры с 1550°C до 1750°C способствует увеличению содержания фазы cBN с 10-15% до 90%. При этом размер зерен cBN, синтезированных при давлениях 2.5 и 5.5 ГПа, находится в пределах 200–500 нм и 40–120 нм соответственно. Увеличение количества Al, температуры и продолжительности синтеза cBN приводит к образованию крупных зерен cBN размером около 10-50 мкм.

**Ключевые слова:** механическая активация, фазовое превращение, наноструктурный кубический нитрид бора, высокое давление и температура, синтез.

*Волокитина И.Е., Волокитин А.В., Панин Е.А., Латыпова М.А., Касымов С.С.*

**«Тең арналы бұрыштық престеу-созу» әдісімен деформациялау кезіндегі болат алюминий сымның микроқұрылымының эволюциясы**

Тең арналы бұрыштық престеу-созудың микроқұрылым эволюциясына және сымның механикалық қасиеттерінің өзгеруіне әсерін эксперименттік зерттеулер кешені барысында ультра ұсақ түйіршікті құрылымды қалыптастыру және болат алюминий сымның беріктік қасиеттерін арттыру үшін ұсынған үздіксіз әдісті қолданудың негізгі мүмкіндігі мен қолдану тиімділігі дәлелденген. Деформация бөлме температурасында үш өту кезінде жүргізілген. Биметал сымның екі қабаты да біркелкі өңделмегені көрсетілген. Бастапқы дән өлшемі 22 мкм болатын алюминий қабығы орташа есеппен 2 мкм-ге дейін өңделеді. Болат өзекшеде көлденең және бойлық қималарда әр түрлі дән өлшемдері кездеседі. Сонымен, бастапқы өлшемі 18 мкм дәндер деформациядан кейін дәндердің өлшемі бойлық қимада шамамен 10 мкм, ал көлденең қимада – 8 мкм құрайды.

**Кілт сөздері:** қарқынды пластикалық деформация, микроқұрылым, биметалл сым, болат, алюминий, механикалық қасиеттер.

*Волокитина И.Е., Волокитин А.В., Панин Е.А., Латыпова М.А., Касымов С.С.*

**Эволюция микроструктуры сталеалюминиевой проволоки при деформации методом «равноканального углового прессования-волочения»**

В ходе комплекса экспериментальных исследований влияния равно-канального углового прессования-волочения на эволюцию микроструктуры и изменение механических свойств проволоки доказана принципиальная возможность и эффективность использования предлагаемого непрерывного способа для формирования ультра мелкозернистой структуры и повышения прочностных свойств сталеалюминиевой проволоки. Деформирование проводилось при комнатной температуре за три прохода. Показано, что оба слоя биметаллической проволоки обрабатываются неравномерно. Алюминиевая оболочка с начальным размером зерен 22 мкм прорабатывается в среднем до 2 мкм. Стальной сердечник имеет различную величину зерна в поперечном и продольном сечениях. Так с начальным размером зерен 18 мкм после деформирования в продольном сечении размер зерен составляет порядка 10 мкм, а в поперечном – 8 мкм.

**Ключевые слова:** интенсивная пластическая деформация, микроструктура, биметаллическая проволока, сталь, алюминий, механические свойства.

*Кубиц В.И., Чернета О.Г., Юров В.М., Балтабеков А.С., Гученко С.*

**«CuCrNiZrTi – KЧ50», «CuCrNiZrTi – 40X», «CuCrNiZrTi – 12X2H2» материалдар жүйесіндегі трибологиялық байланыс**

Үйкелістің молекулалық құраушысы - адгезивтік байланыстың ығысу беріктігі және әрбір нақты зерттеу үшін молекулалық құраушының пьезоэлектрлік коэффициенті параметрлерінің абайқалуы туралы шектеулі ақпарат - нәтижені бағалаудың объективтілігі мен дәлдігін арттыру мақсатында кіші көлемді үлгілерде ығысуды модельдеу арқылы параметрлерді мақсатты түрде алдын-ала анықтайды. Мақалада болатпен, шойынмен жанасу кезіндегі жүктеме-майлау режимдеріне бейімделуін және кіші өлшемді үлгілерде ығысуды модельдеу арқылы адгезия қасиеттерінің параметрлерін байқалуын бағалау үшін жоғары энтропиялы CuCrNiZrTi қорытпасының анықталған триботехникалық сынақтарды өткізу есебі қойылған. Триботехникалық сынақтар СМЦ-2 үйкеліс машинасында екі сатыда «жылжымалы диск - тұрақты колодка» үйкеліс сұлбасы бойынша кіші өлшемді үлгілерде жүргізілді. Үлгілер - дискілер келесі материалдардан жасалған: болат 40X, болат 12X2H2, шойын KЧ50. Үлгілер – колодкалар жоғары энтропиялы CuCrNiZrTi (890 HV) қорытпасынан жасалған. Майлаушы материал ретінде 50°C кезінде динамикалық тұтқырлығы 0,106 Па • с болатын ТАД-17И 85W90 трансмиссиялық майы қолданылды. Зерттелінетін материалдар үлгілерінің беттерін тамшылатып майлау жағдайында үйлесімді болып көрінеді және қанағаттанарлықтай жұмыс істейді. Бұл жағдайда жылдамдық пен күштің жүктелуінің параметрлері шекаралық майлаудың көрінісін анықтайды. Орнатылған үйкеліс режиміне жету уақыты барлық жүйелер үшін іс жүзінде бірдей және 7,5 минуттан кейін байқалады. Сонымен қатар, майлау кезіндегі материалдар жүйелері 140-тан 230 Н-қа дейінгі қалыпты жүктеме күшінің интервалында бірдей тұрақты болды және үйкелістің динамикалық коэффициентінің келесі мәндерін көрсетті: «KЧ50-CuCrNiZrTi»  $\mu=0,13$ ; «40X-CuCrNiZrTi»  $\mu=0,22$ ; «12X2H4-CuCrNiZrTi»  $\mu=0,17$ . Алынған графикалық заңдылықтар және олардың математикалық жуықтау параметрлері ығысу жылдамдығының өзгерісі кезіндегі CuCrNiZrTi жүйесінің адгезиялық қасиеттерінің өзгеру сипатын анықтауға мүмкіндік берді.

**Кілт сөздері:** материалдар жүйесі, үйкеліс коэффициенті, пьезоэлектрлік коэффициент, ығысу, тангенциалдық беріктік, майлау.

*Кубиц В.И., Чернета О.Г., Юров В.М., Балтабеков А.С., Гученко С.*

**Трибологический контакт в системах материалов «CuCrNiZrTi – KЧ50», «CuCrNiZrTi – 40X», «CuCrNiZrTi – 12X2H2»**

Ограниченность сведений о проявлении параметров молекулярной составляющей трения – сдвиговой прочности адгезионной связи и пьезокоэффициента молекулярной составляющей для каждого конкретного исследования предопределяет использование целенаправленного определения параметров моделированием сдвига на малогабаритных образцах с целью повышения объективности и точности оценки результата. В статье поставлена задача о проведении определительных триботехнических испытаний высокоэнтропийного сплава CuCrNiZrTi для оценки его приспособляемости к режимам нагружения и смазыванию при контактно-взаимодействии со сталью, чугуном и проявления параметров адгезионных свойств моделированием сдвига на малогабаритных образцах. Триботехнические испытания проводились на машине трения СМЦ-2 в два этапа на малогабаритных образцах по схеме трения «подвижный диск – неподвижная колодка». Образцы – диски изготавливались из следующих материалов: сталь 40X, сталь 12X2H2, чугун KЧ50. Образцы – колодки изготавливались из высокоэнтропийного сплава CuCrNiZrTi (890 HV). В качестве смазочного материала использовалось трансмиссионное масло ТАД-17И 85W90 с динамической вязкостью 0.106 Па•с при 50°C. В условиях капельного смазывания поверхности образцов исследуемых материалов представляются совместимыми и удовлетворительно прирабатываются. При этом параметры скоростного и силового нагружения обуславливают проявление граничной смазки. Выход по времени на режим установившегося трения практически одинаков для всех систем, и наблюдается через 7,5 мин. При этом системы материалов при смазывании были одинаково стабильны в интервале силы нормального нагружения от 140 до 230 Н и показали следующие значения динамического коэффициента трения: «KЧ50- CuCrNiZrTi»  $\mu=0,13$ ; «40X- CuCrNiZrTi»  $\mu=0,22$ ; «12X2H4- CuCrNiZrTi»  $\mu=0,17$ . Полученные графические закономерности и параметры их математического аппроксимирования позволили определить характер изменения адгезионных свойств системы CuCrNiZrTi при изменении скоростей сдвига.

**Ключевые слова:** система материалов, коэффициент трения, пьезокоэффициент, сдвиг, тангенциальная прочность, смазочное образование.

*Утепов Е.Б., Толкынбаев Т.А., Анискин А., Ахажанов С.Б., Жарасов Ш.Ж., Тулебекова А.С., Акишев М.С.*

**Бетонның қатаю жағдайларын бақылау және бағалау үшін мультисенсорлы құрылғыны құрастыру**

Бетонның механикалық сипаттамаларын зерттеудің дәстүрлі тікелей және жанама әдістері негізінен оның беріктігі мен сапасына айтарлықтай әсер етуі мүмкін бетон денесінде болатын үздіксіз ішкі және сыртқы құбылыстарды елемей, дискретті өлшеулер жүргізеді. Бұл зерттеу мультисенсорлық құрылғыны және қатаю

температурасының, қоршаған орта температурасының және салыстырмалы ылғалдылықтың бетонның беріктігіне әсерін бір уақытта өлшеуге және бағалауға мүмкіндік беретін әдісті ұсынады. Құрылғы Arduino Pro Mini микроконтроллерінің негізінде әртүрлі сенсорлармен, сондай-ақ сағат оқу және жад модульдерімен біріктірілген. Бетонның беріктігіне әртүрлі факторлардың әсерін бағалаудың ұсынылған әдісі беріктік сынақтары мен олардың сенімді қисығына, бетонның қатаю жағдайларын бақылауға, корреляция және өлшеу әдістеріне негізделген. Ұсынылған құрылғының және оның әдісінің тиімділігі әр түрлі мөлшердегі бетонның текше үлгілерін қолдана отырып, эксперименттік түрде негізделді. Үлгілерді бақылау нәтижелерін визуализациялау үшін көп сенсорлы құрылғыға арналған бағдарламалық интерфейсті жасау кезінде ескерілетін түсті градациялар, жапырақ және бағаналы диаграммалар қолданылды.

**Кілт сөздері:** бетон беріктігі, сенсорлар, үздіксіз құбылыстар, Arduino, мониторинг.

*Утепов Е.Б., Толкынбаев Т.А., Анискин А., Ахажанов С.Б., Жарасов Ш.Ж., Тулебекова А.С., Акишев М.С.*

#### **Сборка мультисенсорного устройства для мониторинга и оценки условий твердения бетона**

Традиционные прямые и косвенные методы исследования механических характеристик бетона в основном проводят дискретные измерения, упуская из виду непрерывные внутренние и внешние явления, происходящие в теле бетона, которые могут существенно повлиять на его прочность и качество. В данном исследовании представлены мультисенсорное устройство и метод, позволяющие одновременно измерять и оценивать влияние температуры твердения, температуры окружающей среды и относительной влажности на прочность бетона. Устройство было собрано на основе микроконтроллера Arduino Pro Mini, соединенного с различными датчиками, а также модулями чтения часов и памяти. Предложенный метод оценки влияния различных факторов на прочность бетона основан на испытаниях прочности и их доверительной кривой, мониторинге условий твердения бетона, методах корреляции и взвешивания. Работоспособность предлагаемого устройства и его метода была обоснована экспериментально с использованием кубических образцов бетона различного размера. Для визуализации результатов мониторинга образцов использовались цветные градации, лепестковые и столбчатые диаграммы, которые будут учтены при разработке программного интерфейса для мультисенсорного устройства.

**Ключевые слова:** прочность бетона, сенсоры, непрерывные явления, Arduino, мониторинг.

*Нусупбеков Б.Р., Сақыпова С.Е., Edris A., Хасенов А.К., Нусупбеков У.Б., Болатбекова М.*

#### **Құрамында фосфоры бар шламды өңдеудің электрогидравликалық әдісі**

Фосфор өндірісінің улы қалдықтарын өңдеудің тиімді әдісін құру, сонымен қатар шлам түзілу процесінің өзін басу әлі де өзекті болып табылады. Бұл мақалада электрогидравликалық импульстар көмегімен улы фосфор шламын өңдеу әдісі қарастырылады. Фосфор шламының құрылымдары электр разрядтарымен өңдеуге дейін және кейін көрсетілген. Электрогидравликалық импульстермен өңдеуден кейінгі фосфор шламының бөлшектерінің өлшемдік таралу гистограммалары қарастырылған. Электрогидравликалық өңдеу нәтижесінде фосфор шламында ірі тамшылардың төмен мөлшері және керісінше, ұсақ тамшылардың жоғары мөлшері бар анықталды.

**Кілт сөздері:** фосфор, шлам, электрогидравликалық өңдеу, құрылым, импульстардың саны, дисперстік құрам, улы қалдықтар.

*Нусупбеков Б.Р., Сақыпова С.Е., Edris A., Хасенов А.К., Нусупбеков У.Б., Болатбекова М.*

#### **Электрогидравлический способ обработки фосфорсодержащих шламов.**

Создание эффективного способа переработки токсичных отходов фосфорного производства также как и подавление самого процесса шламообразования являются актуальными до сих пор. В данной статье рассматривается способ переработки токсичных фосфорных шламов с помощью электрогидравлических импульсов. Показаны структуры фосфорных шламов до и после обработки электрическими разрядами. Рассмотрены гистограммы распределения частиц фосфорного шлама по размерам после обработки электрогидравлическими импульсами. Установлено низкое содержание крупных капель и, наоборот, высокое содержание мелких капель в фосфорном шламе в результате электрогидравлической обработки.

**Ключевые слова:** фосфор, шламы, электрогидравлическая переработка, структура, число импульсов, дисперсный состав, токсичные отходы.

*Yadawa P.K., Rai S., Chaurasiya N., Prajapati A.K.*

#### **Серпімді, жылуфизикалық және ультрадыбыстық талдау әдістерімен GdFeAl интерметалды үштік қосылысын зерттеу**

Леннард-Джонстың потенциалдық әдіс-тәсілін қолдана отырып, GdFeAl интерметалдық үштік қосылысы үшін екінші ретті серпімді тұрақтылар есептелген. Екінші ретті серпімді тұрақтыларды, ығысу модулі, көлемдік модуль, Юнг модулі, Пью коэффициенті, серпімді қатаңдық тұрақтылары және Пуассон коэффициенті сияқты серпімділік тұрақтыларды қолдана отырып, бөлме температурасында механикалық



және серпімді сипаттамалар бағаланады. Борнның тұрақтылығы мен Пью критерийлері интерметаллдық үштік қосылыстың табиғаты мен беріктігін зерттеу үшін қолданылады және оның механикалық тұрақты қосылыс екенін көрсетеді. Анизотропты тәртібін пен жылуфизикалық қасиеттерді зерттеу үшін ультрадыбыстық жылдамдық пен жылу релаксация уақыты кристаллдың бірегей осінен әртүрлі бағыттармен бірге есептелген. Ультрадыбыстық жылдамдықтың, Дебайдың орташа жылдамдығының және Z осі бойындағы жылулық релаксация уақытының температуралық өзгерісі екінші ретті серпімді тұрақтылармен бағаланды. Температураға байланысты серпімді, жылу және механикалық қасиеттермен байланысты ультрадыбыстық қасиеттер де талқыланады. Фонон-фонон (p-p) өзара әрекеттесулермен шартталған әр түрлі температураларда ультрадыбыстың өшуі есептеледі. Өшудің жауапты себебі - p-p - өзара әрекеттесулер болып табылады; ал жылу өткізгіштік температураға байланысты ультрадыбыстың өшу сипаттамасына әсер ететін негізгі фактор болып табылады. GdFeAl үштік қосылыс төмен температурада таза формаға және иілімді болады, ал бұл минималды өшуді дәлелдейді.

**Кілт сөздері:** интерметаллдық үштік қосылыс, серпімді қасиеттер, механикалық қасиеттер, жылу өткізгіштік, ультрадыбыстық қасиеттер.

*Yadawa P.K., Rai S., Chaurasiya N., Prajapati A.K.*

**Исследование интерметаллического тройного соединения GdFeAl методами упругого, теплофизического и ультразвукового анализа**

С использованием подхода потенциала Леннарда-Джонса для интерметаллического тройного соединения GdFeAl были рассчитаны упругие константы второго порядка. С использованием констант упругости второго порядка, другие модули упругости такие как модуль сдвига, объемный модуль, модуль Юнга, коэффициент Пью, константы упругой жесткости и коэффициент Пуассона оцениваются механических и упругих характеристик при комнатной температуре. Стабильность Борна и критерии Пью используются для изучения природы и прочности интерметаллического тройного соединения и показывают, что оно является механически стабильным соединением. Для исследования анизотропного поведения и теплофизических свойств были также рассчитаны скорости ультразвука и время тепловой релаксации наряду с различными ориентациями от уникальной оси кристалла. Температурное изменение скорости ультразвука, средней скорости Дебая и времени тепловой релаксации вдоль оси z оценивается с помощью констант упругости второго порядка. Также обсуждаются ультразвуковые свойства, коррелирующие с упругими, тепловыми и механическими свойствами, которые зависят от температуры. Рассчитано затухание ультразвука при различных температурах, обусловленное фонон-фононными (p-p) взаимодействиями. Ответственной причиной затухания являются p-p-взаимодействия; было получено, что теплопроводность является основным фактором, влияющим на характеристику затухания ультразвука в зависимости от температуры. Тройное соединение GdFeAl ведет себя как самая чистая форма при более низкой температуре и более пластично, о чем свидетельствует минимальное затухание.

**Ключевые слова:** интерметаллическое тройное соединение, упругие свойства, механические свойства, теплопроводность, ультразвуковые свойства.

*Waleed Subhi Hwash*

**Бордың аса ауыр изотопының ядролық құрылымы**

Берілген жұмыс аясында  $^{19}\text{B}$  бордың екі нейтронды гало зерттелді. Бұл зерттеуде микроскопиялық кластерлік модель қолданылды. Бұл зерттеуде гало ядроларының байланыс энергиясы, ядроның радиусы және деформациясы сияқты негізгі қасиеттері есептелген.  $^{19}\text{B}$  боры ядро n-p түрінде анықталды.  $^{17}\text{B}$  - жүйенің ядросы болып табылады. Үш денеден құрылған жүйенің ерекшелігі ядроның құрылымы мен деформациясынан тәуелді.  $^{17}\text{B}$  ядросы ішкі ядро ретінде қарастырылмады, бірақ белгілі бір еркіндік дәрежесіне ие. Бұл дәреже үш денелі жүйенің құрылымына көп әсер етеді. Сондықтан микроскопиялық кластерлік модель қолданылды. Бұл зерттеудің негізгі мақсаты - микроскопиялық кластер моделі деп аталатын жаңа нұсқада бұл кластер моделін қолдануын кеңейту.

**Кілт сөздері:** Гало ядролары,  $^{19}\text{B}$ , микроскопиялық кластерлік режим, нейтрондық гало құрылымы, Вудс-Саксон теңдеуі.

**Ядерная структура сверхтяжелого изотопа бора**

В рамках этой работы было исследовано двухнейтронное гало 19-бора. В этом исследовании использовалась микроскопическая кластерная модель. В этом исследовании были рассчитаны основные свойства ядер Гало, такие как энергия связи, радиус и деформация ядра.  $^{19}\text{B}$  была определена в форме ядра-n-p.  $^{17}\text{B}$  является ядром системы. Особенность системы из трех тел зависит от структуры и деформации ядра. Ядро  $^{17}\text{B}$  не рассматривалось как внутреннее ядро, но обладает некоторой степенью свободы. Эта степень оказывает большое влияние на структуру системы из трех тел. Поэтому использовано микроскопическая кластерная модель. Основная цель данного исследования - расширить использование модели кластера в новой версии, называемой моделью микроскопического кластера.

**Ключевые слова:** Гало-ядра,  $^{19}\text{B}$ , микроскопический кластерный режим, структура нейтронного гало, уравнение Вуда-Саксона.

**Касенова Т.Қ.**

**Параметрленген сегіз шыңды модель және  $10_{136}$  түйін инварианты**

Мақалада матрицаның параметрлеуіне ерекше назар аударып отырып, сегіз шыңды модельдің белгілі элементтері талқыланады және кеңейтіледі. Матрицаның мәндері осы модель арқылы өрілген түйін арқылы өзара байланысты екі өлшемді кеңістіктегі соңғы шаршы торларда жарамды. Эллиптикалық функциялардың күрделі нұсқасы бар бос фермиондардың параметрленген сегіз шыңды моделінің шектеулі торда жарамды жаңа шешімі құрастырылады. Якоби эллиптикалық функциясының элементтері бар сегіз шыңды модельдің қолдану аймағы және модель үшін аналитикалық жолмен алынған нәтижелерді салыстыру арқылы оның негізінде түйін инвариантын құру. Клебш-Гордан коэффициенттерін және Янг-Бакстер теңдеуінің статистикалық механикасының негізгі құралын қолданып түйін инвариантын құру толық зерттеледі.

**Кілт сөздері:** түйін, эллиптикалық функция, Клебш-Гордан коэффициенттері.

**Касенова Т.К.**

**Параметризованная восьмивершинная модель и инвариант узла  $10_{136}$**

В статье обсуждаются и расширяются известные элементы восьмивершинной модели, уделяя особое внимание параметризации матрицы. Значения матрицы связаны между собой узлом через косы и эта модель справедлива на конечных квадратных решетках в двумерном пространстве. Будет построено новое решение параметризованной восьмивершинной модели свободных фермионов с комплексной версией эллиптических функций, справедливое на конечной решетке. Обсуждается область применимости восьмивершинной модели с элементами эллиптической функции Якоби и построения на ее основе инварианта узла путем сравнения результатов, полученных аналитически для модели. Будет подробно изучено построение инварианта узла с использованием коэффициентов Клебша-Гордана и основного инструмента статистической механики уравнения Янга-Бакстера.

**Ключевые слова:** узел, эллиптическая функция, коэффициенты Клебша-Гордана.

**INFORMATION  
ABOUT AUTHORS**

**АВТОРЛАР ТУРАЛЫ  
МӘЛІМЕТТЕР**

**СВЕДЕНИЯ  
ОБ АВТОРАХ**

- Aimukhanov, A.K.** – PhD, Associate Professor, Professor, Department of Radiophysics and Electronics, E.A. Buketov Karaganda University, Scientific Center for Nanotechnology and Functional Nanomaterials, Karaganda, Kazakhstan
- Akhatova, Zh.Zh.** – PhD student, Researcher, E.A. Buketov Karaganda University, Scientific Center for Nanotechnology and Functional Nanomaterials, Karaganda, Kazakhstan
- Akhazhanov, S.B.** – PhD, Associate Professor, E.A. Buketov Karaganda University, Karaganda, Kazakhstan
- Akishev, M.S.** – Master (Sci.), BI Group (JSC), Nur-Sultan, Kazakhstan
- Alkina, A.D.** - Master, Senior Lecturer, Department of Information Technologies and Security, Karaganda Technical University, Karaganda, Kazakhstan
- Aniskin, A.** – Candidate of techn. sciences, Assistant Professor, University North, Varaždin, Croatia
- Baltabekov, A.S.** - Candidate of techn.sciences, Associate Professor, E.A. Buketov Karaganda University, Karaganda, Kazakhstan
- Bayatanova, L.B.** - PhD, Senior Researcher, "PlasmaScience" LLP, Ust-Kamenogorsk, Kazakhstan
- Bolatbekova, M.** – Master, Junior Researcher, E.A. Buketov Karaganda University, Karaganda, Kazakhstan
- Chaurasiya, Navin** – PhD, Master, Assistant Professor, Department of Physics, Prof. Rajendra Singh (Rajju Bhiya) Institute of Physical Sciences for Study and Research, VBS Purvanchal University, Jaunpur, Uttar Pradesh, India
- Cherneta, O.G.** - Candidate of techn.sciences, Associate Professor of the Department "Cars and Automotive Industry", Dniprovsk State Technical University, Kamenskoe, Ukraine
- Dzhumanov, S.** – Doctor of phys.-math. sciences, Professor, Chief Researcher, Institute of Nuclear Physics of the Uzbekistan Academy of Sciences, Tashkent, Uzbekistan
- Edris, A.** – Master, Researcher, E.A. Buketov Karaganda University, Karaganda, Kazakhstan
- Guchenko, S.A.** - Master of physics, Junior Researcher, E.A. Buketov Karaganda University, Karaganda, Kazakhstan
- Hwash, Waleed S.** - PhD, Assoc. Prof., Faculty of Education for Pure Sciences, University of Anbar, Ramadi, Iraq
- Ilyassov, B.R.** - PhD, Associate Professor, Professor, Department of Intelligent Systems and Cybersecurity, Astana IT University, Nur-Sultan, Kazakhstan
- Kalitova, A.A.** - PhD, Senior Researcher, Institute of Composite Materials, Ust-Kamenogorsk, Kazakhstan
- Kaluzhsky, D.L.** - Dr. Sci., Professor of the Department of Electronics and Electrical Engineering, Novosibirsk State Technical University, Novosibirsk, Russia
- Kassenova, T.K.** – PhD student, Master, M.Kh.Dulaty Taraz Regional University, Taraz, Kazakhstan
- Kassymov, S.S.** – Candidate of phys.-math.sciences, Associate Professor, Head of the Science and Commercialization Department E.A. Buketov Karaganda University, Karaganda, Kazakhstan
- Khassenov, A.K.** – PhD, Associate Professor, Professor, E.A. Buketov Karaganda University, Karaganda, Kazakhstan
- Khudayberdiev, Z.S.** – Junior Researcher at Institute of Nuclear Physics, Uzbekistan Academy of Sciences, Tashkent, Uzbekistan
- Klimova, G.N.** - PhD, Associate Professor, School of Energy & Power Engineering National Research Tomsk Polytechnic University, Tomsk, Russia
- Kowalewski, P.** - PhD, Professor, Wroclaw University of Science and Technology, Wroclaw, Poland
- Kozhanova, R.S.** – PhD student, Researcher, "PlasmaScience" LLP, Ust-Kamenogorsk, Kazakhstan
- Kozlovskiy, A.L.** - PhD, Associate Professor, Head of the Laboratory of Solid State Physics, Astana branch of the Institute of Nuclear Physics of the Ministry of Energy of the Republic of Kazakhstan, Nur-Sultan, Kazakhstan
- Kubich, V.I.** - Candidate of techn.sciences, Associate Professor of the Department "Cars", National University "Zaporozhye Polytechnic", Zaporozhye, Ukraine
- Kurbanov, U.T.** – Doctor of phys.-math. sciences, Senior Researcher, Head of the laboratory at Institute of Nuclear Physics, Uzbekistan Academy of Sciences, Tashkent, Uzbekistan
- Latypova, M.A.** – Master, Senior Lecturer, Karaganda Industrial University, Temirtau, Kazakhstan
- Lysenko, E.N.** - Doctor of techn. sciences, Professor, Head of the Research Laboratory, National Research Tomsk Polytechnic University, Tomsk, Russia
- Malyshev, A.V.** – Candidate of phys.-math. sciences, Senior Researcher, National Research Tomsk Polytechnic University, Tomsk, Russia
- Mekhtiyev, A.J.** - Candidate of techn. sciences, Professor, Department of Operation of Electrical Equipment, S. Seifullin Kazakh Agrotechnical University, Nur-Sultan, Kazakhstan
- Neshina, Ye.G.** - Candidate of techn. sciences, Head of the Department of Power Systems, Karaganda Technical University, Karaganda, Kazakhstan

- Novoselov, I.Yu.** - Lecturer in Division for Nuclear Fuel Cycle, School of Nuclear Science and Engineering, National Research Tomsk Polytechnic University, Tomsk, Russia
- Nussupbekov, B.R.** – Candidate of techn.sciences, Associate Professor, Professor, E.A. Buketov Karaganda University, Karaganda, Kazakhstan
- Nussupbekov, U.B.** – PhD student, Master, E.A. Buketov Karaganda University, Karaganda, Kazakhstan
- Obukhov, S.G.** – Doctor of techn. sciences, Professor, School of Energy & Power Engineering National Research Tomsk Polytechnic University, Tomsk, Russia
- Omarbekova, G.I.** - Master, PhD student, Faculty of Physics and Technology, E.A. Buketov Karaganda University, Karaganda, Kazakhstan
- Panin, E.A.** – PhD, Associate Professor, Department "Metal Processing by Pressure", Karaganda Industrial University, Temirtau, Kazakhstan
- Plotnikov, I.A.** - PhD, Associate Professor, School of Energy & Power Engineering National Research Tomsk Polytechnic University, Tomsk, Russia
- Prajapati, Aadesh Kumar** – PhD, Pursuing, Junior Research Fellow, Department of Physics, Prof. Rajendra Singh (Rajju Bhiya) Institute of Physical Sciences for Study and Research, VBS Purvanchal University, Jaunpur, Uttar Pradesh, India
- Rai, Sachin** – PhD, Pursuing, Master, Senior Research Fellow, Department of Physics, Prof. Rajendra Singh (Rajju Bhiya) Institute of Physical Sciences for Study and Research, VBS Purvanchal University, Jaunpur, Uttar Pradesh, India
- Rakhadilov, B.K.** – PhD, Associate Professor, "PlasmaScience" LLP, Ust-Kamenogorsk, Kazakhstan
- Rozhkova, X.S.** – PhD student, Researcher, E.A. Buketov Karaganda University, Scientific Center for Nanotechnology and Functional Nanomaterials, Karaganda, Kazakhstan
- Sakipova, S.E.** - Candidate of phys.-math.sciences, Associate Professor, Professor, E.A. Buketov Karaganda University, Karaganda, Kazakhstan
- Sarsikejev, Ye.Zh.** – PhD, Head of the Department of Electrical Equipment Operation, S. Seifullin Kazakh Agrotechnical University, Nur-Sultan, Kazakhstan
- Satbaeva, Z.A.** – PhD student, Researcher, "PlasmaScience" LLP, Ust-Kamenogorsk, Kazakhstan
- Senyut, V.T.** - Candidate of techn. sciences, Leading Researcher, Laboratory "Nanostructured and Superhard Materials" of the State Scientific Institution " The Joint Institute of Mechanical Engineering of the National Academy of Sciences of Belarus", Minsk, Belarus
- Shrager, E.R.** - Doctor of phys.-math. sciences, Professor, National Research Tomsk State University, Tomsk, Russia
- Stary, O.** - Doctor of techn. sciences, Professor, Vice-rector, Czech Technical University in Prague, Prague, Czech Republic
- Surzhikov, A.P.** - Doctor of phys.-math. sciences, Professor, Head of Department of Control and Diagnostics, National Research Tomsk Polytechnic University, Tomsk, Russia
- Tikhonov, A.E.** - PhD student, School of Nuclear Science and Engineering, National Research Tomsk Polytechnic University, Tomsk, Russia
- Tolkynbayev, T.A.** – Doctor of techn. sciences, Professor, Dean of the Faculty of Architecture and Civil Engineering, L.N. Gumilyov Eurasian National University, Nur-Sultan, Kazakhstan
- Tulebekova, A.S.** – PhD, Associate Professor, L.N. Gumilyov Eurasian National University, Nur-Sultan, Kazakhstan
- Uteпов, Ye.B.** – PhD, Associate Professor, Head of R&D, CSI Research & Lab (LLP), Professor, L.N. Gumilyov Eurasian National University, Nur-Sultan, Kazakhstan
- Volokitin, A.V.** – PhD, Associate Professor, "Metal Processing by Pressure" Department, Karaganda Industrial University, Temirtau, Kazakhstan
- Volokitina, I.E.** – PhD, Associate Professor, Department of Metallurgy and Mining, Rudny Industrial Institute, Rudny, Kazakhstan
- Yadawa, Pramod Kumar** – PhD, Associate Professor, Department of Physics, Prof. Rajendra Singh (Rajju Bhiya) Institute of Physical Sciences for Study and Research, V.B.S Purvanchal University, Jaunpur, Uttar Pradesh, India
- Yurov, V.M.** - Candidate of phys.-math.sciences, Associate Professor, Professor, Karaganda Technical University, Karaganda, Kazakhstan
- Zeidenov, A.K.** – PhD, Associate professor, Dean of the Physical-Technical Faculty, E.A. Buketov Karaganda University, Scientific Center for Nanotechnology and Functional Nanomaterials, Karaganda, Kazakhstan
- Zharassov, Sh.Zh.** – PhD student, L.N. Gumilyov Eurasian National University, Nur-Sultan, Kazakhstan

### **About «Eurasian Physical Technical Journal»**

ISSN 1811-1165 (Print); ISSN 2413-2179 (Online)

Abbreviated key title: Eurasian phys. tech. j.

Eurasian Physical Technical Journal (Eurasian phys. tech. j.) is a peer-reviewed open access international scientific journal publishing original research results on actual problems of technical physics and other related fields. Since 2004 «Eurasian phys. tech. j.» is published in English. The international editorial board consists of leading physicists from 9 countries.

Since May 2019 «Eurasian phys. tech.j.» has been indexed in the Scopus database on four scientific areas: Energy, Engineering, Materials Science, Physics and Astronomy.

Re-registration Certificate No.KZ50VPY00027647 of the «Eurasian phys. tech. j.» issued October 6, 2020 by Information Committee of the Ministry of Information and Public Development of the Republic of Kazakhstan. Now Eurasian phys. tech. j. will be published quarterly.

In January 28, 2021, the “Eurasian Physical Technical Journal” is included in the updated list of journals recommended by the Committee in the following areas: Physics, Energy, Materials Science.

### **Publication Ethics and Malpractice Statement**

Submission of an article to the Eurasian phys. tech. j. implies that the paper described has not been published previously, that it is not under consideration for publication elsewhere, that its publication is approved by all authors and tacitly or explicitly by the responsible authorities where the paper was carried out, and that, if accepted, it will not be published elsewhere in the same form, in English or in any other language, including electronically without the written consent of the copyright holder. In particular, translations into English of papers already published in another language are not accepted.

For information on Ethics in publishing and Ethical guidelines for journal publication see <http://www.elsevier.com/publishingethics> and <http://www.elsevier.com/journal-authors/ethics>.

The Eurasian phys. tech. j. follows the Code of Conduct of the Committee on Publication Ethics (COPE), and follows the COPE Flowcharts for Resolving Cases of Suspected Misconduct ([http://publicationethics.org/files/u2/New\\_Code.pdf](http://publicationethics.org/files/u2/New_Code.pdf)).

To verify originality, your article may be checked by the originality detection service Cross Check <http://www.elsevier.com/editors/plagdetect>.

**Authors** are responsible for the content of their publications. No other forms of scientific misconduct are allowed, such as plagiarism, falsification, fraudulent data, incorrect interpretation of other works, incorrect citations, etc. Authors are obliged to participate in peer review process and be ready to provide corrections, clarifications, retractions and apologies when needed. All authors of a paper should have significantly contributed to the research.

**Reviewers** should provide objective judgments and should point out relevant published works which are not yet cited. Reviewed articles should be treated confidentially. The reviewers will be chosen in such a way that there is no conflict of interests with respect to the research, the authors and/or the research funders.

**Editors** have complete responsibility and authority to reject or accept a paper, and they will only accept a paper when reasonably certain. They will preserve anonymity of reviewers and promote publication of corrections, clarifications, retractions and apologies when needed.

The acceptance of a paper automatically implies the copyright transfer to the Eurasian phys. tech. j.

All submitted papers will be sent for reviewing to leading experts in the given area.

The Editorial Board of the Eurasian phys. tech. j. will monitor and safeguard publishing ethics.

The editors reserve the right to accept or reject manuscripts.

---



---

## GUIDELINES FOR AUTHORS

Research articles are accepted for exclusive publication in the «**Eurasian phys. tech. j.**» in English. The manuscripts must contain original results of investigation in the 4 scientific areas:

**ENERGY; ENGINEERING; MATERIALS SCIENCE; PHYSICS AND ASTRONOMY.**

The publications of manuscripts should be recommended by official a Cover letter of the organization (University) in which the work was performed.

The author who submitted an article for publication will be considered as a corresponding author.

A scientific article should contain the results of original scientific research previously unpublished and not intended for publication in other publications. Scientific articles submitted for publication in scientific journals should comprise at least 70% of the original text.

The structure of the article includes the following sections:

**Title:** includes a separate line on the left the **UDC** index, information about the authors (surname and initials, name of institution, city, country, e-mail of a corresponding author, title of the article.

**Abstract** should consist of at least 5-6 sentences, not exceeding 200 words without formula, references, abbreviations. An abstract is a short and powerful summary that describes the focus of a research paper. It could contain the information about why the research study was done, background, what the methodology was and something about the findings of the author(s).

**Keywords:** at least 3-10 basic terms or short phrases used in the article.

The text should be divided on structural parts: **Introduction, Theoretical part, Methods and materials or Experimental technique, Results and Discussion, Conclusions.**

**Conclusions:** formulating main results; a comparison of the results with the existing data on this topic; assessment of scientific novelty and practical value of the results.

**Acknowledgments** may be shown at the end of the article text, before References.

**References:** a bibliographic list is compiled according to the requirements:

- Books, abstracts, patents: Surname and initials of the authors (it is enough to indicate the first three or one surnames, et al), *Title of the book* in italics, publish house or city, year and total number of pages.

- Journals, collections of papers, conference proceedings - Surname and initials of the authors (the first three are enough), the title of the article, the *Title of the journal* in italics (you can use the abbreviated title), city and / or country, year, volume, issue number, pages of the "begining and end" (pp. ... - ... ).

- Internet links also must to indicated the authors, the title and URL

**Title, Abstract and Keywords** are given in English, Qazaq, and Russian.

The volume of the article, including bibliography, should not exceed 6-10 pages including tables, figures (no more than 6-8) and references (no more than 30-35) of text typed on a computer (Microsoft Word editor. A review paper must not be more than 15-20 pages (including no more than 10 figures).

Fields of the manuscript should be: left, upper, lower - 30 mm, right - 15 mm; font - Times New Roman, size - 11 pt; line spacing - single; alignment - in width; indent - 0.8 cm.

All abbreviations and acronyms, with the exception of obviously well-known, should be deciphered at first use in the text.

All references must be numbered in the text (for example, [1], [2-4]) and listed in numerical order.

Equations in your paper have to be written using the Microsoft Equation Editor or the MathType.

**Tables** must be inserted into the text.

**Figures** should be prepared in a digital form suitable for direct reproduction. Figures shall be submitted on the separate sheets or can be included into the text.

The following files must be submitted via e-mail:

- Article text (\*.doc);

